

# Quantum Chemical Studies of Transition-Metal Complexes and Aqueous Solvent Effects

vorgelegt von

Dipl.-Chem.

**Kolja Theilacker**

geb. in Heilbronn

von der Fakultät II – Mathematik und Naturwissenschaften

der Technischen Universität Berlin

zur Erlangung des akademischen Grades

Doktor der Naturwissenschaften

– Dr. rer. nat. –

genehmigte Dissertation

Promotionsausschuss:

Vorsitzender: Prof. Dr. rer. nat. Reinhard Schomäcker

Gutachter: Prof. Dr. rer. nat. Martin Kaupp

Gutachter: Prof. Dr. rer. nat. Sebastian Hasenstab-Riedel

Tag der wissenschaftlichen Aussprache: 28.11.2016

**Berlin 2016**



---

## Zusammenfassung

Dank der rasanten Entwicklung im Bereich der Computer-Hardware und großer Fortschritte bei Algorithmen und Methoden der theoretischen Chemie sind quantenchemische Rechnungen über die letzten Jahrzehnte hinweg ein zentrales Werkzeug geworden, um tiefere Einblicke in die elektronische Struktur von Molekülen zu erhalten. Besonders wichtig ist dies bei der Entwicklung und Verbesserung neuer Katalysatoren und bei der Einschätzung von Lösungsmiteleinflüssen auf die Stabilität und Reaktivität von Molekülen. In situ-erzeugte einkernige hochvalente Eisen-Oxo-Komplexe werden als aussichtsreiche und interessante Kandidaten für aktive Spezies in Katalyseprozessen betrachtet. Ihr Vorbild sind die hochreaktiven Eisen-Oxo Intermediate in den aktiven Zentren diverser Enzyme, die für eine Vielfalt von Reaktionen, von C-H-Aktivierung bis zu Sauerstoffatom-Transfer, als aktive Spezies in katalytischen Prozessen wirken. Eisen als katalytisch aktives Metall ist natürlich auch besonders für die Industrie relevant, die ein Interesse daran hat, teure Metalle wie Platin und Palladium durch billigere Alternativen zu ersetzen. Die synthetischen Eisen-Oxo-Komplexe werden üblicherweise nach Art ihres Liganden in Häm- und nicht-Häm-Eisen-Oxo-Komplexe unterteilt. Diese Arbeit beschäftigt sich mit letzteren. Für die Berechnung von größeren Übergangsmetallkomplexen spielt die Dichtefunktionaltheorie als beliebteste quantenchemische Methode der Wahl eine zentrale Rolle. Sie verbindet niedrige Rechenkosten und niedrige Anforderungen an die Größe der verwendeten Basissätze mit einer hohen Genauigkeit. Diese hohe Genauigkeit wird aber nur erreicht, wenn ein geeignetes Funktional für das chemische Problem gewählt wird, was eine Validierung verschiedener Funktionale für den jeweiligen Problemfall nötig macht. In vielen Fällen lässt sich die Geschwindigkeit einer Reaktion auch durch die Wahl eines geeigneten Lösungsmittels gewaltig erhöhen. Besonders protische Lösungsmittel, die durch Wasserstoffbrückenbindungen einen Übergangszustand stabilisieren oder destabilisieren können und somit die Reaktionsbarriere entweder absenken oder erhöhen, zeigen großes Potenzial. Die Simulation von Wasser als Lösungsmittel stellt eine große Herausforderung für Kontinuum-Solvensmodelle dar. Das gleiche galt auch für Lösungsmittelgemische und andere protische Lösungsmittel wie Ethanol. Wer heutzutage auf aufwendige Molekulardynamik Simulationen verzichten möchte, hat mit dem kürzlich eingeführten D-COSMO-RS eine hervorragende Alternative, die kaum teurer ist als die Verwendung von Standard-Kontinuum-Solvensmodellen.

Die vorliegende Arbeit gliedert sich in drei Teile. Im ersten Teil wird eine Reihe wichtiger Vertreter von nicht-Häm Eisen-Oxo-Komplexen untersucht. Es wird der Frage nachge-

---

gangen, ob die Eisen(IV)- und Eisen(V)-Oxo-Komplexe nicht besser als Eisen(III)- und Eisen(IV)-Oxyl Radikale beschrieben werden sollten. Dazu wurden die Spinverteilungen untersucht und die Richtigkeit der berechneten elektronischen Strukturen durch etliche Vergleiche mit experimentellen Werten bestätigt. Außerdem werden neue Eisen-Oxo-Komplexe vorgestellt, die in Kooperation mit Experimentatoren eingehend erforscht wurden. In ihnen lassen sich Reaktivität und Energieunterschiede zwischen Triplett- und Quintett-Spinzustand durch geschickte Verzerrung des Ligandenfeldes steuern. Der letzte Abschnitt des ersten Teils beschäftigt sich mit einem Eisen(V)-Nitrido Komplex, bei dem überraschende Schwierigkeiten in den Berechnungen von Schwingungsfrequenzen aufgetreten waren. Der zweite Teil der Dissertation umfasst Kapitel 4 und beschäftigt sich mit Lösungsmittelleffekten auf Diels-Alder Reaktionen und auf die Stabilität von Gold(III)-Halogeniden. Im Fokus steht hier Wasser als Lösungsmittel, das mit D-COSMO-RS simuliert wird. Dies dient zugleich auch als Validierung dieser relativ jungen Methode. Die berechneten Diels-Alder Reaktionen zeigen die Wichtigkeit der Wahl des Dichtefunktional und dass D-COSMO-RS in der Tat zur Simulation von wässrigen Lösungen geeignet ist. Im Zusammenhang der Speziation von Goldhalogeniden in Wasser konnte erstmals das Zusammenspiel relativistischer und wässriger Lösungsmittelleffekte analysiert werden. Der dritte Teil der Dissertation befasst sich mit der erstmaligen Validierung lokaler Hybridfunktionale für den großen GMTKN30 Testsatz für Hauptgruppen-Energetik. Dank der Einführung von Kalibrierungsfunktionen konnten große Teile des sogenannten Eichursprungproblems der Austausch-Energiedichten behoben werden. Die neueste Generation der lokalen Hybride zeigt daher eine Genauigkeit, die mit hochparameterisierten globalen Hybriden konkurrieren kann.

---

## Abstract

Thanks to the rapid development in the area of computer hardware, and appreciable advances in algorithms and theoretical chemistry methods, quantum chemical calculations have become a crucial tool over the last decades to gain deeper insights into the electronic structure of molecules. This is especially important for the development and improvement of new catalysts and in the assessment of solvent effects on the stability and reactivity of molecules. In situ-generated mononuclear high-valent iron-oxo complexes are seen as promising and interesting active species for catalytic processes. They are modeled after the highly reactive iron-oxo intermediates in the active centers of various enzymes, that act as catalysts for a variety of reactions, from C-H activation to oxygen atom transfer. Of course, iron as catalytically active metal is also especially relevant for industry, which has an interest in replacing expensive metals like palladium or platinum by cheaper alternatives. The synthetic iron-oxo complexes are usually divided into heme and non-heme iron-oxo complexes, based on the type of their ligand. This work is concerned with the latter. Density functional theory has been widely accepted as the most popular quantum chemical method of choice for the calculation of larger transition metal complexes. It combines low computational costs and low basis set requirements with high accuracy. However, this high accuracy is only reached if a suitable functional is chosen for the given chemical problem, which makes validation of different functionals necessary for each problem case. In many cases, the speed of a reaction can also be massively increased by the choice of a suitable solvent. Especially protic solvents, that can stabilize or destabilize transition states by hydrogen-bonding, and thereby lower or increase the kinetic barrier, show great potential. The simulation of water as a solvent is a challenge for continuum solvent models. The same has been true for solvent mixtures and other protic solvents like ethanol. Nowadays, whoever wants to do without costly molecular dynamics simulations, has a cost-effective alternative provided by the relatively young D-COSMO-RS, which is hardly more expensive than a normal quantum chemical calculation.

This work is subdivided into three parts. In the first part, a series of important representatives of non-heme iron-oxo complexes is investigated. The question is pursued, whether iron(IV)- and iron(V)-oxo complexes should better be described as iron(III)- and iron(IV)-oxyl radicals instead. To this end, the spin distributions have been investigated and the correctness of the calculated electronic structures were confirmed by multiple comparisons to experimental data. In addition, new iron-oxo complexes are

---

presented, which have been thoroughly investigated in cooperation with experimentalists. In these compounds, reactivity and energy gaps between triplet and quintet spin states can be controlled by clever distortion of the ligand field. The last section of the first part is concerned with an iron(V)-nitrido complex, for which surprising difficulties had arisen in the vibrational frequency calculations. The second part of the dissertation encompasses chapter 4, dealing with solvent effects on Diels-Alder reactions and with the stability of gold(III) halides. The focus lies on water as solvent, which is simulated by D-COSMO-RS. This also serves as validation for this relatively recent method. The studied Diels-Alder reactions reveal a high importance of the choice of density functional and show that D-COSMO-RS is indeed suitable for the simulation of aqueous solutions. In context of the speciation of aqueous gold halides, the interplay of relativistic and aqueous solvent effects has been analyzed for the first time. The third part of this work centers on the first validation of local hybrid functionals, on the large main-group energy GMTKN30 test set. Thanks to the introduction of calibration functions, large parts of the so-called gauge problem of exchange-energy densities could be fixed. Therefore the most recent generation of local hybrids shows an accuracy, that can compete with highly parameterized global hybrids.

---

## List of Abbreviations

aug	Augmented
Bn-TPEN	N-benzyl-N,N',N'-tris(2-pyridylmethyl)-1,2-diaminoethane
bTAML	Biuret-modified Tetra-Amido Macrocyclic Ligand
CBS	Complete-Basis-Set Extrapolation
cc	Correlation Consistent (basis sets)
CCSD	Coupled-Cluster Singles and Doubles (method)
COSMO	Conductor-like Screening Model
CP	Cyclopentadiene
D-COSMO-RS	Direct COSMO for Real Solvents
DFT	Density Functional Theory
ECP	Effective Core Potential
EPR	Electron Paramagnetic Resonance
EXAFS	Extended X-Ray Absorption Fine Structure
EXX	Exact Exchange
GEA	Gradient Expansion Approximation
GGA	Generalized Gradient Approximation
HF	Hartree-Fock (method)
HR-ESI	High-resolution Electrospray Ionisation (spectroscopy)
H <sub>3</sub> buea	1,1,1-tris[(N-tert-butylureaylato)-N-ethyl]aminato
IRMPD	Infra-red-multi-photon-dissociation Spectroscopy
KS	Kohn-Sham (theory)
LDA	Local Density Approximation
LMF	Local-Mixing Function
LSDA	Local Spin Density Approximation
MAE	Mean Absolute Error
mCPBA	Meta-chloroperbenzoic Acid
MP <sub>n</sub>	<i>n</i> th-Order Møller-Plesset Perturbation Theory
MS	Mass Spectrometry

---

MSE	Mean Signed Error
MVK	Methyl-Vinyl-Ketone
NPA	Natural Population Analysis
NQ	1,4-Naphthoquinone
N4Py	N,N-bis(2-pyridylmethyl)-N-bis(2-pyridyl)methylamine
pV(D,T,Q,5)Z	Polarized Valence (Double, Triple, Quadruple, Quintuple)-Zeta (basis set)
QZVP	Quadruple Zeta Valence Polarization (basis set)
RI	Resolution-of-the-Identity (approximation)
SCF	Self-Consistent Field (method)
SCS	Spin-Component-Scaled
SIE	Self-Interaction Error
TAML	Tetraamido Macrocylic Ligand
TMC	1,4,8,11-tetramethyl-1,4,8,11-tetraazacyclotetradecane
TMCS	1-(2- mercaptoethyl)-4,8,11-trimethyl-1,4,8,11-tetraazacyclo- tetradecane
TMG <sub>3</sub> tren	1,1,1-tris(2-[N2-(1,1,3,3-tetramethylguanidino)]ethyl)amine
tpa <sup>Ph</sup>	tris(5-phenylpyrrol-2-ylmethyl)amine
TZVP	Triple Zeta Valence Polarization (basis set)
UV/Vis	Ultra-Violet/Visible (spectroscopy)
WTMAD	Weighted Total Mean Absolute Deviation

# Contents

Zusammenfassung . . . . .	I
Abstract . . . . .	III
List of Abbreviations . . . . .	V
<b>1 Introduction</b>	<b>1</b>
<b>2 Theory</b>	<b>3</b>
2.1 Density Functional Theory . . . . .	3
2.1.1 Introduction to DFT . . . . .	3
2.1.2 Exchange-Correlation Functionals . . . . .	6
2.1.3 Local Hybrid Functionals . . . . .	10
2.1.4 D3 Dispersion Corrections . . . . .	22
2.2 Calculation of Mössbauer parameters with DFT . . . . .	25
2.3 COSMO and D-COSMO-RS . . . . .	30
2.3.1 COSMO . . . . .	31
2.3.2 D-COSMO-RS . . . . .	32
<b>3 High-Valent Non-Heme Iron-Oxo Complexes</b>	<b>36</b>
3.1 Overview . . . . .	36
3.2 The Question of Iron(IV)-Oxo vs Iron(III)-Oxyl Character . . . . .	37
3.2.1 Introduction . . . . .	37
3.2.2 Computational Details . . . . .	38
3.2.3 Results and Discussion . . . . .	39
3.2.3.1 A Selection of Non-Heme Iron-Oxo Complexes . . . . .	39
3.2.3.2 Spin States and the Iron-Oxo Character . . . . .	43
3.2.3.3 Verification of the Correct Electronic Structure . . . . .	52
3.2.3.4 Bonding Character of the Transition States for Hydrogen- Atom Transfer . . . . .	59
3.2.4 Conclusions . . . . .	66

3.3	Structurally Distorted Iron(II) Complexes with N <sub>5</sub> Pentadentate Ligands	69
3.3.1	Introduction . . . . .	69
3.3.2	Computational Details . . . . .	70
3.3.3	Results and Discussion . . . . .	71
3.3.3.1	Structural Distortions . . . . .	71
3.3.3.2	Spin States . . . . .	74
3.3.3.3	Competing Ligand Conformations . . . . .	76
3.3.4	Conclusions . . . . .	77
3.4	Structurally Distorted Iron(IV)-Oxo Complexes with N <sub>5</sub> Pentadentate Ligands . . . . .	79
3.4.1	Introduction . . . . .	79
3.4.2	Computational Details . . . . .	81
3.4.3	Results and Discussion . . . . .	81
3.4.3.1	Spin-State Energetics of Iron(IV)-Oxo Species . . . . .	81
3.4.3.2	Structural Distortions . . . . .	84
3.4.3.3	Intrinsic Decay Reactions of [1(O)] <sup>2+</sup> . . . . .	88
3.4.3.4	Mössbauer Parameters and Hydrogen Abstraction from Acetonitrile . . . . .	91
3.4.4	Conclusions . . . . .	96
3.5	Dramatic Effects of Spin Contamination on Vibrational Frequencies and Structure of a Formal Iron(V)-Nitrido Complex . . . . .	97
3.5.1	Introduction . . . . .	97
3.5.2	Computational Details . . . . .	98
3.5.3	Results and Discussion . . . . .	98
3.5.4	Conclusions . . . . .	101
<b>4</b>	<b>Reactions in Aqueous Solution modeled by D-COSMO-RS</b>	<b>102</b>
4.1	Validation of the Direct-COSMO-RS Solvent Model for Diels-Alder Reactions in Aqueous Solution . . . . .	104
4.1.1	Introduction . . . . .	104
4.1.2	Computational Details . . . . .	104
4.1.3	Results and Discussion . . . . .	106
4.1.3.1	Validation of Density Functionals against Wave-Function Methods in the Gas Phase . . . . .	106
4.1.3.2	Modeling (Aqueous) Solvent Effects . . . . .	110

4.1.4	Conclusions . . . . .	124
4.2	Relativistic and Solvation Effects on the Stability of Gold(III) Halides in Aqueous Solution . . . . .	126
4.2.1	Introduction . . . . .	126
4.2.2	Computational Details . . . . .	127
4.2.3	Results and Discussion . . . . .	128
4.2.3.1	Gas-Phase Reaction $\text{AuX}_4^- \rightarrow \text{AuX}_2^- + \text{X}_2$ . . . . .	128
4.2.3.2	$\text{AuX}_4^- \rightarrow \text{AuX}_2^- + \text{X}_2$ Reaction in Aqueous Solution: Relativistic and Solvation Effects at the B3LYP Level . . .	132
4.2.3.3	Interpretation of Trends in Solvent and Relativistic Effects	136
4.2.3.4	On the Hydrolysis of $\text{AuCl}_4^-$ . . . . .	137
4.2.3.5	Disproportionation of $\text{AuCl}_2^-$ . . . . .	139
4.2.4	Conclusions . . . . .	140
<b>5</b>	<b>Validation of Local Hybrid Functionals for the GMTKN30 Test Set</b>	<b>141</b>
5.1	Introduction . . . . .	141
5.2	Computational Details . . . . .	143
5.3	Evaluation for the GMTKN30 Database . . . . .	145
5.4	Conclusions . . . . .	150
<b>6</b>	<b>General Summary</b>	<b>152</b>
	<b>References</b>	<b>156</b>
	<b>Appendix I</b>	<b>173</b>
	<b>Appendix II</b>	<b>189</b>
	<b>Appendix III</b>	<b>200</b>
	<b>List of Publications</b>	<b>209</b>
	<b>Acknowledgements</b>	<b>211</b>

# 1 Introduction

Quantum chemical calculations have come a long way since their first introduction in the late 1920s. They allow insight into chemical reactions, and into the electronic structure of molecules, that were often inaccessible from experiment and spectroscopy. Over time the focus of the scientific community has shifted from the calculation of atoms, very small molecules, and heavily truncated model systems, to the description of more realistic chemical systems. This change was made possible by the rapid and massive improvement of computer hardware over the last decades, and by the development of more and more efficient quantum chemical programs, algorithms, and methods. One of these methods is Kohn-Sham Density Functional Theory (KS-DFT), which has proven to be of such importance to quantum chemistry, that the 1998 nobel prize in chemistry has been awarded to Walter Kohn and John A. Pople in part for their developments and applications in this field. The main advantage of KS-DFT lies in its low computational cost, due to the good scaling with system size. Its good performance is mainly dependent on the choice of the exchange-correlation functional, and better and more flexible exchange-correlation functionals have been developed over the past decades. One particular group of these exchange-correlation functionals are local hybrids which use a position-dependent exact exchange admixture, determined by a local mixing function. Several of these promising functionals are validated in this work with the large GMTKN30 test set database of Grimme and Goerigk. An additional improvement to KS-DFT can be gained by including dispersion interactions which are normally missing in this method, but can be vital to the correct description of molecular structures and relative energies. Using the D3 dispersion corrections by Grimme *et al.* is a popular and widely used inexpensive way to introduce dispersion interactions into KS-DFT calculations, without changing the functional. In this work, such D3 dispersion corrections have been optimized and used for local hybrids.

Moving to more realistic descriptions in theoretical chemistry also means going from the gas-phase to the condensed phase, in which many reactions take place. In the condensed

phase, environmental effects start to play a much larger role, and have to be included in the calculations somehow. This can be achieved either by implicit or explicit modeling of solvent effects. Explicit modeling of solvent effects, that goes beyond adding a few solvent molecules to the calculation, quickly becomes very expensive, as it usually requires QM/MM or molecular dynamics simulations. The much cheaper implicit modeling of solvent effects is often done by using dielectric continuum solvent models like PCM (polarizable continuum model) or COSMO (conductor-like screening model). While continuum solvent models work well for aprotic solvents, they most notably lack terms to describe hydrogen-bonding, which is vital for aqueous and protic environments. One possible solution for this problem is using the D-COSMO-RS approach (direct COSMO for real solvents), an implicit solvent model which includes the necessary hydrogen-bonding terms in its statistical-thermodynamics ansatz, for practically no additional costs compared to a COSMO calculation. In this work, D-COSMO-RS was used to model aqueous solutions in order to investigate such different topics as solvent effects on the reactivity of Diels-Alder reactions and their influence on the stability and speciation of gold(III) halides.

One central area of application for KS-DFT is the calculation of catalytic processes, or of transformations at transition metal centers in general. Here the calculations of compounds and reaction pathways usually involve several dozen atoms, which heavily favors the use of KS-DFT, with its good cost-accuracy ratio, and makes more expensive post Hartree-Fock methods unfeasible. As examples for catalytically active systems with transition metal centers, a variety of synthetic non-heme iron-oxo complexes were investigated in this work. These high-valent complexes often mimic reactive intermediates found at the active sites of iron-containing enzymes like the taurine dioxygenase or cytochrome P450. Provided a suitable exchange-correlation functional is selected, the KS-DFT indeed yields good results for these realistic systems.

# 2 Theory

## 2.1 Density Functional Theory

### 2.1.1 Introduction to DFT

Density functional theory (DFT) is a distinctly different approach to quantum chemical calculations compared to post-Hartree-Fock or wavefunction methods. Its theoretical basis is the proof by Hohenberg and Kohn [1], that the electronic energy of the ground state is completely determined by the electron density  $\rho(\vec{r})$ . We get the density by taking the square of the wavefunction and integrating over the coordinates of  $N-1$  electrons.

$$\rho(\vec{r}) = N \int \dots \int |\Psi(\vec{x}_1, \vec{x}_2, \dots, \vec{x}_N)|^2 ds_1 d\vec{x}_2 \dots d\vec{x}_N \quad (2.1)$$

If the exact electron density of the ground state is known, all properties of the ground state of a system may be derived from it. The energy as a function of the electron density then is

$$E[\rho] = T[\rho] + V_{ne}[\rho] + V_{ee}[\rho] \quad (2.2)$$

with  $T[\rho]$  being the kinetic energy of the electrons,  $V_{ne}[\rho]$  the energy of the nuclei-electron interaction and  $V_{ee}[\rho]$  the electron-electron repulsion. In stark contrast to the wavefunction, whose number of variables increases by 4 times the number of electrons  $N$  (3 spatial and 1 spin variable per electron), the electron density  $\rho(\vec{r})$  is a function that always depends on only 3 spatial variables and 1 spin variable. The electron density vanishes at infinity and integrates to the total number of electrons:

$$\int \rho(\vec{r}) d\vec{r}_1 = N \quad (2.3)$$

This suggests the possibility of determining the ground-state energy of a system, and of all associated properties without the use of any wavefunctions or orbitals. If all system-

independent parts of the energy expression are merged into one functional  $F_{HK}[\rho]$ , we get

$$E[\rho] = \int \rho(\vec{r}) V_{ne} d\vec{r} + F_{HK}[\rho] \quad (2.4)$$

$F_{HK}[\rho]$  is the Hohenberg-Kohn functional and could be considered the holy grail of DFT. With it, the Schrödinger equation could be solved exactly for molecules of all sizes. Unfortunately, the form of this functional is unknown, which is why the approximative ansatz of Kohn-Sham-DFT, introduced in 1965 [2], is used instead. In this ansatz, a non-interacting reference system for  $N$  particles is created, whose density  $\rho_S$  equals the exact ground state density  $\rho_0$  of the system in question. A single Slater determinant  $\Theta_S$  is the exact solution for such a reference system. It consists of orbitals  $\varphi_i$ , usually called Kohn-Sham (KS) orbitals, and the Slater determinant made from KS orbitals reads

$$\Theta_S = \frac{1}{\sqrt{N!}} \begin{vmatrix} \varphi_1(\vec{x}_1) & \varphi_2(\vec{x}_1) & \cdots & \varphi_N(\vec{x}_1) \\ \varphi_1(\vec{x}_2) & \varphi_2(\vec{x}_2) & & \varphi_N(\vec{x}_2) \\ \vdots & \vdots & & \vdots \\ \varphi_1(\vec{x}_N) & \varphi_2(\vec{x}_N) & \cdots & \varphi_N(\vec{x}_N) \end{vmatrix} \quad (2.5)$$

Following the same procedure used for the Hartree-Fock (HF) equations (see, for example, ref. [3, 4] for detailed derivations of the HF and KS equations), we get the following set of one-particle equations:

$$\begin{aligned} \hat{f}_{KS} \varphi_i &= \epsilon_i \varphi_i \\ \left[ -\frac{1}{2} \nabla^2 + V_S(\vec{r}) \right] \varphi_i &= \epsilon_i \varphi_i \end{aligned} \quad (2.6)$$

This means that the connection of the non-interacting reference system to the real system is the potential  $V_S(\vec{r})$ . As already mentioned, it has to be chosen, so that the real density is equal to the density of the reference system:

$$\rho_S(\vec{r}) = \sum_i^N \sum_s \varphi_i(\vec{r}, s)^2 = \rho_0(\vec{r}) \quad (2.7)$$

The resulting value of the kinetic energy  $T_S$  we get by this procedure is already very close to the total kinetic energy. Thus for the total energy of the system, we get the kinetic energy  $T_S$  and the potential  $V_S(\vec{r})$ , which is made up of the nucleus-electron attraction  $E_{ne}$ , a known Coulomb term  $J$  for the electron-electron repulsion and an un-

known exchange-correlation energy  $E_{XC}$ . The full expression of the Kohn-Sham energy with all the known terms is given in equation 2.8. It can be shown easily, that the total energy written in this way is still a functional of the exact density of the system.

$$\begin{aligned}
E[\rho(\vec{r})] &= T_S[\rho] + E_{ne}[\rho] + J[\rho] + E_{XC}[\rho] \\
&= -\frac{1}{2} \sum_i^N \langle \varphi_i | \nabla^2 | \varphi_i \rangle - \sum_i^N \int \sum_A^M \frac{Z_A}{r_{1A}} |\varphi_i(\vec{r}_1)|^2 d\vec{r}_1 \\
&\quad + \frac{1}{2} \sum_i^N \sum_j^N \int \int |\varphi_i(\vec{r}_1)|^2 \frac{1}{r_{12}} |\varphi_j(\vec{r}_2)|^2 d\vec{r}_1 d\vec{r}_2 + E_{XC}[\rho(\vec{r})] \quad (2.8)
\end{aligned}$$

Now we only have one unknown term left, the exchange-correlation energy  $E_{XC}$ . This name, however, is slightly misleading as  $E_{XC}$  does not only contain the exchange and correlation energy. It also includes the difference between  $T_S[\rho]$  and  $T[\rho]$ . If we set the equations 2.8 and 2.2 equal, we find the following expression for the exchange-correlation energy:

$$E_{XC}[\rho] = (T[\rho] - T_S[\rho]) + (V_{ee}[\rho] - J[\rho]) \quad (2.9)$$

The term in the first set of parentheses can be interpreted as kinetic correlation energy, the second one as potential exchange and correlation energy. If we now use the variational principle on the set of one-particle equations from 2.6 and minimize the energy by optimizing the KS orbitals  $\varphi_i$  under the usual orthonormality condition  $\langle \varphi_i | \varphi_j \rangle = \delta_{ij}$ , we derive the Kohn-Sham equations and get the following operator:

$$\hat{f}_{KS} = \left( -\frac{1}{2} \nabla^2 + \left[ \int \frac{\rho(\vec{r}_2)}{r_{12}} d\vec{r}_2 + V_{XC}(\vec{r}_1) - \sum_A^M \frac{Z_A}{r_{1A}} \right] \right) \quad (2.10)$$

The expression in the square brackets exactly corresponds to the effective potential  $V_S$  from the equations in 2.6. It also depends on the density of the other electrons, even though it is a one-particle operator, which is why these equation, just like the Hartree-Fock equations, can only be solved iteratively. The potential  $V_{XC}$ , that arises from the exchange-correlation energy, is simply the derivative of  $E_{XC}$  with respect to  $\rho$  and is again the only remaining unknown term.

$$V_{XC} = \frac{\delta E_{XC}}{\delta \rho} \quad (2.11)$$

Unlike the Hartree-Fock method, DFT contains no approximations but is in principle an exact method. If  $V_{XC}$  (or  $E_{XC}$  respectively) were known, density functional theory in the KS framework would give us the exact non-relativistic ground state in the limit of the Born-Oppenheimer approximation. Unfortunately, here begins the problem with DFT, since we do not know the exact exchange-correlation functional, but have to find approximations for it. This in turn means, that the quality of a DFT calculation solely depends on the choice of a suitable exchange-correlation functional. For those functionals a number of important approximations have been developed over time. In most cases the exchange-correlation functional is split into an exchange and a correlation term.

$$E_{XC}[\rho] = E_X[\rho] + E_C[\rho] \quad (2.12)$$

This splitting is of a more formal nature in most approximations, where a real separation of these two physical contributions in a sound way is difficult.

## 2.1.2 Exchange-Correlation Functionals

There are different methods for the approximation of the exchange-correlation energy and the corresponding density functionals can be arranged in an order which has been suggested by Perdew in 2005 [5] (and is appropriately called the 'Jacob's ladder to the heaven of chemical accuracy'). The lowest rung on this Jacob's ladder is the local density approximation (LDA), in which the electron density at every point in space is treated like the corresponding density in a homogenous electron gas and integrated accordingly. This is the only case in which the forms of the exchange and correlational functionals are known exactly. It is the earliest form of a proper exchange-correlation functional and its  $E_{XC}$  can be written as

$$E_{XC}^{LDA}[\rho] = \int \rho(\vec{r}) \epsilon_{XC}(\rho(\vec{r})) d\vec{r} \quad (2.13)$$

$\epsilon_{XC}(\rho(\vec{r}))$  is the exchange-correlation energy per particle of a homogenous electron gas with the density  $\rho(\vec{r})$ . It is multiplied with the probability of actually finding an electron at a certain place, which is why we speak of a local density approximation. The exchange term in its current form was already derived by Dirac back in the late 1920s [6] and was

suggested again by Slater [7] in 1951.

$$\epsilon_X = -\frac{3}{4} \sqrt[3]{\frac{3\rho(\vec{r})}{\pi}} \quad (2.14)$$

There is no similar expression for the correlation term, but the correlation energy itself can be calculated by Quantum-Monte-Carlo simulations [8]. In 1980 Vosko, Wilk and Nussair parameterized the results of such simulations into analytical expressions for  $\epsilon_C$  and thereby created the set of VWN correlation functionals [8]. Together with Slater exchange, one obtains the SVWN exchange-correlation functional. An abbreviation which is sometimes used synonymous with LDA, but is not the only LDA functional available (see, for example, ref. [9, 10]). If two different spin densities  $\rho_\alpha(\vec{r})$  and  $\rho_\beta(\vec{r})$  are used for open-shell systems, which also allows for symmetry breaking, the local density approximation (LDA) turns into the local spin density approximation (LSDA). With  $\rho_\alpha(\vec{r}) + \rho_\beta(\vec{r}) = \rho(\vec{r})$  it can be written as:

$$E_{XC}^{LSDA}[\rho_\alpha, \rho_\beta] = \int \rho(\vec{r}) \epsilon_{XC}(\rho_\alpha(\vec{r}), \rho_\beta(\vec{r})) d\vec{r} \quad (2.15)$$

As the electron density  $\rho(\vec{r})$  of a homogenous electron gas is constant, the LDA is a good model for metals, but a much poorer model for molecules, in which the electron density rapidly changes. It underestimates the exchange energy by about 10% for molecular systems, which leads to errors that are already larger than the entire correlation energy. The error for the correlation energy is usually beneath 1%.

In addition to the local density  $\rho(\vec{r})$ , the gradient expansion approximation (GEA) [4] also includes information on the gradient of the density  $\nabla\rho(\vec{r})$ . This practically treats the LDA as the first term of a Taylor expansion, augmented by the second term for more exact results. Using this expansion, however, means that many conditions for the real exchange-correlation hole are not fulfilled anymore. This can sometimes lead to worse results than the simpler LDA. Because of that, the generalized gradient approximation (GGA) was introduced, which enforces the conditions of the real hole also for the LDA and its gradient expansion. These GGA functionals [11–13] take the next rung on Perdew's suggested Jacob's ladder, with their exchange-correlation energy written as:

$$E_{XC}^{GGA}[\rho_\alpha, \rho_\beta] = \int f(\rho_\alpha, \rho_\beta, \nabla\rho_\alpha, \nabla\rho_\beta) d\vec{r} \quad (2.16)$$

Normally  $E_{XC}^{GGA}$  is split into an exchange and a correlation term just like in the LDA:

$$E_{XC}^{GGA} = E_X^{GGA} + E_C^{GGA} \quad (2.17)$$

$E_X^{GGA}$  and  $E_C^{GGA}$  are chosen and adapted to fulfill the conditions of the exchange-correlation hole and yield good results in test calculations. GGA exchange functionals can include semi-empirical parameters, like in Becke's B88 [13] or be completely parameter-free like the PBE functional by Perdew, Burke and Ernzerhof [14]. The same is true for GGA correlation functionals of which the LYP functional by Lee, Yang and Parr [15], which was fitted to exact calculations of the correlation energy of Helium, and the parameter free PBE correlation functional, are probably the best known. Above the GGA-functionals, on the next rung of Jacob's ladder, stand the meta-GGA functionals. They extend the GGA-functionals by taking the kinetic energy density into account as well [16–18]. Still higher up we find the hyper-GGA functionals, that additionally include the exact exchange energy density per electron.

$$\epsilon_X^{exact}(\vec{r}) = -\frac{1}{2} \sum_i^{occ} \sum_j^{occ} \varphi_i^*(\vec{r}) \varphi_j(\vec{r}) \int \frac{\varphi_j^*(\vec{r}') \varphi_i(\vec{r}')}{|\vec{r} - \vec{r}'|} d\vec{r}' \quad (2.18)$$

At the top of Jacob's ladder we finally find functionals that also include information from unoccupied ('virtual') orbitals. Since some of these functionals not only mix exact exchange with DFT exchange, but also, for example, mix DFT correlation with MP2 correlation, they are often called double-hybrids (see, for example, ref. [19–21]). While Perdew's Jacob's ladder arranges functionals based on a growing number of ingredients, like density gradients, kinetic energy density and exact exchange (and supposedly also their accuracy, but such a ranking is difficult and sometimes dubious at best), it is of course not the only way to classify different exchange-correlation functionals. An alternative method to classify density functionals was proposed by Arbuznikov and Kaupp [22]. Here we are content with three different classes of functionals:

1. Explicit density functionals, which are only dependent on the density and the gradient or Laplacian of the density. All LSDA and GGA functionals fall under this category as well as meta-GGA functionals if they do not include the kinetic energy density.
2. Density functionals which include contributions from occupied orbitals and are therefore only implicit functionals of the density. This category contains all hyper-

GGA functionals and every meta-GGA functional with kinetic energy density, like TPSS, for example.

3. Non-local density functionals that also include information about unoccupied orbitals, like the double-hybrids.

Currently most popular among hyper-GGA functionals are the hybrid functionals. They mix exact Hartree-Fock exchange with DFT exchange in the exchange functional. For global hybrids the amount of exact-exchange admixture is a constant  $a_0$ . The whole expression for  $E_{XC}$  then changes from equation 2.12 to

$$E_{XC}^{hybr} = a_0 E_X^{exact} + (1 - a_0) E_X^{DFT} + E_C^{DFT} \quad (2.19)$$

The main advantage of replacing parts of the DFT exchange with Hartree-Fock exchange lies in the reduction of the self-interaction error caused by the Coulomb term  $J$ . But simultaneously the contribution to the non-dynamical correlation, which is described by the DFT exchange term, is reduced with growing amount of  $E_X^{exact}$ . A good balance between  $E_X^{exact}$  and  $E_X^{DFT}$  regarding thermochemistry and geometries, is achieved by the popular B3LYP hybrid functional [15, 23]. Even though many other functionals have been developed and published since its first appearance, it is still the most often used exchange-correlation functional today. It combines exact exchange with Becke's B88 exchange functional and the LYP correlation by Lee, Yang and Parr. Three parameters ( $a, b$  and  $c$ ) are used to scale the exact-exchange admixture and the amount of GGA exchange and correlation admixture to the LSDA:

$$E_{XC}^{B3LYP} = (1 - a) E_X^{LSDA} + a E_X^{exact} + b \Delta E_X^{B88} + c E_C^{LYP} + (1 - c) E_C^{LSDA} \quad (2.20)$$

The values of these three parameters are  $a = 0.20$ ,  $b = 0.72$  and  $c = 0.81$ . They have been fitted to proton affinities, atomization energies, ionization potentials and total energies of the G2-1 test set (the first part of the larger G3 test set introduced by Curtiss and Pople [24–26]) where they showed deviations of only 2-3 kcal/mol. It should be noted that the three parameters  $a, b$ , and  $c$ , were actually optimized for B3PW91 [23], as Becke originally had used PW91 [27] instead of LYP correlation. The unchanged optimized values were then used for B3LYP as well. The further development of hybrid functionals, for the calculation of molecules, went into two important directions over the last 15-20 years (three directions if we include the conversion of hybrid functionals into double hybrids). In case of the 'range-separated' hybrids the amount of exact-exchange

admixture is varied along the electron-electron coordinate in the system [28–30]. The other direction are local hybrids.

### 2.1.3 Local Hybrid Functionals

Many studies suggest, that DFT calculations of different molecular properties need very different amounts of exact-exchange admixture [31–35] to yield accurate results. The hybrid functionals described in the last chapter all had a constant amount  $a_0$  of exact-exchange admixture, which depending on the size of  $a_0$  makes them all more or less suited for the description of different chemical properties. For example an exact-exchange admixture of 15-30% usually provides good results for thermochemical properties like atomization energies or energy gaps between spin-states, while a higher amount of exact exchange like 50% normally yields much better kinetic barriers and linear response properties. However, having only one global parameter for exact exchange at hand makes it seem quite impossible to achieve good results or at least small errors for a larger variety of molecular properties simultaneously. This fact alone makes different hybrid functionals a more or less favorable choice for the calculation of certain properties with DFT. It should be noted here, that there are in fact a variety of hybrid functionals with a high amount of exact exchange in existence, that are equally well suited for a wide range of thermochemical properties, as they are for barriers [36, 37]. These functionals usually also take the kinetic local energy density into account, but at the same time are very heavily parameterized (sometimes with over 30 semi-empirical parameters at once) and therefore very far away from pure density functionals. One solution for the problem of having a fixed parameter  $a_0$  for the exact exchange are the local hybrid functionals [5, 22, 38].

Here the exact-exchange admixture is not a constant, but a function of coordinates in real space, a local mixing function (LMF). This means that the constant  $a_0$  is replaced by a LMF  $a_\sigma(\vec{r})$ . This changes the common equation for global hybrids from 2.19 to

$$E_{XC}^{loc-hyb} = \sum_{\sigma=\alpha,\beta} \int \{a_\sigma(\vec{r}) \epsilon_{X,\sigma}^{exact}(\vec{r}) + [1 - a_\sigma(\vec{r})] \epsilon_{X,\sigma}^{DFT}(\vec{r})\} d\vec{r} + E_C^{DFT} \quad (2.21)$$

with

$$0 \leq a(\vec{r}) \leq 1 \quad (2.22)$$

As the amount of exact exchange can now be different at every position in space, because

of the LMF, local hybrids are practically by default much more flexible than global hybrids. Of course different areas in the molecule are important for different properties, which in turn require different amounts of exact exchange. Therefore a LMF should be designed in a way that it always allocates the right amount of exact exchange to the right space. The greatly improved flexibility of local hybrids also means that a suitable LMF must find an optimal balance between the description of non-dynamic correlation and the reduction of the self-interaction error in all areas of the molecule. Fulfilling all these requirements in one simple function is certainly not a trivial task, but the choice of a proper local mixing function is essential for the accuracy of a local hybrid functional, together with the choice of the right DFT exchange and correlation functionals  $\epsilon_{X,\sigma}^{DFT}$  and  $E_C^{DFT}$ . For the earliest local hybrids simple LSDA or Slater exchange surprisingly turned out to provide the best results for thermochemistry and barriers [22,39] compared to LMFs combined with GGA and meta-GGA exchange functionals. As for the choice of a suitable mixing function, it could be shown that LMFs with only one parameter already give better atomization energies and barriers than the most popular global hybrid B3LYP [22,40]. Especially the nearly constant size of the errors or deviations in the atomization energies, when going from the small G2 to the bigger molecules of the G3 test set, caught a lot of interest. This is because this constant behavior is very dissimilar to B3LYP, which shows strongly increasing errors with system size for atomization energies. Going from the very small molecules of the G2-1 subset to the bigger molecules of the G3 test set, these errors grow from a quite good 2.5 kcal/mol to a much worse 10.7 kcal/mol in mean absolute error (MAE). Compared to this, the first local hybrids published by Kaupp *et al.* only showed a range in the MAEs for the different G3 subsets of 3.3 to 4.4 kcal/mol [22] (and even the lower MAE of B3LYP for the G2-1 test set could easily be explained by fitting, since the same test set was also used for finding the 3 B3LYP parameters in the first place). One proposed LMF, from now on called the *t*-LMF [22,38], has the following form:

$$a_\sigma(\vec{r}) = 0.48 * t_\sigma(\vec{r}) \quad (2.23)$$

$$t_\sigma(\vec{r}) = \frac{\tau_{W,\sigma}(\vec{r})}{\tau_\sigma(\vec{r})} \quad (2.24)$$

It is named after the inhomogeneity parameter  $t_\sigma(\vec{r})$ , which consists of the ratio between the local kinetic energy density  $\tau_\sigma(\vec{r})$  and the von-Weizsäcker kinetic energy density

$\tau_{W,\sigma}(\vec{r})$ , with

$$\tau_{\sigma}(\vec{r}) = \frac{1}{2} \sum_{i_{\sigma}}^{occ} |\nabla \varphi_{i_{\sigma}}(\vec{r})|^2 \quad (2.25)$$

and

$$\tau_{W,\sigma}(\vec{r}) = \frac{1}{8} \frac{|\nabla \rho_{\sigma}(\vec{r})|^2}{\rho_{\sigma}(\vec{r})} \quad (2.26)$$

For better illustration of the concept, Figure 2.1 shows a cut through the spatial distribution of exact-exchange admixture for a local hybrid calculation of a stacked benzene dimer with the *t*-LMF. The corresponding picture for a global hybrid calculation can naturally be skipped, as it would show the same two molecules, but with only one single background colour, as the exact-exchange admixture in global hybrids equals a constant throughout space [22].

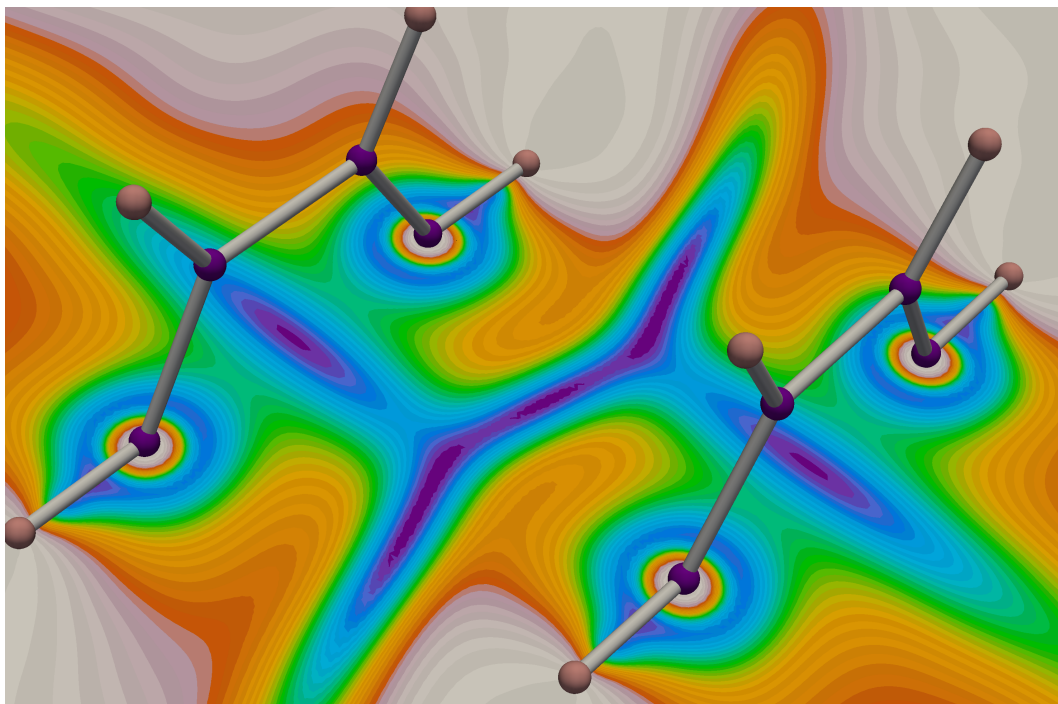


Figure 2.1: 2-dimensional plot of the exact-exchange admixture for a stacked benzene dimer, calculated with a *Lh*-SVWN based local hybrid using the *t*-LMF. Purple color marks areas with very low amounts of exact exchange, white color areas with high amounts.

Besides  $t_{\sigma}(\vec{r})$  a function of the dimensionless density gradient  $F[s_{\sigma}(\vec{r})]$  was also tested as a possible inhomogeneity parameter for a second class of LMFs. These LMFs will be

referred to as  $s$ -LMFs [22].

$$a_\sigma(\vec{r}) = \text{erf}(0.22 * s) \quad (2.27)$$

$$s_\sigma(\vec{r}) = \frac{|\nabla\rho_\sigma(\vec{r})|}{2(3\pi^2)^{1/3}\rho_\sigma^{4/3}(\vec{r})} \quad (2.28)$$

The function of  $s_\sigma(\vec{r})$ , in this case the error function, only has the task of mapping  $s_\sigma(\vec{r})$  to a range of  $0 \leq a_\sigma(\vec{r}) \leq 1$  on a LMF ( $t_\sigma(\vec{r})$  automatically fulfills this vital condition). Inspired by the treatment of non-dynamical correlation in Becke's B05 exchange-correlation functional, both the  $t$ - and  $s$ -LMF were expanded by the inclusion of different terms for the two spins. For this purpose the spin polarization  $\zeta(\vec{r})$

$$\zeta(\vec{r}) = \frac{\rho_\alpha(\vec{r}) - \rho_\beta(\vec{r})}{\rho_\alpha(\vec{r}) + \rho_\beta(\vec{r})} \quad (2.29)$$

was introduced as an additional variable into the existing  $t$ - and  $s$ -LMFs. Two new LMFs, with two semi-empirical parameters each, were created that showed significantly lower deviations for the atomization energies of the G3 test set [40]:

$$\begin{aligned} a_\alpha &= (0.446 + 0.0531\zeta) t_\alpha \\ a_\beta &= (0.446 - 0.0531\zeta) t_\beta \end{aligned} \quad (2.30)$$

$$\begin{aligned} a_\alpha &= \text{erf}[(0.197 + 0.0423\zeta) s_\alpha] \\ a_\beta &= \text{erf}[(0.197 - 0.0423\zeta) s_\beta] \end{aligned} \quad (2.31)$$

Unfortunately these spin-polarized LMFs show larger errors in the calculation of kinetic barriers than their predecessors. The  $t$ -LMF yielded good results for atomization energies and barrier heights in comparison with global hybrids and the same was also true (although to a lesser extent) for the  $s$ -LMF. But further validation unveiled some troubling shortcomings in those local hybrids. Before the introduction of dispersion corrections and the use of calibration functions to reduce the so-called gauge problem of exchange-energy densities, the main problems could be roughly divided into three categories:

1. The semi-empirical parameter for the  $t$ -LMF limits the maximum exact-exchange admixture to less than 50%. This simultaneously leads to a wrong asymptotic behavior with a high self-interaction error and not enough exact exchange at the core regions (high amounts of exact exchange at the nuclei are favorable for the

calculation of EPR properties for example). Still, the *t*-LMF at least has maxima at the nuclei, whereas the *s*-LMF drops to an undesirable cusp at the nuclei. While the *s*-LMF eventually reaches 100% Hartree-Fock exchange in the asymptotic region, the increase of the curve of the LMF going to the asymptotic region seems to be too slow to give good results.

2. While local hybrids with SVWN for the DFT exchange and correlation part showed better thermochemistry than any combination containing GGA or meta-GGA functionals, the LSDA still has severe weaknesses in comparison to these functionals. These drawbacks did not show up in the atomization energies and barriers, but they immediately appeared in ionization potentials, electron affinities and the total energies of atoms. Here the LSDA is the bottleneck for the quality of the local hybrids and just not good enough compared to the DFT exchange and correlation parts of most global hybrids.
3. Local hybrids showed a very repulsive behavior for weak-interaction potential curves, which can be seen easily when we, for example, compare the potential energy curves of rare gas dimers obtained with local hybrids to results with global hybrids or even pure Hartree-Fock calculations. Pure LSDA actually shows an unphysical overbinding, while pure Hartree-Fock exchange with VWN correlation gives a clear repulsive behavior for rare gas dimers. Local hybrids, which would be expected to lie somewhere between these two extremes, are instead much more repulsive (see Figure 2.2).

One minor drawback of local hybrids, that was not mentioned in the list above, is the absence of dispersion interactions. The lack of dispersion interactions does not come as a surprise, as their description is simply not included in the mathematical form of most density functionals. Because of this they have to be added, either intrinsically to the functional, or externally to the total energy (see next chapter for further information). We decided to use the easy and comparatively quick external method of Grimme's D3 dispersion corrections [41]. They proved to be a reliable way to simulate dispersion interactions, without including them directly into the local hybrids. We have optimized the necessary D3 parameters against the S22 test set [42, 43] for weakly-bound complexes, which includes systems driven mostly by dispersion, as well as electrostatic and mixed interactions [44, 45]. However, this ansatz only works if the gauge origin problem (explained in the next section), which is responsible for most of the repulsive behavior of the local hybrids, is reduced as well [45]. The results of this procedure were very promis-

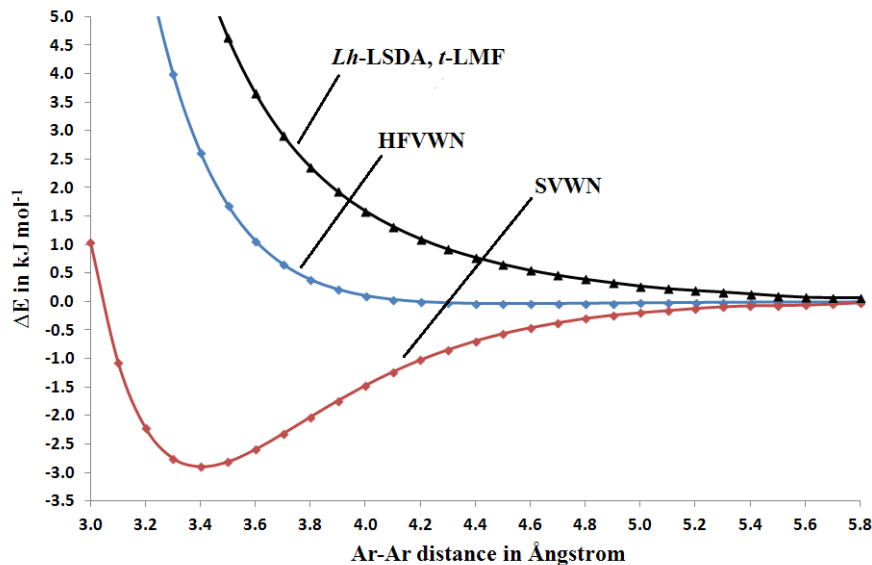


Figure 2.2: Potential energy curves of the argon-dimer for SVWN, HFVWN, and *Lh*-LSDA with *t*-LMF.

ing [45] and showed, that the missing dispersion interactions in local hybrids could be very well described by a DFT-D3 ansatz.

The deterioration of the good thermochemical results for local hybrids, whenever we switched from pure LSDA to combinations of GGA- or meta-GGA exchange and correlation functionals, were much harder to understand, let alone to deal with. One problem local hybrids suffer from, that was known already at the time of their introduction, is the gauge origin problem [46–48] of the energy densities. It is certainly responsible for some of the shortcomings of local hybrids, but its extent and the size of the error caused by it are hard to quantify. The gauge origin problem in short stems from the fact that energy densities in general are never unique. This ambiguity shows itself when we integrate the energy density  $\epsilon(r)$  over real space to gain the energy  $E$ . Here we find that another energy density  $\tilde{\epsilon}$  will give us the same energy  $E$ , if

$$\tilde{\epsilon}(\vec{r}) = \epsilon(\vec{r}) + G(\vec{r}), \quad (2.32)$$

and

$$\int G(\vec{r}) d\vec{r} = 0. \quad (2.33)$$

This function  $G(\vec{r})$  (sometimes called a calibration function, CF) changes the gauge of the energy density  $\epsilon$ . Unlike global hybrids, local hybrids are susceptible to this change,

because their exact-exchange admixture is not a constant but a function of space. We can immediately understand this by looking at the exchange energy density of a local hybrid

$$\epsilon_X^{Lh}(\vec{r}) = a_\sigma(\vec{r}) \epsilon_X^{exact}(\vec{r}) + [1 - a_\sigma(\vec{r})] \epsilon_X^{DFT}(\vec{r}). \quad (2.34)$$

If we replace  $\epsilon_X^{DFT}(\vec{r})$  with  $\epsilon_X^{\tilde{DFT}}(\vec{r}) = \epsilon_X^{DFT}(\vec{r}) + G(\vec{r})$  and integrate this new energy density [49], we find that

$$\begin{aligned} E_X^{\tilde{Lh}} &= \int \epsilon_X^{\tilde{Lh}}(\vec{r}) d\vec{r} \\ &= \int \left\{ a_\sigma(\vec{r}) \epsilon_X^{exact}(\vec{r}) + [1 - a_\sigma(\vec{r})] [\epsilon_X^{DFT}(\vec{r}) + G(\vec{r})] \right\} d\vec{r} \\ &= \int \epsilon_X^{Lh}(\vec{r}) d\vec{r} + \int [1 - a_\sigma(\vec{r})] G(\vec{r}) d\vec{r} \\ &= E_X^{Lh} - \int a_\sigma(\vec{r}) G(\vec{r}) d\vec{r} \end{aligned} \quad (2.35)$$

and therefore  $E_X^{\tilde{Lh}}$  will differ from  $E_X^{Lh}$ , which introduces the gauge origin problem. This means, that the difference between the energies depends on the individual LMF as well as the CF and would also appear (with a change in sign), if the exact exchange energy density had been calibrated instead. There are ideas put forth by Burke *et al.* [46,47], on how to create unambiguous energy densities to solve this problem. However, they require using the optimized effective potential and its gradient, which makes them difficult to implement. The problem of the non-uniqueness of energy densities has been known for many years and a way to tackle this gauge origin problem is the inclusion of a CF in the local hybrid functional itself. Naturally the CF must fulfill the condition from equation 2.33, but it should also meet eight further constraints to avoid artifacts in the exact exchange energy density, when used in a product with the LMF. A complete list and discussion of the constraints for the CF can be found in ref. [49]. In the 2014 work of Arbuznikov *et al.* [49] the CF was created using only semi-local ingredients like the electron density and its derivatives (mainly to avoid having the exact exchange energy density in the CF itself, which would make the implementation very difficult [48]). Equation 2.36 gives the final form of the CF, with the position vector omitted for clarity.

$$G_\sigma = \rho_\sigma^{-1/3} \left\{ f'(s_\sigma) s_\sigma \left[ \frac{\nabla \rho_\sigma \cdot \nabla |\nabla \rho_\sigma|}{|\nabla \rho_\sigma|} - \frac{4}{3} \frac{|\nabla \rho_\sigma|^2}{\rho_\sigma} \right] + f(s_\sigma) \left[ -\frac{1}{3} \frac{|\nabla \rho_\sigma|^2}{\rho_\sigma} + \nabla^2 \rho_\sigma \right] \right\} \quad (2.36)$$

The index  $\sigma$  denotes the spin,  $s_\sigma$  is the dimensionless density gradient and  $f(s_\sigma)$  is a

cut-off function of the following form:

$$f [s_\sigma(r)] = \exp [-\eta s_\sigma^2(r)] \quad (2.37)$$

The cut-off function was chosen for its simplicity and there are many other possible candidates. Some of them can be derived directly from enhancement factors of GGA exchange functionals [50]. Arbuznikov *et al.* have used the aforementioned CF and cut-off function in combination with the *t*-LMF. In general the CF must be tailored to a specific LMF, since the total energy of a system is directly connected to the product of CF and LMF (see equation 2.35). The final local hybrid had the form

$$\begin{aligned} E_{XC}^{Lh-GGAxGGAc-CG} = & \\ \sum_{\sigma=\alpha,\beta} \int & \left\{ a_\sigma(\vec{r}) \epsilon_{X\sigma}^{exact}(\vec{r}) + [1 - a_\sigma(\vec{r})] \left[ \epsilon_{X\sigma}^{LSDA}(\vec{r}) + a_X \Delta \epsilon_{X\sigma}^{GGAx}(\vec{r}) + cG_\sigma(\vec{r}) \right] \right\} d\vec{r} \\ & + E_C^{LSDA} + a_C \Delta \epsilon_C^{GGAc}(\vec{r}) \end{aligned} \quad (2.38)$$

and also employed GGA exchange and correlation functionals instead of only LSDA, as had been the case in the original local hybrid with the *t*-LMF (*Lh*-LSDA, *t*-LMF). The number of semi-empirical parameters in the local hybrid that have to be fitted also went up from one in *Lh*-LSDA, *t*-LMF, to five, which is still a reasonable number. Implementing the CF to improve the local hybrids already turned out to be of great help for dealing with two of the main problems of the local hybrids at once:

Firstly it greatly reduces the repulsive behavior, that has been observed previously in the potential energy curves of rare-gas dimers [51](see Figure 2.3 on the effect of using a CF in local hybrids). The extent of the repulsion in local hybrids without a CF far exceeded what would normally be expected from any combination of exact exchange and LSDA. For example chemical intuition tells us, that the *Lh*-LSDA, *t*-LMF should produce a potential energy curve for rare-gas dimers, that lies somewhere between the curve of pure LSDA calculations and the curve from a global hybrid with 48% exact exchange and LSDA exchange and correlation (marking the lower and upper limits, respectively, for the exact exchange in this local hybrid with a LMF-prefactor of 0.48). However, the real curve of the local hybrid (without calibration function) turned out to be more repulsive than even a global hybrid with 100% exact exchange and LSDA correlation (see Figure 2.2). This over-repulsion indeed turned out to be a consequence of the gauge origin problem [49], as further tests revealed. Even small modulations of a fixed exact-exchange

admixture by a LMF, for example a very rigid  $t$ -LMF  $a_\sigma(\vec{r}) = 0.5 + 0.1 * t_\sigma(\vec{r})$  with 50-60% exact exchange everywhere in space, immediately led to much more repulsive curves [49] (in this example more repulsive than global hybrids with 50 or 60% exact-exchange admixture). Using the CF from equation 2.37 improves upon the problem and indeed creates reasonable potential energy curves for rare-gas dimers [49], that even show remnants of the unphysical, slightly attractive behavior due to overbinding, that is common for the LSDA.

Secondly the reduced gauge origin problem enables the use of non-local GGA exchange and correlation parts in the local hybrids, without causing a massive increase in the errors for thermochemistry in comparison to purely LSDA based local hybrids. A deterioration when switching from LSDA to GGA had previously been observed for atomization energies [22], which does not longer occur if a CF is used in the local hybrid [49]. Thereby the more sophisticated GGA functionals can be used in local hybrids, without compromising the latter's good performance for thermochemistry. The benefits of using B88 and LYP or PBE in the DFT exchange and correlation parts of the modified  $t$ -LMF (see equation 2.38) immediately became apparent in great improvements for ionization potentials and electron affinities. These quantities heavily rely on the quality of the correlation functional for a good description, which is the major reason why the older LSDA based local hybrids consistently show worse results than global hybrids for these properties [51]. For the total energies of atoms, another property that particularly suffers from the bad performance of LSDA in local hybrids [51], the results for the local hybrids with CF are so far mixed [49]. The use of PBE greatly reduced the errors for total energies (although still far away from the good results of its PBE0 global hybrid counterpart), while on the other hand calibrations of the local hybrid for BLYP still produced unacceptably large deviations. Recent unpublished research indicates that an overly large damping exponent in the CF for BLYP might be responsible for the observed errors.

So the most important flaw in local hybrids proved to be the apparently poor match between relative calibrations of DFT and exact-exchange energy densities, when they are mixed locally. The gauge origin problem lead to the unphysical repulsive behavior of the local hybrids and created an obstacle for systematically improving them with better non-local DFT exchange and correlation parts. Different attempts to further advance local hybrids have been tried and proposed before the introduction of the CF [52]. In the case of Kaupp *et al.*, these attempts included the use of a common LMF for different spins, a range-separation approach to the LSDA correlation functional, and the reduction

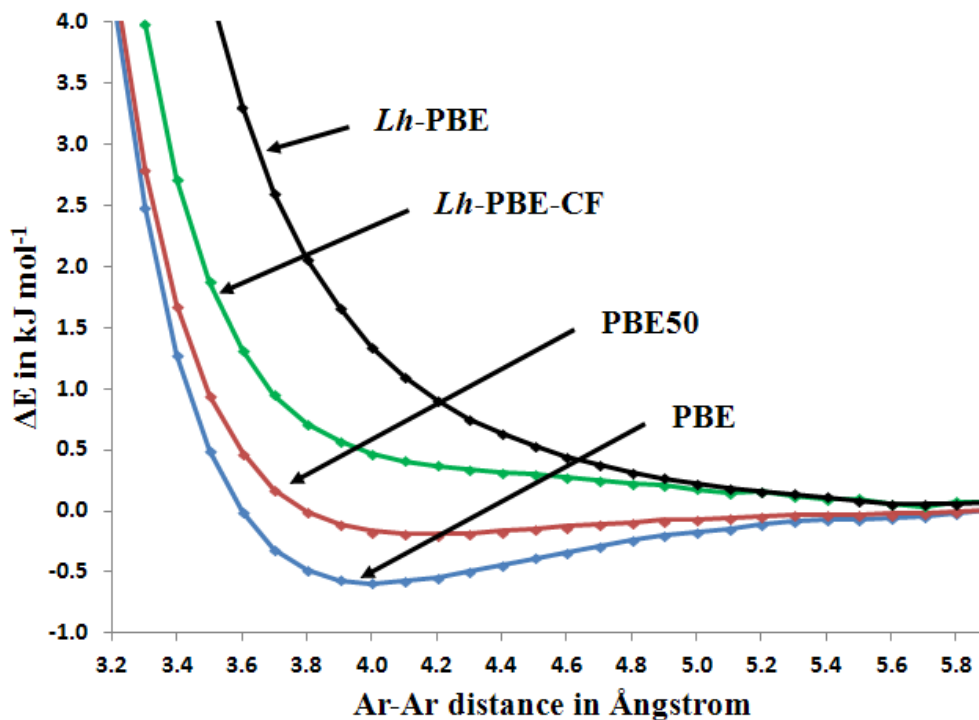


Figure 2.3: Potential energy curves of the argon-dimer for *Lh*-PBE ( $b=0.5$ ) with and without calibration function (CF). PBE (0% exact exchange) and PBE50 (global hybrid with 50% exact exchange) energy curves are shown for comparison.

of the self-interaction error (SIE) in LSDA based local hybrids [52] (see ref. [53–57] for interesting attempts towards new local hybrids by other groups). The original *t*-LMF and its spin-polarized variant used separate expressions for the two spin channels, but work with LMFs based around the adiabatic connection formula [58] showed that a common LMF for both spins can be formulated [52]. Transferring this finding from first principles LMFs to the semi-empirical local hybrids means reformulating equation 2.21 to

$$E_{XC}^{loc-hyb} = \int \left\{ a(\vec{r}) \sum_{\sigma=\alpha,\beta} \epsilon_{X,\sigma}^{exact}(\vec{r}) + [1 - a(\vec{r})] \sum_{\sigma=\alpha,\beta} \epsilon_{X,\sigma}^{DFT}(\vec{r}) \right\} d\vec{r} + E_C^{DFT} \quad (2.39)$$

with

$$0 \leq a(\vec{r}) \leq 1. \quad (2.40)$$

It should be mentioned that while creating LMFs based on first principles, using the adiabatic connection formalism, sounds appealing from a philosophical point of view,

the results showed large errors for thermochemistry and other properties [58]. Changing the original  $t$ -LMF into a common LMF gives the following subtle changes:

$$a(\vec{r}) = b * t(\vec{r}), \quad 0 \leq b(\vec{r}) \leq 1 \quad (2.41)$$

and

$$\tau_W(\vec{r}) = \frac{1}{8} \frac{|\nabla \rho(\vec{r})|^2}{\rho(\vec{r})}, \quad \rho(\vec{r}) = \rho_\alpha(\vec{r}) + \rho_\beta(\vec{r}) \quad (2.42)$$

$$\tau(\vec{r}) = \frac{1}{2} \sum_i^{occ} |\nabla \varphi_i(\vec{r})|^2 = \tau_\alpha(\vec{r}) + \tau_\beta(\vec{r}). \quad (2.43)$$

Although the common LMF seems very similar to the  $t$ -LMF, with the spin label  $\sigma$  just being absent from  $a(\vec{r})$ , using the same value for the semi-empirical parameter  $b$  in both LMF yields different outcomes for the exact-exchange admixture in open shell systems. Thus the common LMF presents us with another way to include the desired alpha-beta spin cross-terms in our functional, besides using a LMF with explicit dependence on spin polarization. It could also be considered a more straightforward approach, since we now have the total quantity of the exchange part, with the spin cross terms built in. This is in contrast to the former splitting into two different spin channels (see equation 2.21).

Range-separation is most commonly done to the exchange functional in global hybrids (see ref. [29, 30, 59–61] for more information about some of the most popular range-separated functionals). However, for a small selection of LSDA based local hybrids validated in this work [52], the range separation was done to their correlation functional.

The repulsion energy of a pair of electrons can be decomposed into its long-range (LR) and short-range (SR) components [52]:

$$v_{ee}(r_{12}) = \frac{1}{r_{12}} = v_{ee}^{LR}(r_{12}) + v_{ee}^{SR}(r_{12}) \quad (2.44)$$

It should be noted that range-separation alone does not change the LSDA correlation, as the overall correlation contributions of the LSDA remain the same. Changes to the correlation functional were made by the inclusion of self-interaction reduction in the SR part. The reason for this will be explained later. Two separation functions were used in ref. [52]; the Gaussian error function 'erf'

$$erf(x) = (2/\sqrt{\pi}) \int_0^x \exp(-t^2) dt \quad (2.45)$$

which is the most widespread ansatz for range-separation, and the sharper 'erfgau' function [62]. The LR repulsion energy now reads as

$$v_{ee}^{LR}(r_{12}) = \frac{\text{erf}(\mu r_{12})}{r_{12}} - \frac{2\mu}{\sqrt{\pi}} \exp(-\mu^2 r_{12}^2/3) \quad (2.46)$$

while the SR interaction becomes

$$v_{ee}^{SR}(r_{12}) = \frac{1}{r_{12}} - v_{ee}^{LR}(r_{12}). \quad (2.47)$$

$\mu$  is a numerical fitting parameter and its reciprocal value decides in which region the switch from SR to LR happens. The final SR-LDA correlation energy, as derived from ref. [62], is

$$E_c^{SR-LSDA} = \int \rho(\vec{r}) e_c^{SR-LSDA}[r_s(\vec{r}), \zeta(\vec{r})] d(\vec{r}) \quad (2.48)$$

with the Seitz radius  $r_s$ , the spin-polarization  $\zeta$  and the short-range LSDA correlation energy density per electron  $e_c^{SR-LSDA}$ .

The motivation for the range separation of the correlation energy comes from the well known error cancellation between LSDA exchange and its correlation counterpart. Regions with a dominant local DFT exchange contribution (where the LMF has a low value) are better described by the LSDA than regions with high exact-exchange admixture, where the error cancellation does not work anymore. This implies that only the SR LSDA needs to be modified, while the LR part can be left in its original state, as it does not operate in regions with high LMF values. This is the reason for range-separating the LSDA correlation functional. The  $E_c^{SR-LSDA}$  was improved by partially eliminating the self-interaction error, creating a self-interaction reduced (SIR) SR-LSDA correlation:

$$\begin{aligned} E_{c;\mu,\lambda}^{SIR-SR-LSDA} = \int \left\{ \rho e_{c,\mu}^{SR-LSDA}[\rho_\alpha, \rho_\beta] \right. \\ \left. - \lambda \left( \frac{\tau_{W,\alpha}}{\tau_\alpha} \right) \rho_\alpha e_{c,\mu}^{SR-LSDA}[\rho_\alpha, 0] \right. \\ \left. - \lambda \left( \frac{\tau_{W,\beta}}{\tau_\beta} \right) \rho_\beta e_{c,\mu}^{SR-LSDA}[0, \rho_\beta] \right\} d(\vec{r}), \\ 0 \leq \lambda \leq 1 \end{aligned} \quad (2.49)$$

As denoted above, the correlation energy density per electron  $e_{c,\mu}^{SR-LSDA}$  for the SR part is now  $\mu$  dependent. It changes the SR version of LSDA to full LSDA for  $\mu \rightarrow 0$  and the

LR part to full LSDA for  $\mu \rightarrow \infty$ , respectively. The parameter  $\lambda$  controls the extent of the self-interaction reduction, and although a complete SIE-free LSDA correlation with  $\lambda = 1$  looks very appealing at first glance, an only partial reduction of the SIE also seems to have its merits. The reason for using a  $\lambda$  value smaller than 1, lies in the fact that the maximum amount of exact-exchange admixture is below 100% for all LMFs presented in this chapter. This means there will always be some LSDA exchange at every point in space, and this LSDA exchange in turn would likely benefit from the error cancellation with the SIE inside the LSDA correlation. One plausible and easy solution was to set  $\lambda$  equal to the main LMF parameter  $b$ , so that the SIE reduction is highest, where the inhomogeneity parameter of the LMF reaches 1. The resulting range-separated and SIE reduced local hybrids were all based on the simple common LMF, as are the later developed *Lh*-GGAxGGAc-CG local hybrids with calibration functions. Since B88 exchange and LYP correlation were used for one GGA dependent local hybrid, and PBE exchange and correlation for the other, they are simply abbreviated as *Lh*-BLYP-CF and *Lh*-PBE-CF in this work and in the latest publications.

### 2.1.4 D3 Dispersion Corrections

Van-der-Waals interactions are an exclusively quantum mechanical phenomenon, caused by electron correlation. The electron densities of two non-interacting systems usually repel each other due to both of them carrying the same negative charge, but at a certain distance the movements of the electrons of one system induce a perturbation in the electron density of the other system. This correlation effect firstly leads to a temporary, then to an induced, dipole moment, which creates a weak attractive interaction between the two systems. That rare gases like argon or xenon can be liquefied at all, is only possible because of the small van-der-Waals interaction. Besides the attractive interaction between two induced dipoles, that decreases with  $r^{-6}$ , dispersion also includes additional terms like induced dipole-quadrupole or quadrupole-quadrupole interactions, which decrease with  $r^{-8}$ ,  $r^{-10}$  and so forth. Common density functionals cannot describe dispersion or van-der-Waals interactions, because they only include the exchange-correlation energy of one local molecular electron density, which cannot be influenced by another electron density it does not overlap with. So a semi-local density functional by definition cannot describe a non-local correlation effect like dispersion in a physically sound way. Nevertheless DFT calculations of van-der-Waals dimers like  $Ne_2$ ,  $Ar_2$  or  $Kr_2$  sometimes show minima on their potential energy hypersurface. However,

these minima are often at the wrong distance and the binding energy of the dimers is usually too low. LDA functionals in particular show an unphysical attractive behavior, while the results for GGA functionals can fall anywhere between a good description of dispersion (still for the wrong reason though) and a purely repulsive behavior.

Different attempts for the approximation of dispersion effects have been made, like the van-der-Waals functional vdW-DF of Lundqvist [63] or the later Becke-Johnson vdW-functional [64] and the highly parameterized variations of meta-hybrid functionals [65], that have been proposed to tackle this problem. But the most popular method to include dispersion corrections into DFT calculations is the D3 method of Grimme [41], which essentially boils down to a sum over  $C_6 R^{-6}$  potentials of atom pairs. Of course this DFT-D3 ansatz does not reach the high accuracy of coupled-cluster calculations with perturbative triples corrections (CCSD(T)), combined with a complete basis set extrapolation scheme (CBS), which currently is the 'gold standard' to decide on the relative energies of conformers. In fact, the DFT-D3 term for dispersion corrections to the total energy of the system only takes the positions of atoms and their chemical element into account. It completely neglects the rest of the electronic structure of the system. The total energy of a system with DFT-D3 corrections is:

$$E_{DFT-D3} = E_{KS-DFT} + E_{disp} \quad (2.50)$$

$E_{KS-DFT}$  is the normal Kohn-Sham energy, that was obtained from the chosen density functional.  $E_{disp}$  is the energy of the dispersion correction, consisting of the sum of two- and three-body terms

$$E_{disp} = E^2 + E^3, \quad (2.51)$$

of which the two-body term is the most important one, and the only one used in this work:

$$E^2 = \sum_{AB} \sum_{n=6,8} s_n \frac{C_n^{AB}}{r_{AB}^n} f_{d,n}(r_{AB}) \quad (2.52)$$

The first sum runs over all atom pairs of the system.  $C_n^{AB}$  are the dispersion coefficients of  $n$ th-order, for the atom pair  $AB$  with the interatomic distances  $r_{AB}$ . The dispersion coefficients are affected by the coordination numbers and are therefore system dependent. In contrast to older versions of Grimme's DFT-D [66, 67], the scaling factor  $s_6$  is set to 1 for most functionals in the DFT-D3 ansatz, to get the right asymptotic behavior for exact  $C_6^{AB}$  values. The scaling parameter  $s_8$  on the other hand is the first of two semi-empirical parameters that has to be customized to each used density functional

individually. The damping-function proposed by Chai and Head-Gordon [68]

$$f_{d,n}(r_{AB}) = \frac{1}{1 + 6(r_{AB}/(s_{r,n}R_0^{AB}))^{-\alpha_n}} \quad (2.53)$$

restricts the range of the dispersion corrections. This damping function is needed to prevent singularities and double counts of correlation effects for small  $r_{AB}$  distances. It includes the second semi-empirical parameter  $s_{r,6}$  of the DFT-D3 method, which scales the cut-off radii  $R_0^{AB}$ . The dispersion coefficients  $C_n^{AB}$  and the cut-off radii  $R_0^{AB}$  of the separate atom pairs are hard-wired as fixed parameters into the DFT-D3 stand alone program and usually should not be changed at all. The parameter  $\alpha_n$  decides how drastic the effect of the damping function will be and is set to 14 for  $n = 6$  and to  $\alpha_{n+2} = \alpha_n + 2$  for other values of  $n$ . The exact form of the damping function is not predefined and other damping functions have been proposed [67,69,70] which lead to similar results (see ref. [71] for a general discussion on damping functions). Another form of damping used in this work was proposed by Becke and Johnson (BJ) [64,72,73]. Here the dispersion energy is

$$E_{disp}^{D3(BJ)} = -\frac{1}{2} \sum_{A \neq B} s_6 \frac{C_6^{AB}}{r_{AB}^6 + [f(R_0^{AB})]^6} + s_8 \frac{C_8^{AB}}{r_{AB}^8 + [f(R_0^{AB})]^8} \quad (2.54)$$

with

$$f(R_0^{AB}) = a_1 R_0^{AB} + a_2 \quad (2.55)$$

The cut-off radii  $R_0^{AB}$  in BJ-damping are slightly different from the ones used in the original D3 dispersion correction [74]. Thus in DFT-D3(BJ) a set of three semi-empirical parameters ( $s_8$ ,  $a_1$  and  $a_2$ ) has to be optimized for every density functional instead of two in DFT-D3 ( $s_{r,6}$  and  $s_8$ ). Although BJ-damping shows a more physically sound behavior at short distances [74], the different damping schemes lead to very similar results [74]. Recently Schwabe *et al.* have reduced the D3(BJ) ansatz to a  $C_6$ -only dispersion correction (D3(CSO)), that only uses one fit parameter without significant loss of accuracy compared to the D3(BJ) corrections [75].

## 2.2 Calculation of Mössbauer parameters with DFT

The resonance absorption of  $\gamma$ -radiation in immobilized nuclei was named Mössbauer effect after its first discoverer Rudolf Mössbauer in 1957 (Nobel prize in physics, together with Robert Hofstadter, in 1961) [76]. The spectroscopy method carrying the same name, uses this Mössbauer effect, in combination with the Doppler effect, to create a substance specific spectrum of solid-state compounds. Even though there are dozens of chemical elements, that have at least one isotope exhibiting the Mössbauer effect, only  $^{57}\text{Fe}$  is of interest for this work, due to its abundance in active centers of enzymes and its role as central metal in non-heme iron-oxo and nitrido complexes with high oxidation states, which are the focus of Chapter 3. These complexes often show promising capabilities as homogeneous catalysts, for example in C-H activation reactions, and are therefore of great interest for science and industry. Mössbauer spectroscopy is most famously used to distinguish between the oxidation states of iron compounds, but it is also heavily employed in geology to search and analyze minerals. Such useful applications even led to a Mössbauer spectrometer being sent to Mars (MIMOSII on NASA's Mars Exploration Rover mission). The present work will concentrate on the theoretical calculation of Mössbauer parameters of different organometallic iron complexes. As a short reminder, Figure 2.4 shows the classical arrangement for a Mössbauer spectrometer: a radioactive  $^{57}\text{Co}$  source decays into  $^{57}\text{Fe}$  and sends  $\gamma$ -radiation through a collimator into the  $^{57}\text{Fe}$  containing sample. The transmitting  $\gamma$ -radiation is then caught by a detector. Energy differences in the radiation, needed to measure a whole spectrum, are achieved by moving the  $^{57}\text{Co}$  source with a linear motor, the Mössbauer drive. Thanks to the Doppler effect this movement introduces an energy change to the  $\gamma$ -radiation and allows scanning over a narrow energy range to obtain a full spectrum. This procedure also explains the use of mm/s as most common energy unit in Mössbauer spectroscopy, as it simply translates to the speed of the motor moving the radioactive source, with the sign referring to the direction of the motion (towards or away from the sample).

Below the figure of the spectrometer are depictions of the two most important nuclear (or nuclear-electron) interactions, that are of interest for chemists, and are usually given, when results of Mössbauer experiments are presented and compared: the isomer shift  $\delta$  and the quadrupole splitting  $\Delta E_Q$ . Those are also the two parameters calculated in this work and the ones most often reproduced by DFT in the literature. The next step of possible interactions in a Mössbauer spectrum, the hyperfine splitting, that is caused by the interaction of the nucleus with a surrounding magnetic field, is omitted in the figure

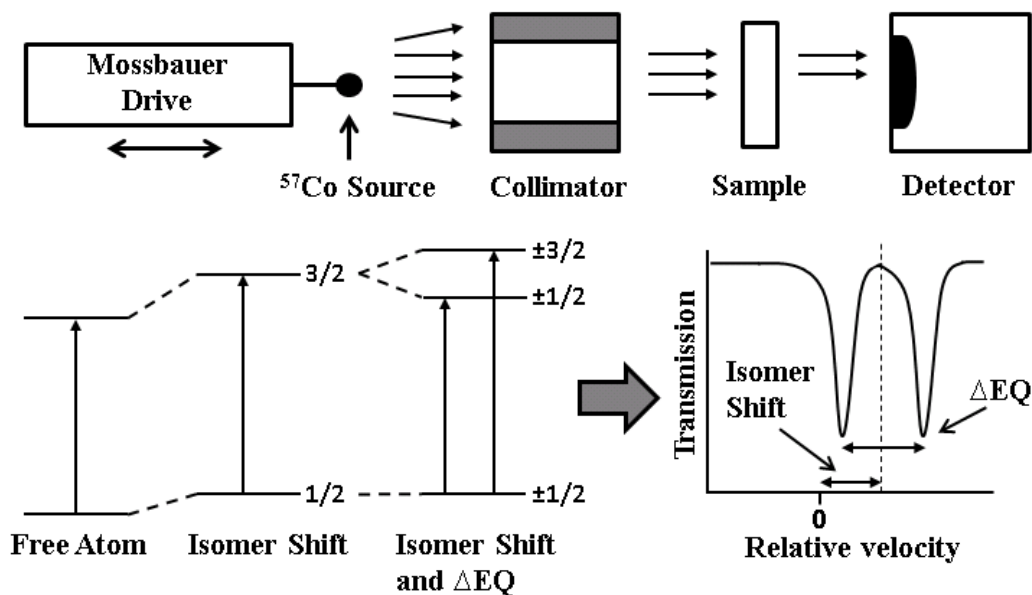


Figure 2.4: Schematic of the typical arrangement for  $^{57}\text{Fe}$  Mössbauer spectroscopy and a short overview of the important energy transitions for the calculated parameters: the isomer shift and the quadrupole splitting.

as it was not part of this work and is therefore not of interest here. It should be briefly mentioned, however, that the hyperfine splitting adds another layer of complexity to the line pattern of the spectrum, that in turn can be used to differentiate between similar species, since the line width in Mössbauer spectroscopy is narrow enough for a proper resolution of the hyperfine structure. We now describe how to calculate isomer shifts and quadrupole splittings in the DFT framework.

**Isomer Shift.** A simple linear equation is used, that treats  $\delta$  as directly proportional to the electron density at the iron nucleus. Two semi-empirical parameters  $a$  and  $b$  connect the electron density to  $\delta$ . They are chosen by fitting calculated electron densities, obtained by a certain combination of density functional and basis set, to experimental values of  $\delta$  from a number of molecules in a given data set.

$$\delta = a \cdot \rho(0) + b \quad (2.56)$$

Such an approach might appear strange and very different from other property calculations with DFT, but indeed the quantum theory behind the Mössbauer isomer shifts is well understood [77, 78] and together with many DFT studies (see, for example, [79–81], and references therein) fully supports the use of this method, to obtain the right results

for the right reason. The complete neglect of relativistic effects in the simple treatment of isomer shifts by standard DFT methods might be surprising, as the fully relativistic Dirac-Fock calculation for a  $d^5$   $^{57}\text{Fe}$  atom gave an electron density of  $\sim 15700 \text{ au}^{-3}$  [82], while the non-relativistic Hartree-Fock limit is around  $3200 \text{ au}^{-3}$  lower [79]. Fortunately these large differences do not seem to matter, as the relativistic effects on iron show a remarkably constant behavior for different atomic configurations and can therefore be neglected altogether within the mentioned scaling procedure, without introducing further approximations or compromising the results. The linear regression should have been done for exactly the computational methodology one intends to use for the compound of interest, leading to optimum error cancellation.

**Quadrupole Splitting.** The interaction between the nuclear quadrupole moment and the electric field gradient (created by the surrounding nuclei and electrons) at the excited  $^{57}\text{Fe}$  nucleus, leads to a splitting of the energy level of the nuclear excited state  $I = 3/2$  into energetic substates with  $I_Z = \pm 1/2$  and  $I_Z = \pm 3/2$ .

$$E_{I,I_Z} = \frac{1}{6} \sum_{\alpha,\beta} Q_{\alpha,\beta}(I, I_Z) V_{\alpha,\beta} \quad (2.57)$$

$\alpha$  and  $\beta$  are Cartesian coordinates, while  $Q_{\alpha,\beta}(I, I_Z)$  are the nuclear quadrupole tensor components. Finally  $V_{\alpha,\beta}$  are the derivatives of the electric field potential with respect to the Cartesian coordinates. After substituting the quadrupole moment expression and using the difference of the states, with their respective correct quantum numbers, we reach the equation for the calculation of the quadrupole splitting, that is used in quantum chemistry:

$$\Delta E_Q = \frac{1}{2} e Q V_3 \left[ 1 + \frac{(V_1 - V_2)^2}{3V_3^2} \right]^{1/2} \quad (2.58)$$

Here  $Q$  is the nuclear electric quadrupole moment for the  $I = 3/2$  state, usually set to a fixed number [83],  $e$  is the electron charge, and  $V_{1-3}$  are the eigenvalues of the  $V_{\alpha,\beta}$  tensor, with the highest absolute value assigned to  $V_3$  by convention. Although this formula looks rather straightforward and does not cause any mathematical problems, calculations of  $\Delta E_Q$  often yield larger errors than the calculations of isomer shifts, using a simple semi-empirical linear equation. Below is a short summary of some of the most common problems encountered, when calculating both Mössbauer parameters with DFT (we note in passing, that most of these problems are also present in wave-function methods, but the latter are not the focus of this work):

(a) Sometimes DFT simply fails completely to agree with experiment for  $\Delta E_Q$ , because of the single-reference limitation of the theoretical method [84,85]. Unfortunately, strong multi-reference character in iron complexes is not exactly exotic or rare. The situation is furthermore complicated, as the behavior of the multi-reference character, and the DFT errors resulting from it, appear not to be systematic at all. Which amount of multi-reference character leads to a completely wrong result, and which amount does not affect the results at all, is difficult to diagnose reliably by pure multi-reference diagnostics alone.

(b) The sign of  $\Delta E_Q$  has a clear physical meaning. It defines the relative positions of the  $I_Z = \pm 1/2$  and  $I_Z = \pm 3/2$  states. Yet the sign is very often not given in experimental studies (instead the absolute value is used), and if it is given, it may very well come out opposite in the DFT calculations. For other properties this would be very troubling if not disastrous, but for  $\Delta E_Q$  the problem is usually ignored, because it is understood that, depending on the situation, a sign change of  $\Delta E_Q$  might only indicate minor inaccuracies. The reason for the sign change can be found in equation 2.58: Since  $e$ ,  $Q$  and the expression in brackets are always positive, the sign can only be determined by  $V_3$ . Since the electric field gradient follows Laplace's equation, we get  $V_1 + V_2 + V_3 = 0$  for the eigenvalues. Since the highest absolute value is used for  $V_3$ , a molecule with a very small  $V_1$  leads to a  $\sim V_2 = -V_3$  situation. Now a very minor effect can cause  $V_2$  to have a higher absolute value than  $V_3$ , thereby becoming the new  $V_3$  and changing the sign of  $\Delta E_Q$ , without really changing its absolute value.

(c) Mössbauer spectra are typically very temperature dependent, and they often are so in a nontrivial manner [86], which renders simple extrapolation schemes to  $\sim 4$  K [87] unusable in many circumstances. The current gold standard are liquid helium cooled measurements at about 4 K, but those are not always available (certainly not in older data in the literature). DFT calculations on the other hand are usually carried out at 0 K, and DFT as a ground-state method cannot account for the different population of low-lying excited states at different temperatures (also important for the isomer shift). Different studies have also found, that the absolute errors for large quadrupole splittings ( $> 2$  mm/s) tend to be much larger, than the errors for smaller ones (see [88] for example). As the coordinates of the compound explicitly enter into the calculation of  $\Delta E_Q$ , small differences between theoretical and experimental structures can lead to large deviations from the experimental reference values. These are often not inaccuracies in DFT, which reproduces gas phase structures quite well, but are more frequently due to the fact that

solid state samples have to be used for the spectra, which might have a highly distorted structure. The structure can also be affected by counterions, which are often left out of the calculation.

## 2.3 COSMO and D-COSMO-RS

Typical quantum-chemical calculations usually involve somewhere between one and ten molecules in the gas phase at 0 K and do not take temperature effects into account. While this is often sufficient, many chemical reactions are carried out in solution and are strongly influenced by their solvent environment. Many molecules show very different stabilities and structures in different solvents. These minor and major solvent-dependencies can influence all sorts of interesting parameters investigated by scientists, from reaction energies, kinetic barriers and minimum structures, to charge distributions, excitation energies and electron transfer parameters. This list is nowhere complete, but already shows, that the solvent environment cannot simply be neglected in quantum chemistry, if we really wish for a broad range of applicability of our methods, especially in order to investigate experimental results, that are very often only available in solution. In some cases, the solvent environment is practically the entire driving force behind an experimentally observed phenomenon and sometimes it is also the most interesting aspect about it. Of all the possible ways to simulate a solvent environment, explicit addition of solvent molecules to a system of interest is of course the most straightforward, but it is often not feasible even for relatively small systems due to the sheer number of molecules needed in order to mimic a solvent.

Such static calculations also lack information about the dynamic interaction of the solvent with the system, that can only be extracted from an even more expensive molecular dynamics (MD) simulation, which in turn often allows only a very poor and inaccurate quantum-chemical treatment of the system of interest (thereby making the whole exercise useless for many investigations). Another way to handle thousands of solvent molecules in static calculations, is to treat them as classical mechanical bodies in a cheap force-field model, while the system of interest is still treated with more accurate quantum-mechanical methods. This combined QM/MM approach is popular and easier to handle than full ab-initio MD, but it is still very computationally expensive. A step between QM/MM and MD is the force-field based RISM (reference interaction site model) method [89,90].

Cheaper options for the treatment of solvent effects, that keep the high quality of the quantum chemical treatment of the system intact, are the polarizable continuum models (PCM). From the variety of PCMs available, the conductor-like screening model (COSMO) [91] was chosen and used in this work. The reason for this is the high effi-

ciency and stability of COSMO and, more importantly, the option to use the COSMO-RS ansatz [92] (COSMO for real solvents) by Klamt. COSMO-RS uses surface charge densities as input for a statistical thermodynamics ansatz, which elevates the method from the restrictions of a mere PCM, especially when it comes to the treatment of hydrogen-bonds and solvent mixtures. In its D-COSMO-RS implementation [93], it can be used for fully self-consistent calculations and structure optimizations.

### 2.3.1 COSMO

The conductor-like screening model (COSMO) has been developed and established more than 20 years ago [94]. It has since been implemented into several quantum chemistry program packages and has been used extensively in combination with DFT. COSMO starts from a perfect conductor, which makes some mathematical formulations easier in comparison to other PCMs. Since no changes have been made by the author, to either the COSMO or the D-COSMO-RS implementation, for any calculation in this work, we only give a short qualitative overview of the solvation models and refer readers, that are interested in more specific mathematical details, to the multitude of textbooks on solvation models in quantum chemistry. COSMO runs together with a normal SCF calculation by following this routine:

1. A cavity consisting of several surface segments is formed around the solute system to separate it from the dielectric continuum, that is used to simulate its solvent environment.
2. Each segment of the cavity gets its own surface charge  $q$  assigned, which is found by solving this set of linear equations:  $\hat{A}q + \hat{B}Q = 0$ . This boundary condition follows that of a vanishing electrostatic potential for a conductor.  $\hat{A}$  and  $\hat{B}$  are linear operators and  $Q$  is the charge distribution of the solute system (based on its nuclear charges and electron density). Operator  $\hat{A}$  sets up a matrix to generate the electric potential, caused by the polarization charges, on every segment, while  $\hat{B}$  practically acts as a counterpart and generates the electric potential of the solute on the surface segments, times a scaling factor  $f(\epsilon)$ .

$$f(\epsilon) = \frac{\epsilon - 1}{\epsilon + 0.5} \quad (2.59)$$

Here  $\epsilon$  is the permittivity of the solvent and the only solvent specific information

- present in the model.
3. The total energy gain of the system due to the polarization of the continuum is calculated and the surface charges  $q$  resubstituted into the next SCF step as external charges, changing the SCF into an SCRF procedure (self-consistent reaction field).
  4. Starting again from step 2, new external charges are created for the new electron density of the solute system and fed into the SCF, until electron density, energy and external charges have converged.
  5. A new step in a structure optimization requires a return to step 1 to create a new cavity for the new coordinates of the system.

A visual depiction of a cavity construction out of different surface segments can be found in Figure 2.5, together with the final converged surface charge density map for the same system.

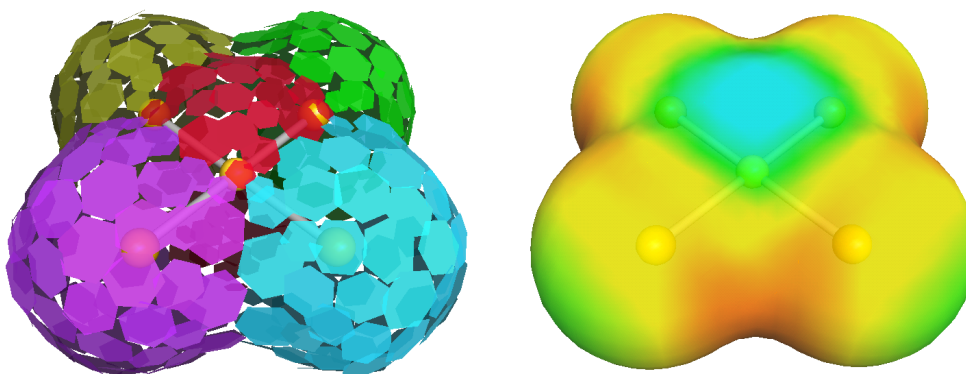


Figure 2.5: Left: surface segments for each atom forming the cavity of  $\text{AuCl}_4^-$ . The colors depict surface segments constructed around the same atom. Right: surface charge density map for  $\text{AuCl}_4^-$ . The colors for the surface charges go from blue (negative) to red (positive).

### 2.3.2 D-COSMO-RS

The COSMO ansatz works well for apolar non-protic solvents and has significant advantages over other PCMs, especially regarding the topic of outlying charge corrections (errors caused by small parts of the electron density reaching outside the cavity). The errors caused by this have been quite problematic for some other PCMs, as they can

easily amount to 20% of the solvation energy for neutral solutes, while for anions the error might be larger than the whole solvation energy. Using the boundary condition for a conductor, rather than for a dielectric continuum, improves the errors by about one order of magnitude, making the method much more robust and reliable [95]. Still PCMs in general have a lot of shortcomings, most notably the absence of hydrogen bonding, but also the restriction to the single parameter  $\epsilon$ , which makes it nearly impossible to differentiate cyclohexane from benzene or acetonitrile from methanol, even though they otherwise have quite different solvent properties. An improvement on this situation was achieved by the COSMO-RS method, which kept the COSMO cavity, but replaced the pure PCM by a statistical thermodynamics ansatz for an ensemble of pairwise interacting surface segments.

In the COSMO reference state of a perfectly conducting medium, the solutes are noninteracting, as long as they are not too close to each other, and they have their individual surface screening charge densities  $\sigma$  and COSMO energies. The COSMO-RS ansatz now introduces energetic corrections to this reference state by adding terms for van der Waals interactions of the conductor with the solutes and energy changes for the close contact of the solutes surface segments to each other ( $\sigma$  to  $\sigma'$  interaction) [92]. Here two contributions are important: (a) the local misfit interaction between the polarization charge densities, that occurs whenever  $\sigma \neq \sigma'$ , and (b) terms that describe hydrogen-bonding [92, 93]. Especially the latter is a radical improvement for modeling aqueous solutions, as strong hydrogen-bonding can severely alter structures and impact barrier heights. The effects of going from COSMO to COSMO-RS (in the form of D-COSMO-RS) are shown for Diels-Alder reactions and gold halides in later chapters. The misfit interaction for  $\sigma + \sigma'$  is

$$\Delta E_{misfit} = a_{contact} c_{misfit} (\sigma + \sigma') \quad (2.60)$$

and the hydrogen-bonding term looks like

$$\Delta E_{HB} = a_{contact} c_{HB} \min(0, \sigma\sigma' - \sigma_{HB}^2) \quad (2.61)$$

with the surface contact term  $a_{contact}$  and a parameter  $c$ . The  $\sigma_{HB}^2$  parameter acts as a threshold, so that only sufficiently polar surface segments of opposite polarity take part in hydrogen-bonding, and the energy correction increases with higher polarities of

hydrogen-bond donor and acceptors. The entire change to the COSMO energy amounts to a calculation of a sum over all surface contacts  $k$  of all molecules of our ensemble  $S$ . This seems easy enough, but in fact we do not know all the contact terms, nor do we know all the polarization charge densities for a single point in time. This gets furthermore complicated as all these contacts are of course constantly changing in a liquid. Instead of finding exact solvation energies for a specific configuration, COSMO-RS uses statistical thermodynamics to calculate the correct average of the total energy of a liquid. This amounts to finding the  $\sigma$ -potential  $\mu(\sigma)$  for a specific solvent molecule

$$\mu_S(\sigma) = -\frac{kT}{a_{eff}} \cdot \ln \left\{ \int d\sigma' p_S(\sigma') \cdot \exp \left[ \frac{-a_{eff} (e_{int}(\sigma, \sigma') + \mu_S(\sigma'))}{kT} \right] \right\} \quad (2.62)$$

$a_{eff}$  is the area of the effective surface segment with polarity  $\sigma$  and  $p_S$  is the histogram of all the surface segments of the ensemble with respect to  $\sigma$ . In  $p_S$  the mole fractions  $x_i$  of the different solvent species of the ensemble with their individual  $\sigma$ -histograms and their molecular surface areas  $A^X$  are taken into account as well.

$$p_S(\sigma) = \sum_i \frac{x_i p^{X_i}(\sigma)}{x_i A^{X_i}} \quad (2.63)$$

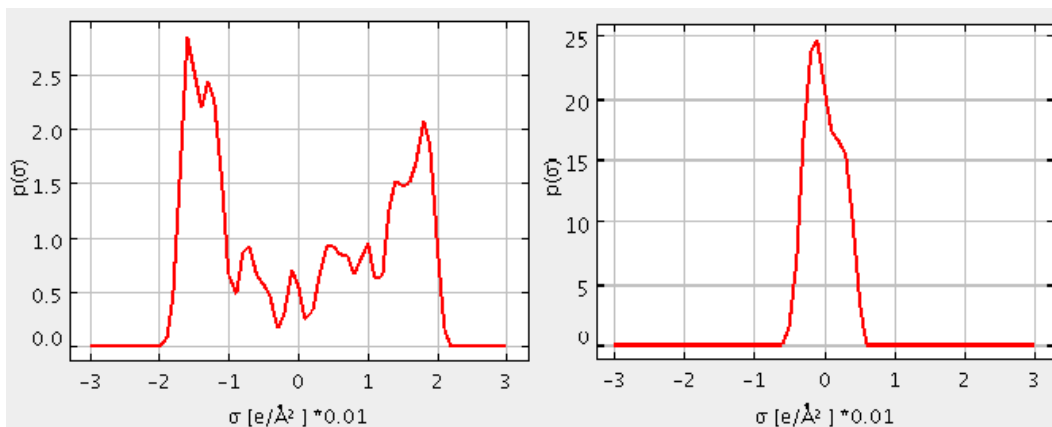


Figure 2.6:  $\sigma$ -profile of water (left) and hexane (right).

This allows the use of solvent mixtures in COSMO-RS, just by weighing in the different solvents by their mole fractions. The molecular  $\sigma$ -histograms  $p^X(\sigma)$  of the components are called  $\sigma$ -profiles and a more chemically intuitive understanding of the differences between water and hexane can be gained by looking at their  $\sigma$ -profiles in Figure 2.6. Here we see, that the vast majority of surface segments for hexane cluster around

$\pm 0.5\sigma/\text{\AA}^2$ . This is of course in perfect accordance to the weakly charged C-H sections of the molecule, not really being different from each other. Water on the other hand does not only show much less surface segments (notice the different scaling on the y-axis for water and hexane in Figure 2.6), due to its smaller size, but it also gives two distinctive peaks in high surface charge areas. These peaks clearly indicate the hydrogen-donor and hydrogen-acceptor regions of the solvent molecule. Their final  $\sigma$ -potentials are shown in Figure 2.7.

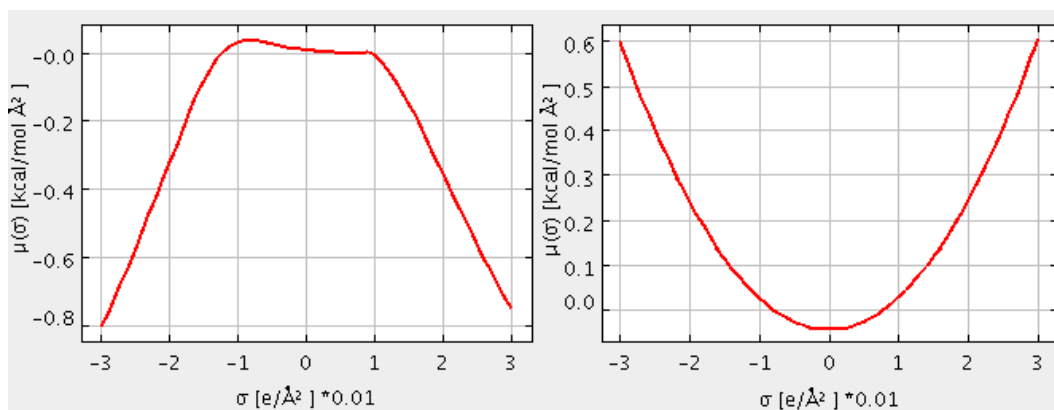


Figure 2.7:  $\sigma$ -potentials of water (left) and hexane (right).

This is the COSMO-RS method, which has been very popular and successful, especially in the field of chemical engineering, as it can be used to predict all kinds of thermodynamical properties of molecules in solution, from phase-equilibrium predictions to ionic liquids. Its most important applications in the industry are the calculation of solubilities and of mixing coefficients of liquids. An important step for its further use in quantum chemistry, especially for the calculation of structures and spectroscopic parameters, was the change of the COSMO-RS free energy of solvation expression into a Fock-matrix contribution. This made it possible to replace the dielectric solvent response by the COSMO-RS  $\sigma$ -potential as a new form of response, that also includes the terms for hydrogen-bonding. With this direct COSMO-RS (D-COSMO-RS) approach, fully self-consistent structure optimizations and response property calculations are possible, for a computational price comparable to a normal PCM. This method is relatively new and has not undergone many tests in quantum chemical applications, but its results are very promising and provide results on the level of high-end extensive molecular dynamics simulations with practically no additional costs to a normal DFT calculation [93,96,97](see Chapter 4).

# 3 High-Valent Non-Heme Iron-Oxo Complexes

## 3.1 Overview

Systematic *in vitro* modelling of heme-based catalytic oxidation was initiated 30 years ago, when Groves and co-workers first described oxoiron(IV) porphyrin-radical complexes as excellent oxygen-atom transfer (OAT) agents toward olefins and hydrocarbons [98]. *In vitro* modeling of non-heme enzyme function via mononuclear iron(IV)-oxo complexes was first reported by the Wieghardt group in 2000 [99]. Since then, the spectroscopic evidence (UV/Vis; Mössbauer; EXAFS) of the existence and nature of iron(IV)-oxo species has been corroborated by solid-state structures of several mononuclear iron(IV) complexes, which unambiguously prove their chemical constitution. Nowadays, high-valent iron-oxo species are frequently proposed as intermediates of dioxygen metabolism [100,101]. They are vital for the function of iron-containing metalloenzymes in general, thus also in non-heme iron-based enzymes. A number of review articles summarize progress in this field [102–106]. Besides OAT, heme and non-heme model complexes support a broad spectrum of oxidation chemistry, such as electron transfer (ET) and hydrogen-atom abstraction (HAT). This of course makes them highly interesting for the use in homogenous catalysis.

In this chapter, different aspects of the electronic structure and reactivity of non-heme iron(IV)-oxo complexes are investigated. The first part concentrated mainly on the correct description of the electronic ground state by DFT, especially the question whether formal iron-oxo complexes should rather be described as iron-oxyl radicals instead, which is studied for a selection of ten relevant formal iron(IV)- and iron(V)-oxo complexes. The motivation behind this was originally based on the discovery of large amounts of spin density on the oxo ligands in the transition states in different catalytic processes [107, 108].

Early work on small iron(IV)-oxo model complexes, within the framework of a UniCat project, quickly revealed that substantial spin on the oxygen atom can already be found in the ground state (see Tables S1 and S2 in Appendix I), which led us to consider the iron-oxo vs iron-oxyl question. The second and third part of this chapter present a set of iron(II) and iron(IV)-oxo complexes with new N<sub>5</sub> pentadentate chelate ligands, synthesized by Grohmann *et al.* [109, 110]. These ligands were used to probe the effects of structural distortions on spin state energetics and reactivity, as a new means to hopefully be able to tune future iron catalysts. Distorting the tetragonal towards trigonal symmetry in the coordination sphere of the iron(II) complexes resulted in a narrowing of the triplet-quintet spin state energy gap and a steep increase in reactivity. In the last part of this chapter, a problem case is shown that highlights the importance of spin contamination, broken-symmetry solutions, and the correct choice of functional, when dealing with high-valent iron complexes. Typically reliable hybrid functionals like B3LYP were found to give very wrong IR-frequencies for the iron-nitrido stretching vibration of an iron(V)-nitrido complex. We found this to be due to unusually large problems with spin contamination. Choosing a functional with low amounts of exact exchange greatly reduces the problem, as do restricted open-shell Kohn-Sham DFT calculations that prevent broken-symmetry solutions.

## 3.2 The Question of Iron(IV)-Oxo vs Iron(III)-Oxyl Character

### 3.2.1 Introduction

Synthetic model complexes, with a prominent high-valent Fe-O group as their active site, that were designed to mimic the active centers of non-heme iron enzymes, are usually described as iron(IV)-oxo species. The assignment of this formal oxidation state is normally justified with the short Fe-O bond lengths of 1.60-1.70 Å in those complexes, which supposedly point to the existence of Fe-O double bonds, and their Mössbauer isomer shifts, that fall between +0.30 and -0.20 mm s<sup>-1</sup> [104], and are therefore in a lower range than typical iron(III) compounds. While this classification of highly reactive iron-oxygen intermediates in non-heme iron enzymes, and their synthetic counterparts, is quick and convenient, it might also convey a wrong picture of their actual electronic structure. Different studies have pointed out, that during the transition states

of H-abstraction, OAT, and related reactions, formal high-valent oxo species of different transition metals often show a high amount of spin density at the oxygen ligand (see, for example, ref. [107, 108]). Since a true iron-oxo compound ideally should not show much spin density at the oxygen at all, these reactive species seem to be much closer to oxyl radicals at the transition state. This would mean, that a lowering of the oxidation state by one must take place on the iron center, combined with the reorganization of spin in the molecule, which would certainly have an energetic effect on the barrier height.

Since there is a profound interest in highly reactive iron(IV)-oxo complexes as catalysts for various applications, the question whether we really have a formation of iron(III)-oxyl radicals at the transition state, is of great importance for the design of catalysts. Of course this is only true, if the description of the ground state as iron-oxo complexes is indeed correct. However, preliminary DFT calculations on small iron(IV)-oxo model complexes revealed substantial amounts of spin on the oxygen, even in their ground state (see Tables S1 and S2 in Appendix I). This could mean that the very assumption of iron(IV)-oxo complexes transforming into iron(III)-oxyl radicals could be wrong, and that we should really treat our formal iron-oxo complexes as iron-oxyl radicals instead. To gain insight into this problem, the electronic structures of ten important representative complexes of synthetic high-valent iron-oxo compounds have been investigated by DFT calculations, to find out whether they should be described as iron-oxo complexes or iron-oxyl radicals. To this end, comparisons to experimental structures and different molecular properties like zero-field splittings and Mössbauer parameters have been made.

### 3.2.2 Computational Details

All DFT calculations were performed using TURBOMOLE6.3 and a locally modified version of the TURBOMOLE6.4 package [111–113]. The latter allows variation of the amount of exact exchange in global hybrid functionals. def2-SVP, def2-TZVP and def2-QZVP basis sets [114] were used. Functionals used in this work were BLYP [12, 15], PBE [14, 31], TPSS [115], B97D [116], B3LYP [15, 23], PBE0 [14, 31, 117], TPSSh [115], BHLYP [118], and BP86 [12, 13]. The resolution-of-the-identity approximation was used for the latter (RI-BP86). Customized BLYP-based global hybrid functionals of the form  $E_{XC}^{hybr} = a_0 E_X^{exact} + (1 - a_0) E_X^{B88} + E_C^{LYP}$  were used as well.

The SCF energies were converged to  $10^{-8}$  Hartree and a fine m5 integration grid was

chosen for the exchange-correlation potential. Dispersion contributions were evaluated using Grimme's DFT-D3 atom-pairwise dispersion corrections [41]. Transition states have been verified by harmonic vibrational frequency analyses. It was verified that the imaginary frequency of a given transition state pertains to the reaction at hand.

For the calculation of Mössbauer parameters, an uncontracted def2-QZVPP basis set was used for iron and def2-TZVP for all other atoms. The structures underlying the Mössbauer calculations were optimized at B3LYP-D3/def2-TZVP level. The in-house MAG program [119] was used to calculate the electron density  $\rho$  at the iron nucleus and the quadrupole splitting. For the isomer shifts the linear equation used is  $\delta[\text{mm s}^{-1}] = -0.3594 * (\rho(\text{DFT}) - 11800) + 10.521$ . This equation was fitted to the isomer-shift test set of Neese [79]. Other linear equations, based on different optimization procedures and different fit sets, were investigated as well. The inhouse MAG program was also used for the calculation of zero-field splittings and g-tensors, taking all integrals for the calculation of Breit-Pauli spin-orbit effects into account. A 9s7p4d all-electron basis set designed for hyperfine calculations was used for iron [120] and IGLO-II [121] for all other atoms.

## 3.2.3 Results and Discussion

### 3.2.3.1 A Selection of Non-Heme Iron-Oxo Complexes

A selection of ten iron-oxo complexes has been investigated by DFT, to find out whether they should really be treated as iron-oxo or rather as iron-oxyl complexes. Eight of them are normally categorized as iron(IV)-oxo complexes, half of them with a quintet ground state ( $S = 2$ ), the other half with a triplet ground state ( $S = 1$ ). The last two complexes are usually described as iron(V)-oxo complexes with a doublet ground state ( $S = 1/2$ ). To cover a wide range of non-heme iron-oxo species, the selected compounds are a mixture of anionic and cationic complexes with fairly different ligands and coordination polyhedra. For the sake of simplicity, we will refer to all these iron species as iron-oxo complexes throughout this chapter, even though this classification is debatable at best (see below). Of the four complexes with quintet ground states, three have a trigonal bipyramidally coordinated iron center and one has an octahedrally coordinated one (see Figure 3.1). The pentaqua iron-oxo complex is currently the only known example of a non-heme octahedral iron-oxo complex with a  $S = 2$  ground state. It is perhaps the simplest but also most peculiar iron-oxo species of the ten complexes discussed here (if

not in general). The other three  $S = 2$  complexes have  $N_4$  tetradentate ligands with short chains connected to the nitrogen trans to the oxo. For the iron(IV)-oxo species with triplet ground states (see Figure 3.2), we only find octahedral coordination.

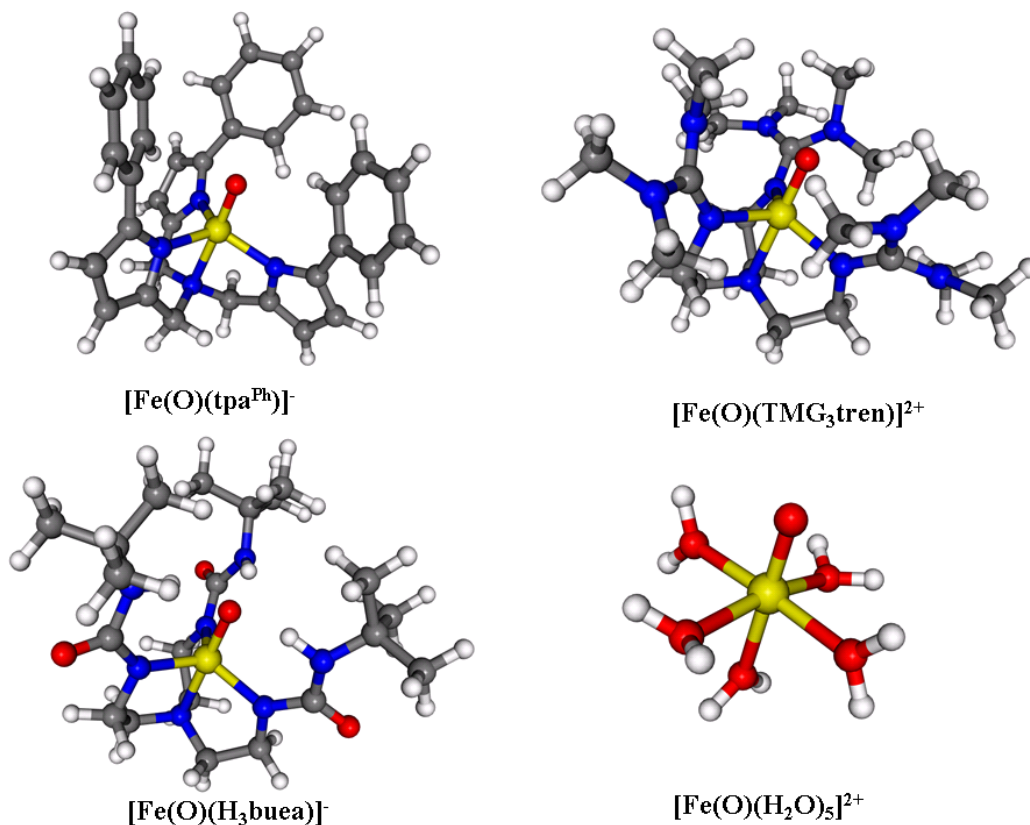


Figure 3.1: Optimized structures (B3LYP-D3/def2-TZVP) of four selected iron(IV)-oxo complexes with  $S = 2$  ground state.

All selected  $S=1$  iron-oxo complexes are cationic, and we note in passing that anionic non-heme iron-oxo complexes with triplet ground states are extremely rare ( $[\text{Fe}(\text{O})(\text{TAML})]^{2-}$ , the iron(IV) pendant to our chosen iron(V)-oxo complexes is one possible example).  $[\text{Fe}(\text{O})(\text{TMC})(\text{NCCH}_3)]^{2+}$  with its macrocyclic ligand was the first successfully crystallized complex with an iron(IV)-oxo unit [122]. It also raised interest because of its ability for quick ligand exchange of acetonitrile with anionic donors. This allowed probing ligand effects trans to the oxo group [123–125] for the first time (but all the newly formed iron-oxo complexes with anionic donors were too reactive to crystallize). Replacing a methyl group of TMC with an alkyl arm changed the macrocycle into a more stable pentadentate ligand. The most important representative of this class of iron-oxo compounds is  $[\text{Fe}(\text{O})(\text{TMCS})]^+$  from our selection [126], as it is the only

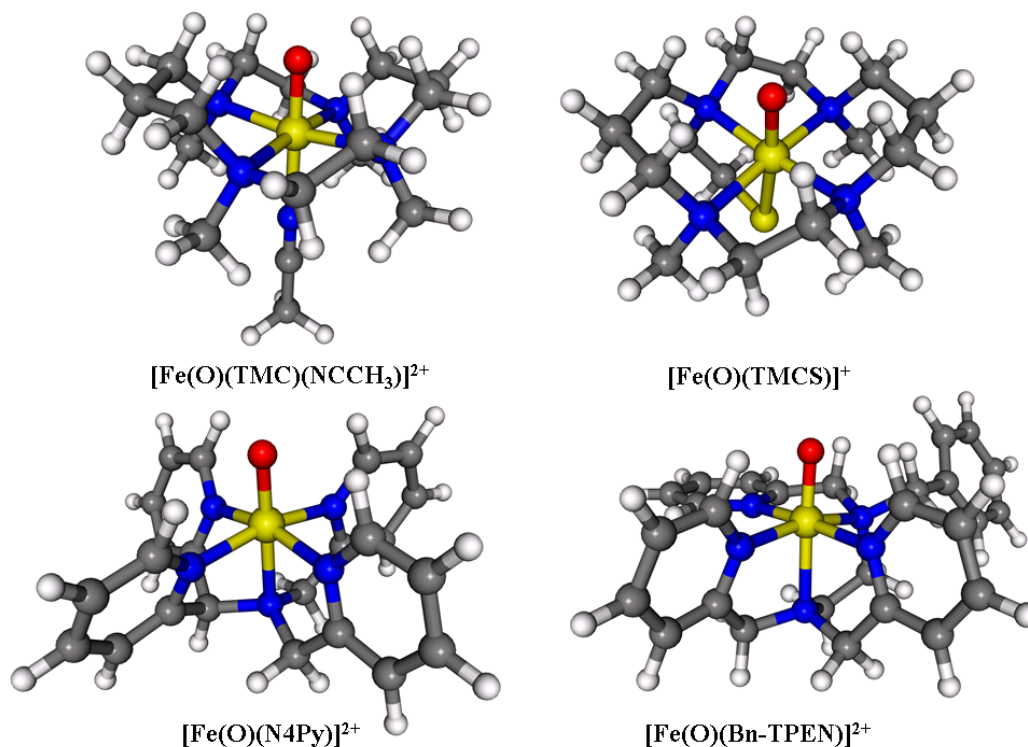


Figure 3.2: Optimized structures (B3LYP-D3/def2-TZVP) of four selected iron(IV)-oxo complexes with  $S = 1$  ground state.

synthetic structural mimic to the  $\text{RS-Fe(IV)=O}$  unit in the high-valent intermediates of cytochrome P450 [127, 128].

In contrast,  $[\text{Fe}(\text{O})(\text{N4Py})]^{2+}$  [129, 130] and  $[\text{Fe}(\text{O})(\text{Bn-TPEN})]^{2+}$  [131], the two remaining  $S = 1$  iron-oxo complexes in the selection, have pentadentate  $\text{N}_5$  ligands and lost the macrocycle motif of the TMC ligand. Like the tetradentate ligands for the  $S = 2$  trigonal bipyramidal complexes, N4Py and Bn-TPEN have a tertiary amine donor trans to the oxo group [129, 132, 133]. In  $[\text{Fe}(\text{O})(\text{N4Py})]^{2+}$  we have four pyridine donors cis to the oxo group, connected to the amine nitrogen via short alkyl chains (see Figure 3.2). This creates one of the most stable non-heme iron(IV)-oxo complexes discovered so far. It has been thoroughly investigated and even crystallized [129, 130]. This is indeed worth mentioning, because successfully obtaining a proper crystal structure is still very rare for non-heme iron(IV)-oxo complexes. In the 2013 review of McDonald and Que [104] we only count seven non-heme oxo-iron species with crystal structures out of a list of over forty different compounds. About half of all the listed non-heme iron(IV)-oxo species do not even have EXAFS (extended X-ray absorption fine structure) data. Our selection includes four of the complexes with known crystal structures (see Table 3.1) and

four with available EXAFS data. The Bn-TPEN ligand on the other hand represents a combination of amine and pyridine donors [132, 133]. It has close structural similarities to a new pair of pentadentate cyclic ligands synthesized by Grohmann *et al.* [134], which will be closely investigated in subsequent chapters for its ligand distortion and the consequences for structure, conformation, and spin-state preferences that come with it.

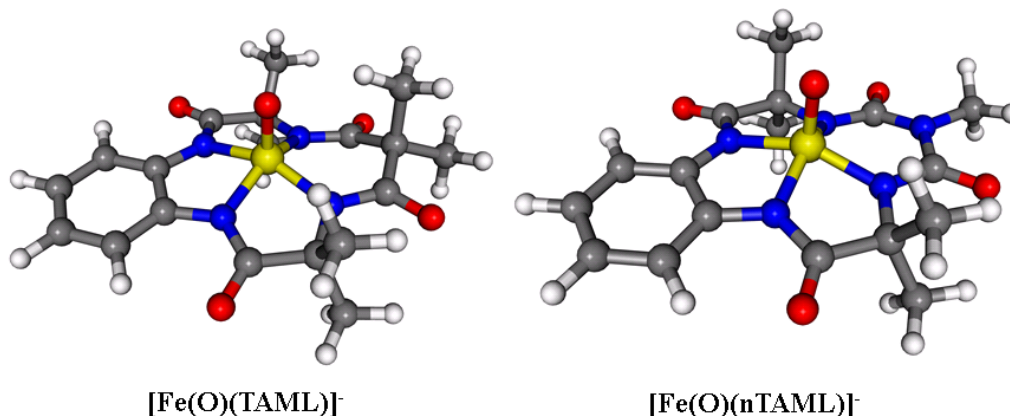


Figure 3.3: Optimized structures (B3LYP-D3/def2-TZVP) of two selected iron(V)-oxo complexes with  $S = 1/2$  ground state.

Even rarer than well characterized non-heme iron(IV)-oxo complexes are synthetic iron(V)-oxo species. The first one,  $[\text{Fe}(\text{O})(\text{TAML})]^-$ , was published in 2007 by Collins *et al.* [135] and is part of our selection, together with its close relative  $[\text{Fe}(\text{O})(\text{bTAML})]^-$ , the final and most recent addition [136] (the 'b' stands for biuret, the replacement of the  $\text{CMe}_2$  unit with a NMe group in the ligand), published in 2014 (see Figure 3.3). There is strong evidence that iron(V)-oxo species are involved in iron-catalyzed oxidations, like in the Rieske dioxygenases [137–139], a group of enzymes responsible for the biodegradation of aromatics in the soil by catalyzing the dehydroxylation of arenes. The tetraanionic tetraamido macrocyclic TAML ligands force the oxo group into a slightly distorted square pyramidal coordination and favor a doublet ground state. Both iron(V)-oxo species show a very different g-tensor from other high-valent iron species that were suggested as oxidants, like  $[\text{Fe}(\text{BPMEN})]$  or  $[\text{Fe}(\text{TPA})]$  [140, 141]. This experimental g-tensor seems to provide a challenge for DFT [142].

### 3.2.3.2 Spin States and the Iron-Oxo Character

A closer look at the spin populations and spin state energy differences of supposed iron(IV)-oxo complexes can help us to shed light on whether or not some of these compounds should rather be considered iron(III)-oxyl complexes instead. Iron(IV) complexes have a formal  $d^4$  configuration, so for an iron(IV)-oxo species with quintet ground state, four unpaired electrons on the iron atom are expected, just as we would expect two paired and two unpaired electrons for a triplet ground state. Table 3.1 shows the spin populations on iron and oxygen for the  $S = 2$  iron-oxo complexes of our selection and we see immediately that this ideal picture is not fulfilled for any of the four molecules. Depending on functional and population analysis method, the number of unpaired electrons on iron varies between 2.92-3.40. This is a remarkably consistent result, considering we compare a pure GGA functional (RIBP86) to two popular global hybrids (B3LYP with 20% exact exchange and PBE0 with 25% exact exchange). Of course the more delocalized character of the spin population for a GGA functional, in comparison to a hybrid functional, is not surprising (for example iron spin population 2.97 for RIBP86 on  $[\text{Fe}(\text{O})(\text{tpa}^{\text{Ph}})]^-$  vs 3.14 for B3LYP), but the fact that there are no qualitative differences for the results based on the functional alone is quite interesting. Nowhere do we even come close to spin populations of four on the iron, as we would normally expect. On the oxo ligand we find spin populations between 0.53-0.69 for  $[\text{Fe}(\text{O})(\text{tpa}^{\text{Ph}})]^-$  and  $[\text{Fe}(\text{O})(\text{TMG}_3\text{tren})]^{2+}$ . Lower values between 0.33-0.47 are found for  $[\text{Fe}(\text{O})(\text{H}_3\text{buea})]^-$ . The rest of the spin density is mostly delocalized onto the nitrogen ligands. While the spin population on the oxygen ligands of the  $S = 2$  species might be considered too low for oxyl radicals, the fact remains that there is not enough spin density on the iron centers to be considered iron(IV) complexes.

Indeed the largest deviation from four unpaired electrons on the iron center is found for  $[\text{Fe}(\text{O})(\text{TMG}_3\text{tren})]^{2+}$  with RIBP86-D3: spin populations give 1.06 unpaired electrons outside iron. Of those 0.61 are localized at the oxygen and 0.45 are spread over the rest of the molecule, mostly onto the four neighboring nitrogen donors. This is evidence that we do not only have strong delocalization of unpaired electrons away from an ideal  $d^4$  configuration on the iron, but might have an iron(III)-oxyl radical character. Of course hybrid functionals give a more localized picture (growing more localized with increased exact-exchange admixture), but even they clearly put far more spin density onto the oxygen atom, than would be reasonably expected for an ideal iron(IV)-oxo system. On the octahedral pentaqua iron(IV)-oxo complex, we find a higher spin population on

the iron than in any of the three trigonal bipyramidal species of our selection, but we also find a high spin population on the oxo ligand, well in line with the picture in  $[\text{Fe}(\text{O})(\text{tpa}^{\text{Ph}})]^-$  and  $[\text{Fe}(\text{O})(\text{TMG}_3\text{tren})]^{2+}$ . The reason for the higher spin population on iron in  $[\text{Fe}(\text{O})(\text{H}_2\text{O})_5]^{2+}$  could be the lack of suitable ligands for delocalization of spin density, compared to the other  $S = 2$  complexes.

The spin populations for the iron(IV)-oxo complexes with triplet ground state (see Table 3.2) are even further away from what we would expect in a  $d^4$  system. Here the numbers of unpaired electrons on iron fall between 1.19-1.48 for the four different species (again taking all three functionals and both population analysis methods into account). The spin population on oxygen is between 0.61-0.87, which is more on average than we find for the oxo complexes with quintet ground state (see Table 3.1). Also the spin populations on iron and oxygen are less affected by the choice of functional, compared to the  $S = 2$  iron(IV)-oxo complexes. In the  $S = 2$  complexes, spin population on the iron increases by up to 0.3 unpaired electrons going from RIBP86 to PBE0, while they change less than 0.1 in the  $S = 1$  complexes. Small amounts of spin population are found on the nitrogen ligands for the  $S = 2$  iron(IV)-oxo complexes (for example a total between 0.2-0.4 unpaired electrons on the nitrogen atoms for B3LYP-D3; also see Figure S2 in Appendix I for spin-density plots). In contrast, nearly all of the spin population is purely concentrated on the Fe-O unit in the  $S = 1$  complexes (see Figure S3 in Appendix I), with only very small bits of negative spin population on the nitrogen donors.

These findings heavily speak against simply classifying the previously discussed eight complexes (see Table 3.1 and 3.2) from our selection as iron(IV)-oxo species. Instead they could rather be described as iron(III)-oxyl radicals. The oxyl radical character is clearer for the iron complexes with triplet ground states, for which we found oxygen spin populations of more than 0.7 a.u. for three of the four compounds. But even for the complexes with quintet ground states, the spin populations on iron were generally too low to just treat them as iron(IV)-oxo compounds, while the spin populations on the oxo ligands were higher than one would normally expect. The last two complexes of our selection,  $[\text{Fe}(\text{O})(\text{TAML})]^-$  and  $[\text{Fe}(\text{O})(\text{bTAML})]^-$ , are formally iron(V)-oxo complexes with a doublet ground state. Table 3.3 shows spin populations of 0.70-0.89 on the iron and 0.14-0.30 on the oxygen for them. This means that for the iron(V)-oxo complexes, the results point much more to a  $d^3$  iron complex with a doublet state, with relatively little spin density delocalized onto the oxo ligand rather than to an iron(IV)-oxyl radical. Going from RIBP86 to B3LYP leads to a stronger localization of spin density at iron

Table 3.1: Important distances, as well as NPA and Mulliken (in brackets) spin populations for four iron(IV)-oxo complexes with  $S = 2$  ground state, calculated for different functionals. A def2-TZVP basis set was used for all atoms. Experimental values are in bold.

Functional	distances in Å			$\langle S^2 \rangle$	spin population NPA [Mulliken]		$\Delta E$ ( $S=2 - S=1$ ) in kJ mol <sup>-1</sup>
	Fe-O	Fe-N <sup>a</sup>	Fe-N <sup>b</sup>		Fe	O	
<b>[Fe(O)(tpa<sup>Ph</sup>)]<sup>-</sup></b>	<b>1.62<sup>c</sup></b>						
RIBP86	1.642	2.132	2.027	6.029	2.97 [2.95]	0.62 [0.68]	-54.2
RIBP86-D3	1.642	2.136	2.003	6.028	2.95 [2.93]	0.62 [0.69]	-40.7
B3LYP	1.620	2.150	2.033	6.055	3.14 [3.06]	0.57 [0.64]	-73.6
B3LYP-D3	1.619	2.150	2.015	6.053	3.12 [3.05]	0.58 [0.64]	-72.9
PBE0	1.605	2.123	2.013	6.067	3.22 [3.16]	0.53 [0.60]	-72.7
PBE0-D3	1.605	2.124	2.001	6.066	3.21 [3.15]	0.54 [0.60]	-71.8
<b>[Fe(O)(TMG<sub>3</sub>tren)]<sup>2+</sup></b>	<b>1.661<sup>d</sup>,</b>	<b>2.112<sup>d</sup>,</b>	<b>2.005<sup>d</sup>,</b>				
	<b>1.65<sup>e</sup></b>	<b>1.99<sup>e</sup></b>	<b>1.99<sup>e</sup></b>				
RIBP86	1.647	2.130	2.038	6.031	2.96 [2.93]	0.61 [0.69]	-62.9
RIBP86-D3	1.650	2.125	2.005	6.029	2.94 [2.92]	0.61 [0.68]	-60.9
B3LYP	1.625	2.140	2.050	6.056	3.14 [3.08]	0.57 [0.64]	-88.6
B3LYP-D3	1.626	2.136	2.022	6.054	3.13 [3.06]	0.57 [0.64]	-86.6
PBE0	1.611	2.120	2.024	6.068	3.22 [3.17]	0.53 [0.60]	-96.4
PBE0-D3	1.612	2.116	2.007	6.066	3.21 [3.16]	0.53 [0.60]	-95.1
<b>[Fe(O)(H<sub>3</sub>buea)]<sup>-</sup></b>	<b>1.680<sup>f</sup></b>	<b>2.064<sup>f</sup></b>	<b>1.983<sup>f</sup></b>				
RIBP86	1.680	2.164	2.005	6.035	2.99 [2.98]	0.43 [0.46]	-42.4
RIBP86-D3	1.681	2.108	2.002	6.034	2.97 [2.97]	0.44 [0.47]	-21.2
B3LYP	1.654	2.173	2.012	6.064	3.20 [3.15]	0.38 [0.41]	-74.4
B3LYP-D3	1.654	2.132	2.007	6.061	3.18 [3.14]	0.39 [0.42]	-57.2
PBE0	1.643	2.142	1.989	6.077	3.29 [3.27]	0.33 [0.35]	-83.2
PBE0-D3	1.643	2.109	1.986	6.074	3.27 [3.26]	0.34 [0.36]	-70.9
<b>[Fe(O)(H<sub>2</sub>O)<sub>5</sub>]<sup>2+</sup></b>							
RIBP86	1.611	2.072	2.090	6.033	3.10 [3.05]	0.63 [0.73]	-24.5
RIBP86-D3	1.611	2.085	2.068	6.033	3.10 [3.05]	0.63 [0.73]	-24.6
B3LYP	1.593	2.084	2.087	6.084	3.26 [3.19]	0.52 [0.63]	-52.9
B3LYP-D3	1.593	2.083	2.079	6.083	3.26 [3.19]	0.52 [0.63]	-52.8
PBE0	1.582	2.096	2.074	6.127	3.40 [3.35]	0.40 [0.50]	-38.6
PBE0-D3	1.581	2.091	2.072	6.126	3.40 [3.35]	0.40 [0.51]	-38.1

<sup>a</sup>Trans to the oxo ligand. <sup>b</sup>Average distance for nitrogens cis to the oxo ligand. <sup>c</sup>Ref. [143]. <sup>d</sup>Ref. [144].  
<sup>e</sup>Ref. [145]. <sup>f</sup>Ref. [146]

Table 3.2: Important distances, as well as NPA and Mulliken (in brackets) spin populations for four iron(IV)-oxo complexes with  $S = 1$  ground state, calculated for different functionals. A def2-TZVP basis set was used for all atoms. Experimental values are in bold.

Functional	distances in Å			$\langle S^2 \rangle$	spin population NPA [Mulliken]		$\Delta E$ ( $S=2 - S=1$ ) in kJ mol <sup>-1</sup>
	Fe-O	Fe-N <sup>a</sup>	Fe-N <sup>b</sup>		Fe	O	
<b>[Fe(O)(TMC)(NCCH<sub>3</sub>)]<sup>2+</sup></b>	<b>1.646<sup>c,d</sup></b>	<b>2.058<sup>c,d</sup></b>	<b>2.09<sup>c,d</sup></b>				
RIBP86	1.640	2.066	2.134	2.020	1.32 [1.34]	0.70 [0.77]	+55.5
RIBP86-D3	1.641	2.042	2.118	2.019	1.31 [1.33]	0.70 [0.77]	+46.7
B3LYP	1.616	2.132	2.135	2.032	1.38 [1.36]	0.70 [0.78]	+16.2
B3LYP-D3	1.617	2.109	2.120	2.030	1.36 [1.35]	0.70 [0.78]	+8.1
PBE0	1.602	2.101	2.101	2.036	1.40 [1.39]	0.67 [0.76]	+5.7
PBE0-D3	1.603	2.087	2.094	2.035	1.40 [1.38]	0.68 [0.76]	+1.1
<b>[Fe(O)(TMCS)]<sup>+</sup></b>	<b>1.70<sup>c</sup></b>	<b>2.33<sup>c</sup></b>	<b>2.09<sup>c</sup></b>				
RIBP86	1.689	2.327	2.132	2.023	1.39 [1.35]	0.61 [0.70]	-32.1
RIBP86-D3	1.690	2.319	2.119	2.022	1.38 [1.35]	0.61 [0.70]	-23.5
B3LYP	1.662	2.355	2.141	2.038	1.46 [1.40]	0.64 [0.72]	-9.0
B3LYP-D3	1.662	2.348	2.129	2.037	1.45 [1.39]	0.63 [0.72]	-17.0
PBE0	1.646	2.327	2.106	2.042	1.48 [1.44]	0.61 [0.70]	-18.5
PBE0-D3	1.646	2.324	2.099	2.041	1.48 [1.44]	0.61 [0.70]	-23.4
<b>[Fe(O)(N4Py)]<sup>2+</sup></b>	<b>1.639<sup>e</sup></b>	<b>2.033<sup>e</sup></b>	<b>1.956<sup>e</sup></b>				
RIBP86	1.644	2.084	1.982	2.016	1.29 [1.24]	0.74 [0.86]	+82.1
RIBP86-D3	1.645	2.082	1.969	2.016	1.29 [1.24]	0.73 [0.86]	+92.2
B3LYP	1.623	2.097	2.004	2.020	1.29 [1.19]	0.74 [0.87]	+30.7
B3LYP-D3	1.623	2.096	1.991	2.020	1.28 [1.20]	0.73 [0.87]	+38.9
PBE0	1.608	2.072	1.977	2.022	1.30 [1.21]	0.72 [0.86]	+23.1
PBE0-D3	1.608	2.072	1.970	2.022	1.30 [1.21]	0.72 [0.86]	+28.1
<b>[Fe(O)(Bn-TPEN)]<sup>2+</sup></b>	<b>1.67<sup>f</sup></b>						
RIBP86	1.647	2.124	2.018	2.016	1.30 [1.27]	0.74 [0.84]	+67.7
RIBP86-D3	1.648	2.115	2.001	2.016	1.30 [1.27]	0.74 [0.84]	+67.2
B3LYP	1.625	2.139	2.036	2.021	1.30 [1.23]	0.73 [0.85]	+22.0
B3LYP-D3	1.625	2.132	2.019	2.021	1.30 [1.23]	0.73 [0.85]	+21.2
PBE0	1.610	2.111	2.005	2.024	1.32 [1.25]	0.72 [0.85]	+14.2
PBE0-D3	1.610	2.107	1.997	2.024	1.32 [1.25]	0.71 [0.84]	+20.3

<sup>a</sup>Trans to the oxo ligand. <sup>b</sup>Average distance for nitrogens cis to the oxo ligand. <sup>c</sup>Ref. [126]. <sup>d</sup>Ref. [122]. <sup>e</sup>Ref. [129, 130]. <sup>f</sup>Ref. [131]

Table 3.3: Important distances, as well as NPA and Mulliken (in brackets) spin populations for two iron(V)-oxo complexes with  $S = 1/2$  ground state, calculated for different functionals. A def2-TZVP basis set was used for all atoms. Experimental values are in bold.

Functional	distances in Å			spin population NPA [Mulliken]		$\Delta E$
	Fe-O	Fe-N <sup>a</sup>	$\langle S^2 \rangle$	Fe	O	( $S=3/2 - S=1/2$ ) in kJ mol <sup>-1</sup>
<b>[Fe(O)(TAML)]<sup>-</sup></b>	<b>1.58<sup>a</sup></b>	<b>1.87<sup>b</sup></b>				
RIBP86	1.603	1.891	0.763	0.76 [0.71]	0.23 [0.29]	+58.8
RIBP86-D3	1.602	1.887	0.763	0.76 [0.71]	0.23 [0.29]	+59.4
B3LYP	1.577	1.887	0.771	0.85 [0.80]	0.18 [0.23]	+37.9
B3LYP-D3	1.577	1.883	0.771	0.85 [0.80]	0.18 [0.23]	+38.9
PBE0	1.559	1.867	0.775	0.89 [0.85]	0.14 [0.18]	+28.7
PBE0-D3	1.559	1.865	0.775	0.88 [0.85]	0.14 [0.19]	+29.4
<b>[Fe(O)(bTAML)]<sup>-</sup></b>						
RIBP86	1.603	1.882	0.762	0.76 [0.70]	0.23 [0.30]	+63.3
RIBP86-D3	1.602	1.879	0.762	0.76 [0.70]	0.23 [0.30]	+63.5
B3LYP	1.577	1.878	0.769	0.84 [0.79]	0.18 [0.23]	+44.6
B3LYP-D3	1.576	1.876	0.769	0.84 [0.79]	0.18 [0.23]	+45.1
PBE0	1.558	1.859	0.773	0.87 [0.84]	0.15 [0.19]	+36.0
PBE0-D3	1.558	1.857	0.773	0.87 [0.84]	0.15 [0.19]	+36.3

<sup>a</sup>Average distance for nitrogens cis to the oxo ligand. <sup>b</sup>Ref. [135].

(increasing the spin population by nearly 0.1 unpaired electrons), further supporting a  $d^3$  iron(V) configuration.

The shape of the spin density at the oxo-group of the iron(V)-oxo complexes is also quite different from what we find for the formal iron(IV)-oxo species from our selection. Figure 3.4 shows an isosurface plot of the spin density of [Fe(O)(TAML)]<sup>-</sup>, together with the respective plots of [Fe(O)(TMC)(NCCH<sub>3</sub>)]<sup>2+</sup> and [Fe(O)(TMG<sub>3</sub>tren)]<sup>2+</sup>, which are shown as representatives of either iron(IV)-oxo compounds or iron(III)-oxyl radicals with triplet and quintet ground states, respectively. The isosurface plots of the spin density of the seven other complexes in their ground states look very similar to the ones shown in Figure 3.4 (see Figures S2, S3, and S4 in Appendix I).

For the formal iron(IV)-oxo complexes, the spin density at oxygen is distributed uniformly in a ring around it. Together with the information from the spin population analysis, the isosurface plots strongly suggest one unpaired electron at oxygen, which can move freely in the xy plane. Such a picture is appropriate for an oxyl radical. While we see almost exclusively positive spin density on [Fe(O)(TMC)(NCCH<sub>3</sub>)]<sup>2+</sup> ( $S = 1$ ), small amounts of negative spin density can be found above and below the ring around

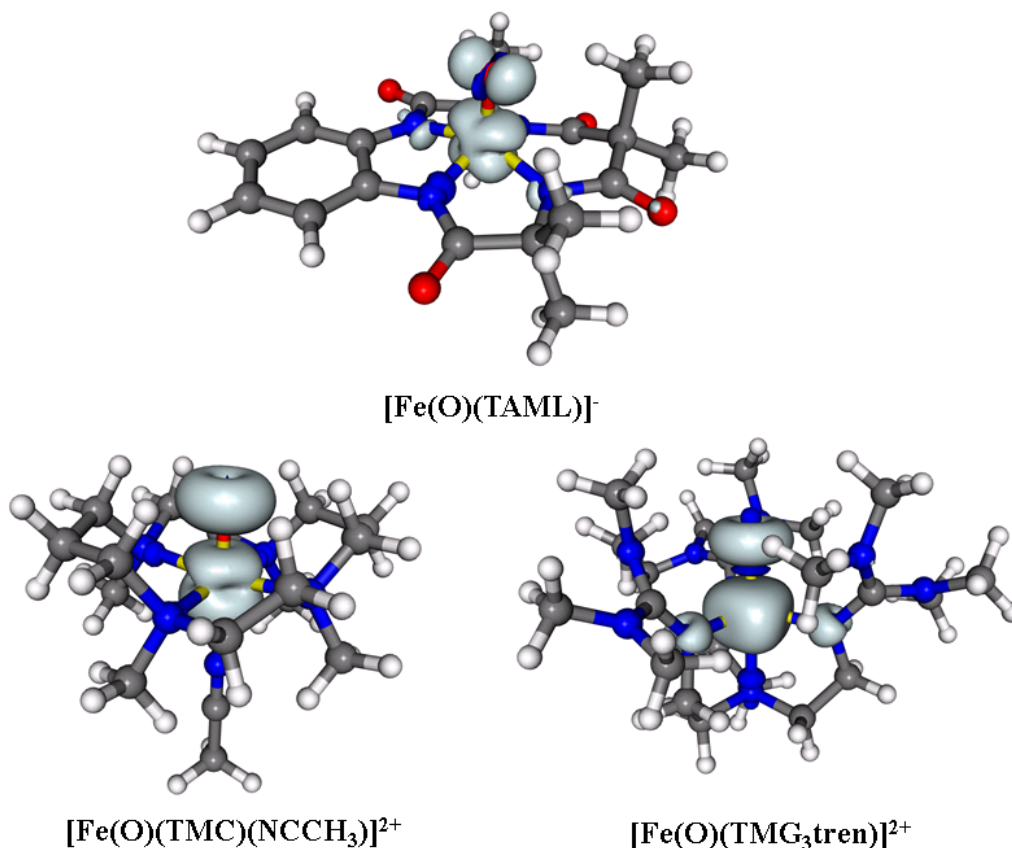


Figure 3.4: Isosurface plots of the spin density ( $\pm 0.005$  a.u.) of  $[\text{Fe}(\text{O})(\text{TAML})]^-$  ( $S = 1/2$ ),  $[\text{Fe}(\text{O})(\text{TMC})(\text{NCCH}_3)]^{2+}$  ( $S = 1$ ) and  $[\text{Fe}(\text{O})(\text{TMG}_3\text{tren})]^{2+}$  ( $S = 2$ ). B3LYP-D3/def2-TZVP optimized structures.

oxygen on  $[\text{Fe}(\text{O})(\text{TMG}_3\text{tren})]^{2+}$  ( $S = 2$ ) and on the axial nitrogen ligand. As already mentioned before, the spin density of  $[\text{Fe}(\text{O})(\text{TAML})]^-$  ( $S = 1/2$ ) presents a very different picture compared to the formal iron(IV) species in Figure 3.4. Here the single unpaired electron seems to be mainly localized in a  $d_{xz}(\text{Fe})\text{-}p_x(\text{O})$  orbital and, as we know from spin population analyses, is mainly localized at iron. In fact, the spin density of  $[\text{Fe}(\text{O})(\text{TAML})]^-$  agrees well with the expected situation for an iron(V) complex, with low-spin  $d^3$  configuration, based on a ligand-field diagram ( $C_{4v}$  symmetry). Altogether the isosurface plots of the spin densities support significant iron(III)-oxyl character for the formal iron(IV)-oxo complexes, in particular for an  $S = 1$  ground state. For the iron(V)-oxo complexes on the other hand much less oxyl character is found. The spin populations calculated by NPA and Mulliken population analysis show noteworthy differences between each other. These differences are nearly independent from the choice of functional. In general Mulliken population analysis gives a stronger oxyl radical charac-

ter than NPA (see Tables 3.1 and 3.2), but overall the differences between the methods are too small to lead to different interpretations of the results.

Since a lot of our argument, whether our selected iron(IV)-oxo complexes should rather be described as iron(III)-oxyl radicals, is based on spin populations, the possibility of spin contamination and broken-symmetry solutions must be taken into account as well. A broken-symmetry DFT solution could lead to significant changes in energy and spin population, compared to the true electronic ground state, and it could in principle present a wrong picture of the electronic structure, leading to a wrong interpretation (for more information about broken-symmetry DFT, see, for example, ref. [147–149]). The ideal  $\langle S^2 \rangle$  value of an  $S = 2$  system is 6, and the first thing we can see is that the  $\langle S^2 \rangle$  expectation values for the iron(IV)-oxo complexes with quintet ground state fall between 6.029 and 6.084 for RIBP86, B3LYP and PBE0 (see Table 3.1). The single exception is  $[\text{Fe}(\text{O})(\text{H}_2\text{O})_5]^{2+}$  with PBE0, where  $\langle S^2 \rangle$  values up to 6.127 are reached. This can probably be attributed to the small ligand-field splitting in  $[\text{Fe}(\text{O})(\text{H}_2\text{O})_5]^{2+}$ , which favors mixing in of spin contaminating excited states.

As expected, all complexes studied here show an increase in the  $\langle S^2 \rangle$  value with growing amounts of exact-exchange admixture (0% for RIBP86, 20% for B3LYP, and 25% for PBE0), but the changes are significantly smaller for the  $S = 1$  species and the iron(V)-oxo complexes, than for the  $S = 2$  complexes. Given an ideal  $\langle S^2 \rangle$  value of 2, the results for  $S = 1$  complexes only range from 2.016 to 2.042 (see Table 3.2), and the  $\langle S^2 \rangle$  values for the two iron(V) molecules only range from 0.763 to 0.775 (compared to ideal 0.75 for a doublet; see Table 3.3). The spin populations of the iron-oxo compounds do not show any signs for significant broken-symmetry character. Weakly antiferromagnetically coupled pairs are absent, for which a significant raise in the  $\langle S^2 \rangle$  value would be expected. Overall, the amount of negative spin population on the non-heme iron-oxo complexes is small and mainly concentrated on the nitrogen donor atoms. This is true for the complexes in their ground states, but it is not generally true for excited states. For example, while nine out of the ten molecules studied have excited states that look very similar in spin population and density to their ground-state counterparts (e.g., the results for the spin populations of  $[\text{Fe}(\text{O})(\text{TMG}_3\text{tren})]^{2+}$  in its excited triplet state is very similar to that of  $[\text{Fe}(\text{O})(\text{N4Py})]^{2+}$  in its triplet ground state),  $[\text{Fe}(\text{O})(\text{tpa}^{\text{Ph}})]^-$  instead gives a broken-symmetry solution with a spin population of 2.45 at iron and -0.62 at oxygen for B3LYP. This broken-symmetry solution is well reflected in the spin density of  $[\text{Fe}(\text{O})(\text{tpa}^{\text{Ph}})]^-$  (see Figure S2 in Appendix I), compared to the other three  $S = 2$

complexes in their excited triplet state. Unsurprisingly no broken-symmetry solutions are created with RIBP86.

Thus, neither spin contamination nor broken-symmetry solutions are serious problems for the correct description of the electronic structure of the present iron-oxo complexes, but the question remains whether the functionals we used yield the correct electronic structure. Do we get the right energetic order of spin states for the molecules studied? In nine out of ten cases the answer is yes. The exception is  $[\text{Fe}(\text{O})(\text{TMCS})]^+$ , a complex with an experimentally assigned triplet ground state [126], for which the quintet state is found lower in energy for all three functionals (see Table 3.2). This makes  $[\text{Fe}(\text{O})(\text{TMCS})]^+$  a peculiar example for an iron(IV)-oxo complex, which was another reason to include it in our selection (the main reason being its axial sulfur ligand, see Chapter 3.2.3.1), as the choice of functional yields very counterintuitive results. While RIBP86 is known to bias towards lower spin states in transition metal complexes (see, for example, refs. [150,151]), it mostly gets the right order of spin states for the complexes in our selection, with the sole exception of  $[\text{Fe}(\text{O})(\text{TMCS})]^+$  (see Tables 3.1, 3.2 and 3.3). The closest result to a correct ground state for  $[\text{Fe}(\text{O})(\text{TMCS})]^+$  is actually gained for B3LYP. Larger exact-exchange admixture does not seem to solve the problem, as PBE0 shows more pronounced deviations from the correct triplet ground state than B3LYP (D3 dispersion corrections also worsen the results for hybrid functionals, but not for RIBP86). The fact that DFT calculations give a different order of spin states for  $[\text{Fe}(\text{O})(\text{TMCS})]^+$  than experiment has been reported by other groups as well [152,153]. A computational study by de Visser found that the molecule only reacts via single-state reactivity on a quintet spin state surface [152], which is in contrast to the experimentally assigned triplet ground state found by Que *et al.* [126]. A very small energy gap between the  $\pi_{xy}^*$  and  $\sigma_{x^2-y^2}^*$  molecular orbitals was suggested as a possible reason why the quintet spin state dropped below the triplet state [153]. The same reason is usually given for the high-spin ground state of five-coordinated non-heme iron(IV)-oxo complexes, including enzymes [154]. While DFT calculations energetically favor the quintet spin state, comparisons of computed and experimental Mössbauer parameters and zero-field splittings (see Chapter 3.2.3.3) nearly exclude the possibility of an  $S = 2$  ground state for  $[\text{Fe}(\text{O})(\text{TMCS})]^+$ .

Besides the above-mentioned exception, RIBP86 generally stabilizes the triplet state of the studied complexes, while the hybrid functionals B3LYP and PBE0 favor the higher quintet spin state. The effect of D3 dispersion corrections on  $\Delta E$  is only around 1-

2 kJ mol<sup>-1</sup> for [Fe(O)(tpa<sup>Ph</sup>)]<sup>-</sup> (with the exception of RIBP86), [Fe(O)(TMG<sub>3</sub>tren)]<sup>2+</sup> and [Fe(O)(H<sub>2</sub>O)<sub>5</sub>]<sup>2+</sup>, but has a stronger influence on [Fe(O)(H<sub>3</sub>buea)]<sup>-</sup>, where it lowers the energy gap by 12-21 kJ mol<sup>-1</sup>. While the  $\Delta E$  values of the  $S = 2$  complexes are sensitive to the choice of functional, no clear trend could be seen for the amount of exact-exchange admixture used (for example, the  $\Delta E$  values for [Fe(O)(tpa<sup>Ph</sup>)]<sup>-</sup> are very similar for B3LYP and PBE0, but go into opposite directions for [Fe(O)(TMG<sub>3</sub>tren)]<sup>2+</sup> and [Fe(O)(H<sub>2</sub>O)<sub>5</sub>]<sup>2+</sup>). For the three complexes with correctly predicted triplet ground state, we see a clear pattern of increased exact-exchange admixture stabilizing the quintet state, thereby lowering the  $\Delta E$  values.

Here we also see that PBE0 might already have too much exact-exchange admixture for the correct description of  $S = 1$  iron-oxo complexes. The smaller energy gaps for the  $S = 1$  complexes (compared to the  $S = 2$  complexes) are no problem for [Fe(O)(N4Py)]<sup>2+</sup> and [Fe(O)(Bn-TPEN)]<sup>2+</sup> (see Table 3.2), but for [Fe(O)(TMC)(NCCH<sub>3</sub>)]<sup>2+</sup> the spin states nearly become degenerate with PBE0 (+6 kJ mol<sup>-1</sup> or +1 kJ mol<sup>-1</sup> with D3 dispersion corrections). Even if we assume that the errors for the relative energies are very small for our chosen functional, achieving accuracy of more than 2 kJ mol<sup>-1</sup> for  $\Delta E$  seems very unlikely. Indeed, such small errors may already be caused by insufficient basis set size alone, which otherwise was not found to be a problem for the iron-oxo compounds (see Table S3 in Appendix I for basis set comparisons).

In order to get a better picture of the influence of different amounts of exact-exchange admixture on the spin populations and relative spin-state energies of non-heme iron(IV)-oxo compounds, a quick scan over the exact-exchange admixture was done for two molecules. One complex with a triplet and another complex with a quintet ground state were chosen ([Fe(O)(N4Py)]<sup>2+</sup> and [Fe(O)(TMG<sub>3</sub>tren)]<sup>2+</sup>, respectively) and the following BLYP based global hybrid was used:

$$E_{XC}^{BXXLYP} = a_0 E_X^{exact} + (1 - a_0) E_X^{B88} + E_C^{LYP} \quad (3.1)$$

The parameter  $a_0$  controls the amount of exact-exchange admixture. Table 3.4 sums up the results and shows that an exact-exchange admixture of up to 30% still leads to the correct ground states for both complexes, without increasing the spin contamination too much. Since  $\Delta E$  for [Fe(O)(N4Py)]<sup>2+</sup> decreases by about 20 kJ mol<sup>-1</sup> for every ten percent step from 10 to 50% exact exchange, a lower value of 20% might be better for complexes with smaller spin-state gaps, like [Fe(O)(TMC)(NCCH<sub>3</sub>)]<sup>2+</sup>.

For trigonal-bipyramidal complexes like  $[\text{Fe}(\text{O})(\text{TMG}_3\text{tren})]^{2+}$ , the amount of exact exchange is not important for getting the correct ground state, due to the extremely large preference for the quintet state. Even GGA functionals (BLYP with 0% exact exchange) give qualitatively the right answer. However, exact-exchange admixtures above 30% cannot be recommended, since the spin contamination drastically increases with higher values. With increased exact-exchange admixture, the spin populations on iron and oxygen move into opposite directions for the triplet and quintet states. For the triplet state, the oxyl radical character gets even more pronounced, as the spin populations change to one unpaired electron on iron and oxygen each. In contrast, the quintet state shows a fast increase in the spin population for iron and a decline for oxygen, gradually moving towards a true iron(IV)-oxo situation with four unpaired electrons on iron. However, at the same time, the spin contamination drastically increases and at exact-exchange admixtures of 50% and more, we find broken-symmetry solutions with negative spin populations at oxygen. In conclusion, exact-exchange admixtures below 30% do not affect our prediction for the iron-oxo vs iron-oxyl radical question. We note that a lower spin population at oxygen in the quintet state, compared to the spin population in the triplet state, seems to be a general rule for formal non-heme iron(IV)-oxo complexes.

### 3.2.3.3 Verification of the Correct Electronic Structure

In the last chapter we have established that our choice of functionals generally yields the correct ground states for the iron-oxo complexes (with the exception of  $[\text{Fe}(\text{O})(\text{TMCS})]^+$ ) and that our results do not suffer from spin contamination or broken-symmetry solutions, which could all potentially explain the surprising results for the spin populations. Still we must also make sure that the electronic structures of our chosen complexes are correctly described in our calculations. That way we can hopefully exclude the possibility that the spin populations pointing to iron(III)-oxyl radicals are really just caused by erroneous electronic structures.

This can only be done by comparison of our DFT results to different experimental data. As already mentioned in previous chapters, structural data for non-heme iron-oxo complexes are quite sparse. Within our selection, four compounds have known structures from X-ray diffraction measurements and four at least have EXAFS data. No interatomic distances are known for the highly unstable pentaqua iron-oxo complex and for the iron(V)-oxo complex  $[\text{Fe}(\text{O})(\text{bTAML})]^-$ .

Table 3.4: Scan over the amount of exact-exchange admixture (EXX) for  $[\text{Fe}(\text{O})(\text{N4Py})]^{2+}$  ( $S = 1$  ground state) and  $[\text{Fe}(\text{O})(\text{TMG}_3\text{tren})]^{2+}$  ( $S = 2$  ground state). BXXLYP/def2-TZVP single-points at B3LYP/def2-TZVP structures. Spin-state energy differences  $\Delta E$  are in  $\text{kJ mol}^{-1}$ . Results for NPA and Mulliken spin population analysis (the latter in brackets) are given as well.

$[\text{Fe}(\text{O})(\text{N4Py})]^{2+}$								
			S = 1			S = 2		
$\Delta E$			spin population			spin population		
EXX	(S=2 - S=1)		NPA [Mulliken]			NPA [Mulliken]		
in %	in $\text{kJ mol}^{-1}$	$\langle S^2 \rangle$	Fe	O	$\langle S^2 \rangle$	Fe	O	
0	+71.6	2.015	1.29 [1.23]	0.72 [0.85]	6.026	3.01 [2.96]	0.61 [0.71]	
10	+48.9	2.017	1.30 [1.21]	0.73 [0.86]	6.038	3.09 [3.02]	0.57 [0.69]	
20	+28.2	2.020	1.28 [1.19]	0.74 [0.87]	6.059	3.18 [3.10]	0.52 [0.64]	
30	+8.6	2.024	1.26 [1.15]	0.76 [0.90]	6.100	3.31 [3.22]	0.42 [0.54]	
40	-12.2	2.025	1.17 [1.05]	0.85 [0.99]	6.281	3.66 [3.61]	0.05 [0.12]	
50	-35.7	2.026	1.08 [0.97]	0.95 [1.06]	6.504	4.03 [3.95]	-0.34 [-0.24]	
60	-61.0	2.029	1.04 [0.94]	0.99 [1.09]	6.624	4.19 [4.12]	-0.49 [-0.41]	
$[\text{Fe}(\text{O})(\text{TMG}_3\text{tren})]^{2+}$								
			S = 1			S = 2		
$\Delta E$			spin population			spin population		
EXX	(S=2 - S=1)		NPA [Mulliken]			NPA [Mulliken]		
in %	in $\text{kJ mol}^{-1}$	$\langle S^2 \rangle$	Fe	O	$\langle S^2 \rangle$	Fe	O	
0	-62.0	2.779	1.36 [1.35]	0.63 [0.72]	6.027	2.93 [2.88]	0.61 [0.69]	
10	-75.0	2.843	1.34 [1.31]	0.68 [0.77]	6.039	3.04 [2.98]	0.60 [0.67]	
20	-87.4	2.889	1.29 [1.25]	0.72 [0.82]	6.057	3.14 [3.07]	0.57 [0.64]	
30	-99.1	2.923	1.23 [1.16]	0.77 [0.88]	6.086	3.26 [3.19]	0.50 [0.57]	
40	-109.4	2.940	1.10 [1.00]	0.89 [1.00]	6.177	3.49 [3.45]	0.29 [0.33]	
50	-118.1	2.941	1.01 [0.92]	0.97 [1.07]	6.438	3.90 [3.90]	-0.19 [-0.18]	
60	-133.0	2.942	0.97 [0.90]	1.01 [1.09]	6.587	4.12 [4.10]	-0.41 [-0.40]	

Compared to the available experimental data, the most accurate Fe-O bond lengths, with a mean absolute error (MAE) of only 1.3 pm, are obtained from BP86 calculations (see Table S4 in Appendix I). The deviations appear to be statistical, with no noticeable trend (the mean signed error for BP86 is less than -0.1 pm). In contrast, B3LYP and PBE0 both give Fe-O bond lengths which are systematically too short for all eight complexes, with MAEs of 2.4 and 3.9 pm, respectively. The Fe-N distances for the nitrogen atoms cis to the oxo ligand are overestimated by all three considered functionals, with the only exception of the iron(V)-oxo complex  $[\text{Fe}(\text{O})(\text{TAML})]^-$  with PBE0. Calculated Fe-N distances for the nitrogen atom trans to the oxo ligand show the largest errors, with MAEs of 6 pm for B3LYP and about 3.6 and 3.4 pm for BP86 and PBE0. In general the effect of D3 dispersion corrections is negligible for the Fe-O distance, but improves the distances for the nitrogen ligand atoms (see Table S4 in Appendix I).

Overall the BP86 structures are closest to experiment, providing very accurate Fe-O distances and, with inclusion of dispersion corrections, good Fe-N bond lengths as well. While PBE0-D3 shows excellent agreement to experiment for the Fe-N distances, the crucial Fe-O bond comes out too short for all complexes. It should be noted that none of the optimized structures deviates appreciably from the experimental values. That is, the DFT description of their electronic structure does not contradict experimental findings in this regard. This is especially important for the DFT spin populations on iron and oxygen, which, as was discussed in previous chapters, strongly point to iron(III)-oxyl radicals. These spin populations should relate to the Fe-O bond length, as one might expect shorter bond lengths for a true iron(IV)-oxo situation

A final word of caution about the quality of EXAFS data in comparison to X-ray diffraction distances: for  $[\text{Fe}(\text{O})(\text{TMG}_3\text{tren})]^{2+}$ , both data from EXAFS and crystal structure are available (see Table 3.1, EXAFS values only have two decimal places) and they show considerable differences. While a 1.1 pm shorter Fe-O distance for EXAFS is acceptable, over 12 pm difference for the Fe-N distance (nitrogen trans to the oxygen) is too far off. The main problem seems to be the inability of EXAFS to distinguish between nitrogen ligands cis and trans to the oxo ligand. This problem is also certainly the reason, why only EXAFS data for the crucial Fe-O distance are available for some complexes. For  $[\text{Fe}(\text{O})(\text{TMCS})]^+$  and  $[\text{Fe}(\text{O})(\text{TAML})]^-$  this problem does not occur, as both have either different kinds of atoms as cis and trans ligands to oxygen or no trans ligand at all. In summary, in the absence of X-ray crystallographic data, EXAFS data may be good enough as reference data for the Fe-O distance, but not for the other metal-ligand distances, if there are inequivalent coordinating atoms with the same atom type (which mainly concerns different nitrogen ligand atoms in non-heme iron-oxo complexes).

Besides the molecular structure, calculated Mössbauer parameters are even better indicators for the correct or incorrect description of the electronic structure in  $^{57}\text{Fe}$ -containing compounds. The experimental isomer shift values for the formal iron(IV)-oxo complexes of our selection fall between -0.04 and 0.38 mm s<sup>-1</sup> (see Table 3.5). Using a linear fit for the calculation of the isomer shifts with a slope of about -0.36 mm s<sup>-1</sup>, means that this entire range of results is covered by a difference of less than 1.2 a.u. in the electron density at the iron nucleus. B3LYP with an uncontracted def2-QZVPP basis set gives an electron density of over 11800 a.u. at the iron atom, so very small changes in the electron density lead to large deviations for the calculated isomer shifts, making them very sensitive indicators for the correct electronic structure. Changing the spin

states of the iron molecules should also have an influence on the Mössbauer parameters, which could make them useful for the assignment of the experimental ground state as well, besides the spin-state energetics. The non-heme iron(V)-oxo complexes have experimental isomer shifts of  $-0.42 \text{ mm s}^{-1}$  and  $-0.44 \text{ mm s}^{-1}$ , separating them well from the iron(IV) complexes. We mention in passing that a clear distinction between formal iron(IV)- and iron(V)-oxo complexes is not generally possible by isomer shifts alone. For example, a proposed iron(V)-oxo complex by Münck and Que [155], with a positively charged  $\text{O}=\text{Fe}=\text{NC}(\text{O})\text{CH}_3$  unit and the neutral TMC macrocycle as supporting ligand, showed an isomer shift of  $0.10 \text{ mm s}^{-1}$ , which would also be in the range for iron(IV)-oxo complexes.

Table 3.5: Calculated Mössbauer parameters and spin-state energy differences for a selected group of ten iron-oxo compounds. B3LYP-D3/def2-TZVP optimized structures.<sup>a,b</sup>

	S	$\delta$ [mm s <sup>-1</sup> ]	$\delta$ expt.	$\Delta E_Q$ [mm s <sup>-1</sup> ]	$\Delta E_Q$ expt.	$\Delta E$ [kJ mol <sup>-1</sup> ]
<b>[Fe(O)(tpa<sup>Ph</sup>)]<sup>-c</sup></b>	1	0.13		1.42		+72.9
	2	0.07	0.09	-0.30	0.51	0
<b>[Fe(O)(TMG<sub>3</sub>tren)]<sup>2+c</sup></b>	1	0.07		-1.50		+86.6
	2	0.08	0.09	-0.35	-0.29	0
<b>[Fe(O)(H<sub>3</sub>buea)]<sup>-c</sup></b>	1	-0.08		2.00		+57.2
	2	0.02	0.02	0.82	0.43	0
<b>[Fe(O)(H<sub>2</sub>O)<sub>5</sub>]<sup>2+c</sup></b>	1	0.31		0.23		+52.8
	2	0.46	0.38	-0.96	-0.33	0
<b>[Fe(O)(TMC)(NCCH<sub>3</sub>)]<sup>2+c</sup></b>	1	0.17	0.17	1.17	1.23	0
	2	0.19		-0.56		+8.1
<b>[Fe(O)(TMCS)]<sup>+c</sup></b>	1	0.21	0.19	0.66	-0.22	+17.0
	2	0.26		-2.31		0
<b>[Fe(O)(N<sub>4</sub>Py)]<sup>2+c</sup></b>	1	0.01	-0.04	0.83	0.93	0
	2	0.18		-0.51		+38.9
<b>[Fe(O)(Bn-TPEN)]<sup>2+c</sup></b>	1	0.04	0.01	0.87	0.80	0
	2	0.18		-0.67		+21.2
<b>[Fe(O)(TAML)]<sup>-c</sup></b>	1/2	-0.49	-0.42	4.30	4.25	0
	3/2	-0.19		3.27		+38.9
<b>[Fe(O)(bTAML)]<sup>-d</sup></b>	1/2	-0.50	-0.44	4.24	4.27	0
	3/2	-0.41		-0.56		+45.1

<sup>a</sup>Linear equation used:  $\delta[\text{mm s}^{-1}] = -0.3594 * (\rho(\text{DFT}) - 11800) + 10.521$ . <sup>b</sup>Uncontracted def2-QZVPP basis set used for iron in all subsequent single-point calculations. <sup>c</sup>Ref. [104]. <sup>d</sup>Ref. [136].

Such overlapping areas of isomer shifts for different oxidation states are also found at the iron(III)-iron(IV) border of the spectrum. This of course means that the assignment of oxidation states, on the basis of measured Mössbauer parameters can be problematic. Indeed, since experimentalists already have great difficulties distinguishing between iron(III)- and iron(IV)-oxo compounds on spectroscopic data alone, it does

not come as a surprise that an unambiguous identification of a non-heme iron(III)-oxyl radical could not be achieved yet. In any case, the possibility of a formal non-heme iron(IV)-oxo complex really being an iron(III)-oxyl radical instead cannot simply be refuted by pointing at measured Mössbauer parameters. However, what can be done is comparing the calculated Mössbauer parameters to experiment, to see whether or not the electronic structure is described correctly. An incorrect description, especially concerning the spin density and spin populations would certainly have an effect on the total density at the iron nucleus and would therefore lead to wrong Mössbauer parameters. We would also expect to see different Mössbauer parameters for triplet and quintet states, which could provide further evidence for the correct ground state. Looking at the isomer shifts in Table 3.5, we see a close agreement of our calculated isomer shifts to experiment, with an overall mean absolute error of  $0.034 \text{ mm s}^{-1}$  and a mean signed error of  $0.002 \text{ mm s}^{-1}$ , respectively. These errors are well in line with other DFT benchmarks for Mössbauer calculations on iron complexes [88], where B3LYP was found to outperform most other tested functionals. Other protocols for structure optimization and subsequent single-point calculations for the Mössbauer parameters have been tried as well (see Tables S5 and S6 in Appendix I for a comparison of different linear fits for isomer shifts and results for quadrupole splittings). The largest deviations are found for the pentaqua iron(IV)-oxo complex and the two iron(V)-oxo species. Considering the distinct nature of the pentaqua iron-oxo complex, compared to the other iron-oxo complexes of our selection, this might not come as a surprise. Its experimental isomer shift of  $0.38 \text{ mm s}^{-1}$  is the largest value ever published for an iron(IV)-oxo complex.

Distinguishing between ground states and excited spin states by comparing calculated isomer shifts to experiment is an overall success, but in the case of  $[\text{Fe}(\text{O})(\text{TMG}_3\text{tren})]^{2+}$  and  $[\text{Fe}(\text{O})(\text{TMC})(\text{NCCH}_3)]^{2+}$  the calculated isomer shifts for triplet and quintet states are too close together to make an unambiguous assignment.  $[\text{Fe}(\text{O})(\text{bTAML})]^-$  can also be considered a problematic case. Its experimental value of  $-0.44 \text{ mm s}^{-1}$  lies between the calculated isomer shifts of the two spin states and is actually leaning closer to the (incorrect) quartet state. Still, the correct ground states can easily be assigned to all three complexes by looking at their quadrupole couplings as additional indicators. The  $\Delta E_Q$  values for the wrong spin states are very far off, for example,  $-0.56 \text{ mm s}^{-1}$  for  $[\text{Fe}(\text{O})(\text{bTAML})]^-$  in its quartet state, in comparison to  $4.24 \text{ mm s}^{-1}$  for the doublet state. This is in extremely good agreement to the experimental value of  $4.27 \text{ mm s}^{-1}$ , making the choice of the correct ground state unambiguous. For the other complexes of our selection, clearly different isomer shifts were found for ground and

excited states. We even find that the calculated isomer shift of  $[\text{Fe}(\text{O})(\text{TMCS})]^+$  points to the experimentally found triplet ground state. This suggests Mössbauer parameters as a more accurate tool to identify the correct ground state than spin-state energetics.  $[\text{Fe}(\text{O})(\text{N4Py})]^{2+}$  and  $[\text{Fe}(\text{O})(\text{Bn-TPEN})]^{2+}$ , the octahedral  $S = 1$  complexes with  $\text{N}_5$  pentadentate ligands, show sharp increases in the isomer shifts upon going from triplet to quintet spin states. A new iron(IV)-oxo complex, with a structurally related  $\text{N}_5$  chelate ligand was recently synthesized by Grohmann *et al.* [134]. It shows the same pattern for the calculated isomer shifts (see Chapter 3.3 and 3.4).

The calculated quadrupole splittings show a more mixed picture than the isomer shifts. Six out of ten calculated  $\Delta E_Q$  values show good or excellent agreement with experiment, while four values are far off. Overall this leads to a mean absolute error of  $0.304 \text{ mm s}^{-1}$  and a mean deviation of  $-0.044 \text{ mm s}^{-1}$  (see Table S6 in Appendix I) for the  $\Delta E_Q$  values of our selection. These are comparatively good results that fall perfectly in line with previous benchmarks on  $^{57}\text{Fe}$  quadrupole splittings [88], but only show part of the problem. Especially the iron(IV)-oxo complexes with quintet ground states seem to cause big difficulties: aside from  $[\text{Fe}(\text{O})(\text{TMG}_3\text{tren})]^{2+}$ , they all show large deviations, making their calculated quadrupole splittings bad indicators for the right experimental spin state. From the complexes with triplet ground states, only the results for  $[\text{Fe}(\text{O})(\text{TMCS})]^+$  are off. Since quadrupole splittings are highly dependent on molecular structure, we also calculated  $\Delta E_Q$  values for RIBP86-optimized structures (see Table S6 in Appendix I). RIBP86-optimized structures featured better agreement with interatomic distances from crystal structures and EXAFS data than structures optimized with B3LYP or PBE0 (see Tables 3.1-3.3 and Table S4 in Appendix I). But while the initial assumption was that improved structures should lead to more accurate quadrupole splittings, the results were actually worse (see Table S6 in Appendix I). Also, changing the optimization protocol did not improve the calculated  $\Delta E_Q$  values for the  $S = 2$  complexes and for  $[\text{Fe}(\text{O})(\text{TMCS})]^+$ . This further supports the use of B3LYP for the calculation of Mössbauer parameters.

In none of the cases do calculated isomer shifts and quadrupole splittings point to a different spin state than the experimental one (see Table 3.5). Interestingly, the largest  $\Delta E_Q$  values, belonging to the two iron(V)-oxo species, are very well reproduced by DFT, even though problems were reported before for calculating  $\Delta E_Q$  values larger than  $2 \text{ mm s}^{-1}$  [88]. In summary, the results for the calculated Mössbauer parameters confirm that our calculated electronic structures are indeed in good agreement with experiment.

Therefore, also the spin populations in our formal iron(IV)-oxo complexes, that strongly pointed to iron(III)-oxyl radicals, are not an indication of incorrect descriptions of electronic structure.

In order to gather additional evidence for the correctness of our DFT-derived electronic structures, the zero-field splitting (ZFS) is another interesting molecular property to look at. Experimental ZFS are available for seven out of the eight non-heme iron(IV)-oxo complexes studied (no ZFS are available for the iron(V) compounds). The experimental D values and the results of the calculations with BP86 and B3LYP are shown in Table 3.6. We can see immediately that the experimental values for the trigonal-bipyramidal complexes, with quintet ground states, are reproduced exceptionally well, and that the BP86 values are slightly better than the B3LYP results, although such decisions should not be based on energy differences as small as  $1.1 \text{ cm}^{-1}$ . Using D3 dispersion corrections in the structure optimizations does not change the results (changes are less than  $2 \text{ cm}^{-1}$  for all complexes), making the ZFS a very robust, although not very characteristic, property against structural changes in the molecule. For the special case of the octahedral pentaqua iron(IV)-oxo complex in its quintet ground state, the D value is not reproduced very well, but the E/D ratio is very close to experiment. This implies that the calculated electronic structure might not be significantly different to experiment either. The larger deviation could perhaps be connected to the higher multi-reference character of the complex, due to its smaller spin-state energy gap, compared to the other  $S = 2$  complexes.

The three formal iron(IV)-oxo complexes with triplet ground states have large experimental zero-field splittings, which have been commented upon by several groups [126,156,157]. Here we find larger deviations (underestimate) from the overall larger experimental D values than for the  $S = 2$  complexes (see Table 3.6) and contrary to the  $S = 2$  complexes, we also find differences in the D values for BP86 and B3LYP, with B3LYP giving better results. The size of the D values for  $S = 1$  iron(IV)-oxo complexes is mainly attributed to spin-orbit coupling between the triplet ground state and the first excited quintet and singlet spin states [158–160]. In such a case the magnitude of the ZFS is inversely proportional to the energy separation between the spin states. This might partly explain the better results for B3LYP, but the results should not be over-interpreted. Also, with the exception of  $[\text{Fe}(\text{O})(\text{tpa}^{\text{Ph}}\text{Ph})]^-$  and  $[\text{Fe}(\text{O})(\text{TMC})(\text{NCCH}_3)]^{2+}$ , the calculated E/D ratios are in excellent agreement with experiment and support the spin distribution in our calculated electronic structures. As the experimentally assigned triplet

ground-state for  $[\text{Fe}(\text{O})(\text{TMCS})]^+$  is not confirmed by DFT calculations [126, 152, 153] (see Chapter 3.2.3.2), ZFS for its triplet and quintet state are compared in Table 3.6. Immediately we see large differences between BP86 and B3LYP, with the latter showing D values of less than  $7 \text{ cm}^{-1}$  for  $S = 2$  which practically excludes a quintet ground-state.

Table 3.6: Comparison of experimental and calculated zero-field splitting parameters of seven non-heme iron(IV)-oxo complexes (see Computational Details for the exact level). Values with D3 dispersion corrections are in parentheses<sup>a</sup>

	S	D [ $\text{cm}^{-1}$ ]			E/D		
		expt.	BP86	B3LYP	expt.	BP86	B3LYP
$[\text{Fe}(\text{O})(\text{tpa}^{\text{Ph}})]^-$	2	4.3	5.3 (5.4)	6.4 (6.4)	0.10	0.03 (0.05)	0.03 (0.02)
$[\text{Fe}(\text{O})(\text{TMG}_3\text{tren})]^{2+}$	2	5.0	5.1 (5.1)	6.2 (6.1)	0.02	0.03 (0.04)	0.03 (0.04)
$[\text{Fe}(\text{O})(\text{H}_3\text{buea})]^-$	2	4.0	3.9 (3.7)	4.8 (4.8)	0.03	0.01 (0.05)	0.01 (0.01)
$[\text{Fe}(\text{O})(\text{H}_2\text{O})_5]^{2+}$	2	9.7	4.0 (4.0)	4.3 (4.3)	0	0.01 (0.01)	0.00 (0.00)
$[\text{Fe}(\text{O})(\text{TMC})(\text{NCCH}_3)]^{2+}$	1	26.95	11.9 (11.5)	17.5 (17.2)	0.07	0.01 (0.01)	0.02 (0.02)
$[\text{Fe}(\text{O})(\text{TMCS})]^+$	1	35	13.6 (13.2)	18.3 (18.1)	0	0.02 (0.02)	0.02 (0.02)
	2		11.3 (13.1)	6.6 (6.7)		0.04 (0.04)	0.07 (0.08)
$[\text{Fe}(\text{O})(\text{N4Py})]^{2+}$	1	22.05	10.1 (10.0)	16.7 (16.6)	0	0.02 (0.02)	0.01 (0.01)

<sup>a</sup>Single-point calculations on fully optimized gas-phase structures. def2-TZVP basis sets were used for all structure optimizations.

### 3.2.3.4 Bonding Character of the Transition States for Hydrogen-Atom Transfer

In the context of the iron(IV)-oxo vs iron(III)-oxyl radical character of non-heme iron oxo complexes, the HAT reactions of those compounds with alkane substrates are of special interest. Homolytic HAT from the alkane to the oxo group is the important rate-determining first step in the activation of aliphatic C-H bonds by iron-oxo compounds. The accepted mechanism (see, for example, refs. [161–163]) begins with the aforementioned H-abstraction, by the iron(IV)-oxo complex, to form an iron(III)-hydroxo species and an alkyl radical. A following OH-rebound process then yields an alcohol as final product. A number of recent studies suggested that non-heme iron(IV)-oxo compounds form highly reactive iron(III)-oxyl radicals during the C-H bond activation [164–166]. If

this holds true, one would expect the following: as the system approaches the transition state for the HAT, the oxyl radical character would increase until the hydrogen atom is actually transferred from the substrate to the oxygen atom, after which the radical character should be quenched. Investigation of the oxygen spin density at the transition state, and possibly of its development along the reaction coordinate, should allow us to judge the importance of the oxyl form throughout the reaction. Since our results from previous chapters strongly point towards significant iron(III)-oxyl character in the ground state, in particular for  $S=1$  complexes, (contrary to their usual classification as iron(IV)-oxo complexes in the literature) the differences between the ground states of these complexes and their transition states during HAT are of importance.

Experimental findings show that non-heme iron(IV)-oxo intermediates in enzymes have a quintet ground state [101], and extensive theoretical studies by Shaik *et al.* revealed that the quintet spin state is much more reactive than the triplet spin state [153, 162, 163]. At first, a flattening of the potential energy surface, due to increased exchange interaction upon approaching the transition state, was proposed as the reason for the higher reactivity of the quintet state [167, 168]. However, Baerends and Solomon gave a different explanation, based on the stabilization of a  $d_{z^2}$  based  $\sigma$  antibonding molecular orbital in the quintet state, that acts as an electron acceptor [169–173]. Since this stabilization is lacking in the triplet state, a  $\pi$  antibonding molecular orbital (mostly centered on Fe- $d_{xz/yz}$  and O- $p_{x/y}$ ) is used instead as electron acceptor during HAT. Correspondingly, reactions with iron(IV)-oxo or iron(III)-oxyl species are usually expected to take a  $\sigma$ -pathway on the quintet surface and a  $\pi$ -pathway on the triplet surface. On the  $\sigma$ -pathway, the substrate is attacking the oxygen from the top, while the  $\pi$ -pathway ideally needs an angle around  $90^\circ$  between substrate and the Fe-O group. The lower reactivity of the triplet species is then said to be caused by steric crowding, effectively prohibiting the right angle for the  $\pi$ -pathway [165]. However, it should be kept in mind, that C-H activations with non-heme iron(IV)-oxo complexes have also been reported, where the triplet reaction used a  $\sigma$ -pathway and the quintet reaction took place on a  $\pi$ -pathway [174–176]. This makes the connection between spin states and reaction pathways more an approximate guideline than a strict rule.

To investigate the iron(III)-oxyl character at the  $S = 2$  transition state of an HAT, we examined the reactions of the trigonal-bipyramidal iron(IV)-oxo complexes ( $[\text{Fe}(\text{O})(\text{tpa}^{\text{Ph}})]^-$ ,  $[\text{Fe}(\text{O})(\text{TMG}_3\text{tren})]^{2+}$ , and  $[\text{Fe}(\text{O})(\text{H}_3\text{buea})]^-$ ) with 1,4-cyclohexadiene, a popular substrate for kinetic measurements of HAT. Since the trigonal-bipyramidal complexes al-

ready start the reaction in the desired more reactive quintet ground state, no two-state reactivity has to be taken into account. Also their triplet-quintet spin-state energy gap is wide enough, and thus the choice of functional does not affect the order of spin states, which makes these complexes ideal candidates for our investigation. A quick look at the optimized structures of our transition states, shown in Figure 3.5, immediately reveals, that  $[\text{Fe}(\text{O})(\text{tpa}^{\text{Ph}})]^-$  and  $[\text{Fe}(\text{O})(\text{TMG}_3\text{tren})]^{2+}$  both react along the so-called  $\sigma$ -pathway, with the substrate attacking from the top (in the case of  $[\text{Fe}(\text{O})(\text{TMG}_3\text{tren})]^{2+}$ , an O-H-C angle of nearly exactly  $180^\circ$  is achieved).  $[\text{Fe}(\text{O})(\text{H}_3\text{buea})]^-$ , on the other hand, appears to react on the so-called  $\pi$ -pathway, as its angle between substrate and Fe-O unit deviates significantly from  $180^\circ$ . The different behavior of  $[\text{Fe}(\text{O})(\text{H}_3\text{buea})]^-$  can be rationalized by looking at the steric strain of the ligand and the substrate: the arms of the ligand are hydrogen-bonded and oriented to the oxo ligand (which was also used as an explanation for the increased Fe-O distance of 1.68 Å [146], compared to other iron(IV)-oxo complexes), which effectively shields the molecule from attacks from the top. At the same time, these arms show a wide opening in the equatorial plane, for the substrate to attack along the  $\pi$ -pathway.

In all transition states, we see an increase in the Fe-O distance between 0.076 und 0.091 Å (see Table 3.7), compared to the ground-state structures. Such an elongation of the Fe-O bond is characteristic for C-H activations and other reactions with iron(IV)-oxo compounds and has been reported by all groups who have done quantum chemical calculations in this field (see, for example, refs. [162,165,167]). For reactions along the  $\sigma$ -pathway, the distance of the axial nitrogen ligand to the iron center increases by 0.11-0.18 Å (see Table 3.7). Besides the angle of attack for the HAT, this is the largest structural difference to the transition state of the  $\pi$ -pathway, where the distance to the axial nitrogen ligand actually decreases substantially. Another difference between  $\sigma$ - and  $\pi$ -pathway lies in the amount of spin contamination in the transition state. The deviations from the ideal  $\langle S^2 \rangle$  value of 6 for a quintet spin state are large for  $[\text{Fe}(\text{O})(\text{tpa}^{\text{Ph}})]^-$  and  $[\text{Fe}(\text{O})(\text{TMG}_3\text{tren})]^{2+}$  but negligible for  $[\text{Fe}(\text{O})(\text{H}_3\text{buea})]^-$ . This difference can be understood by looking at the spin densities (shown in Figure 3.6) of the transition states. While the spin densities on the iron-oxo molecules look very similar for all three compounds, the substrate shows negative spin density for the  $\sigma$ -pathway, but a positive one for the  $\pi$ -pathway. This creates a kind of broken-symmetry situation, with the negative spin density on the substrate being antiferromagnetically coupled to the iron-oxo moiety which leads to the high spin contamination for  $[\text{Fe}(\text{O})(\text{tpa}^{\text{Ph}})]^-$  and  $[\text{Fe}(\text{O})(\text{TMG}_3\text{tren})]^{2+}$ . The most significant structural differences between the RIBP86

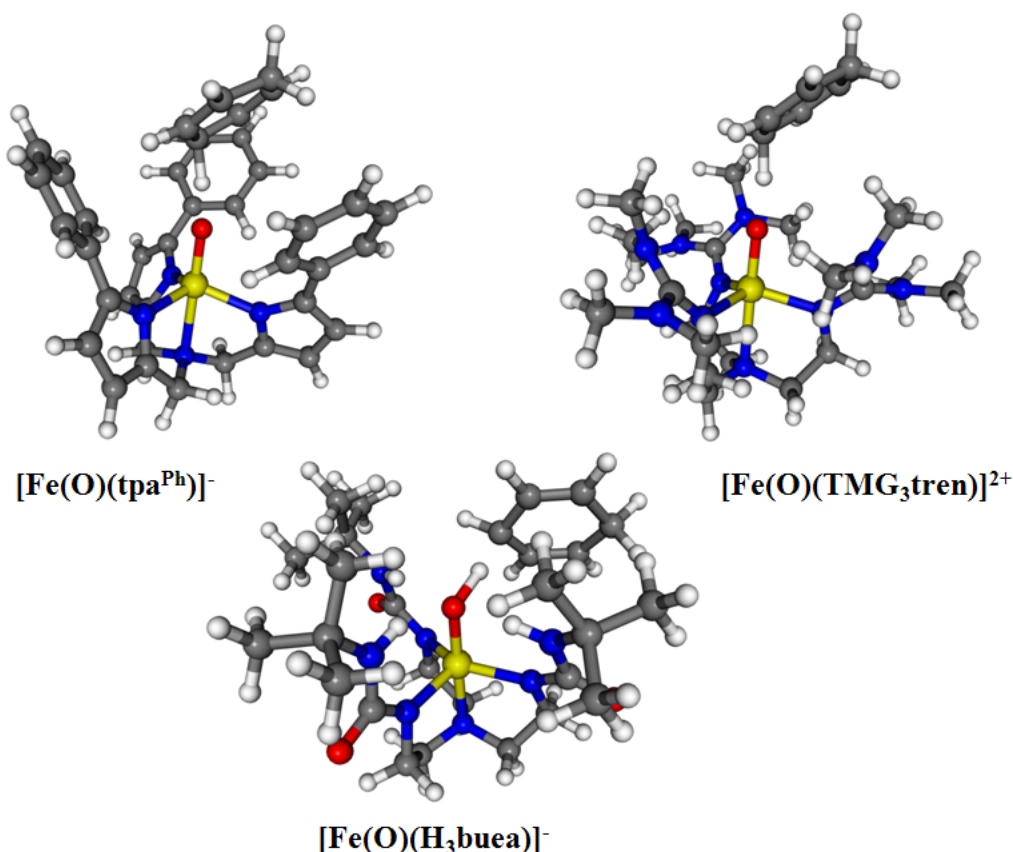


Figure 3.5: Optimized structures (B3LYP/def2-TZVP) of the transition states of  $[\text{Fe}(\text{O})(\text{tpa}^{\text{Ph}})]^-$ ,  $[\text{Fe}(\text{O})(\text{TMG}_3\text{tren})]^{2+}$  and  $[\text{Fe}(\text{O})(\text{H}_3\text{buea})]^-$  with 1,4-cyclohexadiene.

and B3LYP results are the O-H and C-H distances (see Table 3.7) of the transition states: compared to the RIBP86 results, the hydrogen atom is further away from the oxo ligand and closer to the substrate with B3LYP.

So far our results were as expected, perhaps with the possible exception of finding a  $S = 2$  iron(IV)-oxo species reacting along the  $\pi$ -pathway (which again is rare but known, see refs. [174–176]). However, the spin populations on iron and oxygen (see Table 3.7) are interesting, as they contradict the accepted picture mentioned above: instead of a shift in spin population from iron to oxygen, which would be expected during the formation of an iron(III)-oxyl radical, we find clearly the opposite trend for  $[\text{Fe}(\text{O})(\text{tpa}^{\text{Ph}})]^-$  and  $[\text{Fe}(\text{O})(\text{TMG}_3\text{tren})]^{2+}$ . The B3LYP NPA results reveal a sharp decline in spin population at oxygen, from 0.57 in the ground states to 0.18 and 0.21 in the transition states (similar changes are found for the Mulliken populations). The spin population on iron, on the other hand, increases from 3.14 to 3.84 and 3.87, respectively. These findings are not only

Table 3.7: Important distances, as well as NPA and Mulliken (in brackets) spin populations for the transition states of the HAT reaction of different non-heme iron(IV)-oxo complexes with 1,4-cyclohexadiene. Comparisons to the ground-state oxo complexes are given in parentheses.

	distances in Å					spin population NPA [Mulliken]	
	Fe-O	O-H	H-C <sup>a</sup>	Fe-N <sup>b</sup>	<S <sup>2</sup> >	Fe	O
<b>[Fe(O)(tpa<sup>Ph</sup>)]<sup>-</sup> (S = 2)</b>							
RIBP86/def2-TZVP	1.718 (1.642)	1.207	1.379	2.245 (2.132)	6.331 (6.029)	3.54 [3.53] (2.97 [2.95])	0.37 [0.41] (0.62 [0.68])
B3LYP/def2-TZVP	1.702 (1.620)	1.336	1.253	2.273 (2.150)	6.499 (6.055)	3.84 [3.78] (3.14 [3.06])	0.18 [0.22] (0.57 [0.64])
<b>[Fe(O)(TMG<sub>3</sub>tren)]<sup>2+</sup> (S = 2)</b>							
RIBP86/def2-TZVP	1.730 (1.647)	1.272	1.335	2.309 (2.130)	6.378 (6.031)	3.59 [3.60] (2.96 [2.93])	0.37 [0.40] (0.61 [0.69])
B3LYP/def2-TZVP	1.708 (1.625)	1.459	1.218	2.315 (2.140)	6.557 (6.056)	3.87 [3.82] (3.14 [3.08])	0.21 [0.27] (0.57 [0.64])
<b>[Fe(O)(H<sub>3</sub>buea)]<sup>-</sup> (S = 2)</b>							
RIBP86/def2-TZVP	1.762 (1.680)	1.201	1.435	2.113 (2.164)	6.043 (6.035)	2.88 [2.92] (2.99 [2.98])	0.28 [0.25] (0.43 [0.46])
B3LYP/def2-TZVP	1.745 (1.654)	1.263	1.344	2.103 (2.173)	6.064 (6.064)	2.94 [2.95] (3.20 [3.15])	0.36 [0.34] (0.38 [0.41])

<sup>a</sup>Abstracted hydrogen atom, connected to 1,4-cyclohexadiene. <sup>b</sup>Trans to the oxo-ligand.

surprising, but they are also in stark contrast to the situation we would expect to find in a non-heme iron(III)-oxyl radical in its quintet state, i.e. one unpaired electron at oxygen and three unpaired electrons mostly localized at the iron center. The spin distribution we get resembles much more an actual iron(IV)-oxo complex, with nearly four unpaired electrons at iron and a bit of delocalized spin density at oxygen. This is the situation for the  $S = 2$  complexes reacting along the  $\sigma$ -pathway. Figure 3.7 shows an energy profile for a relaxed scan along the O-H coordinate of the HAT with  $[\text{Fe}(\text{O})(\text{TMG}_3\text{tren})]^{2+}$ , together with the NPA spin populations at iron and oxygen. The transfer of spin density to iron while approaching the transition state is clearly visible, as is the simultaneous reduction of spin density at the oxo ligand. In the case of  $[\text{Fe}(\text{O})(\text{H}_3\text{buea})]^-$ , which reacts along the  $\pi$ -pathway, the spin population at iron is reduced from 3.20 to 2.94, but there is no increase in the oxygen spin population. The lower spin population at iron for the transition state of  $[\text{Fe}(\text{O})(\text{H}_3\text{buea})]^-$  (reacting along the  $\pi$ -pathway) compared to the other two compounds can be explained by the amount of positive spin density that has been transferred to the substrate, which now is missing at iron. In summary, for HAT along the sigma-pathway with  $[\text{Fe}(\text{O})(\text{tpa}^{\text{Ph}})]^-$  and  $[\text{Fe}(\text{O})(\text{TMG}_3\text{tren})]^{2+}$  we find a situation where we start from significant Fe(III)-oxyl character in the ground state, which

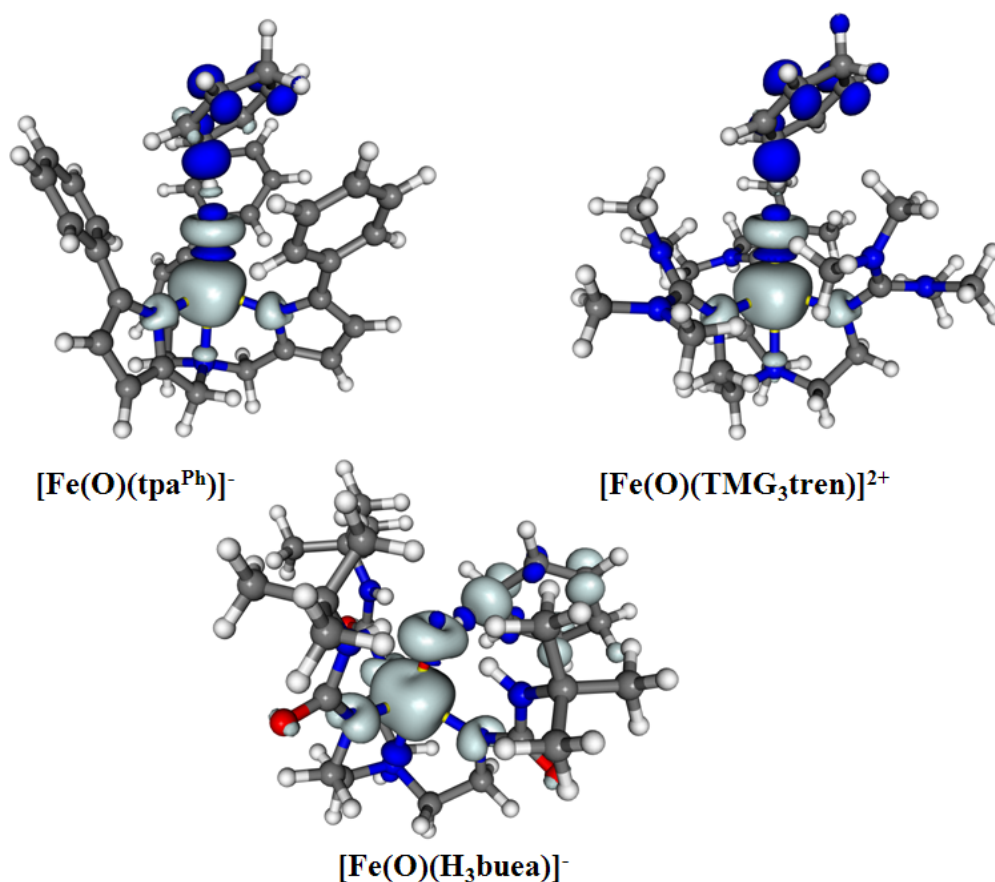


Figure 3.6: Isosurface plots of the spin density ( $\pm 0.005$  a.u.) of the transition states of the hydrogen-abstraction reaction of  $[\text{Fe}(\text{O})(\text{tpa}^{\text{Ph}})]^-$ ,  $[\text{Fe}(\text{O})(\text{TMG}_3\text{tren})]^{2+}$ , and  $[\text{Fe}(\text{O})(\text{H}_3\text{buea})]^-$  with 1,4-cyclohexadiene. B3LYP/def2-TZVP optimized structures.

is diminished at the transition state of HAT. For the  $\pi$ -pathway and  $[\text{Fe}(\text{O})(\text{H}_3\text{buea})]^-$  the roughly three unpaired electrons at iron in the ground state are conserved at the transition state, but the spin population at oxygen remains almost constant. In this case appreciable spin density on the substrate side is found at the transition state.

Regarding the influence and importance of the density functional, the Fe-O distances at the transition states are generally longer with RIBP86 than with B3LYP, and the spin density is more delocalized from iron to oxygen. Also the spin contamination at the transition state is lower for RIBP86. Overall, however, the BP86 and B3LYP results are qualitatively comparable, making our conclusions robust with respect to the choice of functional and the possible error introduced by this choice. Table 3.8 lists the kinetic barriers and reaction energies for the H-abstractions of the three complexes (the

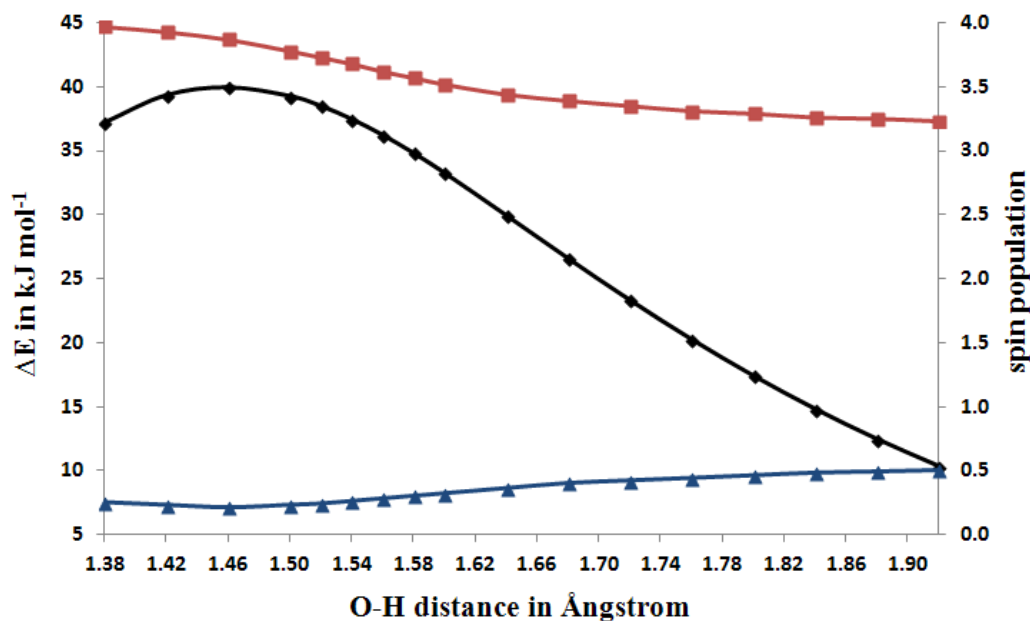


Figure 3.7: Energy profile of the HAT from 1,4-cyclohexadiene to  $[\text{Fe}(\text{O})(\text{TMG}_3\text{tren})]^{2+}$  (black line) along the O-H coordinate. NPA spin populations at iron (red line) and oxygen (blue line) are given as well. B3LYP/def2-TZVP results.

Table 3.8: Kinetic barriers and reaction energies in  $\text{kJ mol}^{-1}$  for the HAT reaction of  $[\text{Fe}(\text{O})(\text{L})]^{2+/-}$  ( $S = 2$ ) +  $\text{C}_6\text{H}_8 \rightarrow [\text{Fe}(\text{OH})(\text{L})]^{2+/-}$  ( $S = 5/2$ ) +  $\bullet\text{C}_6\text{H}_7$  ( $S = 1/2$ ). def2-TZVP basis sets used for all atoms.

	BP86		B3LYP	
	$\Delta E^\ddagger$	$\Delta E$	$\Delta E^\ddagger$	$\Delta E$
$[\text{Fe}(\text{O})(\text{tpa}^{\text{Ph}})]^-$	61.5	8.1	54.7	-65.7
$[\text{Fe}(\text{O})(\text{TMG}_3\text{tren})]^{2+}$	57.3	26.6	40.0	-54.9
$[\text{Fe}(\text{O})(\text{H}_3\text{buea})]^-$	87.6	35.9	109.4	-48.0

values are in good agreement to similar calculations, see refs. [168,177,178]). We can see immediately the higher barrier, and therefore lower reactivity, of  $[\text{Fe}(\text{O})(\text{H}_3\text{buea})]^-$ , compared to the other two compounds. As expected, the complexes reacting along the preferred  $\sigma$ -pathway also show the lower barriers. Compared to B3LYP, RIBP86 gives higher barriers for the complexes reacting along the  $\sigma$ -pathway and a lower barrier for the  $[\text{Fe}(\text{O})(\text{H}_3\text{buea})]^-$  complex. Yet, the same order of barrier heights is found for both functionals. The reaction energies, on the other hand, differ greatly between the functionals, with B3LYP giving  $\Delta E$  values that are 73-84  $\text{kJ mol}^{-1}$  lower than those with RIBP86. The HAT is energetically favored by B3LYP and the resulting product in each reaction is an iron(III)-hydroxo complex in sextet spin state (see Table S8 in Appendix

I for comparison with other possible spin states for the products).

A short note on the lack of D3 dispersion corrections in this chapter is in order here: while dispersion corrections certainly had beneficial effects on the structures and quadrupole splittings of the non-heme iron-oxo complexes in their ground states, they also lowered the kinetic barrier heights of the HAT reactions. This effect was found in early test calculations with  $[\text{Fe}(\text{O})(\text{TMG}_3\text{tren})]^{2+}$ , where the barrier dropped from 40.0 kJ mol<sup>-1</sup> for B3LYP to a negative value of -1.2 kJ mol<sup>-1</sup> for B3LYP-D3. The reaction energies, on the other hand, were nearly unaffected by the use of dispersion corrections (-54.9 kJ mol<sup>-1</sup> vs -53.9 kJ mol<sup>-1</sup> with D3 dispersion corrections). Further tests with other iron-oxo complexes gave very similar results: a dramatic decrease in the kinetic barrier and only minor changes in the reaction energies. One reason for this behavior is the increase in the number of atom-pairwise interactions in the larger transition state, compared to the number of interactions in the individually calculated smaller educts or products. As the educts and products of an HAT do not differ too much in their structures, the smaller effect of D3 dispersion corrections on reaction energies can also be rationalized this way. This dramatic effect of dispersion corrections on barrier heights might also be the reason for their absence in the literature on reaction pathways for non-heme iron-oxo complexes.

### 3.2.4 Conclusions

The possible prospects and benefits of using high-valent iron-oxo intermediates, that are highly reactive in their short lifespans and can act as potent catalysts for a variety of industrial important chemical processes, have spurred a lot of interest with experimental chemists and theoreticians alike. Appreciable effort was concentrated on mimicking the postulated active sites of non-heme iron enzymes, by creating a variety of synthetic iron-oxo complexes with similar structural motifs. The resulting complexes were usually described as iron(IV)- or iron(V)-oxo complexes, and the interpretations on their spin states and their reactivity, as a function of their ligands, were based on this assumption. Analyses of their spin populations, however, revealed, that the supposed iron(IV)-oxo complexes had significant amounts of spin population on the oxygen ligand, making the complexes appear rather like iron(III)-oxyl radicals than like genuine iron-oxo systems with d<sup>4</sup> configuration. Since the formation of highly reactive iron(III)-oxyl radical species at the high-spin transition state of the rate-determining step of C-H activation of alkyl substrates, was also proposed, the question whether some of these formal iron-oxo

complexes should really be described as iron-oxyl radicals became even more important.

Our calculations on a representative collection of eight formal non-heme iron(IV)-oxo compounds, and on two iron(V)-oxo complexes, revealed spin distributions in the supposed iron(IV) species, that were contrary to the idea of existing iron(IV)-oxo units in those molecules. The differences were largest for the complexes with triplet ground states, where spin densities of about 0.7 at the oxo ligand were found in NPA and Mulliken spin population analyses. A similar picture was found for the complexes with quintet ground states, which gave spin populations of less than 3.20 at iron and substantial amounts of spin population (0.4-0.6) at the oxygen ligand. This suggests significant iron(III)-oxyl character already in the ground-state iron(IV)-oxo complexes. In contrast to these findings, the low-spin ( $S = 1/2$ ) iron(V)-oxo complexes, with the TAML and its closely related bTAML ligand, are much closer to a genuine iron(V)-oxo situation. All these spin distribution results, pointing towards iron(III)-oxyl radicals and iron(V)-oxo compounds, turned out to be very robust regarding the choice of functional.

The absence of appreciable spin contamination or of broken-symmetry character in the calculations allowed good verification of the electronic-structure situation for the studied complexes. Important structural parameters, spin-state energetics, and different molecular properties, all highly sensitive to the correct spin and electron density, were calculated and compared to experiment. Using B3LYP with D3 dispersion corrections gave good agreements for the Fe-O bond lengths, and for the other metal-ligand distances in the complexes as well, although the RIBP86 Fe-O distances turned out to be slightly better. With the exception of  $[\text{Fe}(\text{O})(\text{TMCS})]^+$ , which is known to be a problematic case, all experimentally known triplet-quintet spin-states orders could be successfully predicted with B3LYP-D3. Computed zero-field splittings, and especially the Mössbauer parameters, were in good agreement with experiment, providing further evidence that the electronic structures and the spin populations resulting from them are indeed correct. This leads to our conclusion, that the usual description of many non-heme iron-oxygen species as iron(IV)-oxo complexes should be reconsidered in many cases and carefully reexamined. Especially the highly reactive and catalytically interesting iron compounds with triplet ground-states could be more accurately described as iron(III)-oxyl radicals. On the other hand,  $[\text{Fe}(\text{O})(\text{TAML})]^-$ , in its doublet ground state, and the closely related  $[\text{Fe}(\text{O})(\text{bTAML})]^-$ , both seem to be genuine iron(V)-oxo complexes. Their spin populations are fundamentally different from what we would expect to find in iron(IV)-oxyl radicals, which would be the conceivable alternative in their case.

Notably, we did not see a further increase in the oxyl character at the high-spin transition state of the HAT from 1,4-cyclohexadiene. The formation of a more reactive oxyl radical, during HAT on the quintet surface had been suggested before. However, looking at the spin populations at the transition state did not reveal an increase in spin density at oxygen, nor a further decrease in spin density at iron. Instead we find  $d^4$  configurations at iron and highly reduced spin populations at oxygen for the HAT reaction along the preferred  $\sigma$ -pathway on the quintet surface.

## 3.3 Structurally Distorted Iron(II) Complexes with N<sub>5</sub> Pentadentate Ligands

The contents of this chapter have been published in "Controlled ligand distortion and its consequences for structure, symmetry, conformation and spin-state preferences of iron(II) complexes" by N. Spintig, K. Theilacker, M. Schoknecht, D. Baabe, D. Wiedemann, M. Kaupp, A. Grohmann, G. Hörner, *Dalton Trans.* **2015**, 44, 19232. While the study has been a close cooperation between experimental and computational groups, this chapter concentrates mainly on the computational aspects.

### 3.3.1 Introduction

In vitro modelling of the biological function of a metal ion requires both an understanding of the factors governing its reactivity, and their control. An important determinant, which is often difficult to study in isolation from other factors, is the distortion of the ligand sphere as imposed by the biological matrix (cf. the concept of the entatic state [179,180]). Studies of entasis, both in vivo and in vitro [181–184](but see also [185]), are most numerous for copper-based redox catalytic systems. Here, catalytic activity is associated with the mismatch between actual coordination geometry and coordination chemical preference, which is tetrahedral for copper(I) and square planar (pyramidal) for copper(II). We posit that redox processes involving metal centers other than copper are similarly controlled by ligand-field distortion and therefore synthetically addressable. In particular, the electronic nature and reactivity of oxoiron(IV) species deriving from catalytically active iron(II) complexes, both in vivo and in vitro [102–106,131,186–189], are expected to be highly susceptible to ligand-field effects. For instance, variation of the ligand-field strength has been used by Que *et al.* to tune the spin-state energetics of oxoiron(IV) in a functional model of taurine dioxygenase (TauD) through variation of a donor atom (N vs O) [190].

In this work, we describe ligand-imposed distortion of the coordination environment as a powerful tool to tune the structure, electronics, and reactivity of a pair of iron(II) complexes. In two closely related N<sub>5</sub> ligands of identical donor atom set, distortion of the latter allows us to study the effects of changes in ligand-sphere structure and symmetry. This approach decouples the metal center under study from first-order ligand-field strength effects, as induced by donor set variation, either in terms of donor element

(e.g., N vs O, *vide supra*) or in terms of hybridisation state within one class of donor atom (e.g.,  $sp^2$  N vs  $sp^3$  N). Control of ligand-field strength (according to the angular overlap model (AOM) [191]) via incremental distortion of the structure necessitates control of intra-ligand strain [192] and thus the use of "tailor-made" polydentate ligands.

For the study presented here, we have investigated the cyclic ligand  $L^1$  (6-methyl-6-(pyridin-2-yl)-1,4-bis(pyridin-2-ylmethyl)-1,4-diazepane) [109, 110], and its open-chain congener  $L^2$  ( $N^1,N^3$ ,2-trimethyl-2-(pyridine-2-yl)- $N^1,N^3$ -bis(pyridine-2-ylmethyl) propane-1,3-diamine). They both share the trisimine-bisamine donor set of the established pentadentate  $N_5$  ligand N-benzyl-N,N',N'-tris(pyridin-2-ylmethyl)-ethane-1,2-diamine (Bn-TPEN) [132, 133], but differ in the connectivity and hence, structural flexibility of the central diamine unit (Figure 3.8).

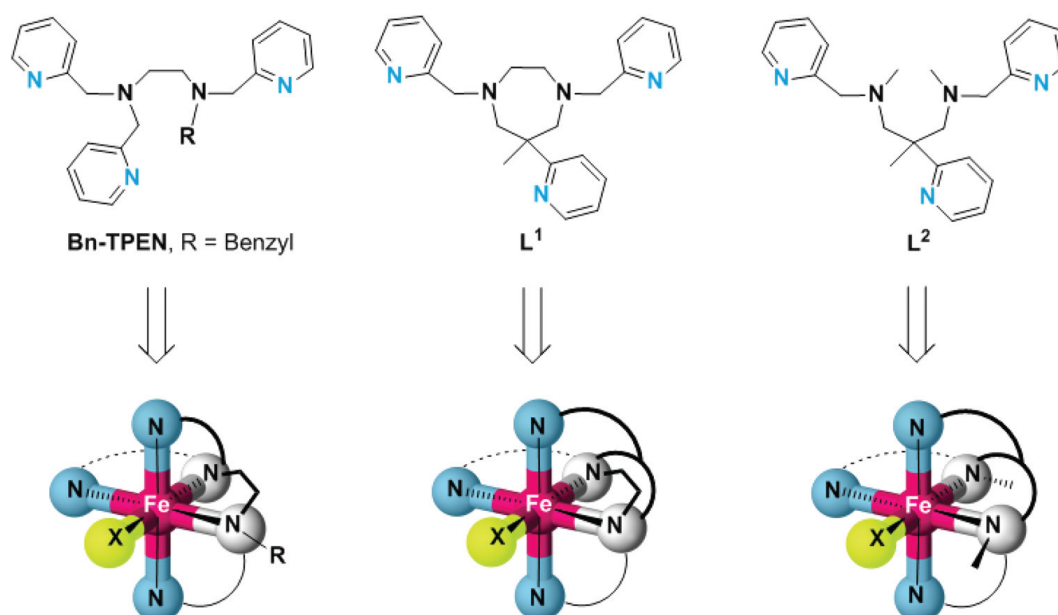


Figure 3.8: Structures of the pentadentate  $N_5$  ligands Bn-TPEN,  $L^1$  and  $L^2$ , and structural sketches of the resulting hexacoordinate iron(II) complexes.

### 3.3.2 Computational Details

All DFT and TDDFT calculations were performed using TURBOMOLE6.3 and a locally modified version of the TURBOMOLE6.4 package [111–113]. The latter allows variation of the amount of exact exchange in global hybrid functionals. def2-TZVP basis sets [114] were used throughout. The B3LYP functional [15, 23] was used (with

20% exact exchange), but for spin-crossover (SCO) energies, B3LYP\* (15% exact exchange) [193] has been used, which had been reparameterized to better describe SCO in iron(II) complexes. The SCF energies were converged to  $10^{-8}$  Hartree in energy and a fine m5 integration grid was chosen. Dispersion contributions were evaluated using Grimme's DFT-D3 atom-pairwise dispersion corrections [41]. In several cases, solvent effects were taken into account at the polarizable continuum model level, using COSMO (Conductor-Like Screening Model) [91] implemented in TURBOMOLE6.3, with permittivity  $\epsilon = 35.688$  for acetonitrile. For the calculation of Mössbauer parameters, an uncontracted def2-QZVPP basis set was used for iron and def2-TZVP for all other atoms. The structures for the Mössbauer calculations were optimized at B3LYP-D3/def2-TZVP level. The inhouse MAG program [119] was used to calculate the electron density  $\rho$  at the iron nucleus and the quadrupole splitting. For the isomer shifts the linear equation used is  $\delta[\text{mm s}^{-1}] = -0.3594 * (\rho(\text{DFT}) - 11800) + 10.521$ . This equation was fitted to the isomer-shift test of Neese's test set [79], using the same methods for structure optimization and density calculation.

### 3.3.3 Results and Discussion

#### 3.3.3.1 Structural Distortions

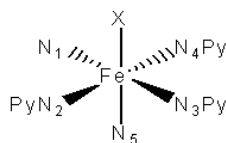
The coordination polyhedron of the iron(II) complexes is a (slightly distorted) octahedron in the case of  $[2(\text{X})]^{n+}$  ( $\text{X} = \text{OTf}$  ( $n=1$ ) or  $\text{MeCN}$  ( $n=2$ )), but fails to obey any regular geometry in the case of  $[1(\text{X})]^{n+}$ . The much stronger distortion of the coordination sphere in  $[1(\text{X})]^{n+}$  is obviously due to constraints imposed by its cyclic ligand backbone. In particular, it is the 1,4-diazepane ring that forces and fixes the cis angle subtended by the amine-donor atoms at a value much smaller than the ideal value of  $90^\circ$ . The Fe-N bonds trans to the co-ligands X, which involve one of the amine N atoms, are elongated in the gas phase structures (Table 3.9) owing to the operation of a strong trans influence. This causes secondary structural effects, which are distinctly different between the two types of  $\text{N}_5$  ligand. The distorted structure of  $[1(\text{X})]^{n+}$  can be analysed as a blend of octahedral and trigonal prismatic arrangements; i.e., the trigonal Bailar twist angle  $\theta$  between co-facial donor triads (see Figure S5 in Appendix I) amounts to  $27.5^\circ$ , intermediate between an ideal octahedron ( $\theta = 60^\circ$ ) and a regular trigonal prism ( $\theta = 0^\circ$ ).

Thus, the spatial arrangement of donor atoms in  $\text{L}^1$  supplies the central atom with a

Table 3.9: Selected bond lengths (pm) and angles ( $^{\circ}$ ) from optimized structures (B3LYP-D3/def2-TZVP/COSMO(MeCN)) of the complex ions  $[1(X)]^{n+}$  and  $[2(X)]^{n+}$  in their quintet-spin states.<sup>a,b</sup>

	$[1(X)]^{n+}$		$[2(X)]^{n+}$	
	X = OTf <sup>c</sup>	X = MeCN	X = OTf <sup>c</sup>	X = MeCN
bond lengths				
Fe-N1	220.3	221.5 (206.7)	224.3	223.0 (209.8)
Fe-N5	228.6	229.6 (203.8)	226.4	225.9 (203.8)
Fe-N4	215.1	216.8 (201.1)	214.6	217.1 (200.6)
Fe-N2	228.8	229.6 (207.3)	216.7	218.5 (202.0)
Fe-N3	214.1	216.4 (197.7)	218.3	220.0 (201.5)
Fe-X	220.7	220.3 (194.8)	218.2	219.8 (193.8)
bond angles				
N1-Fe-N5	72.9	72.5 (77.8)	90.3	90.7 (94.4)
N1-Fe-N3	139.9	139.2 (157.5)	167.1	166.6 (175.7)
N5-Fe-X	164.6	163.6 (173.3)	159.3	164.1 (171.3)
N4-Fe-N2	156.7	153.0 (167.0)	162.2	162.0 (172.1)
distortion parameters				
$\Sigma/^{\circ}$	150.9	153.4 (90.1)	92.5	89.5 (51.0)
S(Oh)	7.36	5.70 (2.21)	2.01	1.62 (0.56)
S(TP)	4.80	5.83 (10.26)	10.29	11.04 (13.69)

<sup>a</sup>Data in italics denote the optimized structures of the acetonitrile complexes in their singlet-spin states.



<sup>b</sup> Positions of nitrogen atoms N1-N5.

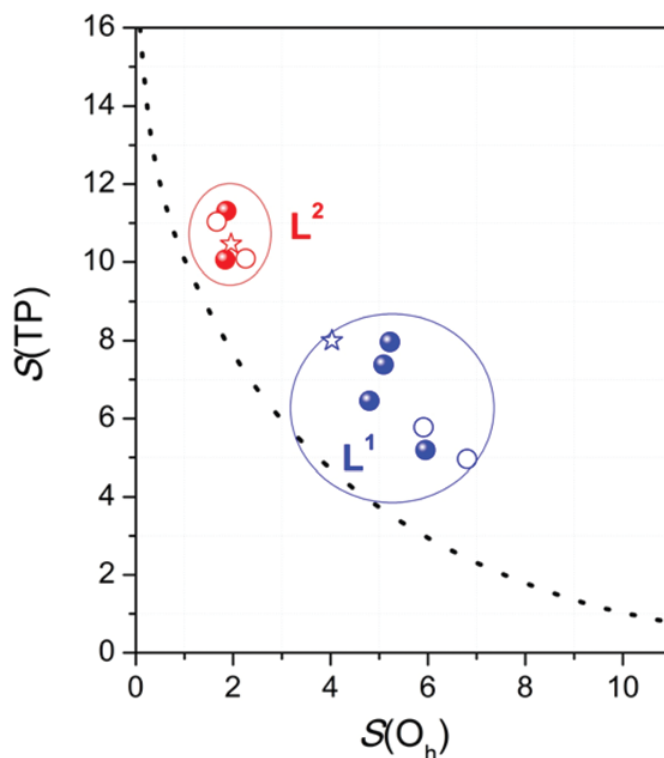


Figure 3.9: Continuous shape map of the octahedron  $\longleftrightarrow$  trigonal prism transition (see text); blue:  $[1(X)]^{n+}$ ; red:  $[2(X)]^{n+}$ ; line: ideal Bailar twist; filled: XRD-derived structures; open: DFT-optimized structures (B3LYP-D3/def2-TZVP/COSMO(MeCN)); stars: crystal structures of Ni(II) complexes with the same ligand (see [134])

ligand field poised between tetragonal and trigonal symmetry. This conclusion is supported by an analysis of continuous symmetry/shape measures  $S(\text{Oh})$  and  $S(\text{TP})$ , which quantify the deviation from regular octahedral and trigonal-prismatic geometry, respectively. The 'continuous shape measures  $S$ ' quantify the minimal distance movement that the points of an object have to undergo in order to be transformed into the desired shape [194]. Calculations were performed by using the online service of the Hebrew University of Jerusalem [195]. In Figure 3.9, the  $S(\text{Oh})$  and  $S(\text{TP})$  values of the iron(II) complexes (from Table 3.9 and experimental values from ref. [134]) are given as a continuous shape map of the octahedron  $\longleftrightarrow$  trigonal prism transition along the trigonal Bailar twist (line) [196]. Evidently, the complexes of either ligand are in distinctly separated regions of this map. The values for  $S(\text{Oh})$ , which is zero for an ideal octahedron, cluster around  $S(\text{Oh}) = 6 \pm 1$ , for complexes  $[1(X)]^{n+}$  of the constrained ligand  $L^1$ , but are substantially smaller for complexes  $[2(X)]^{n+}$  of the open-chain ligand  $L^2$  ( $S(\text{Oh}) =$

$2.0 \pm 0.5$ ).

### 3.3.3.2 Spin States

Optimizations with the B3LYP hybrid functional slightly favor the singlet over the quintet state for  $[2(\text{MeCN})]^{2+}$  but provide a clear preference for the quintet in case of  $[1(\text{MeCN})]^{2+}$  (Table 3.10). As B3LYP SCO energies had been found previously to artificially favor the high-spin forms [193], we have also carried out single-point calculations with the modified B3LYP\* functional with 15% rather than 20% Hartree-Fock exchange. This functional had been suggested previously to better describe SCO in Fe(II) complexes [193]. At B3LYP\* level, the singlet preference for  $[2(\text{MeCN})]^{2+}$  is more pronounced and the quintet preference for  $[1(\text{MeCN})]^{2+}$  much smaller (Table 3.10). Yet, the computed overall difference in the SCO energies of the two complexes remains almost constant around  $27 \text{ kJ mol}^{-1}$ . The weaker ligand field of the co-ligand OTf in  $[1(\text{OTf})]^+$  and  $[2(\text{OTf})]^+$  translates into a clear energetic preference for the high-spin state in both complexes, while comparison of the absolute values signals a marked dependence on the input of the respective  $\text{N}_5$  ligand.

Table 3.10: Electronic SCO energies ( $\Delta_{\text{SCO}}E = E(S = 0) - E(S = 2)$ ), in  $\text{kJ mol}^{-1}$  in  $[1(\text{X})]^{n+}$  and  $[2(\text{X})]^{n+}$ . B3LYP-D3/def2-TZVP/COSMO(MeCN); values in parentheses: B3LYP\*/def2-TZVP/COSMO(MeCN)//B3LYP-D3/def2-TZVP/COSMO(MeCN).

	$L^1$	$L^2$
X = OTf	+50.8 (+36.0)	+22.6 (+15.4)
X = MeCN	+23.6 (+4.0)	-2.4 (-23.9)

With the array of electronic SCO energies in hand, it was possible to isolate the incremental contributions ascribable to the  $\text{N}_5$  ligand ( $\delta\Delta_{\text{SCO}}E(\text{N}_5)$ ) and the coligand ( $\delta\Delta_{\text{SCO}}E(\text{X})$ ). Interestingly, both factors are found to contribute similarly to the SCO energies. The incremental contribution of the co-ligand  $\delta\Delta_{\text{SCO}}E(\text{X})$  (vertical difference in Table 3.10) amounts to ca.  $25\text{--}27 \text{ kJ mol}^{-1}$ , whereas the distortion-related increment of the  $\text{N}_5$  ligand  $\delta\Delta_{\text{SCO}}E(\text{N}_5)$  (horizontal difference in Table 3.10) amounts to ca.  $26\text{--}28 \text{ kJ mol}^{-1}$ . The latter value is a good measure of the difference in d-orbital splitting between the ligand fields as supplied by  $L^1$  and  $L^2$ , in fair agreement with energy differences derived from UV/Vis spectroscopy (vide infra) [134]. Since Mössbauer spectra of  $[1(\text{X})]^{n+}$  and  $[2(\text{X})]^{n+}$  had been measured by Grohmann *et al.* [134], further checks

on the correct assignment of spin states could be made by calculating the Mössbauer parameters of the complexes in their different states and comparing them. This also provides us with a more general verification of the quality of the electronic structure description for the iron(II) complexes by DFT. Table 3.11 summarizes the experimental and DFT results for the nuclear quadrupole splittings and the isomer shifts of  $[1(X)]^{n+}$  and  $[2(X)]^{n+}$ .

Table 3.11: Mössbauer parameters with focus on the main components of the experimental spectra measured at  $T \approx 100$  K. Data in square brackets is from DFT calculations (see Computational Details for the exact level) of the respective complex cations.

	Volume fraction [%]	$\delta$ [mm s <sup>-1</sup> ]	$\Delta E_Q$ [mm s <sup>-1</sup> ]
<b>[1(MeCN)](OTf)<sub>2</sub></b>	16.1	1.220(19)	2.909(43)
	79.5	1.066(5)	2.112(11)
<i>mer</i> -[1(MeCN)] <sup>2+</sup> (S = 2)		[1.00]	[3.56]
<i>fac</i> -[1(MeCN)] <sup>2+</sup> (S = 2)		[0.99]	[2.66]
<b>[1(OTf)](OTf)</b>	58.7	1.098(6)	3.110(18)
	23.5	1.138(15)	2.335(52)
<i>mer</i> -[1(OTf)] <sup>+</sup> (S = 2)		[1.01]	[3.36]
<i>fac</i> -[1(OTf)] <sup>+</sup> (S = 2)		[1.02]	[2.71]
<b>[2(MeCN)](OTf)<sub>2</sub></b>	84.7	0.520(1)	0.353(2)
<b>[2(MeCN)]<sup>2+</sup></b> (S = 0)		[0.61]	[0.46]
<b>[2(OTf)](OTf)</b>	82.1	1.088(3)	2.123(7)
<b>[2(OTf)]<sup>+</sup></b> (S = 2)		[1.00]	[3.53]
<b>[2(OTf)]<sup>+</sup></b> (S = 0)		[0.77]	[1.16]
<b>[2(MeCN)](OTf)<sub>2</sub><sup>a</sup></b>	82.6	1.097(2)	2.069(4)
<b>[2(OTf)](OTf)<sup>b</sup></b>	72.2	1.076(3)	2.033(6)

<sup>a</sup>After tempering [2(MeCN)](OTf)<sub>2</sub> at  $T = 350$  K for three days under reduced pressure.

<sup>b</sup>After tempering [2(OTf)](OTf) at  $T = 350$  K for four days under reduced pressure.

The DFT-derived Mössbauer parameters are in close agreement with the experimental data and fully support our spin-state assignments: quintet states for  $[1(X)]^{n+}$  and  $[2(OTf)]^+$  and a singlet state for  $[2(MeCN)]^{2+}$ . The nature of the *mer*- and *fac*- prefixes will be explained in the next section. Still significant differences to the experimental values can be seen in Table 3.11, but none of them are unexpected or surprising as the experimental data is given for measurements at 100 K. This is far from the gold standard of a helium-cooled measurement at 4 K. Keeping the high temperature dependence of Mössbauer spectra in mind, differences in  $\delta$  and  $\Delta E_Q$  encountered in our case are actually fairly low (see [134] for a longer discussion about the influence of temperature on the different experimental spectra). Also the  $\Delta E_Q$  values are above 2.0 mm s<sup>-1</sup>, which makes

them susceptible to larger errors in the DFT calculations [88] (see Chapter 2.2 for a more detailed discussion on the calculation of Mössbauer parameters) with a magnitude comparable to that shown in Table 3.11. Other effects like the omission of counterions in the calculations and impurities in the experimental spectra are much harder to quantify. It is clear that they do have an effect on the spectra, but in the case of counterions, the effect on the calculated parameters are generally negligible [197–199], except if the whole molecule is very small (like  $\text{FeCl}_4^{2-}$ , which shows different spectra depending on the counterion and the crystallization conditions [200]). The impurities in turn make it difficult to find proper fits to the experimental spectra, which could shift the parameters of the desired compound to a certain extent, but a closer look at the experimental data in ref. [134] shows only very minor effects, if any at all.

### 3.3.3.3 Competing Ligand Conformations

The topologies of complexes  $[1(\text{X})]^{n+}$  and  $[2(\text{X})]^{n+}$  in the solid-state structures agree with the sketches in Figure 3.8. They also agree with the structural characteristics reported for iron(II) complexes of the closely related ligand Bn-TPEN [132]. That is, in all iron(II) complexes under study, the sixth coordination site is trans to one of the tertiary amine donors. The three pyridine donors are arranged in meridional fashion (mer-py<sub>3</sub>). The same holds for the nickel(II) complex salt  $[\text{NiL}^2(\text{OH}_2)](\text{ClO}_4)_2$  of the open-chain ligand  $\text{L}^2$ , which was synthesized by Grohmann *et al.* for structural comparison. However, another option would be to adopt a topology with all three pyridine donors in a facial arrangement (fac-py<sub>3</sub>). This causes the sixth coordination site to be trans to one of the pyridine donors. Obviously, ligand  $\text{L}^1$  is flexible enough to realise two distinctly different arrangements of its donor atoms in the solid state.

This raises the question whether the preference of the iron(II) complexes for the mer conformation in the solid state is conserved for the isolated complex ions  $[1(\text{X})]^{n+}$  and  $[2(\text{X})]^{n+}$  in solution (Figure 3.10). Although we have no definite experimental proof of a conformational equilibrium we will, in the following, discuss results from experiment and theory indicating conformational dynamics in the case of  $[1(\text{X})]^{n+}$ .

DFT computations of relevant complex ions containing  $\text{L}^1$  and  $\text{L}^2$  were performed to gain insight into the energetics of the anticipated conformational equilibrium (Table 3.12). In the case of ligand  $\text{L}^2$ , optimization of the structures of  $[2(\text{X})]^{n+}$  (with  $\text{X} = \text{OTf}, \text{MeCN}$ ) clearly points to a preference for the mer conformation in solution. In

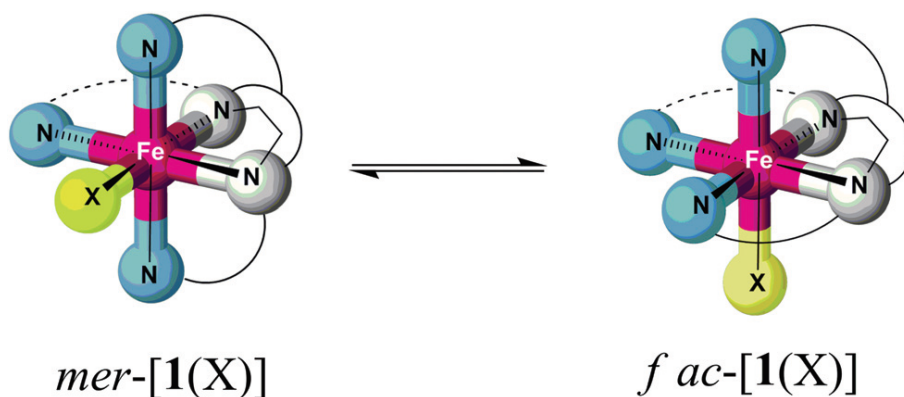


Figure 3.10: Presumed stereodynamic exchange between structural isomers of  $[1(X)]^{n+}$  in solution.

contrast, energy differences  $\Delta E_{\text{conf}}$  between the isomers of  $[1(X)]^{n+}$  remain below  $5 \text{ kJ mol}^{-1}$ , which means that, for complexes of ligand  $L^1$ , a conformational equilibrium in solution must be taken into account.

Table 3.12: Relative electronic energies (in  $\text{kJ mol}^{-1}$ ) of *mer* and *fac* conformers of iron(II) precursors  $[1(X)]^{n+}$  and  $[2(X)]^{n+}$ . Fully optimized structures at B3LYP-D3/def2-TZVP level (S=2). In parentheses: with COSMO solvent model (MeCN).

	<i>mer</i>	<i>fac</i>
$[1(\text{OTf})]^+$	0	+10.1 (+4.4)
$[1(\text{MeCN})]^{2+}$	0	+4.5 (+4.0)
$[2(\text{OTf})]^+$	0	+26.2 (+21.6)
$[2(\text{MeCN})]^{2+}$	0	+22.6 (+22.9)

### 3.3.4 Conclusions

In the present work, we have established incremental ligand-field distortion as a tool to tune the structural, conformational, and spin-state preferences of iron(II) complexes, in ligand fields set up by two pentadentate  $N_5$  ligands. Within our pair of ligands (diazepane-based  $L^1$ ; open chain  $L^2$ ), the donor-atom inherent strength of the donor set (diamine/trisimine) is fully conserved. Accordingly, solely the consequences of ligand sphere distortion are recorded in complexes of the type  $[\text{FeL}^n(\text{X})]^{n+}$ , in isolation from effects caused by a variation of the donor set. The decisive structural distinction between the ligands is introduced as an angular constraint of the diamine unit, by forcing it into

a diazepane ring in  $L^1$ , thereby enhancing the trans effect of the co-ligand X. The combination of both aspects translates into massive radial disorder and renders the coordination sphere intermediate between tetragonal and trigonal symmetry.

DFT calculations and experimental findings [134] show that ligand-field imposed differences are the root cause of the differences in properties observed for the iron(II) complexes of  $L^1$  and  $L^2$ . Ligand-imposed distortion in  $L^1$  reduces the ligand-field strength by ca. 20–30 kJ mol<sup>-1</sup> and, thus, places this factor on an equal footing with ligand-field effects due to variation in the co-ligand. Destabilization of the ligand field translates into a marked preference of the constrained ligand  $L^1$  for high-spin complexes and into high kinetic lability of the derived iron(II) complexes. Experimental results, obtained after reacting the iron(II) complexes with meta-chloroperbenzoic acid, indicate that the influence of ligand-imposed distortion of  $L^n$  is traceable also in the properties of the resulting iron(IV)-oxo complexes.

## 3.4 Structurally Distorted Iron(IV)-Oxo Complexes with N<sub>5</sub> Pentadentate Ligands

### 3.4.1 Introduction

In the last chapter we introduced ligand-imposed distortion of the coordination environment as a powerful tool to tune the structure, electronics, and reactivity of iron(II) species. These complexes can of course in turn act as precursors for highly reactive non-heme iron(IV)-oxo complexes. This has indeed been pursued by Grohmann *et al.*, who have investigated new iron(IV)-oxo species based on this ligand framework by UV/Vis spectroscopy, mass spectrometry, and kinetic studies. Unfortunately, due to the high reactivity and short lifetime of the newly formed complexes, no X-ray diffraction structures could be taken and no experimental Mössbauer data is available.

As already mentioned in previous chapters, heme and non-heme model complexes support a broad spectrum of oxidation chemistry, such as electron (ET), oxygen-atom (OAT), and hydrogen-atom (HAT) transfer. Strongly diverging selectivities and reaction rates are observed in these processes, however, reflecting variations in the geometric and electronic structures of the iron-oxo complexes. Theoretical studies, mainly using density-functional theory methods [177, 201–205] (but see also ref. [142]), identified the spin state of the iron(IV)-oxo species as one key factor in controlling their catalytic activity. As a rule, high reactivity correlates with a high-spin (hs, spin quintet,  $S = 2$ ) ground state. The commonly lower reactivity of intermediate-spin species (is, spin triplet,  $S = 1$ ) has been interpreted as an indirect consequence of massively higher activation barriers associated with the triplet energy surface [168]. Typically, it is assumed that reactions from a triplet ground state involve spin crossover to the more favorable quintet surface en route to the products (two-state reactivity, TSR) [162, 206]. In this way, the energetic order and separation between the spin states control the reactivity and selectivity of iron(IV)-oxo species.

It has been a major challenge for synthetic chemists to create model systems of pre-defined spin-state characteristics. In contrast to nature's preference for high-spin iron(IV)-oxo species [154], synthetic efforts during the past two decades preferentially produced, at least in the case of non-heme models, iron(IV)-oxo species with triplet ground states. In terms of ligand-field theory, the observed spin ground state of the iron(IV)-oxo species is associated with the ligand-field strength (stronger ligand fields reduce d-orbital de-

generacy, thus favoring spin pairing). In turn, spin states of the highest multiplicity of [LFe(IV)=O] demand four (pseudo-) degenerate metal-centered d-orbitals. Variation of the ligand-field strength thus provides a valuable tool to tune the electronic properties. We should recall, however, that in terms of ligand-field theory, the resulting spin of the iron(IV)-oxo complex is largely centered in the metal d-functions. Delocalization of spin density to the ligand is neglected, an assumption in stark contrast to the actual results of quantum mechanical calculations (see section 3.2 above). As was already mentioned in previous chapters, it is found that the spin states of iron(IV)-oxo species in nitrogen-ligand dominated environments are highly susceptible to variable coordination numbers and structures. That is, the electronic ground spin state is clearly a function of the coordination arrangement. In other words, coordination structure and the resulting electronic ground-state multiplicity are pre-determined by the topology and denticity of the multidentate ligand, which in turn means that distortions in the ligand sphere allow tuning of iron(IV)-oxo species with respect to order and energetic separation of spin states.

Experimentally it was found that iron(IV)-oxo species of both N<sub>5</sub> pentadentate ligands L<sup>1</sup> and L<sup>2</sup> were accessible in high yields (see Chapter 3.3 for more details on the ligands). Their reactivity, however, was distinctly different. This work gives a detailed theoretical study of the electronic structures of these two complexes and ascribes the high reactivity observed for the iron(IV)-oxo complex with ligand L<sup>1</sup> to (close to) degenerate triplet and quintet spin-states. For iron(II) complexes of ligand L<sup>1</sup>, a conformational equilibrium in solution between *mer*- and *fac*-form must also be taken into account (see Chapter 3.3 and ref. [134]). This might directly affect the formation of iron(IV)-oxo complexes, since a conformational equilibrium involving the two coordination arrangements at the stage of the precursor complex likely provides competing channels for the formation of isomeric iron(IV)-oxo complexes (see Figure 3.11 in close analogy to Figure 3.10).

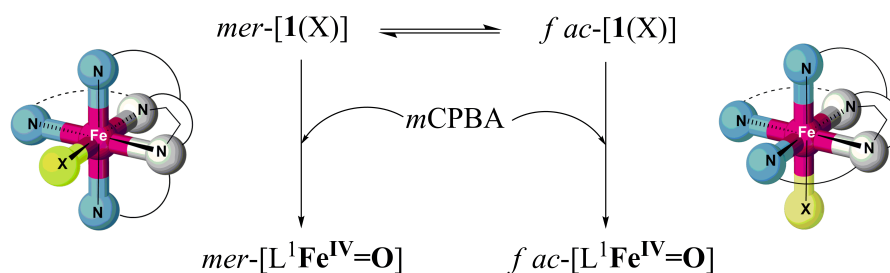


Figure 3.11: Presumed stereodynamic exchange between complex conformers of [1(X)]<sup>n+</sup> in solution and formation of isomeric iron(IV)-oxo species.

## 3.4.2 Computational Details

All DFT and TDDFT calculations were performed using TURBOMOLE6.3 and a locally modified version of the TURBOMOLE6.4 package [111–113]. The latter allows variation of the amount of exact exchange in global hybrid functionals. def2-TZVP basis sets [114] were used throughout. The B3LYP functional [15, 23] was used in most cases, but to evaluate the stability of the results with exact-exchange admixture (20% for B3LYP), in some cases we also compared the BP86 "pure" functional [12, 13] (0%), the PBE0 hybrid functional [14, 31, 117] (25%), as well as customized BLYP-based global hybrid functionals of the form  $E_{XC}^{hybr} = a_0 E_X^{exact} + (1 - a_0) E_X^{B88} + E_C^{LYP}$ , having 15% or 35% exact-exchange admixture, respectively (termed B15LYP, B35LYP in the following). The SCF energies were converged to  $10^{-8}$  Hartree in energy and a fine m5 integration grid was chosen. Dispersion contributions were evaluated using Grimme's DFT-D3 atom-pairwise dispersion corrections [41]. In several cases, solvent effects were taken into account at the polarizable continuum model level, using COSMO (Conductor-Like Screening Model) [91] implemented in TURBOMOLE6.3, with  $\epsilon = 35.688$  for acetonitrile. The first 25 excited states were included in the TDDFT calculations. Gaussian line broadening was used with the computed spectra, with a 'full width at half maximum height' (FWHM) of 100 nm.

For the calculation of Mössbauer parameters, an uncontracted def2-QZVPP basis set was used for iron and def2-TZVP for all other atoms. The structures for the Mössbauer calculations were optimized at B3LYP-D3/def2-TZVP level. The inhouse MAG program [119] was used to calculate the electron density  $\rho$  at the iron nucleus and the quadrupole splitting. For the isomer shifts the linear equation used is  $\delta[\text{mm s}^{-1}] = -0.3594 * (\rho(\text{DFT}) - 11800) + 10.521$ . This equation was fitted to the isomer-shift test of Neese's test set [79], using the same methods for structure optimization and density calculation.

## 3.4.3 Results and Discussion

### 3.4.3.1 Spin-State Energetics of Iron(IV)-Oxo Species

As stereodynamics of the ligand backbone had to be considered, electronic energies of both structural isomers (see Figure 3.11) have been evaluated for both possible spin states ( $S = 1$  vs  $S = 2$ ) of both iron(IV)-oxo species,  $[1(\text{O})]^{2+}$  and  $[2(\text{O})]^{2+}$ . The results indicate a dramatic effect of the ligand on the structural and spin-state preferences of

the iron(IV)-oxo species (Table 3.13). B3LYP/def2-TZVP/COSMO(MeCN) energies for the oxoiron(IV) complex  $[2(\text{O})]^{2+}$  show a clear dominance of the *mer*-py<sub>3</sub> conformation, irrespective of the spin state. The energetic separation of ca. 20-25 kJ mol<sup>-1</sup> between the triplet and the quintet surface is in the typical range of hexacoordinated iron(IV)-oxo species [133,207]. This value compares well with the iron(IV)-oxo species of the closely related ligand Bn-TPEN [132,133] and clearly identifies the triplet state of *mer*- $[2(\text{O})]^{2+}$  as the electronic ground state.

Table 3.13: B3LYP-D3/def2-TZVP results for important bond lengths and energy differences of iron-oxo complex isomers, as well as NPA and Mulliken (in brackets) spin populations. In parentheses: results using the COSMO solvent model (MeCN).

	bond lengths in Å		spin population NPA [Mulliken]		ΔE
	Fe-O	Fe-N <sup>a</sup>	Fe	O	in kJ mol <sup>-1</sup>
<i>mer</i> - <b>[1(O)]</b> <sup>2+</sup> (S = 1)	1.629 (1.637)	2.157 (2.141)	1.29 [1.22] (1.36 [1.28])	0.74 [0.86] (0.69 [0.80])	0 (0)
<i>mer</i> - <b>[1(O)]</b> <sup>2+</sup> (S = 2)	1.620 (1.629)	2.174 (2.146)	3.14 [3.10] (3.16 [3.12])	0.57 [0.65] (0.57 [0.64])	+3.1 (+9.9)
<i>fac</i> - <b>[1(O)]</b> <sup>2+</sup> (S = 1)	1.631 (1.636)	2.156 (2.156)	1.29 [1.22] (1.37 [1.29])	0.75 [0.87] (0.69 [0.81])	+10.0 (+5.8)
<i>fac</i> - <b>[1(O)]</b> <sup>2+</sup> (S = 2)	1.626 (1.632)	2.091 (2.087)	3.10 [3.05] (3.12 [3.06])	0.61 [0.69] (0.58 [0.66])	+0.2 (+6.3)
<i>mer</i> - <b>[2(O)]</b> <sup>2+</sup> (S = 1)	1.623 (1.630)	2.210 (2.196)	1.29 [1.24] (1.34 [1.29])	0.75 [0.85] (0.72 [0.81])	0 (0)
<i>mer</i> - <b>[2(O)]</b> <sup>2+</sup> (S = 2)	1.617 (1.624)	2.188 (2.184)	3.17 [3.12] (3.20 [3.14])	0.56 [0.64] (0.54 [0.63])	+19.1 (+24.6)
<i>fac</i> - <b>[2(O)]</b> <sup>2+</sup> (S = 1)	1.628 (1.635)	2.092 (2.072)	1.29 [1.24] (1.34 [1.29])	0.76 [0.86] (0.72 [0.82])	+86.4 (+88.5)
<i>fac</i> - <b>[2(O)]</b> <sup>2+</sup> (S = 2)	1.621 (1.628)	2.071 (2.055)	3.16 [3.11] (3.18 [3.12])	0.59 [0.68] (0.58 [0.66])	+89.2 (+95.8)

<sup>a</sup>Trans to the oxo ligand.

A very large admixture of exact exchange (35% in B35LYP, see Table S9 in Appendix I) would be required to support a quintet ground state. The experimentally observed optical transition of  $[2(\text{O})]^{2+}$  at 730 nm is attributed to a d → d transition of the triplet state of *mer*- $[2(\text{O})]^{2+}$ . Comparison with the computed spectrum of *mer*- $[2(\text{O})]^{2+}$  in the triplet state (TDDFT; bold blue line in Figure S6 in the Appendix I) shows a blue-shifted transition at 544 nm. Similar blue shifts were observed in a previous TDDFT-based study on iron complexes when comparable functionals were used [208]. Interestingly,  $[1(\text{O})]^{2+}$  exhibits significantly smaller energy differences between the spin

states. At the B3LYP-D3/def2-TZVP/COSMO(MeCN) level of theory, the triplet state of *mer*-[1(O)]<sup>2+</sup> is slightly favored, with the quintet state of this conformer being 10 kJ mol<sup>-1</sup> higher in energy. For *fac*-[1(O)]<sup>2+</sup> both spin states are energetically degenerate and only marginally higher in energy than the *mer*-isomer in the triplet state. The unusually small triplet/quintet separation, comparable to the structural energy differences, is the most remarkable finding at this level.

A brief survey of functionals confirmed the expected strong dependence on the admixture of exact exchange (Tables S9 and S10 in Appendix I). Tests indicate that the switch from quintet to triplet ground states for [1(O)]<sup>2+</sup> occurs between 20% and 25% exact exchange. This well-known dependence of spin-state preferences on exact-exchange admixture on the functional adds significant ambiguity to spin-state assignments. Given the small energy differences of [1(O)]<sup>2+</sup>, a definite assignment of the ground spin state is not possible. The  $\langle S^2 \rangle$  expectation values are not given in Table 3.13, since they all again fall into an inconspicuous range for triplet and quintet spin states alike (2.015-2.029 for triplet and 6.032-6.076 for quintet iron-oxo species for all functionals except B35LYP), as they did for the wider range of iron-oxo complexes in Chapter 3.2. The B35LYP  $\langle S^2 \rangle$  values are still reasonable for the triplet states ( $\leq 2.029$ ), but indicate significant spin contamination for the quintet states ( $\leq 6.157$ ). Considering the large influence of exact exchange on the spin-state energetics of iron(IV)-oxo compounds, these results are not surprising. Clearly B35LYP gives an unphysically large preference for the high-spin state over the triplet state (see Tables S9 and S10 in Appendix I), but spin populations indicate that the calculations did not deteriorate into a broken-symmetry solution, as no anti-ferromagnetically coupled spin pairs can be seen and the divergence from an ideal  $\langle S^2 \rangle$  value remains small. The spin populations again show in general a robustness towards different functionals and exact-exchange admixture. Their numbers are well in range with other iron-oxo complexes and do not seem to be affected by ligand distortion or other steric constraints. Spin-density plots of *mer*-[1(O)]<sup>2+</sup> are shown in Figure 3.12 (see Figures S7 and S8 in Appendix I for spin-density plots of the other isomers and [2(O)]<sup>2+</sup>).

Calculation of the UV/Vis spectra for [1(O)]<sup>2+</sup> (see Figure 3.13) allowed an, at least tentative, assignment of the experimentally observed transition when keeping in mind the blue shift of the computed values (see above) [208]. The experimental spectroscopic data of [1(O)]<sup>2+</sup> at T = 233 K gave a transition at 810 nm [134]. This value may be compared qualitatively with the computed intense transitions at 590 nm and 625

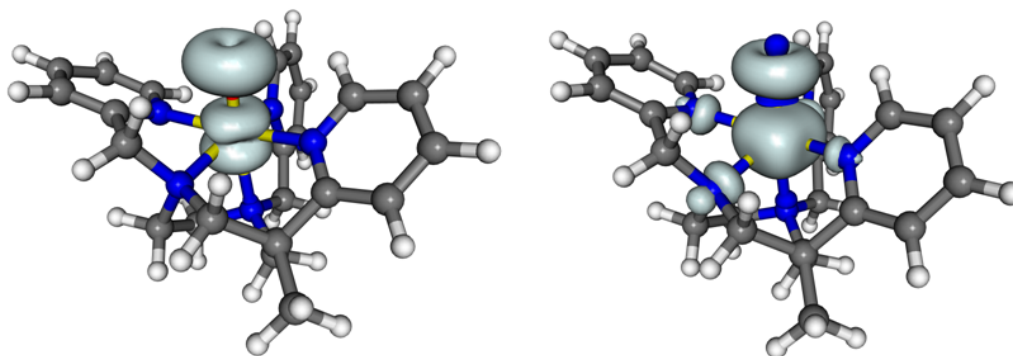


Figure 3.12: Isosurface plots of the spin density ( $\pm 0.005$  a.u.) of  $mer-[1(O)]^{2+}$  with  $S = 1$  (left) and  $S = 2$  (right). B3LYP-D3/def2-TZVP optimized structures.

nm for the triplet states of the *fac*-py<sub>3</sub> and *mer*-py<sub>3</sub> isomers, respectively. We tend to associate the experimental low-temperature transient with the triplet states of one or both conformers of  $[1(O)]^{2+}$ . Note that the blue shift of computed vs experimental frequencies is similar to that discussed above for  $mer-[2(O)]^{2+}$ . In other words, the longer wavelength observed for  $[1(O)]^{2+}$  compared with  $[2(O)]^{2+}$  is reproduced by the calculations (energetically, the computed value is reduced by 0.3 eV compared to an experimental red shift of 0.17 eV). In any case, the computed spectra clearly argue against a quintet ground state as the origin of the experimental spectra.

### 3.4.3.2 Structural Distortions

The quantum-chemical results discussed so far indicate that the spin states of the hexacoordinated iron(IV)-oxo complex  $[1(O)]^{2+}$  are energetically (close to) degenerate. This observation is of significance since pseudo-octahedral non-heme iron(IV)-oxo complexes usually show a clear preference for the triplet ground state. To better understand the behavior of  $[1(O)]^{2+}$ , the DFT-optimized structures of *fac/mer*- $[1(O)]^{2+}$  and *mer*- $[2(O)]^{2+}$  ( $S = 1$  and  $S = 2$ ) have been analyzed with respect to distortion from octahedral structure. Isomer *fac*- $[2(O)]^{2+}$  was excluded as it is energetically too unfavorable (see Table 3.13). The analysis reveals a massive distortion of  $[1(O)]^{2+}$  from a pseudo-octahedral structure for the quintet states of both conformers. The distortion is accompanied by a reduction of the coordination number from 6 ( $[FeN_5O]$ ) in the triplet state to 5+1 ( $[FeN_{4+1}O]$ ) in the quintet state.

The trans-angles O-Fe-N define the easy axis of the  $[FeN_5O]$  polygon. Values in the range of 170° to 175° show minor deviations from the ideal value of 180°, irrespective of

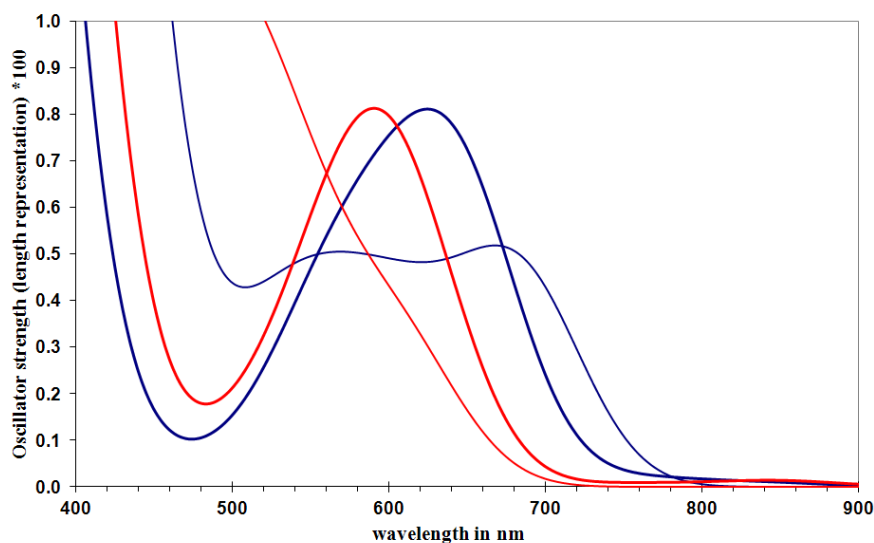


Figure 3.13: Calculated (B3LYP-D3/def2-TZVP/COSMO(MeCN)) UV/Vis spectra of the two isomers *mer*-[1(O)]<sup>2+</sup> (blue) and *fac*-[1(O)]<sup>2+</sup> (red) in the triplet (bold lines) and the quintet state (thin lines). Gaussian line broadening with a 'full width at half maximum height' (FWHM) of 100 nm was used.

ligand, spin state, and ligand conformation. The distortion from octahedral coordination concentrates in the [FeN<sub>4</sub>] equatorial plane, as can be seen from the projections of the structures along the Fe-O bond (Figure 3.14). Distortion parameters of the [FeN<sub>5</sub>O] polygons are summarized in Table 3.14.

As expected, iron(IV)-oxo complexes of the open-chain ligand L<sup>2</sup> give quite regular pseudo-octahedral structures of approximately tetragonal symmetry. Radial expansion of the [FeN<sub>4</sub>] equatorial plane upon going from the triplet to the quintet state causes only minor additional distortion. In contrast, the structures of both isomers of [1(O)]<sup>2+</sup> are very sensitive to the spin state. As a feature diagnostic of coordination-sphere distortion, the trans angles  $\tau_{\text{eq}}$  in the [FeN<sub>4</sub>] equatorial plane are substantially smaller than 180° in the quintet state. The decrease in the trans angles on changing from the triplet to the quintet spin state is accompanied by a substantial opening of one equatorial N-Fe-N cis angle to values greater than 130° (curved arrows in Figure 3.14). In addition, one of the equatorial Fe-N bonds is significantly elongated by up to 30 pm with respect to the others (straight arrows in Figure 3.14). There is little doubt, if any, that this donor atom is far less strongly bound than the others in the equatorial plane. Widening of the cis angle widening and substantial differences in the equatorial Fe-N bond lengths  $\Delta$  render the equatorial [FeN<sub>4</sub>] arrangement trapezoidally distorted. As can be read from

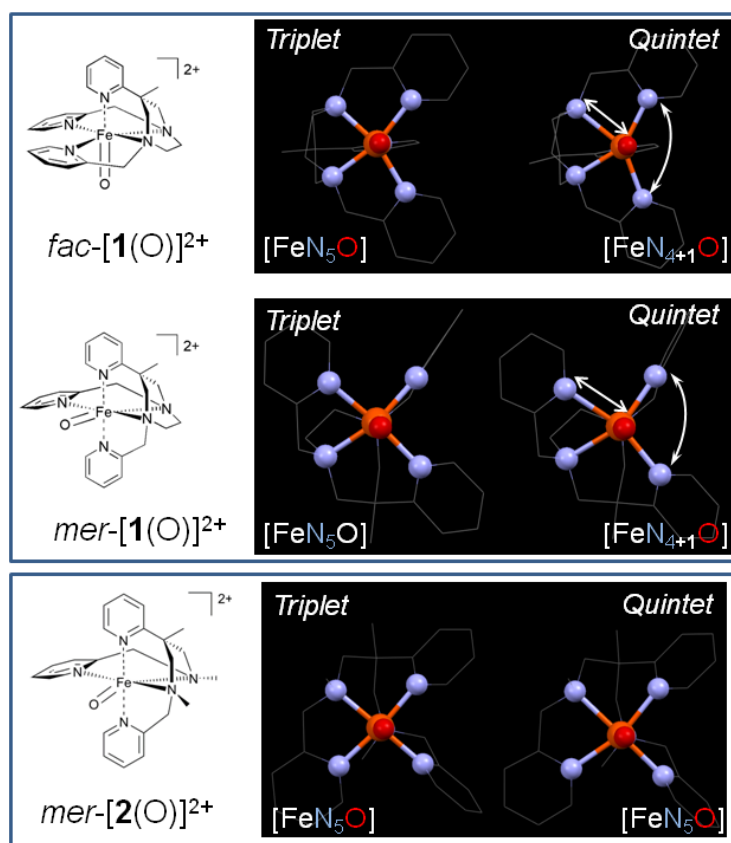


Figure 3.14: Optimized structures (B3LYP-D3/def2-TZVP/COSMO(MeCN)) of the iron(IV)-oxo species, projected along the Fe-O vector.

Figure 3.14, this observation holds for both isomers of  $[1(O)]^{2+}$ .

We conclude that, in the quintet spin states of  $[1(O)]^{2+}$ , the constrained ligand  $L^1$  acts as a tetradentate ligand, to span a trigonal-pyramidal structure, augmented by a weaker close contact. Coordination arrangements in both isomers of  $[1(O)]^{2+}$  thus resemble a trigonal-bipyramidal structure, which is distorted tetragonally by the presence of an additional equatorial donor. In contrast, in the triplet-spin states of  $[1(O)]^{2+}$ , the constrained ligand  $L^1$  acts as a pentadentate ligand, to span a tetragonal-pyramidal structure. Similar changes in effective coordination number in relation to the spin state have been observed in model complexes for taurine dioxygenase (TauD) [190].

That is, in the quintet state of  $[1(O)]^{2+}$  the spatial arrangement of donor atoms applies a ligand field poised between tetragonal and trigonal symmetry. This conclusion is supported by an analysis of the distortion parameters  $S(\text{Oh})$  and  $S(\text{TP})$  [194, 195], which quantify the deviation from regular octahedral and trigonal-prismatic structure,

Table 3.14: Distortion parameters of the  $[\text{FeN}_5\text{O}]$  cores in optimized iron(IV)-oxo complexes (B3LYP-D3/def2-TZVP); in parentheses: results using the COSMO solvent model (MeCN).

	$\Delta d/\text{pm}^{\text{a}}$	$\tau_{\text{eq}}^{\text{b}}$	S(Oh)	S(TP)	
<i>fac</i> - $[\mathbf{1}(\text{O})]^{2+}$ (S = 1)	2.4	162.9	69.8	2.04	9.90
	(2.6)	(163.0)	(70.1)	(2.00)	(10.11)
<i>fac</i> - $[\mathbf{1}(\text{O})]^{2+}$ (S = 2)	28.0	147.4	123.0	5.43	6.44
	(28.6)	(148.2)	(118.3)	(5.11)	(6.76)
<i>mer</i> - $[\mathbf{1}(\text{O})]^{2+}$ (S = 1)	9.5	162.1	100.6	2.60	10.40
	(8.1)	(162.6)	(99.7)	(2.53)	(10.51)
<i>mer</i> - $[\mathbf{1}(\text{O})]^{2+}$ (S = 2)	23.3	152.5	123.6	4.44	7.09
	(30.5)	(153.5)	(121.1)	(4.29)	(7.57)
<i>mer</i> - $[\mathbf{2}(\text{O})]^{2+}$ (S = 1)	5.1	172.4	41.0	0.83	14.43
	(5.1)	(172.3)	(45.6)	(0.76)	(14.51)
<i>mer</i> - $[\mathbf{2}(\text{O})]^{2+}$ (S = 2)	15.3	166.0	70.8	1.65	12.66
	(15.6)	(165.8)	(70.6)	(1.55)	(12.78)

<sup>a</sup>Absolute variation in the equatorial Fe-N bond lengths.

<sup>b</sup>Mean value of the two equatorial N-Fe-N trans angles.

respectively. In Figure 3.15, the S(Oh) and S(TP) values of the iron(IV)-oxo complexes (from Table 3.14) and of their iron(II) precursors (from Table 3.9) are arranged as a continuous shape map of the octahedron  $\leftrightarrow$  trigonal prism transition along the trigonal Bailar twist (line) [196].

Clearly, the degree of trigonal distortion in the structures of  $[\mathbf{2}(\text{O})]^{2+}$  is very similar to the distortion found in the quintet state iron(II) precursors  $[\mathbf{2}(\text{X})]$ . All of these structures may be described as a tetragonally-distorted octahedra (red in Figure 3.15). There is no significant effect of the spin state of  $[\mathbf{2}(\text{O})]^{2+}$  on the distortion. Obviously, the flexible open-chain ligand  $\text{L}^2$  allows for isotropic radial expansion in the  $[\text{FeN}_4]$  equatorial plane during a triplet-quintet transition. The latter conclusion does not hold for complexes of the constrained ligand  $\text{L}^1$ . The structures of  $[\mathbf{1}(\text{O})]^{2+}$  cover an appreciable range on the shape map under the influence of a spin transition (filled blue symbols in Figure 3.15). A tetragonally-distorted octahedron prevails in the triplet state (of both isomers), whereas the quintet state favors structures that are intermediate on the Bailar-twist coordinate. Only in the quintet spin state, trigonal distortion of  $[\mathbf{1}(\text{O})]^{2+}$  is largely the same as the distortion found in the quintet-state iron(II) precursors  $[\mathbf{1}(\text{X})]$ .

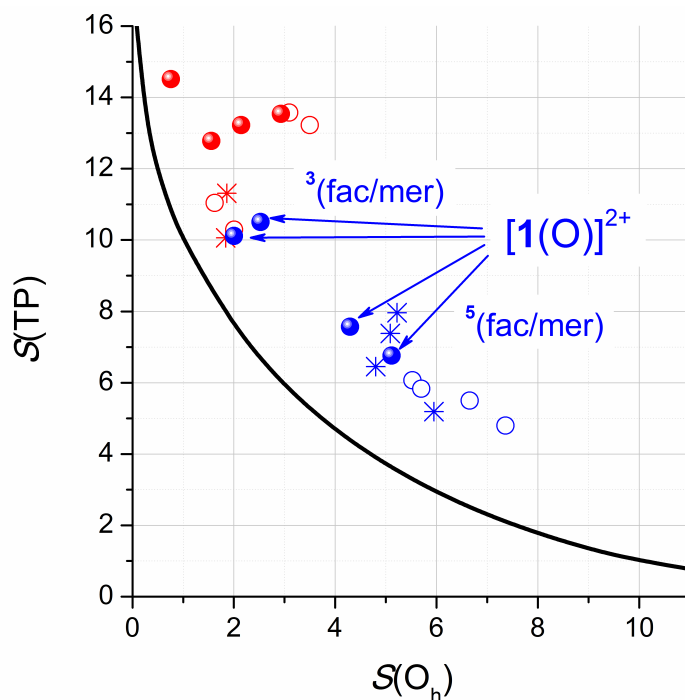


Figure 3.15: Continuous shape map of the octahedron  $\leftrightarrow$  trigonal prism transition (blue:  $[1(X)]$ ; red:  $[2(X)]$ ; solid line: ideal Bailar twist); stars: XRD-derived structures of the iron(II) precursors; circles: DFT-optimized structures (B3LYP-D3/def2-TZVP/COSMO(MeCN)); open circles: iron(II) precursors; filled circles: iron(IV)-oxo species.

### 3.4.3.3 Intrinsic Decay Reactions of $[1(O)]^{2+}$

Grohmann *et al.* have attributed the transients, that dominate the experimental UV/Vis spectra upon reaction of  $[1(OTf)](OTf)$  with mCPBA at ambient temperature, to an intramolecular decay product of a highly reactive iron(IV)-oxo species. Initiation of the intramolecular decay pathway by benzylic C-H bond activation [131, 186] is supported by results from mass spectrometry (MS). HR-ESI mass spectrometry of reaction solutions revealed a dominant signal, which corresponds to the fragment  $[1] + O^{2+}$ . MS experiments show that this molecular ion, when isolated in the gas phase, is unable to oxidize 1,3-cyclohexadiene to benzene. This finding excludes the iron(IV)-oxo species  $[1(O)]^{2+}$  as the source of the signal, but is compatible with an isomeric structure, after completed C-H activation and rebound (species *fac*-II in Figure 3.16;  $m/z$  calculated for II: 222.5777). The two different isomers of the iron(IV)-oxo complex could in principle lead to two different Fe(II) intermediates, *fac*-II (Figure 3.16) and *mer*-II (not shown). Indeed, the B3LYP-D3/def2-TZVP/COSMO(MeCN) optimizations indicate that in-

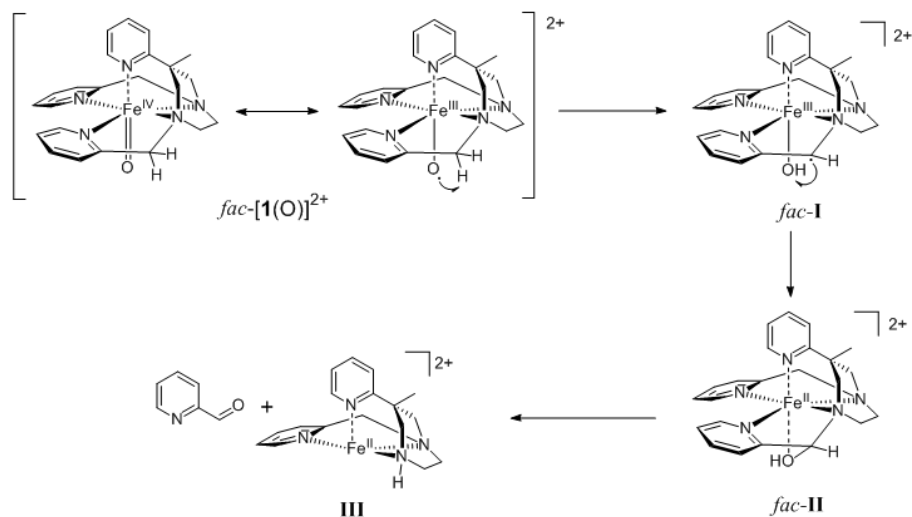


Figure 3.16: Proposed reaction mechanism for the intramolecular decay pathway of  $fac-[1(O)]^{2+}$  to III.

tramolecular benzylic C-H activation of one picolyl residue is thermodynamically possible for both isomers, as indicated by the large energy difference between the iron(IV)-oxo species and the isomers of II in the range of  $-140 \text{ kJ mol}^{-1}$ . Experimentally an additional signal in the mass spectra at  $m/z = 169.0589$  indicated complex fragmentation. Its signature is compatible with the structure of III ( $m/z$  calculated for III: 169.0591), which derives from II through C-N bond dissociation of its hemi-aminal function.

The thermodynamic availability and the spectroscopic properties of possible iron(II) intermediates of intramolecular decay (see Figure 3.17) of both isomers of  $[1(O)]^{2+}$  have been further studied by time-dependent DFT calculations of UV/Vis spectra. From the pentacoordinated ligand-hydroxylation product II, the coordinatively saturated iron(II) complex V and the alkoxido iron(II) complex IV are generated via addition of a triflate ion and deprotonation of the hydroxyl function, to form an alkoxide ligand, respectively. In order to discuss the latter process, we use the isodesmic reaction of the iron(IV)-oxo species with triflate (see Table S11 in Appendix I).

The results show that IV, even if strained, is thermodynamically feasible. The computations greatly favor a quintet ground state for all of these possible intermediates (see Table S12 in Appendix I). TDDFT calculations, however, indicate that none of the suggested iron(II) species II, IV, and V would be consistent with the observed UV/Vis absorption near 600 nm. In contrast, TDDFT/B3LYP/def2-TZVP/COSMO(MeCN) gives a band near 550 nm for the corresponding iron(III) complex VI in the doublet state (blue line

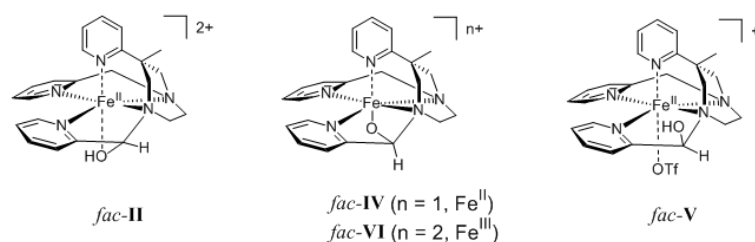


Figure 3.17: Possible iron(II) intermediates in the decay of the highly reactive iron(IV)-oxo species. Only structures derived from conformer  $fac-[1(O)]^{2+}$  are shown.

in Figure 3.18). The alkoxidoiron(III) complex VI is thus the most likely candidate for the species causing the observed band in the experimental UV/Vis spectrum. The rapid decay of the absorption in the visible, following a first-order rate law, may be attributed to cleavage of the hemi-aminal function in the alkoxido iron(III) complex VI, to give the iron(III) analogue of III and pyridine-2-carbaldehyde.

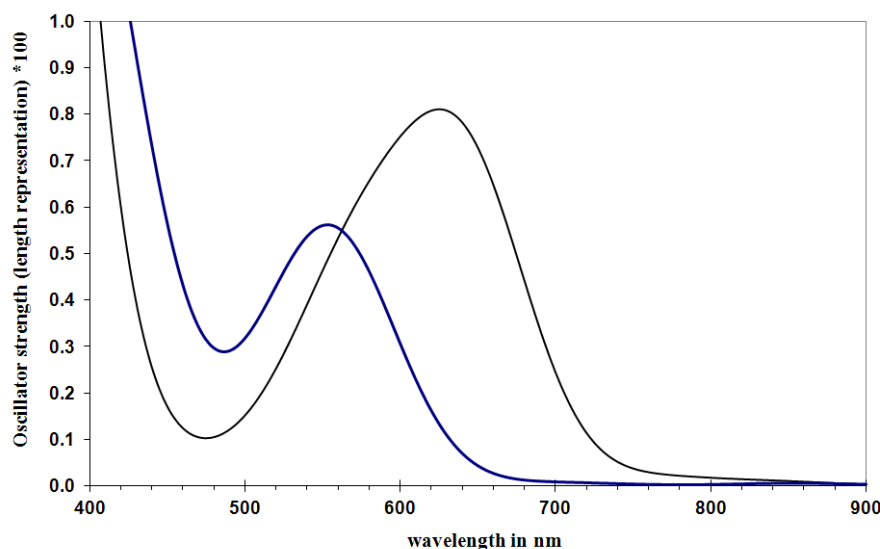


Figure 3.18: Calculated (B3LYP/def2-TZVP/COSMO(MeCN)) UV/VIS spectra of  $mer-[1(O)]^{2+}$  ( $S = 1$ ) (black line) and the intramolecular reaction intermediate VI ( $S = 1/2$ ) (blue line). Gaussian line broadening with a 'full width at half maximum height' (FWHM) of 100 nm was used.

Precedence for the occurrence of alkoxidoiron(III) complexes similar to VI as intermediates of self-decay of oxoiron(IV) species has been provided by Münck, Que and co-workers [186]. These authors suggest that intramolecular ligand hydroxylation, to form an alcohol complex analogous to II, is followed by attack of a second iron(IV)-oxo complex to yield an alkoxidoiron(III) complex and a hydroxidoiron(III) complex as the

products of a bimolecular reaction.

#### 3.4.3.4 Mössbauer Parameters and Hydrogen Abstraction from Acetonitrile

Due to the high reactivity and short lifetimes of the iron(IV)-oxo compounds, reliable Mössbauer parameters could so far not yet be obtained experimentally. As prediction for future experiments, we have computed Mössbauer parameters for all possible isomers of  $[1(\text{O})]^{2+}$  and  $[2(\text{O})]^{2+}$  in different spin states (Table 3.15). The DFT results suggest that assigning future experimental results to spin states using the isomer shifts should be possible. Differences between isomer shifts for triplet and quintet states are quite pronounced for  $[1(\text{O})]^{2+}$  and *mer*- $[2(\text{O})]^{2+}$ , ranging from 0.07-0.08 mm s<sup>-1</sup> for S = 1 to 0.21-0.22 mm s<sup>-1</sup> for S = 2 (*fac*- $[2(\text{O})]^{2+}$  can probably be ruled out, based on the relative energies). A similarly large difference in isomer shifts for triplet and quintet spin states has been found for the octahedral iron(IV)-oxo complex with the structurally related Bn-TPEN ligand (0.04 to 0.18 mm s<sup>-1</sup>). Experimentally,  $[\text{Fe}(\text{O})(\text{Bn-TPEN})]^{2+}$  exhibits an isomer shift of 0.01 mm s<sup>-1</sup> and an S = 1 ground state (see Chapter 3.2), in good agreement with calculations. Another octahedral iron(IV)-oxo complex,  $[\text{Fe}(\text{O})(\text{N}_4\text{Py})]^{2+}$ , seems to follow the same pattern, with  $\delta = 0.01$  mm s<sup>-1</sup> for the triplet (expt. value.: -0.04 mm s<sup>-1</sup>) and 0.18 mm s<sup>-1</sup> for the quintet state, respectively. However, this is not a general trend for octahedral iron(IV)-oxo complexes and holds only for related ligands (see Chapter 3.2 for counterexamples). Other possibilities like the dimerisation of  $[2(\text{O})]^{2+}$ , that have been speculated about from the experimental point of view and cannot be safely excluded, have also been taken into account (see Table S13 in Appendix I).

While the assignment of the spin state for  $[1(\text{O})]^{2+}$  might be done by comparing fairly reliable isomer shift calculations to experimental results, deciding on the correct *mer*- or *fac*- isomers might be more difficult, as their  $\delta$  values are too similar. Here the quadrupole splittings might serve as a better indicator, even though they are usually more difficult to compute. Calculations of  $\Delta E_Q$  for  $[\text{Fe}(\text{O})(\text{Bn-TPEN})]^{2+}$  and  $[\text{Fe}(\text{O})(\text{N}_4\text{Py})]^{2+}$  give quadrupole splittings in good agreement with experiment (see Chapter 3.2). It would thus not be unreasonable to expect good accuracy for  $[1(\text{O})]^{2+}$  as well.

The rapid decay of the very reactive iron(IV)-oxo complex of  $\text{L}^1$  was initially thought to be the result of a reaction with the solvent. This was the main reason why the HAT of  $[1(\text{O})]^{2+}$  with acetonitrile has been investigated (see Figure 3.19). However, unpublished

Table 3.15: Calculated Mössbauer parameters (see Computational Details for the exact level) for all possible isomers of  $[1(\text{O})]^{2+}$  and  $[2(\text{O})]^{2+}$  in different spin states. Relative energies from B3LYP-D3/def2-TZVP in  $\text{kJ mol}^{-1}$ .

	$\delta$ [ $\text{mm s}^{-1}$ ]	$\Delta E_{\text{Q}}$ [ $\text{mm s}^{-1}$ ]	$\Delta E$
<i>mer</i> - $[1(\text{O})]^{2+}$ (S = 0)	0.10	0.78	35.6
<i>mer</i> - $[1(\text{O})]^{2+}$ (S = 1)	0.08	0.68	0
<i>mer</i> - $[1(\text{O})]^{2+}$ (S = 2)	0.22	0.89	3.1
<i>fac</i> - $[1(\text{O})]^{2+}$ (S = 0)	0.08	0.82	47.6
<i>fac</i> - $[1(\text{O})]^{2+}$ (S = 1)	0.08	0.86	10.0
<i>fac</i> - $[1(\text{O})]^{2+}$ (S = 2)	0.21	1.35	0.2
<i>mer</i> - $[2(\text{O})]^{2+}$ (S = 0)	0.07	0.97	37.9
<i>mer</i> - $[2(\text{O})]^{2+}$ (S = 1)	0.07	1.00	0
<i>mer</i> - $[2(\text{O})]^{2+}$ (S = 2)	0.21	0.57	19.1
<i>fac</i> - $[2(\text{O})]^{2+}$ (S = 0)	0.13	0.33	124.1
<i>fac</i> - $[2(\text{O})]^{2+}$ (S = 1)	0.13	0.32	86.4
<i>fac</i> - $[2(\text{O})]^{2+}$ (S = 2)	0.24	1.54	89.2

experimental findings by Grohmann *et al.* refuted HAT from the solvent, based on a far too weak kinetic-isotope effect ( $\text{CD}_3\text{CN}$  vs.  $\text{CH}_3\text{CN}$ ) in the rate constants of the monitored decay in the UV/Vis spectra. Instead the findings pointed to an unimolecular decay from a different source (see 'Intrinsic Decay Reactions of  $[1(\text{O})]^{2+}$ ' in Chapter 3.4.3.3).

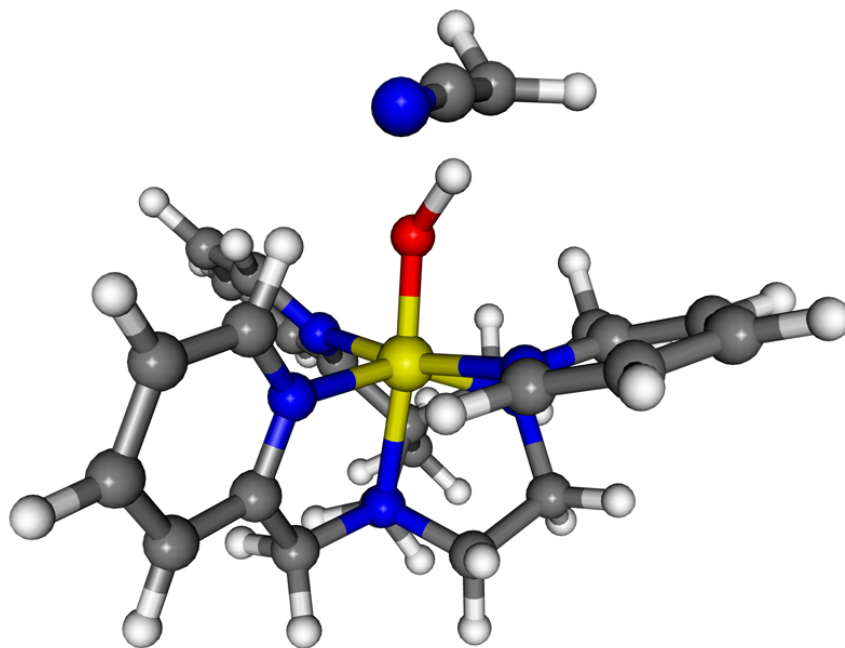


Figure 3.19: Transition state of *mer*- $[1(\text{O})]^{2+}$  (S = 1) + MeCN. B3LYP/def2-TZVP optimized structure.

Another reason for the interest in the HAT of  $[1(\text{O})]^{2+}$  was the comparison with kinetic barriers and reaction energies of the HAT for the other calculated iron-oxo species from Chapter 3.2, especially considering that none of them suffers from a similar amount of steric strain (given the ligand distortion in  $[1(\text{O})]^{2+}$ ). Table 3.16 sums up the kinetic barriers and reaction energies for the different isomers and spin states of  $[1(\text{O})]^{2+}$ . For easier comparison all energies are given relative to the energy of *mer*- $[1(\text{O})]^{2+}$  ( $S = 1$ ) + acetonitrile, as this isomer has the lowest energy. The resulting *mer*- and *fac*- iron-hydroxo complexes were all found to have sextet ground states, and the  $\text{CH}_2\text{CN}$  radical is a doublet (see Table S14 in Appendix I).

Table 3.16: Kinetic barriers and reaction energies in  $\text{kJ mol}^{-1}$  for the HAT reaction of  $[1(\text{O})]^{2+} + \text{CH}_3\text{CN} \rightarrow [1(\text{OH})]^{2+}$  ( $S = 5/2$ ) +  $\bullet\text{CH}_2\text{CN}$  ( $S = 1/2$ ).

Functional and transition state	$\Delta E^\ddagger$ in $\text{kJ mol}^{-1}$	$\Delta E$ in $\text{kJ mol}^{-1}$
B3LYP/def2-TZVP		
<i>mer</i> - $[1(\text{O})]^{2+}$ ( $S = 1$ ) + $\text{CH}_3\text{CN}$	86.6	1.4
<i>mer</i> - $[1(\text{O})]^{2+}$ ( $S = 2$ ) + $\text{CH}_3\text{CN}$	94.9	1.4
<i>fac</i> - $[1(\text{O})]^{2+}$ ( $S = 1$ ) + $\text{CH}_3\text{CN}$	87.6	14.1
<i>fac</i> - $[1(\text{O})]^{2+}$ ( $S = 2$ ) + $\text{CH}_3\text{CN}$	81.6	14.1
B3LYP-D3/def2-TZVP		
<i>mer</i> - $[1(\text{O})]^{2+}$ ( $S = 1$ ) + $\text{CH}_3\text{CN}$	51.8	-1.2
<i>mer</i> - $[1(\text{O})]^{2+}$ ( $S = 2$ ) + $\text{CH}_3\text{CN}$	60.0	-1.2
<i>fac</i> - $[1(\text{O})]^{2+}$ ( $S = 1$ ) + $\text{CH}_3\text{CN}$	62.5	12.4
<i>fac</i> - $[1(\text{O})]^{2+}$ ( $S = 2$ ) + $\text{CH}_3\text{CN}$	50.1	12.4

<sup>a</sup>Energies relative to *mer*- $[1(\text{O})]^{2+}$  ( $S=1$ ) +  $\text{CH}_3\text{CN}$ . See Table 2.5 for energy differences to *mer*- $[1(\text{O})]^{2+}$  ( $S = 2$ ) and *fac*- $[1(\text{O})]^{2+}$  ( $S = 1$  and  $S = 2$ ).

There is no theoretical evidence for two-state reactivity since *mer*- $[1(\text{O})]^{2+}$  ( $S = 1$  ground state) encounters the lowest barrier for a triplet transition state, while *fac*- $[1(\text{O})]^{2+}$  ( $S = 2$  ground state) has the lowest barrier on the quintet surface. Dispersion corrections drastically lower the kinetic barriers from 80-95  $\text{kJ mol}^{-1}$  to 50-63  $\text{kJ mol}^{-1}$  (relative to *mer*- $[1(\text{O})]^{2+}$ ,  $S=1$ ). As with the discussed iron(IV)-oxo complexes from Chapter 3.2, the D3 dispersion corrections only have this large effect on barrier heights, while the changes in reaction energies are less than 3  $\text{kJ mol}^{-1}$ . Looking at the thermochemistry, HAT from acetonitrile seems slightly disfavored for *fac*- $[1(\text{O})]^{2+}$ , but is practically neutral for *mer*- $[1(\text{O})]^{2+}$ . However, since the resulting radical product will quickly react and thereby push the chemical equilibrium to the product site (of course the overabundance of solvent molecules on the educt site is contributing to this end too), the small positive

reaction energies might not be a big problem for a complete and fast reaction of  $[1(\text{O})]^{2+}$ . Again we stress that the experimental decay of the UV/Vis bands of  $[1(\text{O})]^{2+}$  does not come from reaction with the solvent. This might also be an additional indicator of the dispersion corrected barriers being too low, as intermolecular HAT apparently cannot compete with the real decay process in experiment, probably because its real kinetic barriers are too high.

Table 3.17: Important bond lengths, as well as NPA and Mulliken (in brackets) spin populations for the transition states  $[\text{TS}]^{2+}$  of the HAT reaction of  $[1(\text{O})]^{2+}$  and acetonitrile. Comparison to the  $[1(\text{O})]^{2+}$  educts are given in parentheses. B3LYP/def2-TZVP optimized structures, with and without D3 dispersion corrections.

	distances in Å					spin population NPA [Mulliken]	
	Fe-O	O-H	H-C <sup>a</sup>	Fe-N <sup>b</sup>	$\langle S^2 \rangle$	Fe	O
B3LYP							
<i>mer</i> - $[\text{TS}]^{2+}$ (S = 1)	1.745	1.195	1.356	2.148	2.064	1.03 [1.03]	0.55 [0.57]
<i>mer</i> - $[1(\text{O})]^{2+}$ (S = 1)	(1.629)	-	-	(2.163)	(2.023)	(1.29 [1.21])	(0.75 [0.86])
<i>mer</i> - $[\text{TS}]^{2+}$ (S = 2)	1.736	1.182	1.364	2.187	6.076	2.94 [2.98]	0.43 [0.41]
<i>mer</i> - $[1(\text{O})]^{2+}$ (S = 2)	(1.621)	-	-	(2.184)	(6.062)	(3.15 [3.10])	(0.57 [0.65])
<i>fac</i> - $[\text{TS}]^{2+}$ (S = 1)	1.745	1.199	1.353	2.137	2.043	1.04 [1.05]	0.58 [0.58]
<i>fac</i> - $[1(\text{O})]^{2+}$ (S = 1)	(1.629)	-	-	(2.173)	(2.023)	(1.30 [1.22])	(0.76 [0.87])
<i>fac</i> - $[\text{TS}]^{2+}$ (S = 2)	1.733	1.185	1.366	2.082	6.061	2.92 [2.93]	0.44 [0.45]
<i>fac</i> - $[1(\text{O})]^{2+}$ (S = 2)	(1.625)	-	-	(2.104)	(6.055)	(3.11 [3.06])	(0.60 [0.69])
B3LYP-D3							
<i>mer</i> - $[\text{TS}]^{2+}$ (S = 1)	1.742	1.193	1.356	2.133	2.053	1.04 [1.03]	0.55 [0.57]
<i>mer</i> - $[1(\text{O})]^{2+}$ (S = 1)	(1.629)	-	-	(2.157)	(2.023)	(1.29 [1.22])	(0.74 [0.86])
<i>mer</i> - $[\text{TS}]^{2+}$ (S = 2)	1.732	1.185	1.361	2.177	6.071	2.92 [2.95]	0.44 [0.43]
<i>mer</i> - $[1(\text{O})]^{2+}$ (S = 2)	(1.620)	-	-	(2.174)	(6.060)	(3.14 [3.10])	(0.57 [0.65])
<i>fac</i> - $[\text{TS}]^{2+}$ (S = 1)	1.746	1.197	1.348	2.120	2.038	1.04 [1.04]	0.58 [0.58]
<i>fac</i> - $[1(\text{O})]^{2+}$ (S = 1)	(1.631)	-	-	(2.156)	(2.023)	(1.29 [1.22])	(0.75 [0.87])
<i>fac</i> - $[\text{TS}]^{2+}$ (S = 2)	1.731	1.181	1.366	2.068	6.058	2.90 [2.91]	0.45 [0.45]
<i>fac</i> - $[1(\text{O})]^{2+}$ (S = 2)	(1.626)	-	-	(2.091)	(6.054)	(3.10 [3.05])	(0.61 [0.69])

<sup>a</sup>Abstracted hydrogen, connected to  $-\text{CH}_2\text{CN}$ .

<sup>b</sup>Trans to the oxo ligand.

Concerning the structure of the transition states (see Table 3.17), we find a strongly elongated Fe-O bond, stretched by more than 0.1 Å compared to the iron-oxo educt, which is well in line with what we find for most of the investigated iron-oxo transition states in Chapter 3.2. The distance from the oxo ligand to the abstracted hydrogen atom is less than 1.2 Å, which is a good bit shorter in comparison to the other complexes, where it mostly was between 1.3-1.5 Å. This could indicate a later transition state, but it might just as well be due to the different hydrogen donor (acetonitrile vs 1,4-

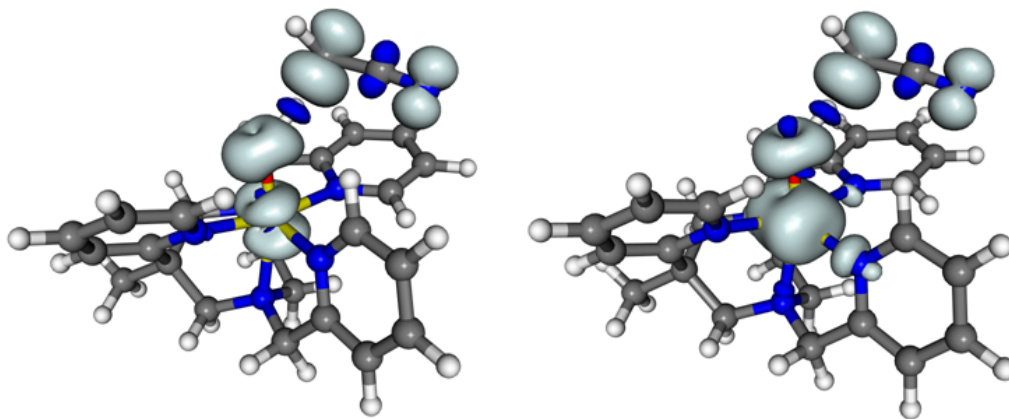


Figure 3.20: Isosurface plots of the spin density ( $\pm 0.005$  a.u.) of the transition state *mer*-[1(O)]<sup>2+</sup> + MeCN with  $S = 1$  (left) and  $S = 2$  (right) from B3LYP/def2-TZVP optimized structures.

cyclohexadiene) or both. As much as dispersion corrections influence the barrier height, they leave the important interatomic distances between iron, oxygen and hydrogen very much unchanged (less than 1 pm differences for all isomers and spin states).

Perhaps more surprising are the small changes in the  $\langle S^2 \rangle$  values for the transition states and the subsequent low amount of spin contamination observed. This is especially interesting for the quintet state, as it was very susceptible to larger  $\langle S^2 \rangle$  changes for trigonal-bipyramidal iron(IV)-oxo complexes, but not for [1(O)]<sup>2+</sup>. For triplet ground-state complexes, the results are well in line with other octahedral iron(IV)-oxo complexes. Regarding the spin populations we find a high iron(III) character in the transition state. The iron spin density is going down from 3.11-3.15 for the quintet and 1.29-1.30 for the triplet to 2.90-2.94 and 1.03-1.04, respectively, for the corresponding transition states. We can thus again not confirm an increase of oxyl character when going from the oxo complex to the HAT transition state, in contrast to some claims in the literature [164–166]. We also find that results from NPA and Mulliken spin population analysis become very similar for the transition state. This holds especially true for oxygen, where differences of 0.1 a.u. between the two methods were not uncommon for the iron-oxo educts. Isosurface plots of the spin-density of the transition states are shown in Figure 3.20. They show a very similar picture to the HAT transition states from Chapter 3.2.

### 3.4.4 Conclusions

Most synthetic models of non-heme iron(IV)-oxo-containing enzymes use tailor-made polydentate ligands, and the denticity of the ligand typically acts as a rough preselector for structure, spin state, and function. The flexibility of such models to mimic enzyme function is necessarily limited. In the present work, we have investigated established incremental ligand-field distortion as a tool to tune the spin-state preferences of iron(IV)-oxo fragments, in ligand fields set up by pentadentate ligands. Within our pair of ligands ( $L^1$  diazepane-based;  $L^2$  open chain), nature and strength of the donor set (diamine-trisimine) are fully conserved. Combined experimental and quantum-chemical findings show that ligand-field imposed differences are the root cause of the differences in properties observed for the iron(IV)-oxo complexes of  $L^1$  and  $L^2$ . The decisive structural distinction between the ligands is introduced as an angular constraint of the diamine unit, by forcing it into a diazepane ring in  $L^1$ . This approach enabled us to study solely the consequences of ligand-sphere distortion, in isolation from effects caused by variation of the donor set. Under the action of this angular constraint, we have found both the conformation and the denticity of the chelate ligand to be no longer invariant but to become functions of the iron(IV)-oxo spin state.

Grohmann *et al.* have unambiguously identified the oxoferryl complexes by in situ spectroscopy as the products of reaction of iron(II) precursors with meta-chloroperbenzoic acid or iodosobenzene in dilute acetonitrile solutions. The fact that  $L^1$  supplies a highly distorted ligand field is indicated by the distinctly red-shifted  $d \rightarrow d$  transition in  $[1(O)]^{2+}$ . This distortion engenders high reactivity towards hydrogen-atom donors (inter- and intramolecular) and oxygen-atom acceptors. Notably, experimental findings for the reactivity of  $[1(O)]^{2+}$  suggest that in either situation it exceeds the reactivity of its open-chain congener by several orders of magnitude. Based on our DFT studies, we attribute this sharp distinction to ligand-field imposed effects on the energetic order and separation of the spin states of the iron(IV)-oxo species. A high degree of trigonal distortion is observed for the quintet states of the highly reactive oxoferryl complexes of  $L^1$ . This coincides with energetic degeneracy of the triplet and quintet spin states. Finally, we note that the interdependence we observe between ligand-imposed coordination-arrangement, spin state, and ligand denticity may be a general principle by which nature controls the outcome of oxoferryl-dependent reactions. A change in coordination number may be essential to bring about what then is the catalytically poised (i. e., entatic) state.

## 3.5 Dramatic Effects of Spin Contamination on Vibrational Frequencies and Structure of a Formal Iron(V)-Nitrido Complex

### 3.5.1 Introduction

A formal iron(V)-nitrido species, with the tetrapodal nitrogen ligand 2,6-bis(1,1-di(aminomethyl)ethyl)pyridine [209] has been prepared and investigated by Schwarz and Grohmann [210]. The complex was of special interest, because it was discovered in mass-spectrometry studies to perform alkyne-metathesis [211]. Since metathesis at iron was previously unknown, this provided further motivation to look into the electronic structure and the properties of this supposed iron(V) complex. Infra-red-multi-photon-dissociation-spectroscopy (IRMPD), together with  $N^{15}$  labeling experiments, showed an iron-nitrido stretching frequency of  $890\text{ cm}^{-1}$ . This result was well in line with expectations from previous studies (see, for example, ref. [212–217]), but attempts to reproduce this frequency by DFT calculations gave large deviations for the most widely used B3LYP functional. This problem had not turned up in other iron(V)-nitrido species before, but will be investigated and rationalized in this work.

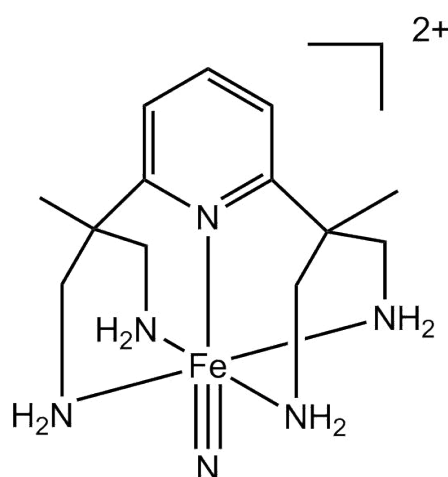


Figure 3.21: Fe(V)(N)(2,6-bis(1,1-di(aminomethyl)ethyl)pyridine).

### 3.5.2 Computational Details

All unrestricted DFT calculations were performed using TURBOMOLE6.3 [111–113]. def2-TZVP [114] basis sets were used for all atoms. The functionals BP86 [12, 13], BLYP [12, 15], PBE [14, 31], B3LYP [15, 23], PBE0 [14, 31, 117], TPSSh [115], and BHLYP [118] were used. The SCF energies were converged to  $10^{-8}$  Hartree in energy and a fine m5 integration grid was used. Frequencies were calculated by harmonic vibrational frequency analyses. Restricted open-shell Kohn-Sham (ROKS) DFT calculations and subsequent frequency calculations were performed using Jaguar V7.7 [218], with triple- $\zeta$  valence basis sets TZV\*\*.

### 3.5.3 Results and Discussion

A doublet ground state was assigned to the system. Frequency analyses for a number of GGA functionals (BP86, BLYP and PBE; see Table 3.18) give iron-nitrido stretching frequencies around 939-965  $\text{cm}^{-1}$ . These results are 5.5-8.5 % higher than the experimentally assigned 890  $\text{cm}^{-1}$ , deviations that may be considered in the expected range for unscaled results with GGA functionals. Switching to B3LYP, however, does not improve the result, but instead leads to a far too low iron-nitrido stretching frequency. Furthermore, the stretching vibration is now split into two frequencies, a situation not found in experiment. Similar results are obtained with PBE0, where again we found a splitting into two frequencies, and with BHLYP, where even lower frequencies around 540-577  $\text{cm}^{-1}$  are found.

A look at the  $\langle S^2 \rangle$  for B3LYP, PBE0, and BHLYP revealed an appreciable amount of spin contamination for these functionals (see Table 3.18). With an ideal value of 0.75 for a doublet, the  $\langle S^2 \rangle$  for BHLYP was more than twice this number and even B3LYP gave a result close to 1. Spin population analyses clearly showed that the B3LYP and PBE0 calculations had converged into broken-symmetry solutions, with negative spin density at iron and more than one a.u. of spin density at nitrogen. BHLYP, on the other hand, localized the unpaired spin completely at iron, resulting in a very high spin contamination, an extreme increase of the iron-nitrido bond length to over 1.75 Å, wrong frequencies, and even a wrong order of spin states, with the quartet state slightly lower in energy than the doublet spin-state. This is in stark contrast to all other tested functionals, that clearly preferred a low-spin doublet ground state. Isosurface plots of the spin density (see Figure 3.22) reveal the strongly metal-ligand antibonding character

of the singly-occupied molecular orbital in the B3LYP and BHLYP calculations, that led to the high levels of spin contamination observed [120].

The first idea to solve the spin contamination problem was performing restricted open-shell Kohn-Sham calculations (ROKS) on the system. This way we could find out whether the problem still persists, if we eliminate spin contamination. Indeed we found substantial improvements (see Table 3.18) for ROB3LYP and ROBHLYP, with ROBHLYP almost exactly reproducing the experimental value. ROBP86 showed no further improvements, but ROB3LYP yielded Fe-N frequencies very close to BP86, although the additional stretching vibration, not observed in experiment, still appeared.

Table 3.18: Important distances, as well as NPA and Mulliken (in brackets) spin populations, spin state energetics and Fe≡N stretching frequencies, calculated for different functionals. def2-TZVP basis set used for all atoms in unrestricted calculations. TZV\*\* basis set used for all atoms in ROKS calculations.

	$\nu(\text{Fe}\equiv\text{N})$ in $\text{cm}^{-1}$	distances in Å				$\langle S^2 \rangle$	spin population NPA [Mulliken]		$\Delta E$ ( $S=3/2 - S=1/2$ ) in $\text{kJ mol}^{-1}$
		Fe≡N	Fe-N <sup>a</sup>	Fe-N <sup>b</sup>	Fe		N		
<b>expt. 890</b>									
BP86	961	1.592	2.042	2.171	0.754	0.40 [0.34]	0.54 [0.67]	93.2	
BLYP	939	1.602	2.072	2.208	0.754	0.41 [0.35]	0.54 [0.65]	87.4	
PBE	965	1.591	2.042	2.170	0.753	0.42 [0.36]	0.53 [0.65]	92.9	
TPSSH	869	1.587	2.031	2.147	0.776	0.21 [0.13]	0.72 [0.86]	74.2	
B3LYP	596/573	1.614	2.050	2.164	0.972	-0.22 [-0.33]	1.18 [1.28]	73.0	
PBE0	547/540	1.658	2.024	2.101	1.259	-0.61 [-0.72]	1.54 [1.63]	32.3	
BHLYP	577	1.759	2.037	2.065	1.590	1.06 [1.09]	-0.09 [-0.02]	-3.7	
ROBP86	963	1.600	2.044	2.168		[0.41]	[0.57]		
ROB3LYP	967/963	1.587	2.050	2.177		[0.34]	[0.64]		
ROBHLYP	889	1.592	2.014	2.101		[0.16]	[0.82]		

<sup>a</sup>Average distance for nitrogens cis to the nitrido ligand. <sup>b</sup>Trans to the nitrido ligand.

Four important aspects were revealed by spin population analyses: i) ROKS calculations prevented broken-symmetry solutions and therefore gave more accurate frequencies than the unrestricted calculations. ii) GGA functionals localize high amounts of spin density at the nitrido ligand, a situation even more pronounced in the ROKS calculations, where the best functional ROBHLYP localized almost the entire unpaired spin at nitrogen (0.82 from Mulliken population analysis). iii) The frequency calculations and spin distributions for the formal iron(V)-nitrido complex are highly sensitive to the amount of exact-exchange admixture in the functional. 20% exact-exchange admixture in B3LYP is already too much and leads to broken-symmetry solutions in UKS calculations. iv)

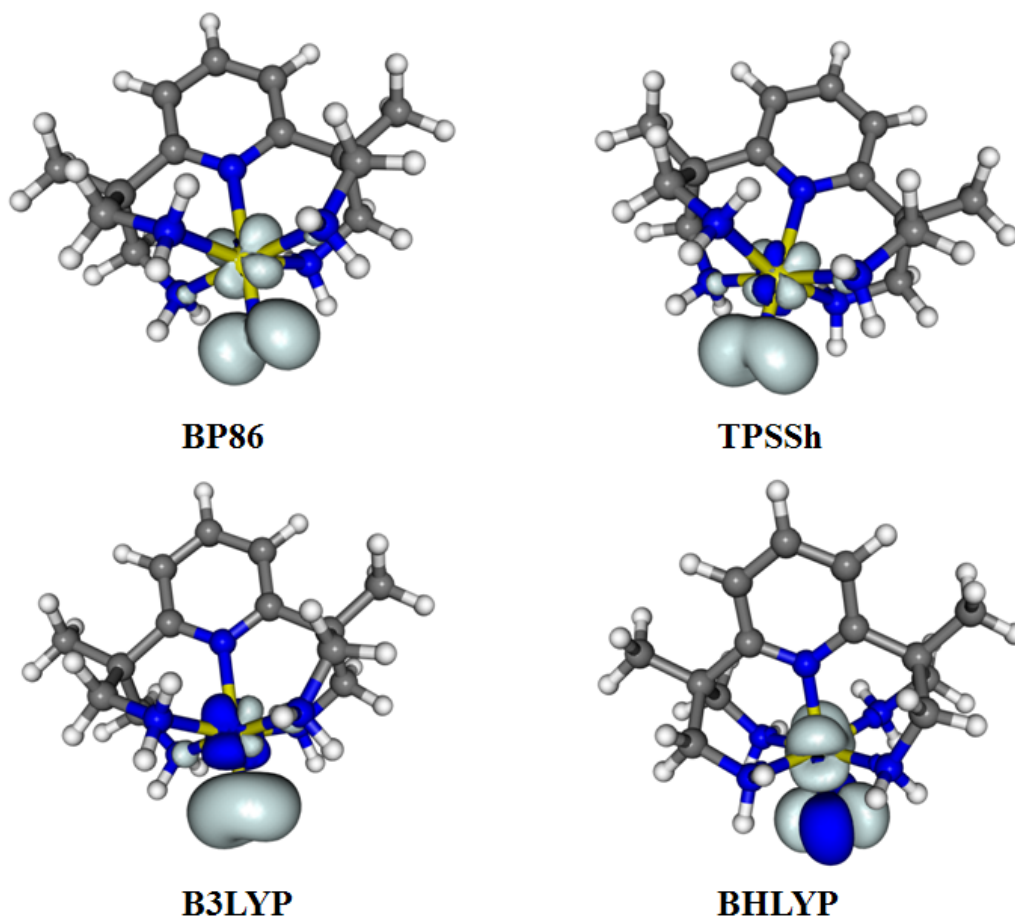


Figure 3.22: Isosurface plots of the spin density ( $\pm 0.005$  a.u.) of the formal iron(V)-nitrido species for different functionals ( $S = 1/2$ ). A def2-TZVP basis set was used for all atoms.

The high amount of spin at nitrogen points to an iron(IV)-nitridyl radical, instead of an iron(V)-nitrido complex. This is made especially clear when we compare the spin population of this complex to the iron(V)-oxo compound  $[\text{Fe}(\text{O})(\text{TAML})]^-$ , where we only find 0.2 a.u. spin density at oxygen (see Chapter 3.2) and the rest localized at iron, as we would expect in a low-spin iron(V) complex with  $d^3$  configuration.

Another way to reduce spin contamination is to reduce the amount of exact exchange in the functional. Avoiding high amounts of exact-exchange admixture by using TPSSh (which has only 10% exact-exchange admixture) gives very good results for the iron-nitrido stretching frequency (see Table 3.18), a clear preference for the low-spin doublet ground state, and a spin distribution very similar to the ROBHLYP result. Thus, functionals with low amounts of exact-exchange admixture can be recommended as an alter-

native to ROKS calculations for systems that are very sensitive to exact exchange, and are likely to converge into wrong broken-symmetry solutions due to spin contamination. We note in passing, that neither this possibility nor the use of ROKS calculations would solve the spin-contamination/spin-polarization dilemma, if we would be interested in the metal hyperfine coupling [120]. Thus, other electronic-structure methods are clearly needed in this field.

### 3.5.4 Conclusions

The difficulties in vibrational frequency calculations with B3LYP, PBE0, and BHLYP for the title iron(V)-nitrido complex arose from their high amount of exact-exchange admixture, which caused a dramatic increase of the spin polarization in the iron(V)-nitrido species, compared to the results for GGA functionals. This change in the electronic structure of the complex led to high spin contamination, which in turn resulted in unphysical broken-symmetry solutions for the three hybrid functionals. High levels of spin contamination and wrong spin density distributions over iron and the nitrido ligand led to wrong frequencies, and in the case of BHLYP to a dramatically overestimated iron-nitrido bond length, presumably because of increased mixing with low-lying excited quartet states in the presence of large exact-exchange admixture. GGA functionals did not show those problems and gave acceptable relative errors for the frequency between 5.5 and 8.5%. In order to obtain more accurate stretching frequencies, two solutions were successfully tried: (i) using ROKS calculations to avoid spin contamination and broken-symmetry solutions, and (ii) using hybrid functionals with low amount of exact-exchange admixture like TPSSh, to reduce the levels of spin polarization and contamination in the complex. In both cases high amounts of spin density were detected at nitrogen, pointing more to an iron(IV)-nitridyl radical than to the formal description as an iron(V)-nitrido complex.

## 4 Reactions in Aqueous Solution modeled by D-COSMO-RS

As most of the technically important chemical reactions are carried out in some kind of solution environment, the quantum-chemical modeling of reactions in solution is of utmost importance in many fields. The bulk solvent effects of aprotic solvents are often most conveniently included into quantum-chemical studies by polarizable dielectric continuum models. In the absence of more specific solute-solvent interactions, these models frequently provide a reasonable description, and they have thus become the workhorse solvent models for routine applications [219]. Successful examples are the family of PCM [220, 221] models or COSMO [91] (conductor-like screening model), available in the TURBOMOLE package used in the present work.

When specific solvation effects are important, the description becomes more difficult. This holds in particular for hydrogen bonding in protic solvents like alcohols or water, which are of appreciable practical importance. Then the most accurate description is typically obtained from an explicit modeling of the solvent molecules, either in cluster models or using periodic boundary conditions. The solvent molecules may be included either quantum-chemically, which is the most accurate but also computationally most demanding approach, or by using some type of classical force field, in a QM/MM treatment. While static cluster models may to some extent capture the strongest strong solute-solvent interactions, in the majority of cases, a realistic description of the dynamical nature of the interactions requires molecular-dynamics or Monte Carlo-type simulations. While these are well-known to provide very powerful tools, it is clear that their application to chemical problems is computationally much more demanding than that of the continuum models described above.

For routine, cost-efficient applications it is thus desirable to realistically include hydrogen-bonding interactions into solvent models at essentially the cost of a continuum solvent model, that is, without the computational effort of an explicit molecular-dynamics treat-

ment. An interesting implicit solvent model that goes beyond a polarizable continuum description with almost no extra cost is Klamt's COSMO-RS approach [92,221] (COSMO for real solvents). COSMO-RS has now been used successfully for almost two decades in an a posteriori mode, where a quantum-chemical calculation with COSMO provides the required surface charge-density distributions ( $\sigma$ -profiles) from which the statistical-thermodynamics ansatz of COSMO-RS constructs effective solvent chemical potentials ( $\sigma$ -potentials) that provide important insight into fluid-phase thermodynamics, but also into solvation free energies. Most importantly, COSMO-RS includes hydrogen-bonding terms parametrized into the  $\sigma$ -potential. More recently, the Direct-COSMO-RS approach (in the following D-COSMO-RS) has been implemented, where the  $\sigma$ -potentials are inserted selfconsistently into quantum-chemical calculations, providing for the first time a refined implicit environment of COSMO-RS quality to wave function or density-matrix optimization. Importantly, this includes molecular gradients and properties, thus allowing the influence of protic solvents on structures, energetics, and properties to be probed self-consistently. The first example of such D-COSMO-RS calculations were computations of electronic g-tensors by Klamt, Neese, and co-workers [93] using the implementation in the ORCA program package. More recently, Kaupp and coworkers have used the TURBOMOLE implementation of D-COSMO-RS to demonstrate how internal electron-transfer reactions of organic mixed-valence systems may be treated [96]. Importantly, D-COSMO-RS was able to faithfully describe the differences between aprotic and protic (alcohol) solvents for the localized/delocalized nature and electron-transfer barriers of mixed-valent radical anions, including the first treatment of solvent mixtures. To establish D-COSMO-RS as a general tool for studies in protic solvents, it is important to establish that the good performance of D-COSMO-RS persists also in other fields of application. Two different and new fields of application for D-COSMO-RS are investigated in this work: Diels-Alder reactions in aqueous solution and the effect of an aqueous solvent environment on the stability of gold(III) halides.

## 4.1 Validation of the Direct-COSMO-RS Solvent Model for Diels-Alder Reactions in Aqueous Solution

### 4.1.1 Introduction

The contents of this chapter have been published in "Validation of the Direct-COSMO-RS Solvent Model for Diels-Alder Reactions in Aqueous Solution" by K. Theilacker, D. Buhrke, M. Kaupp, *J. Chem. Theory Comput.* **2014**, *11*, 111.

In this chapter we extend the validation of D-COSMO-RS to Diels-Alder reactions in aqueous solution. We compare D-COSMO-RS results to gas-phase and COSMO data, as well as to an explicit inclusion of solvent molecules in cluster models (in part embedded in an implicit solvent). These comparisons are made to a large extent at the DFT level, using the PBE0 functional [14,31,117] and Grimme's D3 dispersion corrections [41]. This level is found to reproduce post-Hartree-Fock energetics in the gas phase much more faithfully than other functionals tested. The setup of this chapter is thus as follows: after the Computational Details section, we first describe the comparison of various computational levels and basis sets for two prototypical Diels-Alder gas-phase reactions, namely those of methyl-vinyl-ketone (MVK) and 1,4-naphthoquinone (NQ), respectively, with cyclopentadiene (CP), compare Figure 4.1. On the basis of the outcome of the gas-phase evaluations, we subsequently use the PBE0 and PBE0-D3 levels to evaluate various approaches to include solvent effects for the same two reactions.

### 4.1.2 Computational Details

All calculations have been performed with the TURBOMOLE6.3 package [111–113], using def2-TZVP basis sets [114] in the DFT calculations and Dunning correlation-consistent aug-ccpVXZ-type ( $X = D, T, Q, 5$ ) basis sets [222, 223] for the ab initio single-point calculations. The density functionals B3LYP [15, 23], PBE0 [14, 31, 117], and BP86 [12, 13] were considered, using the resolution-of-the-identity approximation for the latter (RI-BP86). Dispersion contributions for the DFT calculations were evaluated using Grimme's DFT-D3 atom-pairwise dispersion corrections for these three functionals [41].

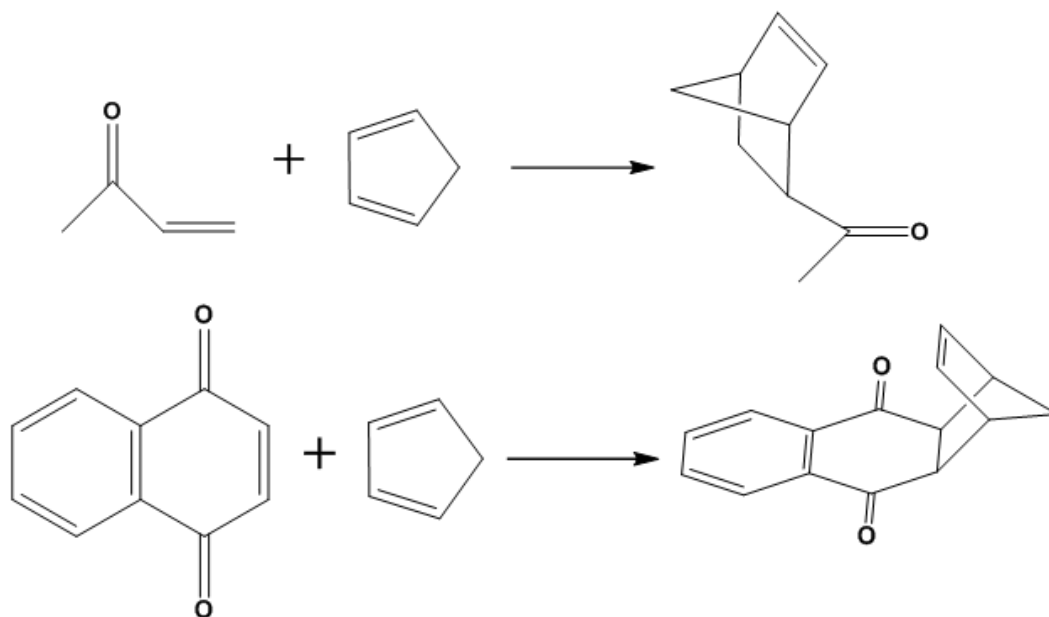


Figure 4.1: The two Diels-Alder reactions discussed in this work. Top MVK+CP reaction, bottom NQ+CP reaction.

Validation of the DFT functionals in the gas phase was done against single-point ab initio wave function calculations at the PBE0-D3 gas-phase structures (use of structures optimized at other levels led to only minor changes, see below). For HF, MP2, and spin-component-scaled (SCS) MP2 calculations [224], complete-basis-set extrapolations (CBS) [225] were done with a two-point extrapolation from aug-cc-pVXZ ( $X = Q, 5$ ) results. CCSD and CCSD(T) calculations were possible only up to the aug-cc-pVTZ basis-set level.

Solvent effects were taken into account in the DFT calculations at different levels: the COSMO (conductor-like screening-model [91]) approach represents a polarizable continuum model. The following solvents have been used, with their respective dielectric constants  $\epsilon$ : water ( $\epsilon = 78.3553$ ), hexane ( $\epsilon = 1.8819$ ), acetonitrile ( $\epsilon = 35.688$ ), and methanol ( $\epsilon = 32.613$ ). The main attention pertains to the self-consistent D-COSMO-RS ansatz. The required  $\sigma$ -potentials have been created with the COSMOtherm program [226] at BP86/TZVP level for 298 K. For comparison, we have also included explicit water molecules, either in gas-phase cluster models or embedded in the COSMO or D-COSMO-RS solvent environments.

All fully optimized minima and transition states have been verified by harmonic vibrational frequency analyses. It was verified that the imaginary frequency of a given

transition state pertains to the reaction at hand. In the COSMO and D-COSMO-RS solvent environments, the frequency calculations had to be done by numerical differentiation of analytical gradients (using the numforce module of TURBOMOLE6.3, while aoforce was employed in the gas-phase calculations). Numerical problems of the solvent cavity models occasionally produced small extra imaginary frequencies in the frequency analyses for some calculations where explicit H<sub>2</sub>O solvent molecules were embedded in COSMO or D-COSMO-RS for the NQ+CP system (the spurious imaginary frequencies pertained to soft H<sub>2</sub>O solvent modes). This gave rise to inaccuracies in the computed entropic contributions (see below).

While the comparison of gas-phase barriers and thermochemistry will focus on the pure electronic contributions to validate the electronic-structure methods, mainly the Gibbs free energies will be compared in solvent environments. This is preferable because (a) the separation into enthalpic and entropic contributions of the solvent contributions is not very well-defined (separate contributions provided pertain essentially to internal degrees of freedom), (b) mostly free energies are available from experiment, and (c) we may better compare our results to those of previous molecular dynamics studies. The entropies and enthalpies at 298 K were evaluated based on the output of harmonic vibrational frequency analyses at the indicated levels. In those few cases, where spurious imaginary frequencies in the vibrational calculations made the entropies unreliable for the NQ + CP reaction (see above), these were estimated from results for more successful, closely similar calculations. Finally I note, that for both reactions I exclusively concentrated on the endo addition mode that has previously been identified as the lowest-energy pathway, and on the s-cis conformation of MVK. Self-consistent COSMO and D-COSMO-RS surface charge densities have been plotted using the COSMOTerm software [226].

## 4.1.3 Results and Discussion

### 4.1.3.1 Validation of Density Functionals against Wave-Function Methods in the Gas Phase

As preliminary calculations revealed a very large sensitivity of activation barriers and reaction energies of the two title reactions to the density functional used, the preferred DFT approach was first selected by benchmarking against gas-phase energies obtained using various post-Hartree-Fock approaches. Table 4.1 shows, first of all, an extremely large influence of electron correlation on both activation barriers and reaction energies,

as exemplified by the differences between the post-HF and HF results. While the computational effort of coupled-cluster calculations prevented CC calculations for the NQ + CP reaction, as well as reliable extrapolation to the complete basis-set limit at the CC level for the MVK + CP reaction, MP2, and SCS-MP2 allowed us to obtain energies up to aug-cc-pV5Z basis sets for both reactions, providing an accurate CBS extrapolation (results for further individual basis-set levels are given in Table S1 in Appendix II). Thus the CBS-limit coupled-cluster energies for the MVK reaction may be estimated by assuming, that the basis-set corrections from the MP2 or SCS-MP2 calculations carry over to the CC levels. Most notably, however, the SCS-MP2 and CCSD(T) energies with the aug-cc-pVTZ basis set are rather close to each other (even closer for the reaction energy than for the barrier). This suggests the direct use of the SCS-MP2/CBS data as a good estimate also for the so far unavailable CCSD(T)/CBS data. This confirms earlier validation work on SCS-MP2 for a number of related pericyclic reactions, where SCS-MP2 with extended basis sets agreed excellently with G3 or CBS-QB3 levels of theory [227]. Increasing the basis set beyond the aug-cc-pVTZ level renders both the activation barriers and the reaction energies higher by about 15-20 kJ mol<sup>-1</sup>. This suggests that the aug-cc-pVTZ basis does still cause notable basis-set superposition errors (BSSE) for the transition states and products of the two title reactions. It appears that BSSE is already small at the aug-cc-pVQZ basis level. Basis-set effects and differences between various computational levels for the NQ + CP reaction are roughly comparable to the results for the MVK + CP reaction, albeit the differences between aug-cc-pVTZ and CBS values are somewhat larger, closer to about 25 kJ mol<sup>-1</sup>. It will be assumed in the following that the SCS-MP2/CBS data provide a good estimate of CCSD(T)/CBS quality energetics also for the NQ + CP reaction. As found earlier [227], the SCS-MP2/CBS energies are a significant improvement over standard MP2 results, in particular for the activation barriers, where MP2 provides even negative values. The effects of triple excitations in the coupledcluster data for the MVK + CP reaction are small (ca. -3 kJ mo<sup>-1</sup>) for the reaction energy but notable (ca. -27 kJ mol<sup>-1</sup>) for the barrier, consistent with a significant importance of nondynamical correlation effects at the transition state (these are also apparent from the poor performance of MP2 for the barriers).

Having thus obtained reasonable benchmark energies for the two title gas-phase reactions, we turn now to an evaluation of DFT results. The dependence on the functional, as well as on the D3 dispersion corrections, is striking for both the activation barriers and the reaction energies. While this may seem unusual given the, at first sight,

Table 4.1: Comparison of DFT and wave-function results for gas-phase activation barriers,  $\Delta E^\ddagger$ , and reaction energies,  $\Delta E^\ddagger$ , in kJ mol<sup>-1</sup> for Diels-Alder reactions with cyclopentadiene<sup>a</sup>

Method and basis set	MVK+CP		NQ+CP	
	$\Delta E^\ddagger$	$\Delta E$	$\Delta E^\ddagger$	$\Delta E$
HF/CBS <sup>b</sup>	162.4	-52.5	167.1	-31.5
MP2/aug-cc-pVTZ	-24.9	-172.8	-57.2	-166.5
MP2/CBS <sup>b</sup>	-6.3	-160.2	-33.2	-150.0
SCS-MP2/aug-cc-pVTZ	13.1	-154.2	-12.2	-145.6
SCS-MP2/CBS <sup>b</sup>	33.5	-141.2	13.7	-128.8
CCSD/aug-cc-pVTZ	46.6	-149.1	-	-
CCSD(T)/aug-cc-pVTZ	19.5	-152.3	-	-
PBE0/def2-TZVP	46.9	-115.9	46.7	-92.7
PBE0-D3/def2-TZVP	27.4	-132.6	20.1	-114.5
B3LYP/def2-TZVP	78.1	-49.5	85.8	-24.5
B3LYP-D3/def2-TZVP	48.4	-75.6	46.5	-57.8
RIBP86/def2-TZVP	45.6	-71.1	52.3	-44.7
RIBP86-D3/def2-TZVP	10.6	-101.5	5.8	-83.9

<sup>a</sup>PBE0-D3/def2-TZVP gas-phase structures were used for the single-point wave-function calculations. Fully optimized DFT/def2-TZVP and DFT-D3/def2-TZVP gas-phase results are shown for comparison.

<sup>b</sup>Complete basis-set estimates for HF, MP2, and SCS-MP2 from two-point extrapolations of aug-cc-pVQZ and aug-cc-pV5Z data (see Table S1 in Appendix for complete data).

simple symmetry-allowed DA-reactions chosen for the present study, the observation is well in line with previous findings. This holds in particular for the extremely poor performance of the B3LYP functional, which has been noted also for related pericyclic reactions, including DA reactions [224, 227]. For example, the DARC subset [228, 229] of Grimme’s large GMTKN30 test set database [230] deals specifically with Diels-Alder reaction energies. It was found that even the local density approximation (SVWN functional) outperforms B3LYP (with mean absolute errors of 49.4 kJ mol<sup>-1</sup> for SVWN and 64.5 kJ mol<sup>-1</sup> for B3LYP, using def2-QZVP basis sets). While dispersion corrections reduce both barriers and reaction energies (Table 4.1) and thus improve agreement with the benchmark data, the B3LYP-D3 barriers are still overestimated by about 10-15 kJ mol<sup>-1</sup> and, more notably, the reaction energies are too large by about 55-60 kJ mol<sup>-1</sup>. This is likely related to the poor description of medium-range correlation effects by the B3LYP functional, which has been noted also for other organic reaction energies, for ex-

ample, for rearrangements of hydrocarbons [231] or protobranching ratios [232,233] (the transition-state energies may actually benefit from some error compensation between different types of deficiencies for correlation effects). Notably, in the bimolecular reactions studied here, the errors are likely larger in the transition states and particularly in the products than in the separated reactants (including the dispersion contributions). The B3LYP hybrid functional overestimates the barriers and particularly underestimates the exothermicity of the two reactions. The “pure” gradient-corrected BP86 functional performs significantly better for the reaction energies than B3LYP: after inclusion of dispersion corrections, it seems that this functional underestimates the reaction energies by about 30 kJ mol<sup>-1</sup> (the barriers are underestimated by about 20-25 kJ mol<sup>-1</sup>). Overall, dispersion corrections reduce both activation barriers and reaction energies for all three functionals. While this generally improves the reaction energies, the barriers are in some cases deteriorated, in particular for BP86.

Compared to the benchmark data, the PBE0 functional provides the by far best reaction energies of the three functionals studied and, after inclusion of dispersion corrections, also excellent barriers. PBE0-D3 dispersion corrections are somewhat smaller than those for the other two functionals, likely reflecting a somewhat more attractive exchange-correlation potential provided by PBE0 itself. Its good agreement with the SCS-MP2/CBS and estimated CCSD(T)/CBS data makes the PBE0-D3 approach clearly suitable for the subsequent examination of solvent effects (possibly with errors in the barriers of up to about 10 kJ mol<sup>-1</sup> and slightly larger deviations for the reaction energies; Table 4.1). This is in line with the much better performance of PBE0-D3 compared to B3LYP or B3LYP-D3 for the DARC Diels-Alder reaction energy and BH-PERI [97, 234–237] pericyclic reaction barrier test sets (previous B3LYP results with smaller basis sets sometimes gave the right answer for the wrong reason; see also Table S2 in Appendix II for some PBE0 results with smaller basis sets and Tables S3 and S4 in Appendix II for comparisons of the three functionals with solvent models). While other functionals have been identified previously to also provide reasonable barriers and thermochemistry of DA reactions [229], the PBE0-D3 approach has the advantage of being available in the TURBOMOLE6.3 program package that was used to evaluate the performance of COSMO and D-COSMO-RS solvent models (see below). Use of different structures for the post-HF single-point calculations does not appreciably alter the benchmark energetics nor the conclusions on the performance of DFT functionals (see Table S5 in Appendix II).

Our evaluations so far have concentrated on the energetics. We note that dispersion corrections alter the structures of reactants, transition states and products relatively little. At PBE0-D3 level, changes in the important interatomic distances of the transition states because of dispersion (i.e., compared to PBE0) were less than 1% (see Figure 4.2 for the bond lengths in question). A slight reduction of the longer distance  $d_2$  in the highly unsymmetrical transition state of the MVK + CP reaction by 2.1 pm was the largest structural change observed.

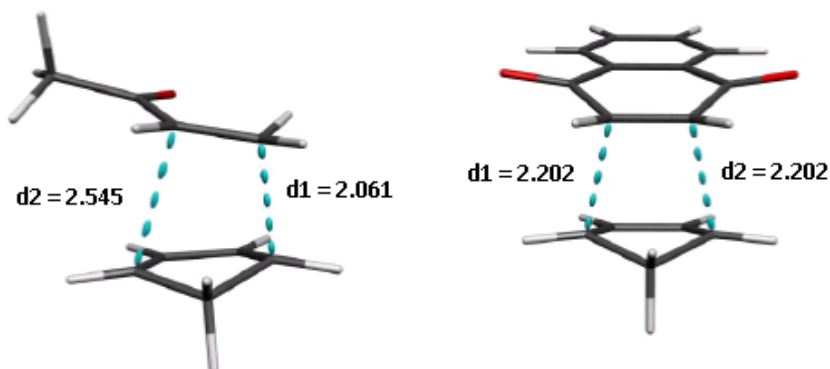


Figure 4.2: Definition of important interatomic distances of the transition states for the MVK + CP and NQ + CP reactions. PBE0-D3/def2-TZVP optimized distances in Å.

#### 4.1.3.2 Modeling (Aqueous) Solvent Effects

The nature of the solvent may have a large impact on the kinetics (and partly the thermochemistry) of Diels-Alder cycloadditions. It is well known that protic solvents like water and alcohols may lower reaction barriers by forming hydrogen bonds with polar groups [238–240]. For the two DA reactions studied here, these are largely the ketone/quinone oxygen atoms of MVK and 1-4-naphthoquinone, respectively. The hydrogen bonds are known to polarize the C=O bonds, which in turn affects the MO coefficients also throughout the entire dienophile and thereby stabilizes the transition state [241–243]. The concentration of this work will be on the solvent water. It is important in its own right, it is the most polar solvent used here ( $\epsilon = 78.3553$ ), and it is moreover expected to exhibit maximal effects of hydrogen bonding. Here, in addition to COSMO and D-COSMO-RS, the explicit inclusion of two water molecules hydrogen-bonded to a given ketone oxygen atom (i.e., overall two molecules for the MVK reaction and four molecules for the naphthoquinone reaction; see Figure 4.3) will also be evaluated

in static cluster models. Additionally, for COSMO and D-COSMO-RS, also methanol ( $\epsilon = 32.613$ ) as another protic solvent will be evaluated, as well as acetonitrile as polar aprotic solvent of similar dielectric constant ( $\epsilon = 35.688$ ), and hexane as apolar aprotic solvent ( $\epsilon = 1.8819$ ).

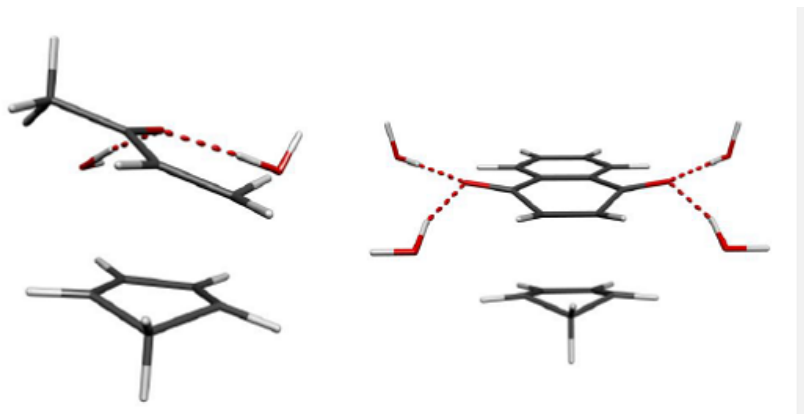


Figure 4.3: Transition states of the reactions of MVK and 1-4-naphthoquinone, respectively, with cyclopentadiene, including additional water molecules. PBE0-D3/def2-TZVP optimized structures.

**Thermochemical Considerations.** Tables 4.2 and 4.3 summarize energies and Gibbs free energies of activation and reaction for the two title reactions, at various levels of treating the solvent effects. Dispersion effects turned out to substantially influence the energetics of the gas-phase reaction (see above). The two tables thus include data both with and without dispersion corrections in solution. Because of the partial inclusion of dispersion between solute and solvent in the implicit solvent models (COSMO and D-COSMO-RS), it is of interest to first evaluate explicit (D3) dispersion effects on the energetics in the different environments to be able to decide which data are to be preferred in the analysis. Starting with the MVK + CP reaction (Table 4.2), the reduction due to dispersion (D3) of  $\Delta E^\ddagger$  by 19.5 kJ mol<sup>-1</sup> and of  $\Delta E$  by 16.7 kJ mol<sup>-1</sup> in the gas phase is affected almost negligibly for a COSMO treatment of the aprotic solvents hexane and acetonitrile, as well as for the D-COSMO-RS treatment of all solvents except water. COSMO-water reduces the dispersion contributions slightly to -15.4 and -13.0 kJ mol<sup>-1</sup>, respectively. COSMO-methanol gives -15.4 and -17.0 kJ mol<sup>-1</sup>, respectively. D-COSMO-RS-water leaves the overall smallest D3 contributions of -14.0 and -13.3 kJ mol<sup>-1</sup>, respectively. That is, in the absence of explicit solvent molecules, the maximum effect of the implicit solvent (in this case D-COSMO-RS-water) on the D3 contributions is -5.5 kJ mol<sup>-1</sup> for  $\Delta E^\ddagger$  and -3.5 kJ mol<sup>-1</sup> for  $\Delta E$ , compared to the gas-

phase dispersion contributions. This corresponds to almost additive behavior between D3 corrections and implicit solvent models. In contrast, the presence of two explicit water molecules enhances the D3 contributions to  $-26.6$  and  $-20.0$   $\text{kJ mol}^{-1}$ , respectively, in the gas phase. This is modified to  $-24.3$   $\text{kJ mol}^{-1}$  and  $-24.1$   $\text{kJ mol}^{-1}$ , respectively, for COSMOwater+2H<sub>2</sub>O and to  $-23.5$  and  $-19.2$   $\text{kJ mol}^{-1}$ , respectively, for D-COSMO-RS-water+2H<sub>2</sub>O. An even clearer trend emerges for the 1,4-naphthoquinone + cyclopentadiene reaction (Table 4.3): in the gas phase and in any implicit solvent model (for any of the solvents studied), D3 corrections to  $\Delta E^\ddagger$  are between  $-26.5$  and  $-27.3$   $\text{kJ mol}^{-1}$ , and those to  $\Delta E$  remain also almost constant between  $-21.8$   $\text{kJ mol}^{-1}$  and  $-22.6$   $\text{kJ mol}^{-1}$ . In contrast, inclusion of four explicit water molecules enhances the D3 contributions to  $\Delta E^\ddagger$  to about  $-33$   $\text{kJ/mol}$  and those to  $\Delta E$  to between  $-26$  and  $-28$   $\text{kJ mol}^{-1}$ . It is thus clear that the explicit dispersion corrections to both energies become more negative for both reactions, when explicit water molecules are present, whereas differences between the various implicit solvent treatments remain small. This has to be kept in mind when evaluating the solvent effects computed with explicit vs implicit solvent modeling.

As discussed above, computed entropic contributions to the Gibbs free activation and reaction energies arise only from internal degrees of freedom, whereas the experimental estimates contain to some degree solvent contributions as well. We should therefore not attempt to directly compare the entropy contributions (and thus the exclusively enthalpic contributions) with experiment. Yet we may compare the different models. Starting with the entropic contributions to  $\Delta G_{298K}^\ddagger$  of the MVK + CP reaction (difference between  $\Delta G_{298K}^\ddagger$  and  $\Delta H_{298K}^\ddagger$ ), we see in Table 4.2 that the implicit solvent model data vary only between  $+51$  and  $+58$   $\text{kJ mol}^{-1}$ . Dispersion contributions influence these values by less than  $5$   $\text{kJ mol}^{-1}$ . Addition of explicit water molecules in cluster models increases the entropic contributions only slightly. In fact the variations found are probably within the numerical noise caused by numerical differentiation of analytical gradients in the vibrational analyses. The entropic contributions to the Gibbs free reaction energies ( $\Delta G_{298K}$ ) vary over an even narrower range, from  $+59$  to  $+63$   $\text{kJ mol}^{-1}$  (Table 4.2). These values are close to the activation entropy contributions, in keeping with a late transition state of a bimolecular reaction, where the new bonds have already been formed to a great extent. Turning to the NQ + CP reaction, results are very similar, with computed entropic activation contributions between  $+58$  and  $+64$   $\text{kJ mol}^{-1}$  and contributions to the reaction energies between  $+60$  and  $+67$   $\text{kJ mol}^{-1}$ . Here three models with embedded water molecules gave spurious imaginary H<sub>2</sub>O vibrational frequencies (see Computational Details and Table 4.3). Thus, the corresponding entropic

Table 4.2: Calculated activation and reaction energies, enthalpies and Gibbs free energies (in  $\text{kJ mol}^{-1}$ ) for the MVK+CP Diels-Alder reaction in different environments<sup>a</sup>

	$\Delta E^\ddagger$	$\Delta H_{298K}^\ddagger$	$\Delta G_{298K}^\ddagger$	$\Delta E$	$\Delta H_{298K}$	$\Delta G_{298K}$
gas phase	46.9	47.6	100.3	-115.8	-104.0	-44.7
gas phase+D3	27.4	32.2	89.2	-132.6	-116.9	-54.8
gas phase+2H <sub>2</sub> O	27.0	31.1	94.2	-116.1	-101.6	-40.0
gas phase+2H <sub>2</sub> O+D3	0.4	6.0	70.9	-136.1	-120.3	-57.6
COSMO-water	44.3	46.9	101.2	-109.9	-96.6	-37.2
COSMO-water+D3	28.9	34.1	91.4	-122.9	-107.1	-44.6
D-COSMO-RS-water	29.4	31.7	85.8	-115.4	-102.1	-42.9
D-COSMO-RS-water+D3	15.4	18.8	70.2	-128.7	-114.3	-54.7
COSMO-water+2H <sub>2</sub> O	38.3	42.5	98.8	-105.2	-90.4	-28.6
COSMO-water+2H <sub>2</sub> O+D3	14.0	19.6	79.6	-129.3	-112.6	-39.9
D-COSMO-RS-water+2H <sub>2</sub> O	30.4	37.1	94.5	-110.0	-91.6	-31.9
D-COSMO-RS-water+2H <sub>2</sub> O+D3	6.9	14.3	70.7	-129.2	-113.3	-44.5
<b>Exp. (water)</b>		<b>39.4<sup>b</sup></b>	<b>80.4</b>			
COSMO-methanol	44.4	47.0	100.9	-110.2	-96.9	-37.4
COSMO-methanol+D3	25.0	27.9	82.5	-127.2	-113.7	-53.8
D-COSMO-RS-methanol	39.9	42.7	97.8	-109.4	-95.8	-35.7
D-COSMO-RS-methanol+D3	20.3	23.2	78.6	-126.3	-112.6	-52.4
<b>Exp. (1-propanol (ethanol))</b>		<b>45.1<sup>b</sup></b>	<b>90.3</b>			
			<b>(90.5)</b>			
COSMO-acetonitrile	44.4	47.0	101.0	-110.1	-96.9	-37.5
COSMO-acetonitrile+D3	24.9	27.8	82.8	-127.2	-113.6	-53.8
D-COSMO-RS-acetonitrile	49.5	52.0	105.5	-106.5	-93.0	-33.8
D-COSMO-RS-acetonitrile+D3	30.1	32.9	86.7	-123.5	-109.8	-49.5
<b>Exp. (acetonitrile)</b>			<b>94.4</b>			
COSMO-hexane	48.0	50.9	104.3	-112.4	-98.6	-39.1
COSMO-hexane+D3	28.6	31.8	85.7	-129.2	-115.2	-55.9
D-COSMO-RS-hexane	55.5	58.4	111.5	-103.2	-89.5	-29.9
D-COSMO-RS-hexane+D3	36.2	39.4	92.9	-119.9	-106.1	-46.8

<sup>a</sup>PBE0/def2-TZVP results with and without D3 dispersion corrections. See Computational Details for evaluation of enthalpies and Gibbs free energies. Experimental data from ref. [238, 239]

<sup>b</sup>From pseudothermodynamic analysis.

Table 4.3: Calculated activation and reaction energies, enthalpies and Gibbs free energies (in kJ mol<sup>-1</sup>) for the NQ+CP Diels-Alder reaction in different environments<sup>a</sup>

	$\Delta E^\ddagger$	$\Delta H_{298K}^\ddagger$	$\Delta G_{298K}^\ddagger$	$\Delta E$	$\Delta H_{298K}$	$\Delta G_{298K}$
gas phase	46.7	49.7	108.5	-92.7	-79.7	-19.3
gas phase+D3	20.1	24.5	84.2	-114.5	-100.1	-38.8
gas phase+4H <sub>2</sub> O	17.8	21.6	85.4	-100.2	-86.7	-23.6
gas phase+4H <sub>2</sub> O+D3	-15.7	-10.6	53.3	-128.1	-112.9	-46.0
COSMO-water	42.2	45.3	103.9	-86.1	-73.1	-12.4
COSMO-water+D3	15.5	20.0	79.6	-108.5	-94.1	-32.3
D-COSMO-RS-water	25.4	28.6	86.9	-95.5	-82.4	-21.2
D-COSMO-RS-water+D3	-1.9	1.5	60.4	-118.1	-104.6	-42.8
COSMO-water+4H <sub>2</sub> O	32.5	(34.0 <sup>c</sup> )	(98.0 <sup>c</sup> )	-92.0	(-78.0 <sup>c</sup> )	(-14.0 <sup>c</sup> )
COSMO-water+4H <sub>2</sub> O+D3	0.3	2.0	65.6	-118.2	-103.4	-39.8
D-COSMO-RS-water+4H <sub>2</sub> O	29.1	(30.5 <sup>c</sup> )	(94.5 <sup>c</sup> )	-94.2	(-80.0 <sup>c</sup> )	(-16.0 <sup>c</sup> )
D-COSMO-RS-water+4H <sub>2</sub> O+D3	-3.3	(-1.5 <sup>c</sup> )	(62.5 <sup>c</sup> )	-120.4	(-105.5 <sup>c</sup> )	(-41.5 <sup>c</sup> )
<b>Exp. (water)</b>		<b>36.6<sup>b</sup></b>	<b>69.4</b>			
COSMO-methanol	42.5	45.6	104.2	-86.3	-73.2	-12.6
COSMO-methanol+D3	15.8	18.9	77.7	-108.7	-95.3	-33.6
D-COSMO-RS-methanol	43.1	45.4	103.5	-83.7	-70.9	-10.4
D-COSMO-RS-methanol+D3	16.3	19.0	78.0	-106.0	-92.9	-31.5
<b>Exp. (1-propanol)</b>		<b>42.9<sup>b</sup></b>	<b>83.1</b>			
COSMO-acetonitrile	42.4	45.6	104.2	-86.3	-73.2	-12.5
COSMO-acetonitrile+D3	15.8	19.2	78.5	-108.7	-95.2	-33.7
D-COSMO-RS-acetonitrile	49.2	52.1	110.7	-80.2	-67.2	-6.6
D-COSMO-RS-acetonitrile+D3	22.6	25.8	84.8	-102.5	-89.2	-28.3
<b>Exp. (acetonitrile)</b>			<b>86.2</b>			
COSMO-hexane	45.8	48.9	107.6	-90.3	-77.2	-16.0
COSMO-hexane+D3	19.2	22.6	81.8	-112.3	-99.0	-38.2
D-COSMO-RS-hexane	54.0	57.1	115.5	-81.0	-68.1	-7.1
D-COSMO-RS-hexane+D3	27.5	31.0	90.3	-103.0	-89.7	-28.6
<b>Exp. (hexane)</b>			<b>90.4</b>			

<sup>a</sup>PBE0/def2-TZVP results with and without D3 dispersion corrections. See Computational Details for evaluation of enthalpies and Gibbs free energies. Experimental data from ref. [238]

<sup>b</sup>From pseudothermodynamic analysis.

<sup>c</sup>Due to spurious imaginary frequencies, the entropic and thermal contributions were estimated by analogy to closely related calculations.

and thermal contributions are only estimates (albeit reasonable ones).

With these considerations in mind, we compare now the performance of the different solvent models overall. Our main focus is on the effect of aqueous solvent, and we thus start our discussion with the pertinent data. When trying to establish a benchmark level for aqueous solvent effects on the energetics, against which D-COSMO-RS-water may be compared, we note that addition of explicit hydrogen-bonded water molecules in the gas phase is expected to overestimate the overall solvent effects, as the added H<sub>2</sub>O molecules lack an embedding into the bulk. Indeed, embedding the explicitly solvated cluster models into a COSMO-water environment reduces the overall effects on both  $\Delta E^\ddagger$  and  $\Delta E$  (and thus on  $\Delta G_{298K}^\ddagger$  and on  $\Delta G_{298K}$ ) compared to the clusters in vacuum (Tables 4.2 and 4.3). These embedded clusters appear a reasonable starting point for the evaluation of D-COSMO-RS-water, keeping in mind the abovementioned differences in the D3 dispersion for explicit vs implicit solvation.

However, we have to account for the fact that semiempirical QM/MM molecular dynamics simulations on both reactions by Acevedo and Jorgensen [244] provided solute-solvent radial distribution functions more consistent with an average of three hydrogen bonds per keto oxygen atom, in particular for the transition state, and more pronouncedly so for the MVK + CP than for the NQ + CP reaction. While the quantitative accuracy of the QM/MM simulations is limited by the semiempirical PDDG/PM3 method used for the QM part (e.g., the method underestimates significantly the transition state asymmetry for the gas-phase MVK + CP reaction compared to CBS-QB3 data, and free activation energies tend to be overestimated by up to 65 kJ mol<sup>-1</sup> [244]), qualitatively the increase of hydrogen bonding interactions at the transition state is convincing. We have thus attempted to also optimize static cluster models with three water molecules for MVK and with six water molecules for NQ. However, these optimizations did not lead to usable minima or transition states. In case of the NQ + CP reaction, during optimization the third water molecule generally dissociated from the quinone oxygen atom and formed hydrogen bonds with one of the other water molecules present. For the transition state of the MVK + CP reaction, structures with three water molecules hydrogen-bonded to the keto oxygen atom could indeed be obtained. However, these structures nevertheless revealed hydrogen bonds between the water molecules. This suggests that the energetics obtained with these structures would not faithfully represent the average situation in aqueous solution, where the most unstrained hydrogen bonds likely are with further surrounding water molecules. It appears likely, nevertheless, that

the true average situation in aqueous solution would be somewhere between 2 and 3 hydrogen bonds per keto oxygen atom at the transition states, with the MVK-CP systems favoring stronger interactions than the NQ + CP system.

We first compare directly the D-COSMO-RS results with experiment, focusing on Gibbs free energies rather than enthalpies, due to the abovementioned difficulties of separating the solvent entropic from enthalpic contributions for implicit solvent models. In case of the MVK + CP reaction, for the three solvents for which experimental Gibbs free activation energies are available, the PBE0/D-COSMO-RS data without D3 corrections tend to overestimate the experimental  $\Delta G_{298K}^\ddagger$  values by  $\sim 14$  kJ mol<sup>-1</sup> for water, by  $\sim 8$  kJ mol<sup>-1</sup> for methanol (experimental data for 1-propanol or ethanol are almost identical), and by  $\sim 9$  kJ mol<sup>-1</sup> for acetonitrile. Adding D3 corrections provides a remarkably consistent underestimate by 8-10 kJ mol<sup>-1</sup> instead. This underestimate may well reflect the intrinsic error of the PBE0+D3/def2-TZVP approach (see above and Table 4.1), so that we conclude the D-COSMO-RS results at this level to provide systematically good agreement with experimental  $\Delta G_{298K}^\ddagger$  values for the different solvents.

This may be appreciated better when we concentrate on relative Gibbs free activation energies for different solvents, as has been done previously for both title reactions by Acevedo and Jorgensen using their semiempirical PDDG/PM3/MM/MC approach [244]. Figures 4.4 and 4.5 provide this type of comparison of the pure relative solvent effects for the MVK + CP and NQ + CP reactions, respectively. We show the values relative to acetonitrile solvent, as the more natural reference point with the nonpolar solvent hexane has so far not been studied experimentally for the MVK + CP reaction (the corresponding point lacks therefore in Figure 4.4).

The negative experimental values for the protic solvents show clearly the reduction of the Gibbs free-energy barrier relative to acetonitrile, while the positive hexane value for the NQ + CP reaction is consistent with the lower polarity of hexane compared to acetonitrile. The previous PDDG/PM3/MM/MC results reproduce the experimental differences excellently for the NQ + CP reaction, in spite of the rather large errors in the absolute Gibbs free activation energies at this computational level (see above). An incorrect positive value for methanol is obtained for the MVK + CP reaction, for unclear reasons.

COSMO provides clearly very poor relative values. One might have expected small negative values for water, due to its larger dielectric constant compared to acetonitrile. However, an appreciably positive value is obtained for the MVK + CP reaction (Figure

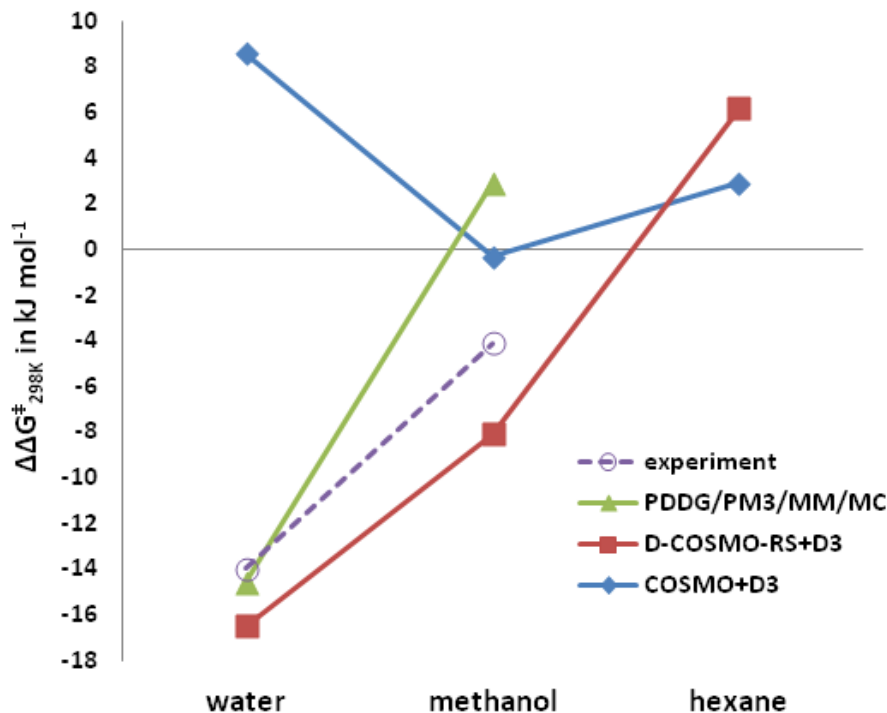


Figure 4.4: Solvent contributions to the Gibbs free activation energy of the MVK+CP reaction relative to acetonitrile using different methods. The semi-empirical PDDG/PM3/MM/MC calculations are from ref. [244]. The present calculations are provided at PBE0/def2-TZVP+D3 level (see Figure S1 in Appendix II for corresponding results without dispersion corrections). Experimental data from ref. [240].

4.4), and a small positive one for the NQ + CP reaction (Figure 4.5). The positive values seem to be an artifact of the combination of COSMO with the D3 dispersion corrections: Figures S1 and S2 in Appendix II show that without dispersion contributions the expected small COSMO values for water are obtained.

D-COSMO-RS seems to be affected less by this problem: for the MVK + CP reaction, dispersion contributions reduce the difference between methanol and water slightly (Figure 4.4 and Figure S1 from Appendix II), but for NQ+CP the curves with and without dispersion are very similar (Figure 4.5 and Figure S2 from Appendix II). While overall somewhat too large reductions of the Gibbs free-energy barriers by the protic solvents are found compared to experiment, the trends are reproduced rather well for both reactions, in sharp contradiction to the COSMO data, but in relatively good agreement with the previous semiempirical MC data.

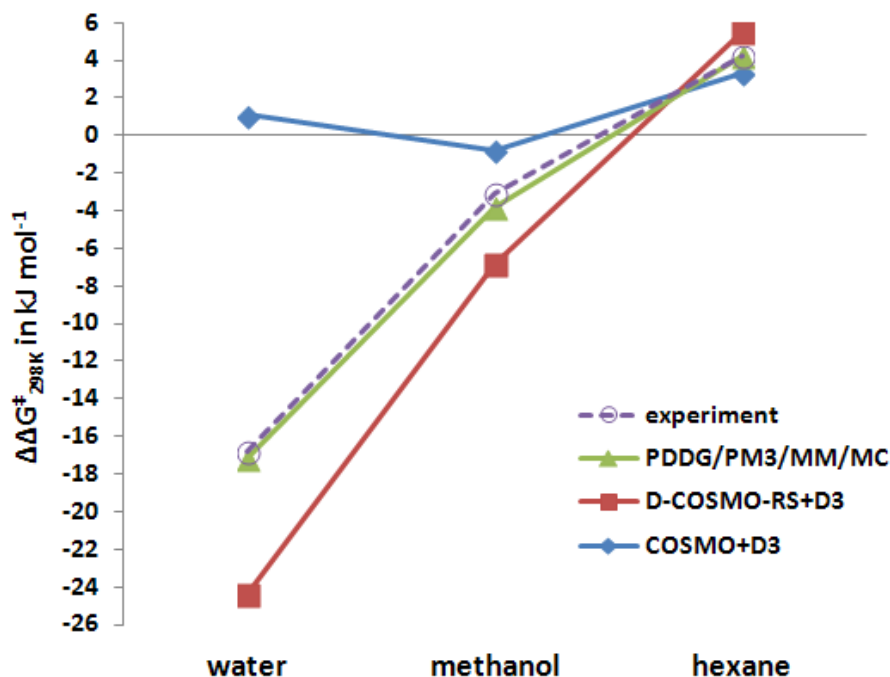


Figure 4.5: Solvent contributions to the Gibbs free activation energy of the NQ+CP reaction relative to acetonitrile using different methods. The semi-empirical PDDG/PM3/MM/MC calculations are from ref. [244]. The present calculations are provided at PBE0/def2-TZVP+D3 level (see Figure S1 in Appendix II for corresponding results without dispersion corrections). Experimental data from ref. [240].

Turning to the comparison of D-COSMO-RS-water data with the cluster-model results for the MVK+CP reaction (Table 4.2), we see that without D3 corrections, D-COSMO-RS provides  $13 \text{ kJ mol}^{-1}$  lower  $\Delta G_{298K}^\ddagger$  than the embedded-cluster model (COSMO-water +  $2\text{H}_2\text{O}$ ). After inclusion of D3 corrections, the difference shrinks to about  $9 \text{ kJ mol}^{-1}$ . For the Gibbs free reaction energies ( $\Delta G_{298K}$ ), we see that the D-COSMO-RS-water value is about  $14 \text{ kJ mol}^{-1}$  more exothermic than COSMO-water+ $2\text{H}_2\text{O}$ . Here the difference remains essentially constant upon inclusion of D3 corrections. These results suggest that D-COSMO-RS-water simulates a situation with somewhat more differential hydrogen-bonding interactions than provided by the COSMO-water+ $2\text{H}_2\text{O}$  embedded-cluster models, regarding both the Gibbs free activation energy (more H-bonding in the transition state than in the reactants) and the Gibbs free reaction energy (more H-bonding in the product than in the reactants). This result would be consistent with the situation described by the previous QM/MM MC studies [244], where more than an average number of two hydrogen bonds were found for the transition state and

the product (see above). In contrast to the Gibbs free activation energy, we have no experimental value for the Gibbs free reaction energy to compare with. Combining the D-COSMO-RS-water approach with two explicit water molecules provides somewhat less consistent results. While the two added water molecules render the reactions about 10 kJ mol<sup>-1</sup> less endergonic, independent of the presence or absence of the D3 corrections, the effect on the Gibbs free activation energies depends on the dispersion terms (increased  $\Delta G_{298K}^\ddagger$  without dispersion, an almost constant value with D3 correction). Overall, use of D-COSMO-RS-water without added explicit water molecules appears to be preferable.

Turning to the NQ + CP reaction (Table 4.3) we find again that PBE0+D3/def2-TZVP with D-COSMO-RS-water provides a  $\sim 9$  kJ mol<sup>-1</sup> too low  $\Delta G_{298K}^\ddagger$  value compared to experiment, similar to the results for MVK + CP above (Table 4.2). The underestimate of the Gibbs free activation energy at PBE0+D3/def2-TZVP/D-COSMO-RS level is smaller for the other solvents ( $\sim 6$  kJ mol<sup>-1</sup> for alcohols,  $\sim 1$ -2 kJ mol<sup>-1</sup> for acetonitrile, essentially zero for hexane). Without D3 corrections, the Gibbs free activation energies are overestimated more clearly (by  $\sim 17$  kJ mol<sup>-1</sup> for water, by  $\sim 20$  kJ mol<sup>-1</sup> for alcohol, by  $\sim 14$ -15 kJ mol<sup>-1</sup> for acetonitrile, and by  $\sim 25$  kJ mol<sup>-1</sup> for hexane). That is, the MVK + CP and NQ + CP results together are not sufficiently systematic to attribute beyond doubt the underestimate of the Gibbs free activation energies for most cases to the underlying PBE0+D3/def2-TZVP level.

Comparison of the D-COSMO-RS-water data with the embedded-cluster models for the NQ + CP reaction (Table 4.3) gives a somewhat different picture than discussed above (Table 4.2) for the MVK + CP reaction: now D-COSMO-RS-water is much closer to the embedded-cluster data (COSMO-water+4H<sub>2</sub>O), both with and without D3 corrections, and for both Gibbs free activation and reaction energies. Differences are generally below 5 kJ mol<sup>-1</sup> (note the only estimated entropy contributions, see above). This is in keeping with the notion (based on QM/MM MD data [244]) of somewhat weaker and longer hydrogen bonds for a given keto oxygen atom in the NQ + CP reaction. Two hydrogen bonds per keto (here: quinone) oxygen atom appears to be a better average description for NQ + CP than for MVK + CP, even for the transition state and the product. Again, experimental data for the Gibbs free reaction energies are lacking. We may take the approximately -40 kJ mol<sup>-1</sup> obtained both with D-COSMO-RS-water+D3 and with COSMO-water+4H<sub>2</sub>O+D3 as reasonable estimate (within the limits of accuracy of the underlying PBE0+D3/def2-TZVP level). We note in passing that D-COSMO-RS-water+4H<sub>2</sub>O+D3 provides an unrealistically low Gibbs free activation energy, consistent

with the discussion above, which disfavored the use of explicit water molecules together with the D-COSMO-RS-water model.

On the other hand, it is obvious and in agreement with previous work [244] that, for both reactions studied here, a polarizable continuum model without explicit water molecules cannot provide the observed, appreciable lowering of the Gibbs free activation energies in aqueous solution (Figures 4.4 and 4.5). The effects on the Gibbs free reaction energies are smaller. Yet the errors of a COSMO treatment may also exceed already the accuracy limitations provided by the underlying electronic-structure method. In the absence of reliable experimental data we may judge this only indirectly from the good performance of PBE0+D3/def2-TZVP for the gas-phase reaction energy (see Table 4.1). For methanol, the second protic solvent studied here, COSMO reproduces the D-COSMO-RS data better, both for activation and reaction energies (Tables 4.2 and 4.3). While this seems surprising at first, it might reflect the somewhat smaller hydrogen bonding effects in alcoholic solutions.

For the aprotic solvents one expects little differences between COSMO and D-COSMO-RS. This holds indeed for acetonitrile, where the COSMO and D-COSMO-RS data agree within less than 5 kJ mol<sup>-1</sup> (for both  $\Delta G_{298K}^\ddagger$  and  $\Delta G_{298K}$ ; Tables 4.2 and 4.3). Note, however, that the D-COSMO-RS data are systematically more positive by this amount. Maximal differences between COSMO and D-COSMO-RS increase to about 10 kJ mol<sup>-1</sup> for hexane, with D-COSMO-RS again systematically providing more positive Gibbs free activation and reaction energies (see also Figures 4.4 and 4.5). This is similar to observations made for electron-transfer barriers in organic mixed-valence systems [96,97].

**Interpretation of Solvent Effects in Terms of Electronic Structure.** The above results suggest that the D-COSMO-RS surface charge densities may implicitly incorporate different effective numbers or spatial extent of hydrogen-bonding hotspots. To evaluate how this functions in practice, we have graphically and numerically analyzed these surface charge densities. For the MVK reactant and the MVK + CP transition state and product, plots of surface charge densities obtained after the self-consistent COSMO-water and D-COSMO-RS-water calculations are shown in Figure 4.6 (further plots are given in Figures S3 and S4 in Appendix II). It is clear that the surface charge polarization around the keto oxygen atom is a) significantly enhanced at D-COSMO-RS compared to COSMO level, and b) the polarization is substantially more pronounced at the transition state compared to reactant or product, again in particular for D-COSMO-RS. At the transition state, enhanced D-COSMO-RS surface charge densities cover a

much larger area around the oxygen atom. This is consistent both with stronger hydrogen bonding and with a larger average number of contacts. We note that the largest surface charge densities are not distributed in a cylindrical arrangement but show a distinct accumulation away from the more sterically hindered parts of the transition-state structure. The polarization for the NQ + CP transition state (Figure S3 in Appendix II) is also enhanced significantly compared to the NQ reactant (or the product). However, it is appreciably less pronounced compared to the MVK + CP transition state (Figure 4.6). This likely reflects less effective hydrogen bonding in the NQ + CP transition state, consistent with our inability to optimize static model clusters with three water molecules hydrogen-bonded to each of the quinone oxygen atoms (see above). Similarly, the D-COSMO-RS surface charge densities of reactant and product of the NQ + CP reaction also feature less pronounced maxima than for MVK + CP (Figure 4.6, Figure S3 in Appendix II). We thus conclude that D-COSMO-RS surface charge densities apparently reflect differences not only between the intensity of average hydrogen-bonding contacts at the transition states compared to reactants or products but also differences between the two reactions studied here. This is notable in view of the fact that the D-COSMO-RS-water energetics of the NQ + CP agree well with the COSMO-water+4H<sub>2</sub>O static cluster model results (see Table 4.3), whereas they provide a larger reduction of Gibbs free activation energy than COSMO-water+2H<sub>2</sub>O data for the MVK + CP reaction (see Table 4.2).

The environmental effects on electronic structure may be evaluated additionally from partial atomic charges, in particular for the oxygen atoms that may act as acceptors for hydrogen bonding. Table 4.4 provides oxygen NPA charges for reactant, transition state, as well as product of the MVK + CP reaction, using different solvent environments. We note in passing that dispersion contributions influence these charges only indirectly by structural modifications. First of all, the oxygen charges of reactant and product differ relatively little, while they are distinctly more negative at the transition state, consistent with previous analyses [242, 244, 245]. This explains why protic solvents have a much larger lowering effect on the activation barriers than on the reaction energies (see above). The charges are generally rendered more negative by polar solvents, and the changes due to solvent are also largest at the transition state. Let us focus on aqueous solution: most notably, the enhancement of the charges (compared to the gas-phase values) is largest for D-COSMO-RS-water, somewhat less pronounced for COSMO-water+2H<sub>2</sub>O, and still much less for COSMO-water without explicit solvent molecules. This confirms that (a) the COSMO continuum solvent does not capture the hydrogen-bonding effects

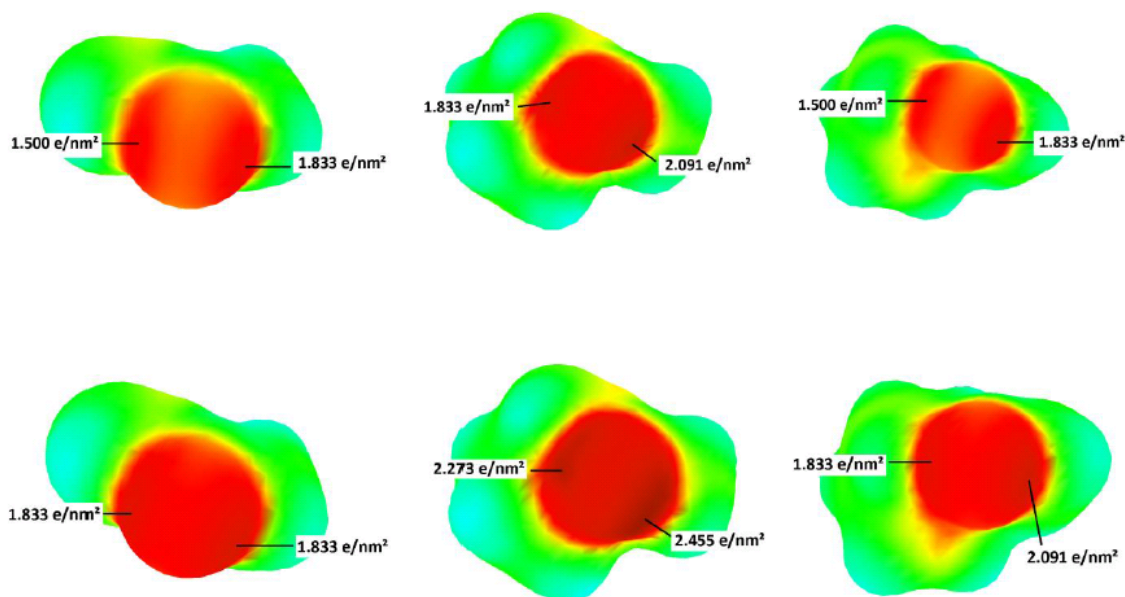


Figure 4.6: Surface charge density maps for the MVK+CP reaction. The upper row from left to right shows reactant (MVK), transition state and product, respectively, with COSMO (water). The lower row from left to right shows reactant, transition state and product, respectively, with D-COSMO-RS (water).

adequately and (b) D-COSMO-RS seems to provide a stronger hydrogen-bonding environment than the COSMO-water+2H<sub>2</sub>O embedded-cluster model, consistent with the larger average number of hydrogen bonds obtained in MD simulations [243, 244]. And as the overall effects are largest at the transition state (charges relative to the gas-phase values -0.14 for reactant, -0.16 for the transition state, and -0.13 for the product, Table 4.4), the appreciable lowering of the activation barrier with D-COSMO-RS-water is easily understood. We furthermore note also that addition of explicit water molecules to D-COSMO-RS-water has almost no additional effect on the oxygen charges. The interpretation of the oxygen atomic charges is thus fully consistent with the above analyses of the surface-charge density profiles.

**Transition State Structures.** A main difference between the two title reactions is that for MVK + CP the transition state is very unsymmetrical (see  $d_1$  vs  $d_2$  in Table 4.4, Figure 4.2), whereas it is essentially symmetrical for the NQ + CP reaction (Table S6 in Appendix II). This influences the magnitude of dispersion and solvent effects at the transition-state structures: the two almost equivalent C-C distances,  $d_1$ ,  $d_2$ , of the latter

Table 4.4: Important distances (in Å) in the transition state and natural charges on the ketone oxygen atom for the MVK+CP Diels-Alder reaction in different environments<sup>a</sup>

	$d_1$	$d_2$	$q_{educt}$	$q_{trans}$	$q_{product}$
gas phase	2.064	2.566	-0.52	-0.58	-0.53
gas phase+D3	2.061	2.545	-0.52	-0.58	-0.53
gas phase+2H <sub>2</sub> O	2.058	2.739	-0.60	-0.69	-0.61
gas phase+2H <sub>2</sub> O+D3	2.054	2.711	-0.60	-0.69	-0.61
COSMO-water	2.055	2.634	-0.60	-0.67	-0.60
COSMO-water+D3	2.056	2.607	-0.59	-0.67	-0.60
D-COSMO-RS-water	2.068	2.706	-0.67	-0.75	-0.66
D-COSMO-RS-water+D3	2.060	2.645	-0.66	-0.74	-0.66
COSMO-water+2H <sub>2</sub> O	2.068	2.729	-0.63	-0.72	-0.64
COSMO-water+2H <sub>2</sub> O+D3	2.062	2.715	-0.63	-0.72	-0.63
D-COSMO-RS-water+2H <sub>2</sub> O	2.064	2.730	-0.64	-0.73	-0.64
D-COSMO-RS-water+2H <sub>2</sub> O+D3	2.071	2.737	-0.64	-0.74	-0.64
COSMO-methanol	2.055	2.631	-0.59	-0.67	-0.60
COSMO-methanol+D3	2.055	2.611	-0.60	-0.67	-0.60
D-COSMO-RS-methanol	2.061	2.696	-0.60	-0.73	-0.60
D-COSMO-RS-methanol+D3	2.061	2.676	-0.60	-0.73	-0.60
COSMO-acetonitrile	2.055	2.631	-0.60	-0.67	-0.60
COSMO-acetonitrile+D3	2.054	2.603	-0.60	-0.67	-0.60
D-COSMO-RS-acetonitrile	2.054	2.609	-0.58	-0.64	-0.58
D-COSMO-RS-acetonitrile+D3	2.051	2.587	-0.58	-0.65	-0.58
COSMO-hexane	2.060	2.579	-0.54	-0.61	-0.55
COSMO-hexane+D3	2.057	2.561	-0.54	-0.61	-0.55
D-COSMO-RS-hexane	2.059	2.582	-0.55	-0.61	-0.56
D-COSMO-RS-hexane+D3	2.057	2.559	-0.55	-0.61	-0.56

<sup>a</sup>PBE0/def2-TZVP results with and without D3 dispersion corrections. See Figure 4.2 for definition of the distances.

reaction vary over an intermediate range of maximally 0.075 Å (Table S6 in Appendix II), whereas in the former reaction, the long distance  $d_2$  changes by up to 0.194 Å, the shorter  $d_1$  only by maximally 0.020 Å. For the MVK + CP reaction, the asymmetry of the transition state is typically enhanced by solvent effects and decreased by dispersion (Table 4.4). This is mainly because of the changes in  $d_2$ : dispersion contracts the longer distance much more than  $d_1$ , by typically up to 0.03 Å (but by exceptional 0.06 Å for D-COSMO-RS-water). Solvent effects on  $d_2$  are even more pronounced. They increase the distance by up to almost 0.2 Å at some levels (by 0.140/0.100 Å for D-COSMO-RS-water+D3). Here the solvent and dispersion effects are clearly nonadditive. For the NQ + CP reaction (Table S6 in Appendix II), only D-COSMO-RS with very polar solvents introduces a slight asymmetry into the transition-state structure. And this might even

be a small numerical artifact of the solvent treatment. Here we should thus evaluate the overall shortening or lengthening effects on the average of  $d_1$  and  $d_2$ : dispersion shortens these intermediate distances typically only by up to 0.010 Å (0.015 Å for gas phase+4H<sub>2</sub>O, whereas D-COSMO-RS-water+4H<sub>2</sub>O even exhibits a slight lengthening due to dispersion). Solvent effects on the two distances also remain small, except for D-COSMO-RS-water+4H<sub>2</sub>O, where a lengthening by about 0.02-0.04 Å is found, depending on dispersion.

#### 4.1.4 Conclusions

COSMO-RS is an implicit solvent model, which requires comparable computational effort and can be carried out essentially in the same black-box mode as standard polarizable dielectric continuum solvent models like COSMO. Nevertheless, the implicitly included hydrogen-bond terms make COSMO-RS much more suitable for protic solvents, in particular for aqueous solution, and it may be applied to solvent mixtures. While we should not expect a completely quantitative treatment of specific solvent contributions, COSMO-RS has clearly been shown in the past to offer great potential for many applications. These advantageous properties of COSMO-RS obviously carry over to its self-consistent variant, D-COSMO-RS, which allows computations of structures or vibrational frequencies. Its favorable performance in recent electron-transfer studies has been confirmed here for kinetics and thermochemistry of Diels-Alder reactions, and it is likely to hold for many other chemical reactions as well. Together with the possibility of computing further molecular properties, this opens many areas of application for this convenient solvent model. These findings are remarkable in view of the fact that COSMO-RS and D-COSMO-RS do not require MD or MC simulations. While QM/MM MC simulations had been carried out previously for the two title reactions of the present work, they had been limited to a rather approximate semiempirical MO method, due to the substantial effort involved in carrying out millions of QM calculations. In contrast, the much lower computational effort involved in D-COSMO-RS has allowed us to use much better underlying QM methods. Other methods, such as RISM-SCF, should of course be mentioned as interesting alternatives.

A useful feature of the present D-COSMO-RS simulations is the capture of fractional and variable average numbers of hydrogen bonds, which turned out to differ between reactants, transition states and products of the two reactions studied here. We further-

more observed slight numerical instabilities of vibrational frequency computations with COSMO, but particularly with D-COSMO-RS, as a moderate drawback of the current implementation, in particular for transition states and in the presence of explicit water molecules. This will require further evaluation.

As a basis for comparison with experimental Gibbs free energies of activation and reaction, it also turned out to be crucial to carefully choose the underlying electronic-structure method. Here we concentrated on the PBE0+D3/def2-TZVP level, which compared favorably with benchmark ab initio calculations in the gas phase. Other functionals are known to show comparable accuracy for pericyclic reactions, while the previously observed deficiencies of the B3LYP functional for certain types of organic reactions were clearly exposed in our evaluations. It is also important to reiterate that B3LYP calculations with small basis sets like 6-31G(d) may give the right answer for the wrong reason.

## 4.2 Relativistic and Solvation Effects on the Stability of Gold(III) Halides in Aqueous Solution

The contents of this chapter have been published in "Relativistic and Solvation Effects on the Stability of Gold(III) Halides in Aqueous Solution" by K. Theilacker, H. B. Schlegel, M. Kaupp, P. Schwerdtfeger, *Inorg. Chem.* **2015**, *54*, 9869.

### 4.2.1 Introduction

The important role of relativistic effects in the chemical and physical properties of heavy-element compounds is now well established [246–248], and the stability of oxidation states in such compounds is also a well-documented field where relativistic effects may be crucial [249–253]. A recent spectacular example is the computational proof that the lead battery is of practical use (compared to the corresponding tin cell) only because of the destabilization of the highest-oxidation-state Pb(IV) species by scalar relativistic effects [254]. The destabilization of the highest oxidation state by relativity is a general observation in p-block main-group chemistry, leading to an enhancement of the well-known inert-pair effect. The relativistic contributions in this case are largely due to the relativistic contraction of the 6s orbitals, which renders the hybridization between 6s and 6p orbitals particularly unfavorable, enhancing so-called hybridization defects [255–257]. In contrast, relativity stabilizes the highest oxidation states of the 5d elements. This is partly due to the relativistic expansion of the 5d orbitals and the associated improved covalent bonding and better transfer of charge from metal to ligands. In the spectacular case of the stability of oxidation state + IV in mercury chemistry in form of HgF<sub>4</sub> [251,258,259] (and the related predicted stability of the heavy homologue CnF<sub>4</sub> [260]), it has been shown that destabilization of the lower + II oxidation state by contraction of the 6s orbitals is even more important. These works have been preceded by computational studies on the relativistic stabilization of oxidation state + III in gold chemistry about 25 years ago [252,253]. Gas-phase calculations on gold(III) halides carried out at the time showed clearly how equilibria like AuX<sub>3</sub> ⇌ AuX + X<sub>2</sub> are shifted to the left by scalar relativistic effects (see also ref. [261]).

While such calculations show the principal stabilization of Au(III) by relativity, the more chemically relevant processes involve gold(III) compounds in solution. In particular, the aqueous AuCl<sub>4</sub><sup>-</sup> anion is an important constituent in the industrial electrochemical

refinement of gold in a hydrochloric acid ( $\text{HAuCl}_4$ ) solution (Wohlwill process), in the extraction of gold by chlorine in hydrochloric acid, in the dissolution of elemental gold by aqua regia, or in certain oxidation reactions in organic synthesis [262]. The influence of relativity on the redox stability of this and similar species in aqueous solution is thus a practically important question but has hitherto not been addressed by quantum-chemical studies. The computational modeling in this case is complicated by the need to include the hydrogen bonding from the aqueous solvent with the species involved in the chemical equilibria. Moreover, the interplay between solvation and relativistic effects has not been addressed previously in the literature. In the present study we therefore use a comparison between state-of-the-art relativistic and nonrelativistic quantum-chemical methodology in combination with the Direct Conductor-like Screening Model for Real Solvents (D-COSMO-RS) [96] to address the stability of gold halide complexes  $\text{AuX}_4^-$  ( $X = \text{F}, \text{Cl}, \text{Br}, \text{I}$ ) in aqueous solution against reductive elimination of halogen.

## 4.2.2 Computational Details

Initial gas-phase calculations for the decomposition reaction  $\text{AuX}_4^- \rightarrow \text{AuX}_2^- + \text{X}_2$  ( $X = \text{F}, \text{Cl}, \text{Br}$  and  $\text{I}$ ) were carried out in order to select a suitable exchange-correlation functional from density functional theory (DFT) to be further applied to reactions in solution. To this end, benchmark calculations at post-Hartree-Fock coupled-cluster levels (CCSD and CCSD(T)), as well as at the Møller-Plesset MP2, MP3, MP4(SDQ) levels, were carried out with the Gaussian09 program [263]. The influence of relativistic effects has been computed by comparison of scalar-relativistically and nonrelativistically adjusted energy-consistent effective core potentials (ECPs) [264] for gold, bromine, and iodine [265–267], while disregarding the much less important relativistic contributions from the lighter halogen atoms. Against the obtained CCSD(T) benchmark data, a range of density functionals has been screened for the relativistic and nonrelativistic gas-phase energetics, including “pure” functionals within the generalized gradient approximation (GGA) such as PW91 [27] and PBE [14], the popular global hybrid B3LYP [15, 23], which has been previously shown to perform well for the stability of high oxidation states in transition-metal chemistry [268–277], and finally the range-separated hybrids CAM-B3LYP [29] and LC- $\omega$ PBE [30, 59]. The basis sets used were an uncontracted relativistic MP2 optimized (10s10p6d3f) set for gold (see Appendix II for details), and aug-cc-pVTZ basis sets for the halides [222, 267, 278].

Solvent effects were subsequently evaluated at B3LYP level with the TURBOMOLE6.3 package [111–113], using both the COSMO and D-COSMO-RS models. These calculations have been performed using the same ECPs and basis sets as for the gas-phase calculations, performing full-structure optimizations at all levels. We note in passing that the definition of the VWN correlation functional occurring in this case is slightly different from the definition in Gaussian (VWN5 instead of VWN3 [8]). As a dielectric continuum solvent model, in this case the COSMO (Conductor-like Screening Model [91]) approach was employed, using dielectric constant  $\epsilon = 78.3553$  for water. To go beyond a continuum model, which does not capture hydrogen bonding, the self-consistent D-COSMO-RS method [93, 96] was used. The required  $\sigma$ -potentials have been created with the COSMOtherm program [226] at BP86/TZVP level for 298 K. Self-consistent COSMO and D-COSMO-RS surface charge densities have been plotted using the same program. In the COSMO and D-COSMO-RS solvent environments, the frequency calculations had to be done by numerical differentiation of analytical gradients (using the numforce module of TURBOMOLE6.3). The computed vibrational frequencies were subsequently used to estimate thermal and entropic contributions to the Gibbs free energies of reaction.

Spin-orbit contributions to the reaction energies of the bromide and iodide complexes have been estimated by gas-phase two-component ECP calculations [279,280] with TURBOMOLE6.3 (B3LYP/dhf-QZVP-2c level [266, 267] with corresponding dhf-QZVP-2c RI-JK auxiliary basis sets [281]). Two-component ECPs and valence basis sets for gold, bromine and iodine [266, 267] have been used, and SO energies were obtained by taking energy differences between two-component and scalar relativistic ECP energies (as single points on scalar-relativistically optimized structures).

## 4.2.3 Results and Discussion

### 4.2.3.1 Gas-Phase Reaction $\text{AuX}_4^- \rightarrow \text{AuX}_2^- + \text{X}_2$

As a background for the discussion of solvent effects and to validate the use of computationally more efficient DFT methods, we first compare a number of DFT functionals against benchmark coupled-cluster calculations for the gas-phase reaction of the halide systems, and we evaluate the magnitude of relativistic effects in the absence of any solvent. Tables 4.5 and 4.6 provide nonrelativistic and (scalar) relativistic ECP calculations at various computational levels for  $\text{X} = \text{F}, \text{Cl}$  and  $\text{X} = \text{Br}, \text{I}$ , respectively. Taking

the CCSD(T) data as reference values, and starting with the ab initio methods, we see that the importance of electron correlation (measured by the difference between HF and CCSD(T)) is dramatically reduced at the relativistic level. Therefore, deviations of the different electron-correlation methods from the benchmark data, and the importance of the triple excitations at coupled-cluster level, are also substantially diminished by relativity. This is not unexpected, as the relativistic expansion of the Au 5d-orbitals improves the overlap with the ligand orbitals in the Au(III) species and reduces the “stretched-bond situation” typical for transition-metal complexes, in particular in high oxidation states. Partly stretched bonds, due to Pauli repulsion between 5s and 5p semicore-shells with the bonding orbitals, are responsible for the large nondynamical correlation effects found at the nonrelativistic level, while the relativistic expansion of the 5d orbitals improves the overlap and strengthens the bonds [282,283]. Notably, the d-orbital participation in bonding in the AuX<sub>2</sub> reductive elimination product is much smaller (see below), which is why the correlation effects are much less critical on the product than on the educt side of the reaction. Such considerations have been discussed previously, e.g. for the reaction  $\text{HgF}_4 \rightarrow \text{HgF}_2 + \text{F}_2$ , or for other redox reactions in transition-metal chemistry [259]. We note in passing that the Møller-Plesset perturbation series shows the oscillatory behavior expected for such a situation, with the MP4SDQ data being somewhat closer to CCSD(T) than to CCSD [253]. Furthermore, differences between MP2 and CCSD(T) structures influence the computed MP2 reaction energies by less than 2 kJ mol<sup>-1</sup>.

As these correlation contributions stabilize Au(III) relative to Au(I), the CCSD(T) reaction energies are more positive compared to the HF data, albeit the effects are much less dramatic once scalar relativity has been included (Table 4.5). At the CCSD(T) reference level, scalar relativity stabilizes AuX<sub>4</sub><sup>-</sup> with respect to reductive elimination of X<sub>2</sub> by between 133.4 kJ mol<sup>-1</sup> (X = F) and 81.8 kJ mol<sup>-1</sup> (X = I).

As expected, the effect decreases with decreasing electronegativity of the halogen. This is related mainly to the scalar relativistic destabilization of the Au-X bonds in the Au(I) species, where the relativistic contraction of the Au 6s orbital reduces substantially the bond ionicity and the associated electrostatic stabilization [260]. As this destabilizing effect is most pronounced with the most electronegative ligands, the decrease of the relativistic stabilization of Au(III) against Au(I) from X = F toward X = I is understandable.

These gas-phase data can now be used to judge the performance of DFT methods. The

Table 4.5: Computed nonrelativistic and scalar-relativistic gas-phase reaction energies for  $\text{AuX}_4^- \rightarrow \text{AuX}_2^- + \text{X}_2$  ( $\text{X} = \text{F}, \text{Cl}$ ) at various levels, and their deviations from CCSD(T) data in  $\text{kJ mol}^{-1}$ .<sup>a</sup>

X=F	nonrelativistic		scalar relativistic	
	$\Delta E$	dev. from CCSD(T)	$\Delta E$	dev. from CCSD(T)
HF	159.4	-116.7	392.9	-16.6
MP2	291.3	15.2	404.8	-4.7
MP2//CCSD(T)	292.0	15.9	405.6	-3.9
MP3//CCSD(T)	244.6	-31.5	401.6	-7.9
MP4SDQ//CCSD(T)	261.4	-14.7	408.8	-0.7
CCSD//CCSD(T)	251.8	-24.3	404.4	-5.1
CCSD(T)	276.1	-	409.5	-
LC- $\omega$ PBE	288.5	12.4	428.9	19.4
CAM-B3LYP	293.8	17.7	418.2	8.7
B3LYP	295.4	19.3	399.2	-10.3
PBE	333.3	57.2	409.1	-0.4
PW91	338.4	62.3	413.9	4.4
X=Cl	nonrelativistic		scalar relativistic	
	$\Delta E$	dev. from CCSD(T)	$\Delta E$	dev. from CCSD(T)
HF	-142.3	-174.5	57.5	-91.7
MP2	75.6	43.4	171.2	22.0
MP2//CCSD(T)	76.5	44.3	172.2	23.0
MP3//CCSD(T)	-2.0	-34.2	123.6	-25.6
MP4SDQ//CCSD(T)	-1.1	-33.3	134.5	-14.7
CCSD//CCSD(T)	-4.6	-36.8	127.9	-21.3
CCSDT(T)	32.2	-	149.2	-
LC- $\omega$ PBE	9.8	-22.4	141.5	-7.7
CAM-B3LYP	21.5	-10.7	130.8	-18.4
B3LYP	40.1	7.9	126.7	-22.5
PBE	88.0	55.8	157.3	8.1
PW91	91.5	59.3	160.1	10.9

<sup>a</sup>For fully optimized structures at the given computational level, unless indicated otherwise.

Table 4.6: Computed nonrelativistic and scalar-relativistic gas-phase reaction energies for  $\text{AuX}_4^- \rightarrow \text{AuX}_2^- + \text{X}_2$  ( $\text{X} = \text{Br}, \text{I}$ ) at various levels, and their deviations from CCSD(T) data in  $\text{kJ mol}^{-1}$ .<sup>a</sup>

X=Br	nonrelativistic		scalar relativistic	
	$\Delta E$	dev. from CCSD(T)	$\Delta E$	dev. from CCSD(T)
HF	-171.7	-183.4	0.6	-115.8
MP2	66.2	54.5	155.8	39.4
MP2//CCSD(T)	67.0	55.3	156.9	40.5
MP3//CCSD(T)	-25.7	-37.4	82.2	-34.2
MP4SDQ//CCSD(T)	-19.9	-31.6	103.2	-13.2
CCSD//CCSD(T)	-25.2	-36.9	92.6	-23.8
CCSD(T)	11.7	-	116.4	-
LC- $\omega$ PBE	-22.1	-33.8	93.4	-23.0
CAM-B3LYP	-10.1	-21.8	83.0	-33.4
B3LYP	10.2	-1.5	82.2	-34.2
PBE	58.0	46.3	116.1	-0.3
PW91	61.5	49.8	119.1	2.7

X=I	nonrelativistic		scalar relativistic	
	$\Delta E$	dev. from CCSD(T)	$\Delta E$	dev. from CCSD(T)
HF	-197.4	-193.1	-61.4	-138.9
MP2	56.3	60.6	133.8	56.3
MP2//CCSD(T)	56.1	60.4	134.4	56.9
MP3//CCSD(T)	-45.5	-41.2	33.2	-44.3
MP4SDQ//CCSD(T)	-33.3	-29.0	65.9	-11.6
CCSD//CCSD(T)	-42.2	-37.9	50.1	-27.4
CCSDT(T)	-4.3	-	77.5	-
LC- $\omega$ PBE	-57.1	-52.8	45.5	-32.0
CAM-B3LYP	-47.2	-42.9	32.1	-45.4
B3LYP	-25.0	-20.7	34.5	-43.0
PBE	22.3	18.0	73.3	-4.2
PW91	25.9	21.6	76.3	-1.2

<sup>a</sup>For fully optimized structures at the given computational level, unless indicated otherwise.

PW91 and PBE GGA functionals show excellent agreement with the reference data at the scalar relativistic level but overestimate the stability of the Au(III) complexes appreciably at the nonrelativistic level. They thus do not provide a very accurate account of the overall relativistic contributions, overestimating them by up to 60 kJ mol<sup>-1</sup> (Table 4.5). The B3LYP global hybrid and the CAM-B3LYP and LC- $\omega$ PBE range-separated hybrids show a somewhat more uniform behavior and thus seem better suited to discuss relativistic effects. While the range hybrids perform more consistently overall, the deviations of the B3LYP data from the CCSD(T) reference are sufficiently small (smaller than or comparable to those of the CCSD values). We may therefore, in the following, use with confidence the B3LYP functional for the evaluation of solvent effects. We note that other functionals may well perform better than the ones tested here, but an exhaustive evaluation is beyond the scope of the present work.

We note in passing that spin-orbit (SO) effects on the gasphase reactions turn out to be minor: at two-component ECP level (B3LYP, gas phase), spin-orbit contributions to the reaction energies of the bromide and iodide complexes are only about +5 kJ mol<sup>-1</sup> (Table S8 in Appendix II). While the absolute SO effects stemming from iodine are, as expected, larger than for bromine, the differential effects on the reaction energy are almost the same, and the very small halogen SO contributions even cancel part of the also small gold SO contributions for these closed-shell reactions (Table S8). SO effects are therefore only marginally involved in the trend of decreasing reaction energies with heavier halide ligands, which is largely due to the decreasing ligand electronegativity (see above). We also conclude that we may, to a good approximation, discuss the reaction energies in solution at the scalar relativistic level.

#### **4.2.3.2 AuX<sub>4</sub><sup>-</sup> → AuX<sub>2</sub><sup>-</sup> + X<sub>2</sub> Reaction in Aqueous Solution: Relativistic and Solvation Effects at the B3LYP Level**

As we move to the solution phase, our focus will be on Gibbs free reaction energies rather than taking solely electronic energy differences. The solvent models cover solvent enthalpic and entropic contributions, and it is thus more consistent to include those as well for the internal degrees of freedom. The Gibbs free energies are in any case the decisive thermochemical measure determining the equilibrium. We will concentrate on the interplay between relativistic and solvent effects. It is important to note that the data provided pertain to 298 K and to neutral pH (Table 4.7). For the chloride species, it is well-known that both pH and temperature affect the speciation in solution

appreciably, a point we will address further below. Furthermore, we may need to include other reactions than halogen elimination (e.g., disproportionation of  $\text{AuCl}_2^-$ ), which we will also do below. We also note that the behavior of  $\text{AuF}_4^-$  deviates from that of the other three Au(III) halides by exhibiting a strongly endergonic elimination reaction already at nonrelativistic level, due to the inherent instability of  $\text{F}_2$  (Table 4.7).

In general, solvent effects are larger at the D-COSMO-RS compared to the COSMO level of theory, consistent with the lack of explicit hydrogen-bonding terms in the COSMO dielectric continuum model. The consequently larger reduction of the gas-phase Gibbs free energies of reaction at D-COSMO-RS level is expected to be more realistic, as has been shown recently for organic reactions in aqueous [284] or alcoholic solution [96, 97], and in the following, we will concentrate on these. Solvent and relativistic effects on  $\Delta G$  are clearly nonadditive (Figure 4.7): while the reduction of  $\Delta G$  from gas phase to D-COSMO-RS ranges from  $-99 \text{ kJ mol}^{-1}$  ( $X = \text{F}$ ) to  $-40 \text{ kJ mol}^{-1}$  ( $X = \text{I}$ ) at nonrelativistic levels, it is much smaller upon inclusion of scalar relativistic effects, between  $-40 \text{ kJ mol}^{-1}$  ( $X = \text{F}$ ) and  $-28 \text{ kJ mol}^{-1}$  ( $X = \text{I}$ ). In both cases, however, the solvent contributions become less negative from  $X = \text{F}$  to  $X = \text{I}$  (Figure 4.7, Table 4.7). As a result of the smaller reduction of the Gibbs free energy of reaction by solvent effects at the relativistic level, the overall relativistic stabilization of the Au(III) complexes against reductive elimination by relativity is enhanced in solution compared to the gas phase. This “extra relativistic effect by solvation” is most pronounced for  $X = \text{F}$  ( $+59 \text{ kJ mol}^{-1}$ ) and decreasing (from  $+35 \text{ kJ mol}^{-1}$  for Cl to  $+12 \text{ kJ mol}^{-1}$  for I) for the other halides.

While at nonrelativistic levels only the Au(III) fluoride complex would be stable with respect to reductive elimination, the final scalar relativistic Gibbs free reaction energies in solution (D-COSMO-RS data; Table 4.7) are even larger for  $X = \text{F}$ , still appreciably positive for  $X = \text{Cl}$ , less positive for  $X = \text{Br}$ , and negative for  $X = \text{I}$  (while the gas-phase reaction would be predicted to be almost thermoneutral at this level; Table 4.7). These results are consistent with the observation of  $\text{AuCl}_4^-$  and  $\text{AuBr}_4^-$  in aqueous solution [262] and the known instability of the iodide complex under the same conditions. The fact that  $\text{AuF}_4^-$  exists only in water-free environments is due to its sensitivity to hydrolysis rather than to its oxidation power.

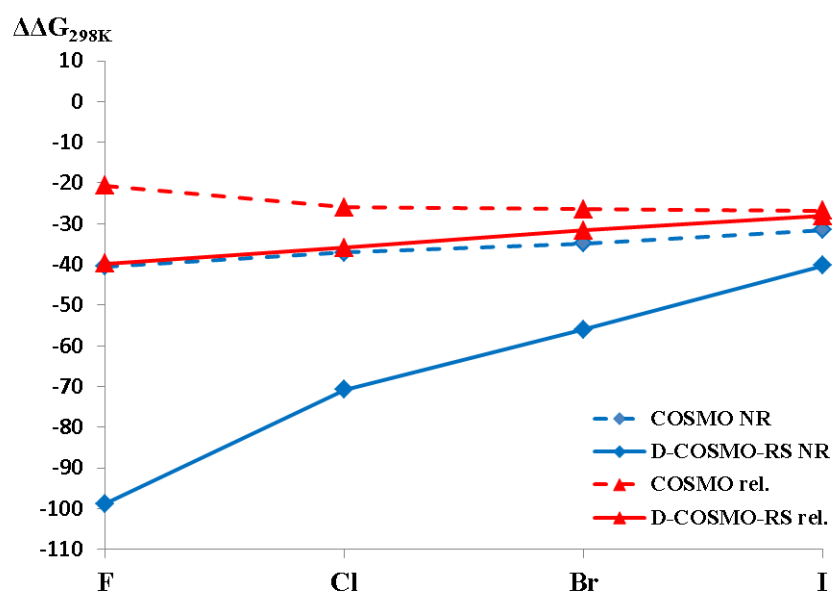


Figure 4.7: Differential solvent effects on Gibbs free energies,  $\Delta\Delta G = \Delta G(\text{aq}) - \Delta G(\text{gas phase})$ , at standard conditions for reaction  $\text{AuX}_4^- \rightarrow \text{AuX}_2^- + \text{X}_2$  ( $\text{X} = \text{F}, \text{Cl}, \text{Br}, \text{I}$ ), at COSMO and D-COSMO-RS levels (B3LYP).

Table 4.7: Reaction energies, enthalpies, and Gibbs free energies (in kJ mol<sup>-1</sup>) for the AuX<sub>4</sub><sup>-</sup> → AuX<sub>2</sub><sup>-</sup> + X<sub>2</sub> reaction (X =F, Cl, Br, I), together with NPA charges and Au-X distances (in Å) of educt AuX<sub>4</sub><sup>-</sup>(e) and product AuX<sub>2</sub><sup>-</sup>(p)<sup>a</sup>

reaction	$\Delta E$	$\Delta G_{298K}$	nonrelativistic				scalar relativistic					
			$\Delta H_{298K}$	q(Au) <sub>e</sub> q(Au) <sub>p</sub>	q(X) <sub>e</sub> q(X) <sub>p</sub>	d(Au-X) <sub>e</sub> d(Au-X) <sub>p</sub>	$\Delta E$	$\Delta G_{298K}$	$\Delta H_{298K}$	q(Au) <sub>e</sub> q(Au) <sub>p</sub>	q(X) <sub>e</sub> q(X) <sub>p</sub>	d(Au-X) <sub>e</sub> d(Au-X) <sub>p</sub>
X=F												
gas phase	295.4	254.9	292.8	1.60 0.76	-0.65 -0.88	2.008 2.160	399.2	359.8	396.4	1.57 0.53	-0.64 -0.76	1.941 1.990
COSMO	256.6	214.4	253.9	1.64 0.83	-0.66 -0.91	2.007 2.199	378.3	339.1	375.5	1.60 0.55	-0.65 -0.77	1.939 1.990
D-COSMO-RS	200.2	156.1	197.6	1.70 0.90	-0.67 -0.95	2.012 2.289	359.5	320.0	356.8	1.64 0.62	-0.66 -0.81	1.941 2.017
X=Cl												
gas phase	40.1	2.3	37.7	1.09 0.66	-0.52 -0.83	2.428 2.505	126.7	88.7	124.2	0.96 0.37	-0.49 -0.68	2.335 2.322
COSMO	4.4	-34.8	1.9	1.10 0.72	-0.53 -0.86	2.424 2.525	100.9	62.7	98.3	0.97 0.37	-0.49 -0.68	2.331 2.314
D-COSMO-RS	-29.5	-68.5	-31.9	1.11 0.80	-0.53 -0.90	2.426 2.566	91.2	52.8	88.6	0.97 0.40	-0.49 -0.70	2.332 2.322
X=Br												
gas phase	10.2	-26.2	7.7	0.93 0.62	-0.48 -0.81	2.588 2.632	82.2	44.9	79.6	0.77 0.31	-0.44 -0.65	2.488 2.452
COSMO	-23.0	-61.0	-25.5	0.95 0.67	-0.49 -0.83	2.583 2.649	55.8	18.5	53.3	0.77 0.29	-0.44 -0.65	2.484 2.442
D-COSMO-RS	-42.9	-82.2	-45.5	0.95 0.73	-0.49 -0.87	2.584 2.699	50.7	13.3	48.1	0.77 0.31	-0.44 -0.66	2.484 2.444
X=I												
gas phase	-25.0	-59.8	-27.5	0.72 0.54	-0.43 -0.77	2.813 2.800	34.5	-1.5	31.9	0.53 0.22	-0.38 -0.61	2.697 2.621
COSMO	-55.4	-91.3	-58.0	0.73 0.58	-0.43 -0.79	2.808 2.808	7.8	-28.3	5.2	0.52 0.19	-0.38 -0.60	2.693 2.611
D-COSMO-RS	-64.4	-100.1	-67.0	0.72 0.60	-0.43 -0.80	2.808 2.816	7.2	-29.6	4.6	0.52 0.20	-0.38 -0.60	2.693 2.617

<sup>a</sup>Comparison of gas-phase and aqueous solution results (with COSMO and D-COSMO-RS) at B3LYP level with Turbomole, using a nonrelativistic or scalar relativistic Au ECP, respectively.

#### 4.2.3.3 Interpretation of Trends in Solvent and Relativistic Effects

It is important to rationalize why (a) relativistic effects stabilize, (b) solvent effects destabilize the Au(III) oxidation state, and (c) the solvent destabilization is much less pronounced at relativistic than at nonrelativistic levels (nonadditivity of solvent and relativistic effects). Point a has been discussed in detail in previous work by Schwedtfeger [252], and we thus only summarize the salient features here: the relativistic stabilization of the Au-X bonds in the Au(III) halides due to the relativistic expansion of the 5d orbitals and the ensuing improved bonding in the higher oxidation state dominate. The destabilization of the Au(I) halides by the relativistic contraction of the 6s-orbital provides an additional, smaller driving force in favor of the higher oxidation state.

Point b, that is, the fact that solvent effects destabilize the higher oxidation state is in keeping with previous studies on, for example, mercury fluorides regarding environmental effects on the relative stability of different oxidation states. For example, it has been shown that aggregation of  $\text{HgF}_2$  in the solid state disfavors the formation of  $\text{HgF}_4$  [285]. The reason is the larger M-X bond polarity of the halides in the lower oxidation state, in the present case  $\text{AuX}_2$  compared to  $\text{AuX}_4^-$ . This is obvious from the halogen natural population analysis (NPA) charges in Table 4.7, which generally have more negative values for the Au(I) than for the Au(III) complex. Solvation enhances the negative halogen charge (and thus the bond polarity) further, again in particular for the Au(I) complexes, and in particular at the nonrelativistic level. Due to the larger interactions for the more ionic Au(I) halides, this leads to a destabilization of the Au(III) state, most pronouncedly so for the fluoride. However, as the relativistic contraction of the 6s orbital reduces substantially the bond polarity in the Au(I) halides and far less for the Au(III) halides (due to the 5d orbital involvement in bonding), the differences in halogen charges between Au(I) and Au(III) complex are diminished considerably at the scalar relativistic level (Table 4.7). Therefore, the ability of the solvent effects to destabilize the Au(III) oxidation state relative to the Au(I) state is reduced appreciably by relativity. This explains the nonadditivity of solvent and relativistic effects, point c.

We note further that all of these observations are more pronounced for D-COSMO-RS than for COSMO, in line with the additional effect of hydrogen bonding beyond the bulk solvent contribution. Figure 4.8 provides a further illustration of these considerations by plotting surface charge densities for all species studied, comparing COSMO and D-COSMO-RS results for  $\text{X} = \text{Cl}$ . It is clear that the charge densities around the

chlorine atoms are much more negative for  $\text{AuCl}_2^-$  compared to  $\text{AuCl}_4^-$ , and that this difference is far less pronounced at the scalar relativistic than at the nonrelativistic level. Moreover, the COSMO and D-COSMO-RS surface charge densities for  $\text{AuCl}_2^-$  show the most pronounced differences as well: at the nonrelativistic level, the main effect of D-COSMO-RS over COSMO is a more negative surface charge density along the molecular axis, corresponding to a less pronounced “ $\sigma$ -hole”. In contrast, at the scalar relativistic level, D-COSMO-RS enhances the surface charge density cylindrically around the chlorine atoms, whereas the  $\sigma$ -hole is even enhanced slightly. Moreover, the surface charge densities around the gold center are increased (they become positive) by relativity, and they are decreased (they become more negative or less positive) at D-COSMO-RS compared to COSMO level (note that the surface charge densities are those induced by the solute at the surface of the COSMO cavity, i.e., the signs are complementary to, e.g., the atomic charges).

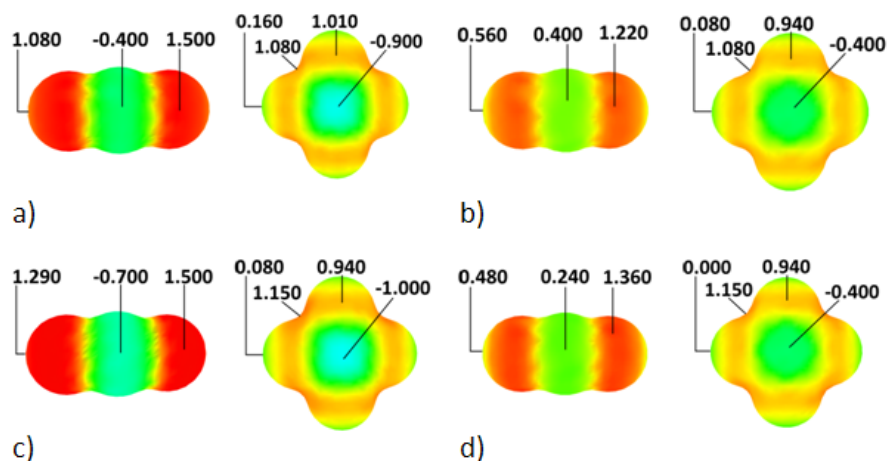


Figure 4.8: COSMO and D-COSMO-RS surface charge density plots for  $\text{AuCl}_2^-$  and  $\text{AuCl}_4^-$ . Numbers for areas with maximum or minimum surface charges (in  $\text{e}/\text{nm}^2$ ). (a) COSMO nonrelativistic, (b) COSMO scalar relativistic, (c) D-COSMO-RS nonrelativistic, (d) D-COSMO-RS scalar relativistic.

#### 4.2.3.4 On the Hydrolysis of $\text{AuCl}_4^-$

Speciation of gold chlorides in aqueous solution is of substantial geochemical importance, for example, in the context of Au transport, deposition, and concentration [286]. While  $\text{AuCl}_4^-$  clearly dominates in acidic chloride solutions (with reduction to  $\text{AuCl}_2^-$  occurring only at hydrothermal temperatures) [287], hydrolysis is known to play an increasing role at higher pH values [288]. Resonance Raman spectroscopy of dilute solutions at room

temperature has indicated that  $\text{AuCl}_4^-$  is the dominant species below  $\text{pH} = 5$ ; at  $\text{pH} = 5.8$ ,  $\text{AuCl}_3\text{OH}^-$  starts to form, becomes about equally important as  $\text{AuCl}_4^-$  at  $\text{pH} = 6.2$ , and should dominate near  $\text{pH} = 7$ . At still higher  $\text{pH}$  values, further hydrolysis takes place, and at  $\text{pH} > 10$ ,  $\text{AuCl}(\text{OH})_3^-$  is the dominant species. EXAFS spectroscopy also suggests that  $\text{AuCl}_3\text{OH}^-$  is the dominant species between  $\text{pH} = 7.5$  and  $9.2$  [289].

As our D-COSMO-RS calculations should most closely approximate the situation in dilute solution near neutral  $\text{pH}$  and ambient temperatures, we have computed the reaction energies for  $\text{AuCl}_4^- + \text{OH}^- \rightleftharpoons \text{AuCl}_3\text{OH}^- + \text{Cl}^-$  (Table 4.8). The results clearly show that both in the gas phase and for the solvent models used, the equilibrium is on the right-hand side. Solvation stabilizes  $\text{AuCl}_4^-$  more than  $\text{AuCl}_3\text{OH}^-$  and thus renders the reaction less exergonic. This effect is more pronounced with the more realistic D-COSMO-RS than with COSMO (Table 4.8). Relativity enhances the exergonicity slightly (by ca.  $13 \text{ kJ mol}^{-1}$  at D-COSMO-RS level). Most of this relativistic increase ( $9.3 \text{ kJ mol}^{-1}$ ) is already present in the gas phase, suggesting a largely intramolecular origin. Indeed, gold NPA charges in  $\text{AuCl}_4^-$  are relativistically reduced from 1.11 (1.09) to 0.97 (0.96) at the D-COSMO-RS (gas phase) level, and those in  $\text{AuCl}_3\text{OH}^-$  from 1.21 (1.19) to 1.10 (1.09). These charges point to an overall more polar bonding and to a smaller relativistic loss of ionic contributions to the binding energy in the hydroxo complex.

Table 4.8: Reaction energies, enthalpies, and Gibbs free energies (in  $\text{kJ mol}^{-1}$ ) for the  $\text{AuCl}_4^- + \text{OH}^- \rightleftharpoons \text{AuCl}_3\text{OH}^- + \text{Cl}^-$  and  $\text{AuCl}_3\text{OH}^- \rightleftharpoons \text{AuClO}^- + \text{Cl}_2$  reactions<sup>a</sup>

reaction	nonrelativistic			scalar relativistic		
	$\Delta E$	$\Delta G_{298K}$	$\Delta H_{298K}$	$\Delta E$	$\Delta G_{298K}$	$\Delta H_{298K}$
$\text{AuCl}_4^- + \text{OH}^- \rightleftharpoons \text{AuCl}_3\text{OH}^- + \text{Cl}^-$						
gas phase	-148.6	-133.4	-141.3	-158.6	-142.7	-150.6
COSMO	-84.8	-70.9	-78.4	-96.0	-81.3	-88.6
D-COSMO-RS	-65.4	-49.6	-59.0	-77.2	-62.6	-70.0
$\text{AuCl}_3\text{OH}^- \rightleftharpoons \text{AuClO}^- + \text{Cl}_2$						
gas phase	115.3	65.1	109.6	187.6	137.8	182.1
COSMO	66.4	16.2	60.9	147.6	98.6	142.4
D-COSMO-RS	22.0	-30.6	16.1	127.6	78.1	122.4

<sup>a</sup>Comparison of gas-phase and aqueous solution results (with COSMO and D-COSMO-RS) at B3LYP level with Turbomole, using a nonrelativistic or scalar relativistic Au ECP, respectively.

In view of the likely predominance of  $\text{AuCl}_3\text{OH}^-$  under the chosen conditions, it is also of interest to examine its redox stability (Table 4.8): the redox reaction  $\text{AuCl}_3\text{OH}^- \rightleftharpoons \text{AuClO}^- + \text{Cl}_2$  exhibits again the above-mentioned interplay between relativity and

solvation for the relative stabilities of Au(III) and Au(I) species. Relativity strongly favors  $\text{AuCl}_3\text{OH}^-$ , solvation favors reduction, and the nonadditivity between the two influences (larger solvent destabilization at nonrelativistic level) leads to the largest relativistic stabilization at D-COSMO-RS level ( $108.7 \text{ kJ mol}^{-1}$ ). The overall results are consistent with an overall predominance of  $\text{AuCl}_3\text{OH}^-$  in solution at neutral pH under the chosen ambient conditions, which clearly is a relativistic effect.

#### 4.2.3.5 Disproportionation of $\text{AuCl}_2$

In the abovementioned geochemical context, the disproportionation reaction  $3 \text{AuCl}_2 \rightleftharpoons \text{AuCl}_4^- + 2 \text{Au}_{(s)} + 2 \text{Cl}^-$  is of fundamental interest, and Table 4.9 provides computational data in solution that are again closest to dilute solution at neutral pH and ambient temperature. While the gas-phase data would suggest the equilibrium to be clearly on the left side, the interplay between solvation/aggregation and relativity shifts it to the right side. Here, the cohesion energy of solid gold is obviously a major contributor. We have taken the nonrelativistic and scalar relativistic computed energies ( $219.0$  and  $333.8 \text{ kJ mol}^{-1}$ , respectively) for it from the DFT-based work of ref. [290] (local density approximation with mixed plane-wave and Gaussian basis sets, scalar- vs nonrelativistic norm-conserving pseudopotentials). The scalar-relativistic value agrees reasonably well with the experimental cohesive energy ( $367.6 \text{ kJ mol}^{-1}$ ). It is clear that relativity shifts the equilibrium strongly to the right (a) due to the enhanced cohesion energy of solid gold, but also (b) due to the stabilization of  $\text{AuCl}_4^-$  relative to  $\text{AuCl}_2$  (see above). Solvation does in this case also contribute to a more exergonic reaction (Table 4.9), due to the efficient solvation of the chloride ions.

Table 4.9: Reaction energies, enthalpies, and Gibbs free energies (in  $\text{kJ mol}^{-1}$ ) for the disproportionation reaction  $3 \text{AuCl}_2 \rightleftharpoons \text{AuCl}_4^- + 2 \text{Au}_{(s)} + 2 \text{Cl}^-$ <sup>a</sup>

reaction	nonrelativistic			scalar relativistic		
	$\Delta E$	$\Delta G_{298K}$	$\Delta H_{298K}$	$\Delta E$	$\Delta G_{298K}$	$\Delta H_{298K}$
gas phase	616.0	664.0	605.3	506.2	539.1	494.5
gas phase (+cohesive energy <sup>b</sup> )	333.3	372.6	322.1	98.4	130.4	86.7
COSMO	192.1	236.2	181.2	-74.0	-42.0	-85.8
D-COSMO-RS	177.9	226.0	167.3	-161.5	-128.6	-173.2

<sup>a</sup>Comparison of gas-phase and aqueous solution results (with COSMO and D-COSMO-RS) at B3LYP level with Turbomole, using a nonrelativistic or scalar relativistic Au ECP, respectively.

<sup>b</sup>Cohesive energy for solid gold from non- and scalar relativistic DFT calculations, respectively (see text), added to the gas-phase data.

## 4.2.4 Conclusions

Not unexpectedly, scalar relativistic effects stabilize Au(III) halide complexes  $\text{AuX}_4^-$  ( $\text{X} = \text{F}, \text{Cl}, \text{Br}, \text{I}$ ) in solution against reductive elimination of halogen. Due to a strong nonadditivity between relativistic and solvent effects, the relativistic stabilization of the higher oxidation state is enhanced in solution. The D-COSMO-RS model, which simulates implicitly the effects of hydrogen bonding between solute and solvent, thus also provides larger relativistic stabilizations. DFT methods were calibrated against CCSD(T) gas-phase calculations. B3LYP calculations with D-COSMO-RS indicate that in dilute aqueous solution at neutral pH and ambient conditions, the  $\text{AuX}_4^-$  complexes are stable with respect to halogen elimination, except for the iodide, which exhibits a slightly exergonic reaction at this level. Calculations at the same level indicate that under the same conditions,  $\text{AuCl}_4^-$  is unstable against hydrolysis to  $\text{AuCl}_3\text{OH}^-$ , whereas the latter species in turn is redox-stable. Under these conditions,  $\text{AuCl}_2$  would exergonically disproportionate. All of these computational data are consistent with the available experimental observations on speciation of gold halides in dilute aqueous solution at neutral pH and ambient temperature, and they clearly expose the large role of relativity. Closer examination of the nonadditivity between relativity and solvent effects by analyses of NPA charges and surface charge densities has confirmed that the relativistic reduction of bond polarity, in particular for the AuI halide complexes, diminishes solvent effects compared to nonrelativistic levels. This, in turn, leads to smaller solvent destabilization of the Au(III) oxidation state.

# 5 Validation of Local Hybrid Functionals for the GMTKN30 Test Set

The contents of this chapter have been published in "Gauge effects in local hybrid functionals evaluated for weak interactions and the GMTKN30 test set" by K. Theilacker, A. V. Arbuznikov, M. Kaupp, *Mol. Phys.* **2016**, *114*, 1118.

## 5.1 Introduction

The accuracy of a single density functional can highly differ between the calculations of different properties. Chapters 3 and 4 of this work have highlighted the importance of selecting the right exchange-correlation functional for the specific quantum-chemical problem at hand. Often comparisons to experiment or high-quality benchmark calculations are used as a guideline to decide on a suitable density functional, but sometimes such data is not available. In such cases careful validation of functionals for a wide variety of reactions and properties is necessary to provide a good overview of the strengths and weaknesses of different density functionals. Ideally a good approximate exchange-correlation functional should perform well for all quantum-chemical tasks, and one goal in the development of local hybrids, as a new group of density functionals, is indeed to achieve consistently good results for a wide range of properties and applications.

While our initial successful local hybrids have been based on a mixing of only LSDA and exact exchange [22, 39, 40, 52, 291, 292], we have recently shown that calibration functions (CF) constructed only from (semi-)local ingredients can improve performance of GGA-based local hybrids for thermochemistry appreciably [49]. Importantly, we could identify too repulsive potential-energy curves for weakly interacting dimers, such

as the Ar<sub>2</sub> complex, as 'smoking gun' for the gauge problem. Indeed, adding suitable CFs corrected such unphysical Pauli repulsions and provided curves between those of the underlying GGA (LSDA) and the corresponding global hybrid incorporating the maximum exact-exchange admixture occurring in the local hybrid, as one might expect. We had previously optimized atom-pairwise additive dispersion corrections of Grimme's DFT-D3 type [41] for some of our local hybrids [44]. While these were LSDA-based local hybrids, the recent observations regarding a gauge problem for weak interactions suggested that the optimized DFT-D3 parameters may have partly compensated not only for van der Waals-type dispersion interactions but also for too repulsive curves caused by gauge problems.

Here we therefore compare local hybrids with and without calibration for the entire GMTKN30 test set of Goerigk and Grimme [230,293]. It contains distinct subsets of thermochemical and kinetic data with or without a strong dependence on dispersion interactions. By evaluating the effects of DFT-D3 corrections for calibrated and uncalibrated local hybrids for each subset, we aim at gaining insight into the role of calibration of exchange-energy densities, and at obtaining a wider validation of several existing local hybrid functionals on the large GMTKN30 data set. The obtained results should subsequently aid in constructing more refined local hybrids that properly take into account the calibration of exchange-energy densities.

Figure 5.1. gives an overview on the GMTKN30 test set database and its division into three big areas; basic properties, reaction energies and noncovalent interactions. It also gives a feeling for the amount of data points gathered in each subset and the average reference values, to better judge the relative accuracy of DFT calculations for each property. For example PBE0 gives a relative error of less than 2% for the atomization energies of the W4-08 subset, but a staggering 22% for the kinetic barriers in the BH76 subsets, even though the absolute MAE in both cases is roughly in the same ballpark (3.7 and 4.1 kcal/mol respectively). Overall more than 1200 single-points were done to collect over 800 data points of information in every single run of this extensive test set database. Since the structure and ideas behind local hybrids are shown in detail in Chapter 2.1.3, their exact mathematical forms and parameters will not be discussed again in this chapter. This includes information about the calibration function to counter the gauge origin problem and the range-separation of the correlation part for the latest uncalibrated LSDA based local hybrids. Table S1 in Appendix III gives an overview over local hybrids used in this work for the interested reader and their semi-empirical

parameters.

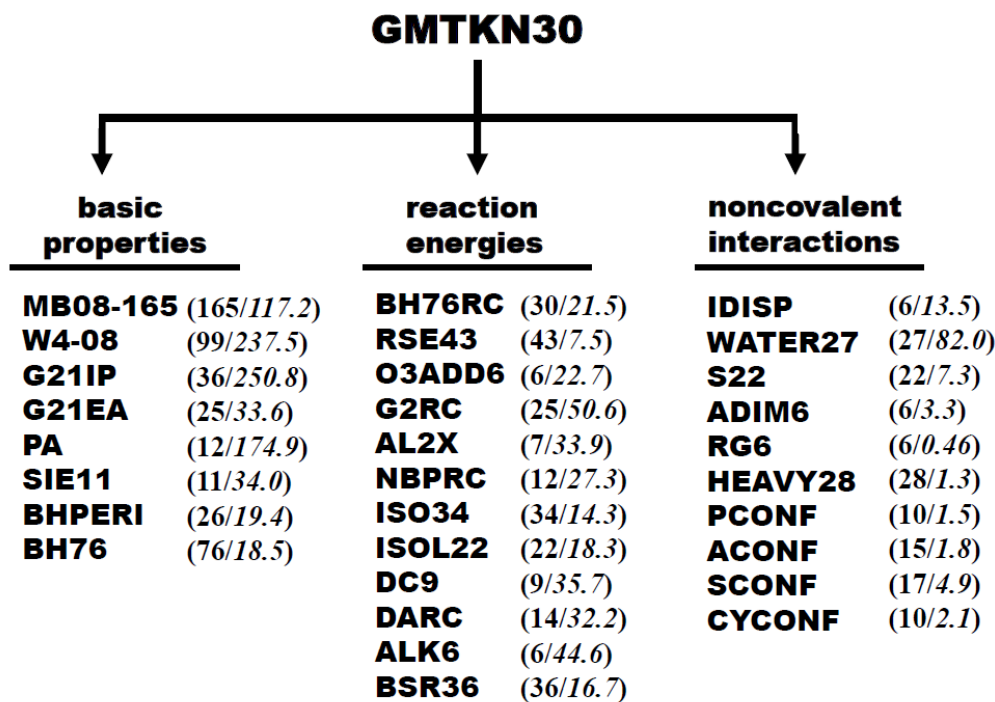


Figure 5.1: Rough breakdown of the GMTKN30 test set database into its three areas and their subsets. The number of data points for each subsets is given in parentheses, followed by the absolute of the average reference values in kcal/mol.

## 5.2 Computational Details

All calculations were performed with a local development version of the TURBOMOLE program V6.4 [111–113]. Uncontracted def2-QZVP basis sets have been employed throughout. Energies have been evaluated non-self-consistently, based on B3LYP orbitals, a procedure that is adequate for the present preliminary evaluation of new functionals for energies (see ref. [294] and references therein). We have additionally checked this by comparison with fully self-consistent calculations on the MB08-165 subset (selected for having the electronically most difficult cases within the GMTKN30 test set). Using the LSDA-based local hybrid with *t*-LMF (with D3 corrections), the self-consistent calculations provided an MAE (MSE) of 7.27 kcal/mol (-0.66 kcal/mol), whereas the post-B3LYP calculations with the same functional gave 7.31 kcal/mol (-0.68 kcal/mol). This

confirms the negligible differences between the two setups for relative energies. Evaluation of the exact exchange energy density used a recently implemented semi-numerical implementation [295].

The functional-specific D3 parameters  $s_{r,6}$  and  $s_8$  for each local hybrid (with Chai/Head-Gordon damping [68]) were fitted to the S22 weak-interaction test set [42], using the refined reference data of Takatani *et al.* [43]. A Simplex algorithm was used for the optimization of the D3 parameters, as was used for the optimization of the LMF parameters beforehand (joint optimizations of LMF and D3 parameters have been tried [44], but did not prove to be useful for LMFs with calibration functions and more than two semi-empirical parameters). The optimized D3 parameters are listed in Table 5.1 (those for the global (PW6B95) and double hybrids (DSD-BLYP) are from the literature [296]).

We followed Goerigk/Grimme’s [230, 293] prescription for a weighted mean absolute deviation (WTMAD):

$$\begin{aligned} \text{WTMAD} = & \frac{1}{3091.4} [445.5 \cdot \{\text{MB08-165}\} + 222.75 \cdot \{\text{W4-08}\} + 72.0 \cdot \{\text{G21IP}\} \\ & + 60.0 \cdot \{\text{G21EA}\} + 19.2 \cdot \{\text{PA}\} + 26.4 \cdot \{\text{SIE11}\} + 117.0 \cdot \{\text{BHPERI}\} \\ & + 222.75 \cdot \{\text{BH76}\} + 90.0 \cdot \{\text{BH76RC}\} + 150.5 \cdot \{\text{RSE43}\} + 13.2 \cdot \{\text{O3ADD6}\} \\ & + 77.5 \cdot \{\text{G2RC}\} + 49.7 \cdot \{\text{AL2X}\} + 62.4 \cdot \{\text{NBPRC}\} + 98.6 \cdot \{\text{ISO34}\} \\ & + 72.6 \cdot \{\text{ISOL22}\} + 36.9 \cdot \{\text{DC9}\} + 86.8 \cdot \{\text{DARC}\} + 15.0 \cdot \{\text{ALK6}\} \\ & + 222.75 \cdot \{\text{BSR36}\} + 69.0 \cdot \{\text{IDISP}\} + 75.6 \cdot \{\text{WATER27}\} + 222.75 \cdot \{\text{S22}\} \\ & + 96.6 \cdot \{\text{ADIM6}\} + 22.2 \cdot \{\text{RG6}\} + 114.8 \cdot \{\text{HEAVY28}\} + 138.0 \cdot \{\text{PCONF}\} \\ & + 52.5 \cdot \{\text{ACONF}\} + 88.4 \cdot \{\text{SCONF}\} + 50.0 \cdot \{\text{CYCONF}\}]. \end{aligned}$$

We note in following that during this work on local hybrids, D3 parameters were also fitted in the same way for the B35LYP global hybrid introduced by Kaupp *et al.*. B35LYP is used as the functional of choice in a quantum chemical protocol to calculate properties of mixed-valence systems, especially spin-localisation and excitation energies of the inter-valence charge-transfer (IV-CT) band in the UV/VIS spectra. Its latest application, together with the optimized D3 dispersion correction was for the description of electron transfer pathways in paracyclophane-bridged mixed-valence systems [297]. The dispersion parameters for B35LYP and its performance for the GMTKN30 and S22 test sets can be found in Tables S6 and S9 in Appendix III.

## 5.3 Evaluation for the GMTKN30 Database

We evaluate overall nine local hybrids of different generations, of which seven are LSDA-based functionals without calibration (going from the *t*- and *s*-LMF to their spin-polarized counterparts, and to their latest range-separated and self-interaction free/reduced versions), and two are GGA-based (*Lh*-BLYP-CG and *Lh*-PBE-CG) with calibration according to equation 2.37 [49]. We chose 'CG' instead as 'CF' to stress the fact, that we used simple gaussian functions as CFs. For comparison, we provide data from [296] for three global hybrids (B3LYP [15, 23], PBE0 [14, 31, 117], and PW6B95 [298]), and for the DSD-BLYP double hybrid [19]. While B3LYP and PBE0 were chosen as 'parent' global hybrids related to the two GGA-based local hybrids we will evaluate, we have included PW6B95 as the 'best-performing global hybrid' (the highly parameterized,  $\tau$ -dependent M06-2X [299] gave a still slightly lower WTMAD in [296]) and DSD-BLYP as the best-performing double hybrid (and overall best-performing functional) from ref. [296]. Table 5.1 provides the total WTMAD values for all functionals, which are graphically presented (with and without D3 corrections) in Figure 5.2. Let us start with the performance in the absence of the dispersion corrections: we first note the order of performance of the global hybrids (with PW6B95 performing best) and of the clearly superior DSD-BLYP double hybrid (the main-group energetics of GMTKN30 appears to be particularly suitable to emphasise the strengths of double hybrids).

Strikingly, the uncalibrated local hybrids perform relatively poorly in the absence of D3 correction terms, either comparable or somewhat better/worse than B3LYP. Only the calibrated GGA-based local hybrids perform better without D3 terms, in particular *Lh*-PBE-CG. This functional is close to the quality of the best global hybrid, PW6B95. While the performance of all functionals benefits from the dispersion corrections (below we will analyse the most affected subsets in detail), the 'improvement' for the uncalibrated local hybrids is by far most pronounced. Indeed, after addition of D3 terms, the differences in the performance of the local hybrids become rather small, and even some of the uncalibrated LSDA-based ones can now compete with the best global hybrids. This confirms our previous suspicion (see above) that exaggerated Pauli repulsions due to the gauge problem affect appreciably the performance of the uncalibrated local hybrids for cases where weak interactions become important. This will be evaluated in more detail below. Regarding the overall WTMADs, we see that reduction by D3 terms tends to be below 1 kcal/mol for PBE0, PW6B95, and DSD-BLYP (B3LYP exhibits a reduction by 2 kcal/mol or by a factor of 1.54; it is known to have some problems with

Table 5.1: Summary of WTMAD for the global and local hybrids studied. D3 dispersion-correction parameters are also provided.<sup>a</sup>

	D3 dispersion parameters		WTMAD	WTMAD+D3	ratio
	$s_{r,6}$	$s_8$	in kcal/mol	in kcal/mol	WTMAD/WTMAD+D3
global and double hybrids					
B3LYP	1.261	1.703	5.7	3.7	1.54
PBE0	1.287	0.928	4.3	3.7	1.16
PW6B95	1.523	0.862	3.3	2.5	1.32
DSD-BLYP <sup>b</sup>	1.569	0.705	2.2	1.5	1.47
local hybrids					
<i>Lh</i> -LSDA, <i>t</i> -LMF	0.959	1.021	5.5	2.8	1.96
<i>Lh</i> -LSDA, <i>ct</i> -LMF	1.450	3.025	6.3	3.3	1.91
<i>Lh</i> -LSDA, <i>s</i> -LMF	0.863	1.597	6.5	2.9	2.24
<i>Lh</i> -LSDA, $\zeta$ - <i>t</i> -LMF	1.011	0.972	4.9	2.7	1.81
<i>Lh</i> -LSDA, $\zeta$ - <i>s</i> -LMF	0.912	1.452	6.0	2.8	2.14
<i>Lh</i> -LSDA-SIF-SRc	0.765	1.714	6.4	3.0	2.13
<i>Lh</i> -LSDA-SIR-SRc	0.770	1.429	6.3	2.7	2.33
<i>Lh</i> -BLYP-CG	1.060	0.975	4.5	2.6	1.73
<i>Lh</i> -PBE-CG	1.204	0.792	3.7	2.6	1.42

<sup>a</sup>Semi-empirical parameters for the local hybrids and data for additional functionals are provided in Table S1 in Appendix III.

<sup>b</sup>DSD-BLYP has  $s_6=0.5$  instead of 1.0

intermediate-range correlation effects [231, 284]).

A factor between 1.2 and 1.5 is a typical range of reduction also for many other functionals, except possibly for some Minnesota functionals where medium-range correlation effects are already fitted into the functional and the D3 corrections tend to be smaller [296]. In contrast, the effect of the D3 corrections is much larger for the uncalibrated local hybrids, between ca. 2.3 kcal/mol for the *Lh*-LSDA with  $\zeta$ -*t*-LMF and ca. 3.8 kcal/mol for *Lh*-LSDA-SIR-SRc or, probably more revealingly, by factors between 1.81 and 2.33 (Table 5.1). Calibration reduces the effect of the dispersion terms, to ca. 1.8 kcal/mol for *Lh*-BLYP-CG and to ca. 1.1 kcal/mol for *Lh*-PBE-CG, or to factors 1.73 and 1.42, respectively. These results indicate the need for calibration and its effect on weak interactions. They suggest also, however, that the presently used gauge functions may not yet remove the gauge artifacts completely. This holds in particular for *Lh*-BLYP-CG, where we note the relatively large exponent  $\eta = 0.5$  of the Gaussian cut-off function of the CF (equation 1.37 [49]). Obviously, matters are already significantly better for *Lh*-PBE-CG. Here the calibration with a more diffuse cut-off of  $\eta = 0.12$  appears more effective [45], and the effect of the D3 corrections on the WTMAD approaches the genuine physical dispersion contributions found for typical standard functionals (differences

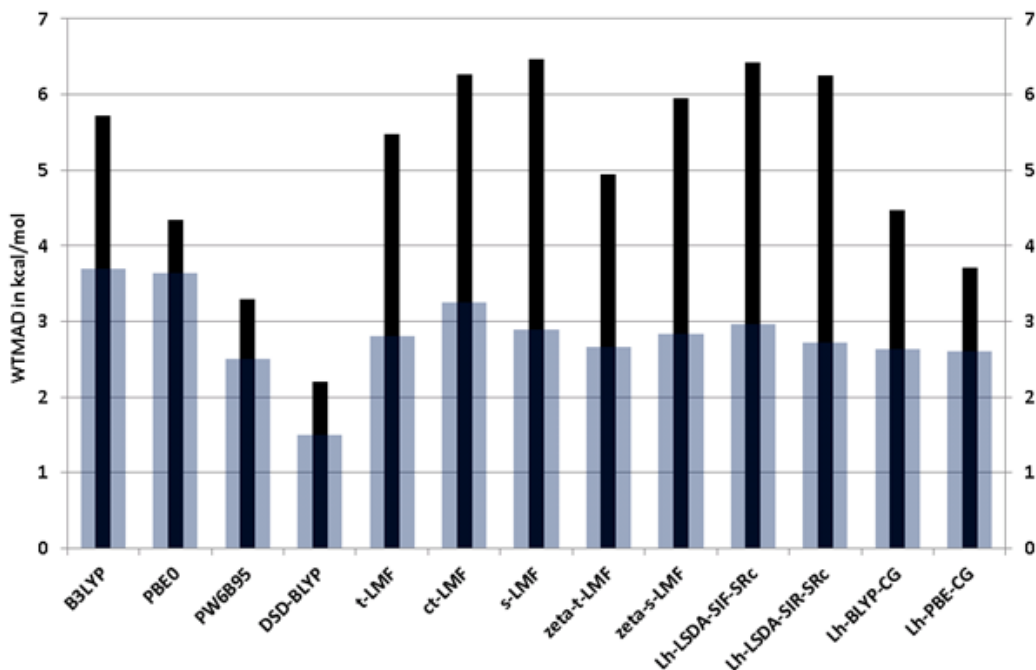


Figure 5.2: Weighted total mean absolute deviation (WTMAD) of different global, double, and local hybrids for the complete GMTKN30 test set database. Black bars give the errors without, grey bars with D3 corrections.

in the medium-range repulsive/attractive character of various functionals notwithstanding). This suggests already the preliminary conclusion that there is substantial room for improvement of the CFs to provide even better performing local hybrid functionals. We note also, however, that even the relatively crudely optimized [49] *Lh*-PBE-CG functional clearly outperforms its 'underlying' global hybrid PBE0, and the same holds for *Lh*-BLYP-CG vs B3LYP (Figure 5.2 and Table 5.1).

To analyse the above observations more closely, Figure 5.3 concentrates on the MAEs for some subsets of GMTKN30, which are known to be particularly sensitive to dispersion contributions (see Tables S2-S6 in Appendix III for detailed statistics for the various GMTKN30 subsets on different functionals). We compare one uncalibrated LSDA-based local hybrid (*Lh*-LSDA-SIF-SRc, blue) and the calibrated *Lh*-PBE-CG (black) with and without dispersion corrections. In the absence of D3 corrections (solid lines), the calibrated functional is vastly superior in most cases. This holds in particular for the WATER27 test set. It is obvious that the gauge problem affects the weak intermolecular interactions in these water clusters appreciably for the uncalibrated functional (leading to far too weak binding and to an MAE of more than 30 kcal/mol). The calibrated

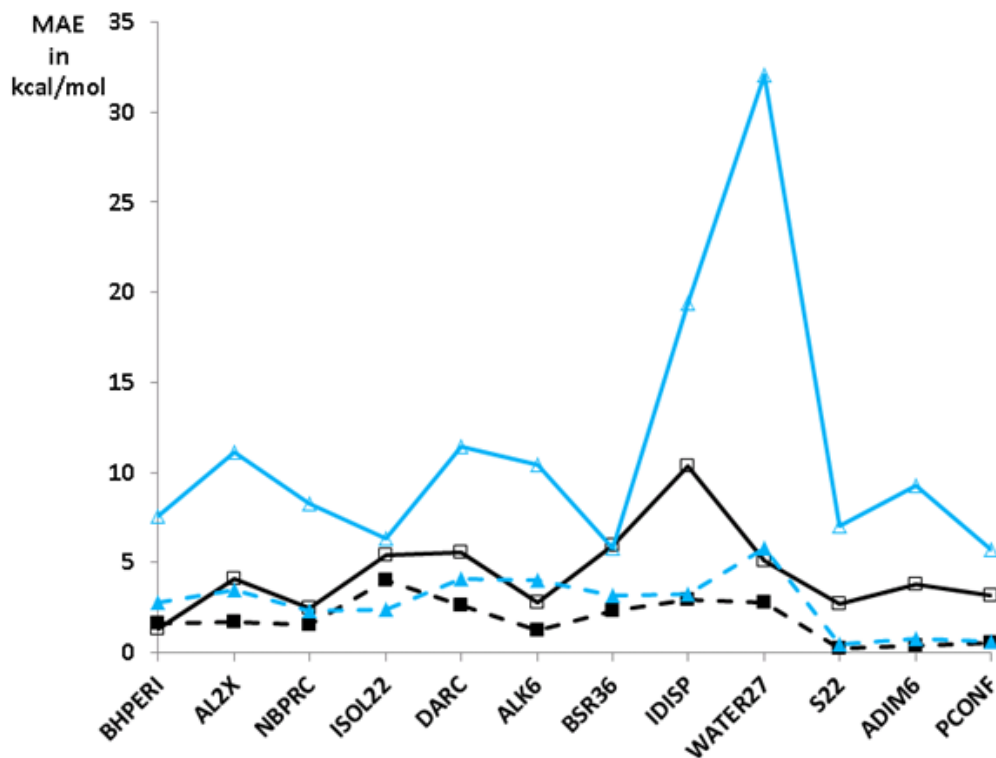


Figure 5.3: Mean absolute errors (MAE) of the *Lh*-PBE-CG (black) and the *Lh*-LSDA-SIF-SRc (blue) local hybrids for twelve GMTKN30 subsets with the largest dependence on dispersion contributions. Solid lines are without, dashed lines with D3 corrections.

functional does not exhibit this problem and has a modest MAE of ca. 5 kcal/mol without dispersion. Consequently, the D3 corrections reduce the MAE dramatically for the uncalibrated local hybrid and much less so for the calibrated one (Figure 5.3 and Tables S5 and S6 from Appendix III). Other subsets where the gauge artefacts apparently spoil the performance of the uncalibrated local hybrid most pronouncedly are BHPERI, AL2X, NBPRC, DARC, ALK6, IDISP, S22, and ADIM6. After adding the D3 corrections, even the uncalibrated functional provides low MAEs for most of the subsets (AL2X, ALK6, DARC, and WATER27 still are reproduced relatively poorly). However, this is likely the right answer for the wrong reason, as we burden the D3 terms with also correcting for the gauge artefacts.

Extending the comparison between the uncalibrated and calibrated functional to all of the subsets of GMTKN30 (Figure 5.4), we seek to evaluate if the gauge problem is also found for cases where dispersion is less important. We see some notable albeit not dramatic effects of the D3 corrections for the uncalibrated functional (but not for the

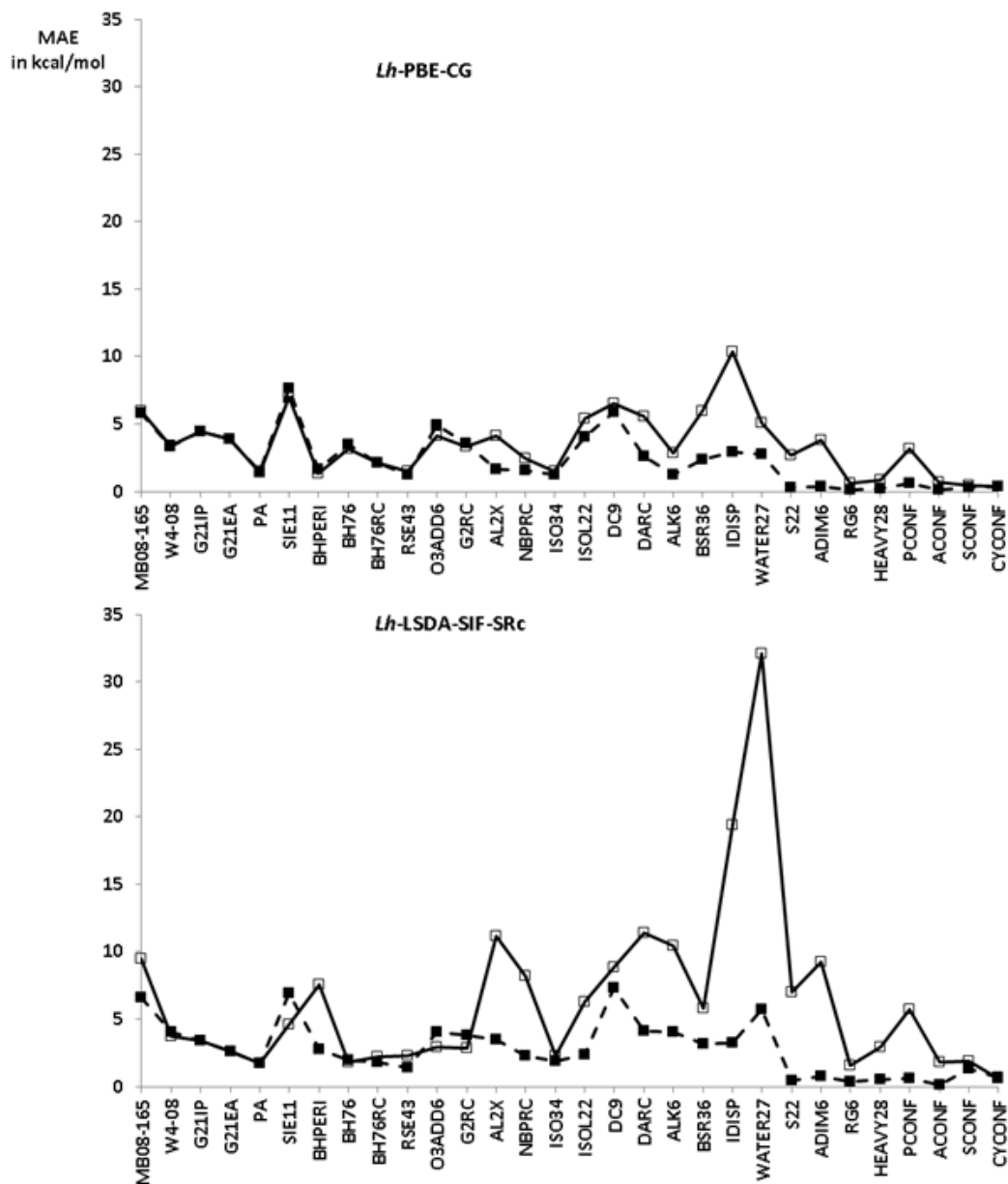


Figure 5.4: Mean absolute errors (MAE) of the *Lh*-PBE-CG and the *Lh*-LSDA-SIF-SRc local hybrids for all subsets of the GMTKN30 test set database. Solid lines are without, dashed lines with D3 corrections.

calibrated one!) for MB08-165, SIE11, ACONF, and HEAVY28. Other sets are clearly unaffected by both dispersion effects and by gauge problems. Examples are W4-08 (atomisation energies), G21IP (ionisation potentials), G21EA (electron affinities), PA (proton affinities), BH76 (barriers), ISO34 (isomerization energies), as well as SCONF and CYCONF. In case of SIE11 (SIE-sensitive energies), it has been found before that

the D3 corrections actually increase the MAE [296]. It appears that this increase is also exaggerated by 'over-fitted' corrections for the uncalibrated local hybrids (Tables S3-5 in Appendix III).

As the S22 set has been used to fit the parameters of the D3 corrections, it is obvious that exaggerated dispersion terms must result from such a fit in case of uncalibrated local hybrids. Indeed, Tables S7 and S8 in Appendix III shows for the individual energies of the S22 set how the gauge problem clearly increases the magnitude of the dispersion terms in an unphysical way. For example, without dispersion corrections the deviations from the reference values for *Lh*-PBE-CG for the dispersion-dominated subclass of complexes are lower than those for the uncalibrated *Lh*-LSDA-SIF-SRc by typically a factor of 2-4. After D3 corrections, deviations for both functionals are generally below 1 kcal/mol.

## 5.4 Conclusions

This chapter has highlighted the influence of the so-called gauge problem of exchange-energy densities of local hybrid functionals for weak interactions. We have subsequently chosen the large GMTKN30 test set of Goerigk and Grimme to shine further light on the interrelations between the gauge/calibration problem of local hybrids and weak interactions. As we focused in particular on subsets that depend crucially on dispersion interactions, we have optimized the adjustable parameters of the DFT-D3 corrections for a larger variety of local hybrids to the S22 weak-interaction energies. The results show clearly that for uncalibrated local hybrids, the D3 corrections not only include the genuine dispersion contributions but also correct for the systematically too repulsive behavior of the underlying functional. In contrast, use of calibrated energy densities diminishes significantly the extent of the D3 corrections, which now largely account indeed only for the physical interactions, as they were intended to do. For example, the calibrated *Lh*-PBE-CG functional performs comparably to the best global hybrids in the literature (and clearly superior to its underlying global hybrid PBE0) for the entire GMTKN30 set and its subsets, and it requires very similar dispersion corrections. The present insights provide us with further directions on how to improve CFs and to thus arrive at improved local hybrid functionals. Due to their enhanced flexibility, these should outperform global hybrids for a wide range of properties. This is important, as position-dependent exact-exchange admixture promises improvements significantly beyond the energy quantities studied here. With the efficient implementation of gradients for struc-

ture optimizations and numerical frequency calculations, local hybrid functionals could be used as good alternatives to global hybrid functionals in the future. Together with dispersion corrections and cheap implicit modeling of solvent effects, these functionals have the potential to improve the usefulness and accuracy of KS-DFT calculations for many applications.

## 6 General Summary

In this work, a variety of different chemical topics and questions has been investigated by density-functional theory methods, ranging from the electronic structure of transition metal complexes, via modeling of solvent effects on chemical reactions to the validation of local hybrid functionals. Chapter 3 deals in with synthetic high-valent non-heme iron-oxo and related complexes, that were created in order to mimic different reactive iron-oxo species in enzymes. These complexes are efficient catalysts for various important redox reactions. Our main interest has been the correct description of the electronic structure, and we thus first dealt with the question, whether some or most of the published iron(IV)- and iron(V)-oxo complexes might be better considered iron(III)- or iron(IV)-oxyl radicals, respectively. To this end a selection of important non-heme complexes was investigated, that are formally described as iron(IV)- or iron(V)-oxo species. For the formal iron(IV)-oxo complexes, closer examination of population analyses revealed a far higher amount of spin on the oxygen than one would expect for a true oxo complex. This was especially pronounced for compounds with a triplet ground state, where we found spin densities of 0.7-0.85 at the oxygen ligand, with only somewhat lower values for complexes with quintet ground states. These results, which support significant iron(III)-oxyl radical character in the formal iron(IV)-oxo complexes, proved to be very stable with regard to the choice of electronic-structure method. Extensive comparisons to experimental data for structure, spin-state energetics, Mössbauer parameters and zero-field splittings confirmed the correctness of the electronic structure interpretations and spin distributions. The iron(V)-oxo complexes, on the other hand, exhibited spin density largely localized at the iron center, with much less oxyl radical character. We furthermore examined the situation at the transition states of H-abstractions from 1,4-cyclohexadiene by formal iron(IV)-oxo species. Contrary to assumptions found in the literature, the oxyl radical character of S=2 species actually decreased towards the transition state of the reaction.

In Chapter 3.4 two formal iron(IV)-oxo complexes with newly designed N<sub>5</sub> pentadentate

ligands, synthesized by Grohmann *et al.*, were examined to study the effects of structural distortion on different molecular properties. An ethylene bridge in one of the ligands introduces high steric strain in the formal iron(IV)-oxo compound, forcing the molecule into a very distorted octahedral coordination compared to its open-chain congener. This structural distortion greatly increases reactivity and nearly closes the energy gap between quintet and triplet spin state, allowing for very easy spin-crossover, but at the same time makes the determination of the ground state very difficult. Additional TDDFT calculations supported a triplet ground state, based on good qualitative agreement to experimental data. Since both compounds could have formed as one of two structural isomers, all possible isomers have been investigated, and the same isomeric form has been found to be the most likely structure for both complexes. The electronic structures of the compounds showed big similarities to the other investigated formal iron(IV)-oxo complexes with triplet ground states. In Chapter 3.5 a formal iron(V)-nitrido complex has been examined, for which unexpected problems in reproducing experimental Fe-N stretching frequencies with hybrid DFT calculations had been found by our collaborators. It turned out that the strongly underestimated vibrational frequencies found with hybrid functionals like B3LYP, PBE0 or in particular BHLYP were due to substantial spin contamination in the unrestricted Kohn-Sham calculations. The underlying reason was the strongly metal-ligand antibonding character of the singly-occupied molecular orbital in the doublet ground-state complex. Increasing exact-exchange admixture in the functional aggravated the contamination by quartet excited states, to the extent that BHLYP even gave completely erroneous Fe-N distances. The problem could be circumvented by carrying out restricted open-shell Kohn-Sham calculations, which provided much better agreement with experimental frequencies. Alternatively, the TPSSh hybrid functional with lower exact-exchange admixture also provided reasonable results.

In Chapter 4 the detailed modeling of solvation effects in aqueous solution have been studied, encompassing such different reactions as Diels-Alder reactions in water and the redox and hydrolysis speciation of aqueous gold(III) halides. In both cases the new D-COSMO-RS solvent model was used and validated, always in comparison to gas-phase calculations and the COSMO continuum solvent model. For the Diels-Alder reactions (4.1), solvents like acetonitrile and methanol were also used in the calculations, as they have a very similar permittivity, but differ in the ability to form hydrogen bonds, which are crucial for the lowering of the kinetic barrier in solution. In order to select the best functional for calculating kinetic barriers and reaction energies of two Diels-Alder reactions, that had been previously studied by expensive QM/MM/MC simulations, ini-

tial gas-phase benchmark calculations with SCS-MP2 and CCSD(T) have been done. Their outcomes immediately showed the importance of a careful choice of functional, as the popular and widely used B3LYP hybrid functional proved completely unsuitable for these Diels-Alder reactions. Based on the benchmark study, the PBE0 functional was selected for the study of reactions in solution, and the inclusion of D3 dispersion corrections turned out to be very important as well. The D-COSMO-RS method, which goes significantly beyond continuum solvent models and includes also crucial hydrogen-bond terms, gave very good results for solvent contributions, and was a significant improvement over COSMO for water and methanol. Effects of hydrogen-bonding were also modeled by explicit addition of water molecules. D-COSMO-RS was found to be best used without explicit solvent molecules. COSMO with some explicit water molecules added gave results very close to D-COSMO-RS. Given its very low computational cost and excellent performance in comparison to QM/MM/MC simulations, the D-COSMO-RS method offers a convenient and easy way to combine an accurate treatment of solvent effects, including mixtures and hydrogen-bonding, with good underlying QM methods.

Similar methodology has been applied in 4.2 to the speciation of Au(III) halides in water, where we have studied both reduction to Au(I) species and hydrolysis. We found a strong nonadditivity between relativistic and solvent effects. Unsurprisingly, scalar relativistic effects played a large role in stabilizing Au(III) halide complexes, while the aqueous solvent environment generally had a destabilizing effect. This destabilizing effect was much smaller in the scalar relativistic calculations, than in the nonrelativistic ones, and the relativistic stabilization in solution was much higher for D-COSMO-RS, than for COSMO. Again, these examples showed the usefulness of implicit simulation of hydrogen-bonding by D-COSMO-RS for accurately simulating aqueous solvents. Our results indicated, that except for the iodide,  $\text{AuX}_4^-$  complexes in aqueous solution are stable with respect to halogen elimination at neutral pH and under ambient conditions. Under the same conditions,  $\text{AuCl}_4^-$  was calculated to be unstable against hydrolysis to  $\text{AuCl}_3\text{OH}^-$ , which in turn is redox-stable, and  $\text{AuCl}_2^-$  would exergonically disproportionate. Analyses of NPA charges and surface charge densities revealed, that the reduction of bond polarity by relativistic effects diminishes solvent effects compared to nonrelativistic levels. All our results were consistent with available experimental data on the speciation in dilute aqueous solution at ambient conditions.

The importance of the exchange-correlation functional has been studied in Chapter 5, which dealt with a validation of the performance of local hybrid functionals for the large

GMTKN30 test set database of Goerigk and Grimme. With thirty subsets that cover not only basic properties like atomization energies, kinetic barriers, ionization potentials and electron affinities but also include test sets for many different reaction energies and noncovalent interactions, the results in this work are the most extensive validation of local hybrids reported so far. Evaluation with and without D3-type dispersion corrections was performed for a large subset of local hybrids with and without calibration of exchange-energy densities published so far, and the results were compared to PW6B95 and DSD-BLYP, the best-performing global and double-hybrid functionals tested previously for the GMTKN30 database as well as to B3LYP and PBE0. Most important in our validation was the influence of the so-called gauge problem of exchange-energy densities in local hybrids. This problem has plagued local hybrids since their very beginning, until the recent introduction of semi-local calibration functions. With the calibration functions present, the overly repulsive behavior of the local hybrids may be greatly reduced, and no drawbacks for atomization energies or kinetic barriers are observed, even when GGA exchange and correlation contributions are used for local hybrids. The D3 dispersion corrections for the local hybrids with calibration functions mostly simulate the physical interactions, as they should, instead of correcting also errors caused by the gauge problem. Supported by a good calibration function, the new local hybrids can compete with the best global hybrids available today and open the way for further improvement of local hybrids.

# References

- [1] P. Hohenberg, W. Kohn, *Phys. Rev. B* **1964**, *126*, 864.
- [2] W. Kohn, L. J. Sham, *Phys. Rev. A* **1965**, *140*, 1133.
- [3] A. Szabo, N. S. Ostlund, *Modern Quantum Chemistry*; Dover Publications Inc.: Mineola, New York, 1996.
- [4] R. G. Parr, W. Yang, *Density Functional Theory of Atoms and Molecules*, Vol. 16; Oxford Science Publications: New York, 1998.
- [5] J. P. Perdew, K. Schmidt, *Density Functional Theory and its Application to Materials*, AIP Conference Proceedings, Vol. 577; V. van Doren, C. van Alsenoy, P. Geerlings; Eds. AIP: Melville, NY, 2001, 1-20.
- [6] P. A. Dirac, *Proc. Cambridge Philos. Soc.* **1930**, *26*, 376.
- [7] J. C. Slater, *Phys. Rev.* **1951**, *81*, 385.
- [8] S. J. Vosko, L. Wilk, M. Nussair, *Can. J. Phys.* **1980**, *58*, 1200.
- [9] J. P. Perdew, A. Zunger, *Phys. Rev. B* **1981**, *23*, 5048.
- [10] J. P. Perdew, Y. Wang, *Phys. Rev. B* **1992**, *45*, 13244.
- [11] J. P. Perdew, *Phys. Rev. Lett* **1985**, *55*, 1665.
- [12] J. P. Perdew, W. Yue, *Phys. Rev. B* **1986**, *33*, 8800.
- [13] A. D. Becke, *Phys. Rev. A* **1988**, *38*, 3098.
- [14] J. P. Perdew, K. Burke, and M. Ernzerhof, *Phys. Rev. Lett* **1996**, *77*, 3865.
- [15] C. Lee, W. Yang, R. G. Parr, *Phys. Rev. B* **1988**, *37*, 785.
- [16] T. Van Voorhis, G. E. Scuseria, *J. Chem. Phys.* **1998**, *109*, 400.
- [17] A. D. Boese, N. C. Handy, *J. Chem. Phys.* **2002**, *116*, 9559.

- [18] Y. Zhao, D. G. Truhlar, *J. Chem. Phys.* **2006**, *125*, 194101.
- [19] S. Kozuch, D. Gruzman, J. M. L. Martin, *J. Phys. Chem. C* **2010**, *114*, 20801.
- [20] S. Grimme, *Chem. Phys.* **2006**, *124*, 034108.
- [21] Y. Zhang, X. Xu, W. A. Goddard III, *Proc. Natl. Acad. Sci. U. S. A.* **2009**, *106*, 4963.
- [22] M. Kaupp, H. Bahmann, A. V. Arbuznikov, *J. Chem. Phys.* **2007**, *127*, 194102.
- [23] A. D. Becke, *J. Chem. Phys.* **1993**, *98*, 5648.
- [24] L. A. Curtiss, K. Raghavachari, P. C. Redfern, J. A. Pople, *J. Chem. Phys.* **1997**, *106*, 1063.
- [25] L. A. Curtiss, K. Raghavachari, P. C. Redfern, V. Rassolov, J. A. Pople, *J. Chem. Phys.* **1998**, *109*, 7764.
- [26] L. A. Curtiss, K. Raghavachari, P. C. Redfern, J. A. Pople, *J. Chem. Phys.* **2000**, *112*, 7374.
- [27] J. P. Perdew, J. A. Chevary, S. H. Vosko, K. A. Jackson, M. R. Pederson, D. J. Singh, C. Fiolhais, *Phys. Rev. B* **1992**, *46*, 6671.
- [28] T. Leininger, H. Stoll, H. Werner, A. Savin, *Chem. Phys. Lett.* **1997**, *275*, 151.
- [29] T. Yanai, D. P. Tew, N. C. Handy, *Chem. Phys. Lett.* **2004**, *393*, 51.
- [30] O. A. Vydrov, J. Heyd, A. V. Krukau, G. E. Scuseria, *J. Chem. Phys.* **2006**, *125*, 074106.
- [31] J. P. Perdew, M. Ernzerhof, K. J. Burke, *Chem. Phys.* **1996**, *105*, 9982.
- [32] Y. Zhao, N. Gonzalez-Garcia, D. G. Truhlar, *J. Phys. Chem. A* **2005**, *109*, 2012.
- [33] L. A. Curtiss, P. C. Redfern, K. Raghavachari, *J. Chem. Phys.* **2005**, *123*, 124107.
- [34] A. Nakata, Y. Imamura, T. Otsuka, H. Nakai, *J. Chem. Phys.* **2006**, *124*, 094105.
- [35] A. V. Arbuznikov, M. Kaupp, *Chem. Phys. Lett.* **2004**, *386*, 8.
- [36] A. D. Boese, J. M. L. Martin, *J. Chem. Phys.* **2004**, *121*, 3405.
- [37] Y. Zhao, N. E. Schultz, D. G. Truhlar, *J. Phys. Chem. A* **2004**, *108*, 2715.
- [38] J. Jaramillo, G. E. Scuseria, M. Ernzerhof, *J. Chem. Phys.* **2003**, *118*, 1068.

- [39] H. Bahmann, A. Rodenberg, A. V. Arbuznikov, M. Kaupp, *J. Chem. Phys.* **2007**, *126*, 011103.
- [40] A. V. Arbuznikov, H. Bahmann, M. Kaupp, *J. Phys. Chem. A* **2009**, *113*, 11898-11906.
- [41] J. Antony, S. Ehrlich, H. Krieg, S. Grimme, *J. Chem. Phys.* **2010**, *132*, 154104.
- [42] P. Jurecka, J. Sponer, J. Cerny, P. Hobza, *Phys. Chem. Chem. Phys.* **2006**, *8*, 1985.
- [43] T. Takatani, E. G. Hohenstein, M. Malagoli, M. S. Marshall, C. D. Sherrill, *J. Chem. Phys.* **2010**, *132*, 144104.
- [44] K. Theilacker, A. V. Arbuznikov, H. Bahmann, M. Kaupp, *J. Phys. Chem. A*, **2011**, *115*, 8990.
- [45] K. Theilacker, A. V. Arbuznikov, M. Kaupp, *Mol. Phys.* **2016**, *114*, 1118.
- [46] F. G. Cruz, K.-C. Lam, K. Burke, *J. Phys. Chem. A* **1998**, *102*, 4911.
- [47] K. Burke, F. G. Cruz, K.-C. Lam, *J. Chem. Phys.* **1998**, *109*, 8161.
- [48] J. Tao, V. N. Staroverov, G. E. Scuseria, J. P. Perdew, *Phys. Rev. A* **2008**, *77*, 012509.
- [49] A. V. Arbuznikov, M. Kaupp, *J. Chem. Phys.* **2014**, *141*, 204101.
- [50] T. M. Maier, M. Haasler, A. V. Arbuznikov, M. Kaupp, *Phys. Chem. Chem. Phys.* **2016**, published online (DOI:10.1039/C6CP00990E ).
- [51] K. Theilacker, "Validierung neuer Dichtefunktionalmethoden", Diploma thesis (Universität Würzburg, 2010).
- [52] A. V. Arbuznikov, M. Kaupp, *J. Chem. Phys.* **2012**, *136*, 014111.
- [53] J. P. Perdew, V. N. Staroverov, J. Tao, G. E. Scuseria, *Phys. Rev. A* **2008**, *78*, 052513.
- [54] B. G. Janesko, G. E. Scuseria, *J. Chem. Phys.* **2007**, *127*, 164117.
- [55] P. de Silva, C. Corminboeuf, *J. Chem. Phys.* **2015**, *142*, 074112.
- [56] E. R. Johnson, *J. Chem. Phys.* **2014**, *141*, 124120.

- [57] T. Schmidt, E. Kraisler, A. Makmal, L. Kronik, S. Kümmel, *J. Chem. Phys.* **2014**, *140*, 18A510.
- [58] A. V. Arbuznikov, M. Kaupp, *J. Chem. Phys.* **2008**, *128*, 214107.
- [59] O. A. Vydrov, G. E. Scuseria *J. Chem. Phys.* **2006**, *125*, 234109.
- [60] J.-D. Chai, M. Head-Gordon *J. Chem. Phys.* **2008**, *128*, 084106.
- [61] J.-D. Chai, M. Head-Gordon *Phys. Chem. Chem. Phys.* **2008**, *10*, 6615.
- [62] J. Toulouse, A. Savin, H.-J. Flad *Int. J. Quantum Chem.* **2004**, *100*, 1047.
- [63] Y. Andersson, D. C. Langreth, B. I. Lundqvist, *Phys. Rev. Lett.* **1996**, *76*, 102.
- [64] A. D. Becke, E. R. Johnson, *J. Chem. Phys.* **2005**, *123*, 154101.
- [65] Y. Zhao, D. G. Truhlar, *Acc. Chem. Res.* **2008**, *41*, 157.
- [66] S. Grimme, *J. Comput. Chem.* **2004**, *25*, 1463.
- [67] S. Grimme, *J. Comput. Chem.* **2006**, *27*, 1787.
- [68] J.-D. Chai, M. Head Gordon, *Phys. Chem. Chem. Phys.* **2008**, *10*, 6615.
- [69] Q. Wu, W. Yang, *J. Chem. Phys.* **2002**, *116*, 515.
- [70] K. T. Tang, J. P. Toennies, *J. Chem. Phys.* **1984**, *80*, 3726.
- [71] Y. Liu, W. A. Goddard III, *Mat. Trans.* **2009**, *50*, 1664.
- [72] E. R. Johnson, A. D. Becke, *J. Chem. Phys.* **2005**, *123*, 024101.
- [73] E. R. Johnson, A. D. Becke, *J. Chem. Phys.* **2006**, *124*, 174104.
- [74] S. Grimme, S. Ehrlich, L. Goerigk, *J. Chem. Theory Comput.* **2011**, *32*, 1456.
- [75] H. Schröder, A. Creon, T. Schwabe, *J. Chem. Theory Comput.* **2015**, *11*, 3163.
- [76] R. L. Mössbauer, *Z. Phys.* **1958**, *151*, 124.
- [77] D. A. Shirley *Rev. Mod. Phys.* **1964**, *36*, 339.
- [78] M. Filatov *Coord. Chem. Rev.* **2008**, *253*, 594.
- [79] F. Neese, *Inorg. Chim. Acta.* **2002**, *337*, 181.
- [80] T. Liu, T. Lovell, W.-G. Han, L. Noodleman, *Inorg. Chem.* **2003**, *42*, 5244.

- [81] V. N. Nemykin, R. G. Hadt, *Inorg. Chem.* **2006**, *45*, 8297.
- [82] A. X. Trautwein, F. E. Harris, A. J. Freeman, J. P. Desclaux, *Phys. Rev. B.* **1975**, *11*, 4101.
- [83] S. Sinnecker, L. D. Slep, E. Bill, F. Neese, *Inorg. Chem.* **2005**, *44*, 2245.
- [84] M. P. Hendrich, W. Gunderson, R. K. Behan, M. T. Green, M. P. Mehn, T. A. Betley, C. L. Lu, J. C. Peters, *Proc. Natl. Acad. Sci. U.S.A* **2006**, *103*, 17107.
- [85] C. V. Popescu, M. T. Mock, S. A. Stoian, W. G. Dougherty, G. P. A. Yap, C. G. Riordan, *Inorg. Chem.* **2009**, *48*, 8317.
- [86] R. M. Silva, C. Gwengo, S. V. Lindeman, M. D. Smith, G. J. Long, F. Grandjean, J. R. Gardinier, *Inorg. Chem.* **2008**, *47*, 7233.
- [87] K. H. Hoppmann, A. Ghosh, L. Noodleman, *Inorg. Chem.* **2009**, *48*, 9155.
- [88] A. D. Bochevarov, R. A. Friesner, S. J. Lippard, *J. Chem. Theory Comput.* **2010**, *6*, 3735.
- [89] N. Yoshida, T. Ishida, F. Hirata, *J. Phys. Chem. B* **2008**, *112*, 433.
- [90] S. Aono, M. Nakagaki, T. Kurahashi, H. Fujii, S. Sakaki, *J. Chem. Theory Comput.* **2014**, *10*, 1062.
- [91] A. Klamt, *J. Phys. Chem.* **1995**, *99*, 2224.
- [92] F. Eckert, A. Klamt, *AIChE J.* **2002**, *48*, 369.
- [93] S. Sinnecker, A. Rajendran, A. Klamt, M. Diedenhofen, F. J. Neese, *Phys. Chem. A* **2006**, *110*, 2235.
- [94] A. Klamt, G. Schüürmann, *J. Chem. Soc. Perkin Trans. 2* **1993**, 799.
- [95] A. Klamt, V. Jonas, *J. Chem. Phys.* **1996**, *105*, 9972.
- [96] M. Renz, M. Kess, M. Diedenhofen, A. Klamt, M. Kaupp, *J. Chem. Theory Comput.* **2012**, *8*, 4189.
- [97] M. Renz, M. Kaupp, *J. Phys. Chem. A* **2012**, *116*, 10629.
- [98] J. T. Groves, R. C. Haushalter, M. Nakamura, T. E. Nemo, B. J. Evans, *J. Am. Chem. Soc.* **1981**, *102*, 2884.

- [99] C. A. Grapperhaus, B. Mienert, E. Bill, T. Weyhermüller, K. Wieghardt, *Inorg. Chem.*, **2000**, *39*, 5306.
- [100] A. B. McQuarters, M. W. Wolf, A. P. Hunt, N. Lehnert, *Angew. Chem., Int. Ed.* **2014**, *53*, 4750.
- [101] C. Krebs, D. G. Fujimori, C. T. Walsh, J. M. Bollinger Jr., *Acc. Chem. Res.* **2007**, *40*, 484.
- [102] W. Nam, *Acc. Chem. Res.* **2007**, *40*, 522.
- [103] J. Hohenberger, K. Ray, K. Meyer, *Nat. Commun.* **2012**, *3*, 720.
- [104] A. R. McDonald, L. Que Jr., *Coord. Chem. Rev.* **2013**, *257*, 414.
- [105] E. I. Solomon, K. M. Light, L. V. Liu, M. Srnec, S. D. Wong, *Acc. Chem. Res.* **2013**, *46*, 2725.
- [106] W. Nam, Y.-M. Lee, S. Fukuzumi, *Acc. Chem. Res.* **2014**, *47*, 1146.
- [107] N. Dietl, M. Schlangen, H. Schwarz, *Angew. Chem.* **2012**, *124*, 5638.
- [108] W. Lai, C. Li, H. Chen, S. Shaik, *Angew. Chem.* **2012**, *124*, 5652.
- [109] M. Schmidt, D. Wiedemann, A. Grohmann, *Inorg. Chim. Acta* **2011**, *374*, 514.
- [110] M. Schmidt, D. Wiedemann, B. Moubaraki, N. F. Chilton, K. S. Murray, K. R. Vignesh, G. Rajaraman, A. Grohmann, *Eur. J. Inorg. Chem.* **2013**, 958.
- [111] R. Ahlrichs, M. Baer, M. Haeser, H. Horn, C. Koelmel, *Chem. Phys. Lett.* **1989**, *162*, 165.
- [112] O. Treutler, R. Ahlrichs, *J. Chem. Phys.* **1995**, *102*, 346.
- [113] TURBOMOLE V6.3/6.4 a development of University of Karlsruhe and Forschungszentrum Karlsruhe GmbH, 1989-2007, TURBOMOLE GmbH, since 2007; available from <http://www.turbomole.com> (last accessed Nov. 12, 2015).
- [114] F. Weigend, R. Ahlrichs, *Phys. Chem. Chem. Phys.* **2005**, *7*, 3297.
- [115] J. M. Tao, J. P. Perdew, V. N. Staroverov, G. E. Scuseria, *Phys. Rev. Lett.* **2003**, *91*, 146401.
- [116] S. Grimme, *J. Comp. Chem.* **2006**, *27*, 1787.
- [117] C. Adamo, V. Barone, *J. Chem. Phys.* **1999**, *110*, 6158-69.

- [118] A. D. Becke, *J. Chem. Phys.* **1993**, *98*, 1372.
- [119] V. G. Malkin, O. L. Malkina, R. Reviakine, A. V. Arbuznikov, M. Kaupp, B. Schimmelpfennig, I. Malkin, K. Ruud, *MAG-ReSpect, version 2.1*, 2007.
- [120] M. Munzarova, M. Kaupp, *J. Phys. Chem. A* **1999**, *103*, 9966.
- [121] W. Kutzelnigg, U. Fleischer, M. Schindler, *NMR Basis Principles and Progress, Vol. 23*, Springer, Berlin/Heidelberg, 1990.
- [122] J.-U. Rohde, J.-H. In, M. H. Lim, W. W. Brennessel, M. R. Bukowski, A. Stubna, E. Münck, W. Nam, L. Que Jr., *Science* **2003**, *299*, 1037.
- [123] T. A. Jackson, J.-U. Rohde, M. S. Seo, C. V. Sastri, R. DeHont, T. Ohta, T. Kitagawa, E. Münck, W. Nam, L. Que Jr., *J. Am. Chem. Soc.* **2008**, *130*, 12394.
- [124] J.-U. Rohde, L. Que Jr., *Angew. Chem., Int. Ed.* **2005**, *44*, 2255.
- [125] C. V. Sastri, M. J. Park, T. Ohta, T. A. Jackson, A. Stubna, M. S. Seo, J. Lee, J. Kim, T. Kitagawa, E. Münck, L. Que Jr., W. Nam, *J. Am. Chem. Soc.* **2005**, *127*, 12494.
- [126] M. R. Bukowski, K. D. Koehntop, A. Stubna, E. L. Bominaar, J. A. Halfen, E. Münck, W. Nam, L. Que Jr., *Science* **2005**, *310*, 1000.
- [127] M. T. Green, J. H. Dawson, H. B. Gray, *Science* **2004**, *304*, 1653.
- [128] J. T. Groves, Models and mechanisms of cytochrome P450 action, in: P.R. Ortiz de Montellano (Ed.), *Cytochrome P450: Structure, Mechanism, and Biochemistry*; Kluwer Academic/Plenum Publishers, New York, 2005, p. 1.
- [129] J. Kaizer, E. J. Klinker, N. Y. Oh, J.-U. Rohde, W. J. Song, A. Stubna, J. Kim, E. Münck, W. Nam, L. Que Jr., *J. Am. Chem. Soc.* **2004**, *126*, 472.
- [130] E. J. Klinker, J. Kaizer, W. W. Brennessel, N. L. Woodrum, C. J. Cramer, L. Que Jr., *Angew. Chem., Int. Ed.* **2005**, *44*, 3690.
- [131] M. Martinho, F. Banse, J.-F. Bartoli, T. A. Mattioli, P. Battioni, O. Horner, S. Bourcier, J.-J. Girerd, *Inorg. Chem.* **2005**, *44*, 9592.
- [132] N. Ortega-Villar, V. M. Ugalde-Saldívar, M. C. Muñoz, L. A. Ortiz-Frade, J. G. Alvarado-Rodríguez, J. A. Real, R. Moreno-Esparza, *Inorg. Chem.* **2007**, *46*, 7285.

- [133] J. Kaizer, E. J. Klinker, N. Young Oh, J. U. Rohde, W. J. Song, A. Stubna, J. Kim, E. Münck, W. Nam, L. Que Jr., *J. Am. Chem. Soc.* **2004**, *126*, 472.
- [134] N. Kroll, K. Theilacker, M. Schoknecht, D. Baabe, D. Wiedemann, M. Kaupp, A. Grohmann, G. Hörner, *Dalton Trans.* **2015**, *44*, 19232.
- [135] F. Tiago de Oliveira, A. Chanda, D. Banerjee, X. Shan, S. Mondal, L. Que, E. L. Bominaar, E. Münck, T. J. Collins, *Science* **2007**, *315*, 835.
- [136] M. Ghosh, K. K. Singh, C. Panda, A. Weitz, M. P. Hendrich, T. J. Collins, B. B. Dhar, S. S. Gupta, *J. Am. Chem. Soc.* **2014**, *136*, 9524.
- [137] E. I. Solomon, T. C. Brunold, M. I. Davis, J. N. Kemsley, S.-K. Lee, N. Lehnert, F. Neese, A.J. Skulan, Y.-S. Yang, J. Zhou, *Chem. Rev.* **2000**, *100*, 235.
- [138] M. D. Wolfe, J. D. Lipscomb, *J. Biol. Chem.* **2003**, *278*, 829.
- [139] M. B. Neibergall, A. Stubna, Y. Mekmouche, E. Münck, J. D. Lipscomb, *Biochemistry* **2007**, *46*, 8004.
- [140] O. Y. Lyakin, K. P. Bryliakov, E. P. Talsi, *Inorg. Chem.* **2011**, *50*, 5526.
- [141] O. Y. Lyakin, K. P. Bryliakov, G. J. P. Britovsek, E. P. Talsi, *J. Am. Chem. Soc.* **2009**, *131*, 10798.
- [142] J. Berry, S. DeBeer George, F. Neese, *Phys. Chem. Chem. Phys.* **2008**, *10*, 4361.
- [143] J. P. Bigi, W.H. Harman, B. Lassalle-Kaiser, D. M. Robles, T.A. Stich, J. Yano, R. D. Britt, C. J. Chang, *J. Am. Chem. Soc.* **2012**, *134*, 1536.
- [144] J. England, Y. Guo, E. R. Farquhar, V. G. Young Jr., E. Münck, L. Que Jr., *J. Am. Chem. Soc.* **2010**, *132*, 8635.
- [145] J. England, M. Martinho, E. R. Farquhar, J. R. Frisch, E. L. Bominaar, E. Münck, L. Que Jr., *Angew. Chem., Int. Ed.* **2009**, *48*, 3622.
- [146] D. C. Lacy, R. Gupta, K. L. Stone, J. Greaves, J. W. Ziller, M. P. Hendrich, A. S. Borovik, *J. Am. Chem. Soc.* **2010**, *132*, 12188.
- [147] F. Neese, *Coord. Chem. Rev.* **2009**, *253*, 526.
- [148] F. Neese, *J. Phys. Chem. Solids* **2004**, *65*, 781.
- [149] S. Schinzel, M. Kaupp, *Can. J. Chem.* **2009**, *87*, 1521.

- [150] S. Ye, F. Neese, *Inorg. Chem.* **2010**, *49*, 772.
- [151] A. Droghetti, D. Alfe, S. Sanvito, *J. Chem. Phys.* **2012**, *137*, 124303.
- [152] S. P. de Visser, *J. Am. Chem. Soc.* **2006**, *128*, 15809.
- [153] H. Hirao, L. Que Jr., W. Nam, S. Shaik, *Chem. Eur. J.* **2008**, *14*, 1740.
- [154] S. P. de Visser, J.-U. Rohde, Y.-M. Lee, J. Cho, W. Nam, *Coord. Chem. Rev.* **2013**, *257*, 381.
- [155] K. M. Van Heuvelen, A. T. Fiedler, X. Shan, R. F. De Hont, K. K. Meier, E. L. Bominaar, E. Munck, L. Que, *Proc. Natl. Acad. Sci. U. S. A.* **2012**, *109*, 11933.
- [156] F. Neese, *J. Inorg. Biochem.* **2006**, *100*, 716.
- [157] O. Pestovsky, S. Stoian, E. L. Bominaar, X. Shan, E. Münck, L. Que Jr., A. Bakac, *Angew. Chem., Int. Ed.* **2005**, *44*, 6871.
- [158] J. C. Schöneboom, F. Neese, W. Thiel, *J. Am. Chem. Soc.* **2005**, *127*, 5840.
- [159] J. Krzystek, J. England, K. Ray, A. Ozarowski, D. Smirnov, L. Que Jr., J. Telser, *Inorg. Chem.* **2008**, *47*, 3483.
- [160] A. Chanda, X. Shan, M. Chakrabarti, W. C. Ellis, D. L. Popescu, F. Tiago de Oliveira, D. Wang, L. Que Jr., T. J. Collins, E. Münck, E. L. Bominaar, *Inorg. Chem.* **2008**, *47*, 3669.
- [161] J. T. Groves, G. A. McGlusky, *J. Am. Chem. Soc.* **1976**, *98*, 859.
- [162] S. Shaik, H. Hirao, D. Kumar, *Acc. Chem. Res.* **2007**, *40*, 532.
- [163] H. Hirao, D. Kumar, L. Que Jr, S. Shaik, *J. Am. Chem. Soc.* **2006**, *128*, 8590.
- [164] S. Ye, F. Neese, *Curr. Opin. Chem. Biol.* **2009**, *13*, 89.
- [165] S. Ye, F. Neese, *Proc. Natl. Acad. Sci. U. S. A.* **2011**, *108*, 1228.
- [166] B. K. Mai, Y. Kim, *Inorg. Chem.* **2016**, *55*, 3844.
- [167] S. P. de Visser, *J. Am. Chem. Soc.* **2006**, *128*, 9813.
- [168] D. Janardanan, Y. Wang, P. Schyman, L. Que Jr., S. Shaik, *Angew. Chem., Int. Ed.* **2010**, *49*, 3342.

- [169] L. Bernasconi, M. L. Louwerse, E. J. Baerends, *Eur. J. Inorg. Chem.* **2007**, *19*, 3023.
- [170] C. Michel, E. J. Baerends, *Phys. Chem. Chem. Phys.* **2007**, *9*, 156.
- [171] C. Michel, E. J. Baerends, *Inorg. Chem.* **2009**, *48*, 3628.
- [172] A. Decker, J.-U. Rohde, E. J. Klinker, S. D. Wong, L. Que Jr, E. I. Solomon, *J. Am. Chem. Soc.* **2007**, *129*, 15983.
- [173] E. I. Solomon, S. D. Wong, L. V. Liu, A. Decker, M. S. Chow, *Curr. Opin. Chem. Biol.* **2010**, *13*, 99.
- [174] M. L. Neidig, A. Decker, O. W. Choroba, F. Huang, M. Kavana, G. R. Moran, J. B. Spencer, E. I. Solomon, *Proc. Natl. Acad. Sci. U. S. A.* **2006**, *103*, 12966.
- [175] Y. Wang, K. Han, *J. Biol. Inorg. Chem.* **2010**, *15*, 351.
- [176] C.-Y. Geng, S. Ye, F. Neese, *Angew. Chem., Int. Ed.* **2010**, *49*, 5717.
- [177] S. Wong, C. Bell III, L. Liu, Y. Kwak, J. England, E. Alp, J. Zhao, L. Que Jr., E. Solomon, *Angew. Chem., Int. Ed.* **2011**, *50*, 3215.
- [178] D. Usharani, D. C. Lacy, A. S. Borovik, S. Shaik, *J. Am. Chem. Soc.* **2013**, *135*, 17090.
- [179] B. L. Vallee, R. J. P. Williams, *Proc. Natl. Acad. Sci. U. S. A.* **1968**, *59*, 498.
- [180] P. Comba, *Coord. Chem. Rev.* **2000**, *200*, 217.
- [181] K. B. Lipkowitz, S. Scheffrick, D. Avnir, *J. Am. Chem. Soc.* **2001**, *123*, 6710.
- [182] G. Chaka, J. L. Sonnenberg, H. B. Schlegel, M. J. Heeg, G. Jaeger, T. J. Nelson, L. A. Ochrymowycz, D. B. Rorabacher, *J. Am. Chem. Soc.* **2007**, *129*, 5217.
- [183] V. Balland, C. Hureau, J.-M. Saveant, *Proc. Natl. Acad. Sci. U. S. A.* **2010**, *107*, 17113.
- [184] A. Hoffmann, S. Binder, A. Jesser, R. Haase, U. Floerke, M. Guida, M. S. Stagni, W. Meyer-Klaucke, B. Lebsanft, L. E. Grünig, S. Schneider, M. Hashemi, A. Goos, A. Wetzels, M. Rubhausen, S. Herres-Pawlis, *Angew. Chem., Int. Ed.* **2014**, *53*, 299.
- [185] U. Ryde, M. H. M. Olsson, *Int. J. Quantum. Chem.* **2001**, *81*, 335.

- [186] J. England, Y. Guo, E. R. Farquhar, V. G. Young Jr., E. Münck, L. Que Jr., *J. Am. Chem. Soc.* **2010**, *132*, 8635.
- [187] Y. M. Lee, S. N. Dhuri, S. C. Sawant, J. Cho, M. Kubo, T. Ogura, S. Fukuzumi, W. Nam, *Angew. Chem., Int. Ed.* **2009**, *48*, 1803.
- [188] J.-U. Rohde, J.-H. In, M. H. Lim, W. W. Brennessel, M. R. Bukowski, A. Stubna, E. Münck, W. Nam, L. Que Jr., *Science* **2003**, *299*, 1037.
- [189] K. Ray, F. F. Pfaff, B. Wang, W. Nam, *J. Am. Chem. Soc.* **2014**, *136*, 13942.
- [190] A. R. McDonald, Y. Guo, V. V. Vu, E. L. Bominaar, E. Münck, L. Que Jr., *Chem. Sci.* **2012**, *3*, 1680.
- [191] C.E. Schäffer, C. K. Jorgensen, *Mol. Phys.* **1965**, *9*, 401.
- [192] P. Comba, *Coord. Chem. Rev.* **1999**, *182*, 343.
- [193] M. Reiher, O. Salomon, B. A. Hess, *Theor. Chem. Acc.* **2001**, *107*, 48.
- [194] H. Zabrodsky, S. Peleg, D. Avnir, *J. Am. Chem. Soc.* **1992**, *114*, 7843.
- [195] A. Zayit, M. Pinsky, H. Elgavi, C. Dryzun, D. Avnir, *Chirality* **2011**, *23*, 17.
- [196] D. Casanova, J. Cirera, M. Lluell, P. Alemany, D. Avnir, S. Alvarez, *J. Am. Chem. Soc.* **2004**, *126*, 1755.
- [197] R. Kurian, M. Filatov, *J. Chem. Theor. Comput.* **2008**, *4*, 278.
- [198] M. Römelt, S. Ye, F. Neese, *Inorg. Chem.* **2009**, *48*, 784.
- [199] R. Kurian, M. Filatov, *Phys. Chem. Chem. Phys.* **2010**, *12*, 2758.
- [200] P. R. Edwards, C. E. Johnson, R. J. P. Williams, *J. Chem. Phys.* **1967**, *47*, 2074.
- [201] D. Usharani, D. Janardanan, C. Li, S. Shaik, *Acc. Chem. Res.* **2013**, *46*, 471.
- [202] A. K. Vardhaman, P. Barman, S. Kumar, C. V. Sastri, D. Kumar, S. P. de Visser, *Angew. Chem., Int. Ed.* **2013**, *52*, 12288.
- [203] S. P. de Visser, M. G. Quesne, B. Martin, P. Comba, U. Ryde, *Chem. Commun.* **2014**, *50*, 262.
- [204] P. Comba, S. Wunderlich, *Chem. Eur. J.* **2010**, *16*, 7293.
- [205] H. Tang, J. Guan, H. Liu, X. Huang, *Dalton Trans.* **2013**, *42*, 10260.

- [206] D. Schröder, S. Shaik, H. Schwarz, *Acc. Chem. Res.* **2000**, *33*, 139.
- [207] K.-B. Cho, X. Wu, Y.-M. Lee, Y. H. Kwon, S. Shaik, W. Nam, *J. Am. Chem. Soc.* **2012**, *134*, 20222.
- [208] M. Rudolph, T. Ziegler, J. Autschbach, *Chem. Phys.* **2011**, *391*, 92.
- [209] J. P. Lopez, H. Kämpf, M. Grunert, P. Gülich, F. W. Heinemann, R. Prakash, A. Grohmann, *Chem. Commun.* **2006**, 1718.
- [210] M. Schlangen, J. Neugebauer, M. Reiher, D. Schröder, J. P. Lopez, M. Haryono, F. W. Heinemann, A. Grohmann, H. Schwarz, *J. Am. Chem. Soc.* **2008**, *130*, 4285.
- [211] J. P. Boyd, M. Schlangen, A. Grohmann, H. Schwarz, *Helv. Chim. Acta* **2008**, *91*, 1430.
- [212] W. Dieter, K. Nakamoto, *J. Am. Chem. Soc.* **1988**, *110*, 4044.
- [213] W. Dieter, K. Nakamoto, *J. Am. Chem. Soc.* **1989**, *111*, 1590.
- [214] T. Petrenko, S. D. George, N. A. Alcalde, E. Bill, B. Mienert, Y. Xiao, Y. Guo, W. Sturhahn, S. P. Cramer, K. Wieghardt, F. Neese, *J. Am. Chem. Soc.* **2007**, *129*, 11053.
- [215] K. Meyer, E. Bill, B. Mienert, T. Weyhermüller, K. Wieghardt, *J. Am. Chem. Soc.* **1999**, *121*, 4859.
- [216] J.-U. Rohde, T. A. Betley, T. A. Jackson, C. T. Saouma, J. C. Peters, L. Que Jr., *Inorg. Chem.* **2007**, *46*, 5720.
- [217] C. Vogel, F. W. Heinemann, J. Sutter, C. Anthon, K. Meyer, *Angew. Chem., Int. Ed.* **2008**, *47*, 2681.
- [218] Jaguar 7.7, Schrödinger, LLC, New York, NY, 2010.
- [219] *Continuum Solvation Models in Chemical Physics*; John Wiley & Sons, Ltd.: Chichester, U.K., 2007.
- [220] M. Cossi, N. Rega, I. Soteras, D. Blanco, O. Huertas, A. Bidon-Chanal, F. J. Luque, D. G. Truhlar, J. R. Pliego, B. M. Ladanyi, M. D. Newton, W. Domcke, A. L. Sobolewski, D. Laage, I. Burghardt, J. T. Hynes, M. Persico, G. Granucci, V. M. Huxter, G. D. Scholes, C. Curutchet, In ref. [219], Ch. 3, pp. 313-498.
- [221] J. Tomasi, E. Cancès, C. S. Pomelli, M. Caricato, G. Scalmani, M. J. Frisch, R.

- Cammi, M. V. Basilevsky, G. N. Chuev, B. Mennucci, In ref. [219], Ch. 1, pp. 1-124.
- [222] T. H. Dunning, *J. Chem. Phys.* **1989**, *90*, 1007.
- [223] R. A. Kendall, T. H. Dunning, R. J. Harrison, *J. Chem. Phys.* **1992**, *96*, 6796.
- [224] S. Grimme, *J. Chem. Phys.* **2003**, *118*, 9095.
- [225] A. Halkier, T. Helgaker, P. Jørgensen, W. Klopper, H. Koch, J. Olsen, A. K. Wilson, *Chem. Phys. Lett.* **1998**, *286*, 243.
- [226] F. Eckert, A. Klamt, COSMOtherm, Version C2.1, Release 01.11; COSMOlogic GmbH & Co. KG, Leverkusen, Germany, 2010.
- [227] M. Orozco, I. Marchán, I. Soteras, T. Vreven, K. Morokuma, K. V. Mikkelsen, A. Milani, M. Tommasini, M. D. Zoppo, C. Castiglioni, M. A. Aguilar, M. L. Sánchez, M. E. Martín, I. F. Galván, H. Sato, In ref. [219], Ch. 4, pp. 499-606.
- [228] S. N. Pieniazek, F. R. Clemente, K. N. Houk, *Angew. Chem., Int. Ed.* **2008**, *47*, 7746.
- [229] E. R. Johnson, P. Mori-Sánchez, A. J. Cohen, W. Yang, *J. Chem. Phys.* **2008**, *129*, 204112.
- [230] L. Goerigk, S. Grimme, *J. Chem. Theory Comput.* **2010**, *7*, 291.
- [231] S. Grimme, *Angew. Chem., Int. Ed.* **2006**, *45*, 4460.
- [232] M. D. Wodrich, C. S. Wannere, Y. Mo, P. D. Jarowski, K. N. Houk, P. v. R. Schleyer, *Chem. Eur. J.* **2007**, *13*, 7731.
- [233] S. Grimme, *Org. Lett.* **2010**, *12*, 4670.
- [234] A. Klamt, *Wiley Interdiscip. Rev.: Comput. Mol. Sci.* **2011**, *1*, 699.
- [235] D. H. Ess, K. N. Houk, *J. Phys. Chem. A* **2005**, *109*, 9542.
- [236] S. Grimme, C. Mück-Lichtenfeld, E.-U. Würthwein, A. W. Ehlers, T. P. M. Goumans, K. Lammertsma, *J. Phys. Chem. A* **2006**, *110*, 2583.
- [237] T. C. Dinadayalane, R. Vijaya, A. Smitha, G. N. Sastry, *J. Phys. Chem. A* **2002**, *106*, 1627.

- [238] W. Blokzijl, M. J. Blandamer, J. B. F. N. Engberts, *J. Am. Chem. Soc.* **1991**, *113*, 4241.
- [239] S. Otto, W. Blokzijl, J. B. F. N. Engberts, *J. Org. Chem.* **1994**, *59*, 5372.
- [240] J. B. F. N. Engberts, *Pure Appl. Chem.* **1995**, *67*, 823.
- [241] A. Fu, W. Thiel, *J. Mol. Struct.: THEOCHEM* **2006**, *765*, 45.
- [242] J. F. Blake, D. Lim, W. L. Jorgensen, *J. Org. Chem.* **1994**, *59*, 803.
- [243] J. Chandrasekhar, S. Shariffskul, W. L. Jorgensen, *J. Phys. Chem. B* **2002**, *106*, 8078.
- [244] O. Acevedo, W. L. Jorgensen, *J. Chem. Theory Comput.* **2007**, *3*, 1412.
- [245] H. Hu, M. N. Kobra, C. Xu, S. Hammes-Schiffer, *J. Phys. Chem. A* **2000**, *104*, 8058.
- [246] P. Pyykkö, *Rev. Phys. Chem.* **2012**, *63*, 45.
- [247] P. Pyykkö, *Chem. Rev.* **1988**, *88*, 563.
- [248] M. Iliáš, V. Kello, M. Urban, *Acta Phys. Slov.* **2010**, *60*, 259.
- [249] P. Pyykkö, *Angew. Chem., Int. Ed.* **2004**, *43*, 4412.
- [250] P. Pyykkö, *Inorg. Chim. Acta* **2005**, *358*, 4113.
- [251] X. Wang, L. Andrews, S. Riedel, M. Kaupp, *Angew. Chem., Int. Ed.* **2007**, *46*, 8371.
- [252] P. Schwerdtfeger, *J. Am. Chem. Soc.* **1989**, *111*, 7261.
- [253] P. Schwerdtfeger, P. D. W. Boyd, S. Brienne, A. K. Burrell, *Inorg. Chem.* **1992**, *31*, 3411.
- [254] R. Ahuja, A. Blomqvist, P. Larsson, P. Pyykkö, P. Zaleski-Ejgierd, *Phys. Rev. Lett.* **2011**, *106*, 018301.
- [255] P. Schwerdtfeger, G. A. Heath, M. Dolg, M. A. Bennett, *J. Am. Chem. Soc.* **1992**, *114*, 7518.
- [256] M. Seth, K. Faegri, P. Schwerdtfeger, *Angew. Chem., Int. Ed.* **1998**, *37*, 2493.
- [257] W. Kutzelnigg, *Angew. Chem., Int. Ed.* **1984**, *23*, 272.

- [258] M. Kaupp, H. G. von Schnering, *Angew. Chem., Int. Ed.* **1993**, *32*, 861.
- [259] M. Kaupp, M. Dolg, H. Stoll, H. G. von Schnering, *Inorg. Chem.* **1994**, *33*, 2122.
- [260] M. Seth, P. Schwerdtfeger, M. Dolg, *J. Chem. Phys.* **1997**, *106*, 3623.
- [261] T. Söhnel, R. Brown, L. Kloo, P. Schwerdtfeger, *Chem. Eur. J.* **2001**, *7*, 3167.
- [262] R. J. Puddephatt, *The Chemistry of Gold*; Elsevier: Amsterdam, 1978.
- [263] M. J. Frisch, G. W. Trucks, H. B. Schlegel, G. E. Scuseria, M. A. Robb, J. R. Cheeseman, G. Scalmani, V. Barone, B. Mennucci, G. A. Petersson, H. Nakatsuji, M. Caricato, X. Li, H. P. Hratchian, A. F. Izmaylov, J. Bloino, G. Zheng, J. L. Sonnenberg, M. Hada, M. Ehara, K. Toyota, R. Fukuda, J. Hasegawa, M. Ishida, T. Nakajima, Y. Honda, O. Kitao, H. Nakai, T. Vreven, J. A. Montgomery Jr., J. E. Peralta, F. Ogliaro, M. J. Bearpark, J. Heyd, E. N. Brothers, K. N. Kudin, V. N. Staroverov, R. Kobayashi, J. Normand, K. Raghavachari, A. P. Rendell, J. C. Burant, S. S. Iyengar, J. Tomasi, M. Cossi, N. Rega, N. J. Millam, M. Klene, J. E. Knox, J. B. Cross, V. Bakken, C. Adamo, J. Jaramillo, R. Gomperts, R. E. Stratmann, O. Yazyev, A. J. Austin, R. Cammi, C. Pomelli, J. W. Ochterski, R. L. Martin, K. Morokuma, V. G. Zakrzewski, G. A. Voth, P. Salvador, J. J. Dannenberg, S. Dapprich, A. D. Daniels, Ö. Farkas, J. B. Foresman, J. V. Ortiz, J. Cioslowski, D. J. Fox, Gaussian, Inc.: Wallingford, CT, USA, 2009.
- [264] P. Schwerdtfeger, *Chem. Phys. Chem.* **2011**, *12*, 3143.
- [265] P. Schwerdtfeger, M. Dolg, W. H. E. Schwarz, G. A. Bowmaker, P. D. W. Boyd, *J. Chem. Phys.* **1989**, *91*, 1762.
- [266] D. Figgen, G. Rauhut, M. Dolg, H. Stoll, *Chem. Phys.* **2005**, *311*, 227.
- [267] K. A. Peterson, D. Figgen, E. Goll, H. Stoll, M. Dolg, *J. Chem. Phys.* **2003**, *119*, 11113.
- [268] T. Schlöder, M. Kaupp, S. Riedel, *J. Am. Chem. Soc.* **2012**, *134*, 11977.
- [269] Y. Gong, M. Zhou, M. Kaupp, S. Riedel, *Angew. Chem.* **2009**, *121*, 8019.
- [270] S. Riedel, M. Kaupp, *Coord. Chem. Rev.* **2009**, *253*, 606.
- [271] X. Wang, L. Andrews, S. Riedel, M. Kaupp, *Angew. Chem.* **2007**, *119*, 8523.
- [272] S. Riedel, M. Renz, M. Kaupp, *Inorg. Chem.* **2007**, *46*, 5734.

- [273] S. Riedel, M. Kaupp, *Inorg. Chem.* **2006**, *45*, 10497.
- [274] S. Riedel, M. Kaupp, *Angew. Chem.* **2006**, *118*, 3791.
- [275] S. Riedel, M. Kaupp, *Inorg. Chem.* **2006**, *45*, 1228.
- [276] S. Riedel, M. Straka, M. Kaupp, *Chem. Eur. J.* **2005**, *11*, 2743.
- [277] S. Riedel, M. Straka, M. Kaupp, *Phys. Chem. Chem. Phys.* **2004**, *6*, 1122.
- [278] D. E. Woon, T. H. Dunning, *J. Chem. Phys.* **1993**, *98*, 1358.
- [279] F. Weigend, F. Furche, R. Ahlrichs, *J. Chem. Phys.* **2003**, *119*, 12753.
- [280] F. Weigend, A. Baldes, *J. Chem. Phys.* **2010**, *133*, 174102.
- [281] F. Weigend, *J. Comput. Chem.* **2008**, *29*, 167.
- [282] M. Kaupp, *J. Comput. Chem.* **2007**, *28*, 320.
- [283] M. Kaupp, In Huheey-Keiter-Keiter *Anorganische Chemie - Prinzipien von Struktur und Reaktivität* (Ed. R. Steudel); 5. Ed. (ed. Steudel, R.); de Gruyter: Berlin, 2014.
- [284] K. Theilacker, D. Buhrke, M. Kaupp, *J. Chem. Theory Comput.* **2015**, *11*, 111.
- [285] M. Kaupp, H. G. von Schnering, *Inorg. Chem.* **1994**, *33*, 4718.
- [286] C. H. Gammons, Y. Yu, A. E. Williams-Jones, *Geochim. Cosmochim. Acta* **1997**, *61*, 1971.
- [287] P. Pan, S. A. Wood, *Geochim. Cosmochim. Acta* **1991**, *55*, 2365.
- [288] J. A. Peck, C. D. Tait, B. I. Swanson, G. E. Brown Jr, *Geochim. Cosmochim. Acta* **1991**, *55*, 671.
- [289] F. Farges, J. A. Sharps, G. E. Brown Jr, *Geochim. Cosmochim. Acta* **1993**, *57*, 1243.
- [290] N. Takeuchi, C. T. Chan, K. M. Ho, *Phys. Rev. B* **1989**, *40*, 1565.
- [291] A. V. Arbuznikov, M. Kaupp, *Chem. Phys. Lett.* **2007**, *440*, 160.
- [292] A. V. Arbuznikov, M. Kaupp, *Int. J. Quantum Chem.* **2011**, *111*, 2625.
- [293] L. Goerigk, S. Grimme, *J. Chem. Theory Comput.* **2010**, *6*, 107.
- [294] A. D. Becke, *J. Chem. Phys.* **2013**, *138*, 074109.

- [295] H. Bahmann, M. Kaupp, *J. Chem. Theor. Comput.* **2015**, *11*, 1540.
- [296] L. Goerigk, S. Grimme, *Phys. Chem. Chem. Phys.* **2011**, *13*, 6670.
- [297] M. Kaupp, S. Gückel, M. Renz, S. Klawohn, K. Theilacker, M. Parthey, C. Lambert, *J. Comput. Chem.* **2016**, *37*, 93.
- [298] Y. Zhao, D. G. Truhlar, *J. Phys. Chem. A* **2005**, *109*, 5656.
- [299] Y. Zhao, D. G. Truhlar, *Theor. Chem. Acc.* **2008**, *120*, 215.

# Appendix I

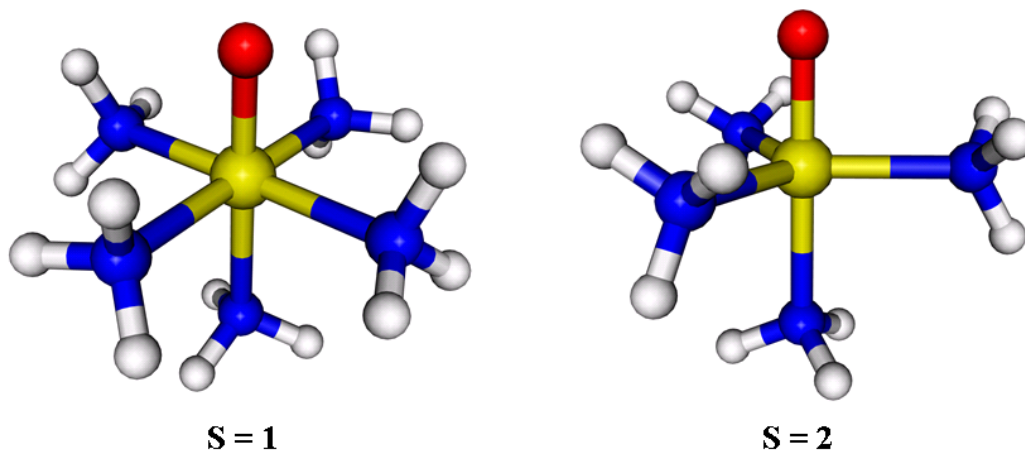


Figure S1: B3LYP-D3/def2-TZVP optimized structures of  $[\text{Fe}(\text{O})(\text{NH}_3)_5]^{2+}$  and  $[\text{Fe}(\text{O})(\text{NH}_3)_4]^{2+}$ .

Table S1: Important distances, as well as NPA and Mulliken (in brackets) spin populations for  $[\text{Fe}(\text{O})(\text{NH}_3)_5]^{2+}$  (see Figure S1), calculated for different functionals and spin states. def2-TZVP basis set used for all atoms.

	distances in Å				spin population NPA [Mulliken]		$\Delta E$
	Fe-O	Fe-N <sup>a</sup>	Fe-N <sup>b</sup>	$\langle S^2 \rangle$	Fe	O	(S=2 - S=1) in kJ mol <sup>-1</sup>
<b>S = 1</b>							
BP86-D3	1.634	2.073	2.211	2.011	1.29 [1.22]	0.73 [0.86]	
BLYP-D3	1.648	2.092	2.209	2.010	1.27 [1.19]	0.75 [0.87]	
PBE-D3	1.634	2.069	2.214	2.011	1.30 [1.23]	0.72 [0.84]	
TPSS-D3	1.633	2.071	2.210	2.011	1.27 [1.19]	0.75 [0.88]	
B97D-D3	1.629	2.075	2.216	2.020	1.31 [1.24]	0.75 [0.87]	
B3LYP-D3	1.615	2.076	2.208	2.016	1.26 [1.15]	0.77 [0.91]	
PBE0-D3	1.601	2.041	2.166	2.018	1.29 [1.17]	0.75 [0.89]	
TPSSh-D3	1.618	2.067	2.217	2.014	1.27 [1.17]	0.76 [0.89]	
BHLYP-D3	1.716	2.055	2.115	2.025	0.99 [0.94]	1.04 [1.10]	
<b>S = 2</b>							
BP86-D3	1.630	2.203	2.147	6.029	3.06 [3.04]	0.66 [0.75]	43.8
BLYP-D3	1.641	2.229	2.175	6.028	3.04 [3.00]	0.67 [0.76]	41.8
PBE-D3	1.630	2.208	2.149	6.029	3.07 [3.05]	0.65 [0.74]	42.6
TPSS-D3	1.629	2.199	2.144	6.035	3.08 [3.05]	0.65 [0.74]	52.7
B97D-D3	1.625	2.209	2.161	6.047	3.13 [3.09]	0.62 [0.71]	6.1
B3LYP-D3	1.610	2.203	2.162	6.058	3.19 [3.11]	0.58 [0.68]	7.8
PBE0-D3	1.595	2.181	2.145	6.078	3.29 [3.22]	0.50 [0.61]	-10.4
TPSSh-D3	1.615	2.189	2.142	6.050	3.15 [3.11]	0.60 [0.70]	32.8
BHLYP-D3	1.817	2.203	2.230	6.938	4.41 [4.40]	-0.74 [-0.70]	-75.5

<sup>a</sup>Average distance for nitrogens cis to the oxo ligand. <sup>b</sup>Trans to the oxo ligand.

Table S2: Important distances, as well as NPA and Mulliken (in brackets) spin populations for  $[\text{Fe}(\text{O})(\text{NH}_3)_4]^{2+}$  (see Figure S1), calculated for different functionals and spin states. def2-TZVP basis set used for all atoms.

	distances in Å				spin population NPA [Mulliken]		$\Delta E$
	Fe-O	Fe-N <sup>a</sup>	Fe-N <sup>b</sup>	$\langle S^2 \rangle$	Fe	O	(S=2 - S=1) in kJ mol <sup>-1</sup>
<b>S = 1</b>							
BP86-D3	1.618	2.096	2.140	2.733	1.99 [2.04]	-0.15 [-0.21]	
BLYP-D3	1.625	2.125	2.169	2.688	1.96 [1.98]	-0.13 [-0.17]	
PBE-D3	1.616	2.094	2.142	2.723	1.98 [2.02]	-0.14 [-0.19]	
TPSS-D3	1.631	2.090	2.133	2.827	2.11 [2.17]	-0.26 [-0.32]	
B97D-D3	1.632	2.105	2.143	2.850	2.22 [2.26]	-0.35 [-0.42]	
B3LYP-D3	1.688	2.109	2.121	3.038	2.71 [2.76]	-0.76 [-0.85]	
PBE0-D3	1.697	2.087	2.093	3.078	2.84 [2.94]	-0.86 [-0.96]	
TPSSh-D3	1.659	2.090	2.111	3.005	2.49 [2.57]	-0.58 [-0.66]	
BHLYP-D3	1.848	2.120	2.138	3.468	3.40 [3.52]	-1.36 [-1.52]	
<b>S = 2</b>							
BP86-D3	1.633	2.106	2.129	6.027	3.08 [3.02]	0.74 [0.80]	-71.0
BLYP-D3	1.644	2.133	2.154	6.026	3.06 [2.97]	0.74 [0.81]	-68.2
PBE-D3	1.633	2.105	2.130	6.027	3.09 [3.02]	0.72 [0.79]	-71.5
TPSS-D3	1.632	2.103	2.125	6.032	3.09 [3.03]	0.73 [0.80]	-68.2
B97D-D3	1.627	2.116	2.140	6.043	3.14 [3.06]	0.70 [0.77]	-95.4
B3LYP-D3	1.613	2.114	2.138	6.052	3.17 [3.07]	0.69 [0.77]	-68.7
PBE0-D3	1.597	2.090	2.119	6.067	3.24 [3.17]	0.64 [0.71]	-64.9
TPSSh-D3	1.618	2.098	2.121	6.045	3.15 [3.08]	0.71 [0.78]	-70.0
BHLYP-D3	1.663	2.113	2.195	6.593	4.12 [4.04]	-0.32 [-0.26]	-10.7

<sup>a</sup>Average distance for nitrogens cis to the oxo ligand. <sup>b</sup>Trans to the oxo ligand.

Table S3: Comparison of B3LYP results with different basis sets for spin state energetics  $\Delta E$  (S = 2 - S = 1) of four iron(IV)-oxo complexes in kJ mol<sup>-1</sup> <sup>a</sup>

	def2-SVP	def2-TZVP	def2-QZVP
$[\text{Fe}(\text{O})(\text{tpa}^{\text{Ph}})]^-$	-70.8	-73.6	-73.3
$[\text{Fe}(\text{O})(\text{TMG}_3\text{tren})]^{2+}$	-85.6	-88.6	-87.5
$[\text{Fe}(\text{O})(\text{TMC})(\text{NCCH}_3)]^{2+}$	14.7	16.2	15.8
$[\text{Fe}(\text{O})(\text{N4Py})]^{2+}$	33.7	30.7	29.3

<sup>a</sup>Single-point calculation at the B3LYP/def2-TZVP gas-phase structure.

Table S4: Deviations, mean absolute errors (MAE) and mean signed errors (MSE) in picometres for important interatomic distances of eight iron-oxo complexes for different density functionals. def2-TZVP basis used for all atoms.

Fe-O	exptl. ref [pm]	deviations in pm		
		BP86 (+D3)	B3LYP (+D3)	PBE0 (+D3)
[Fe(O)(tpa <sup>Ph</sup> )] <sup>-</sup>	162	2.2 (2.2)	0 (-0.1)	-1.5 (-1.5)
[Fe(O)(TMG <sub>3</sub> tren)] <sup>2+</sup>	166.1	-1.4 (-1.1)	-3.6 (-3.5)	-5.0 (-4.9)
[Fe(O)(H <sub>3</sub> buea)] <sup>-</sup>	168.0	0 (0.1)	-2.6 (-2.6)	-3.7 (-3.7)
[Fe(O)(TMC)(NCCH <sub>3</sub> )] <sup>2+</sup>	164.6	-0.6 (-0.5)	-3.0 (-2.9)	-4.4 (-4.3)
[Fe(O)(TMCS)] <sup>+</sup>	170	-1.1 (-1.0)	-3.8 (-3.8)	-5.4 (-5.4)
[Fe(O)(N4Py)] <sup>2+</sup>	163.9	0.5 (0.6)	-1.6 (-1.6)	-3.1 (-3.1)
[Fe(O)(Bn-TPEN)] <sup>2+</sup>	167	-2.3 (-2.2)	-4.5 (-4.5)	-6.0 (-6.0)
[Fe(O)(TAML)] <sup>-</sup>	158	2.3 (2.2)	-0.3 (-0.3)	-2.1 (-2.1)
MSE		-0.05 (0.04)	-2.43 (-2.41)	-3.90 (-3.88)
MAE		1.30 (1.24)	2.43 (2.41)	3.90 (3.88)
Fe-N <sup>a</sup>				
[Fe(O)(TMG <sub>3</sub> tren)] <sup>2+</sup>	211.2	1.8 (1.3)	2.8 (2.4)	0.8 (0.4)
[Fe(O)(H <sub>3</sub> buea)] <sup>-</sup>	206.4	10.0 (4.4)	10.9 (6.8)	7.8 (4.5)
[Fe(O)(TMC)(NCCH <sub>3</sub> )] <sup>2+</sup>	205.8	0.8 (-1.6)	7.4 (5.1)	4.3 (2.9)
[Fe(O)(TMCS)] <sup>+</sup>	233	-0.3 (-1.1)	2.5 (1.8)	-0.3 (-0.6)
[Fe(O)(N4Py)] <sup>2+</sup>	203.3	5.1 (4.9)	6.4 (6.3)	3.9 (3.9)
MSE		3.48 (1.58)	6.00 (4.48)	3.30 (2.22)
MAE		3.60 (2.66)	6.00 (4.48)	3.42 (2.46)
Fe-N <sup>b</sup>				
[Fe(O)(TMG <sub>3</sub> tren)] <sup>2+</sup>	200.5	3.3 (0)	4.5 (1.7)	1.9 (0.2)
[Fe(O)(H <sub>3</sub> buea)] <sup>-</sup>	198.3	2.2 (1.9)	2.9 (2.4)	0.6 (0.3)
[Fe(O)(TMC)(NCCH <sub>3</sub> )] <sup>2+</sup>	209	4.4 (2.8)	4.5 (3.0)	1.1 (0.4)
[Fe(O)(TMCS)] <sup>+</sup>	209	4.2 (2.9)	5.1 (3.9)	1.6 (0.9)
[Fe(O)(N4Py)] <sup>2+</sup>	195.6	2.6 (1.3)	4.8 (3.5)	2.1 (1.4)
[Fe(O)(TAML)] <sup>-</sup>	187	2.1 (1.7)	1.7 (1.3)	-0.3 (-0.5)
MSE		3.13 (1.77)	3.92 (2.63)	1.17 (0.45)
MAE		3.13 (1.77)	3.92 (2.63)	1.27 (0.62)

<sup>a</sup>Trans to the oxo ligand. <sup>b</sup>Average distance for nitrogen cis to the oxo ligand.

Table S5: Calculated isomer shifts for a selected group of ten iron-oxo compounds by different optimization protocols and linear fits. Uncontracted def2-QZVPP basis set used for iron in all single-point calculations (not specified in Table).

			B3LYP-D3/ def2-TZVPP <sup>a,c</sup>	B3LYP-D3BJ/ def2-TZVPP <sup>b,c</sup>	B3LYP-D3/ def2-TZVPP <sup>d,e</sup>
			//B3LYP-D3/ def2-TZVPP	//RIBP86-D3BJ/ def2-TZVPP	//B3LYP-D3/ def2-TZVPP
	S	$\delta$ expt. [mm s <sup>-1</sup> ]	$\delta$ [mm s <sup>-1</sup> ]	$\delta$ [mm s <sup>-1</sup> ]	$\delta$ [mm s <sup>-1</sup> ]
[Fe(O)(tpa <sup>Ph</sup> )] <sup>-</sup>	1		0.13	-0.05	0.12
	2	0.09	0.07	0.07	0.07
[Fe(O)(TMG <sub>3</sub> tren)] <sup>2+</sup>	1		0.07	0.07	0.07
	2	0.09	0.08	0.08	0.07
[Fe(O)(H <sub>3</sub> buea)] <sup>-</sup>	1		-0.08	-0.08	-0.06
	2	0.02	0.02	0.02	0.02
[Fe(O)(H <sub>2</sub> O) <sub>5</sub> ] <sup>2+</sup>	1		0.31	0.31	0.28
	2	0.38	0.46	0.49	0.41
[Fe(O)(TMC)(NCCH <sub>3</sub> )] <sup>2+</sup>	1	0.17	0.17	0.18	0.15
	2		0.19	0.21	0.17
[Fe(O)(TMCS)] <sup>+</sup>	1	0.19	0.21	0.22	0.19
	2		0.26	0.28	0.23
[Fe(O)(N4Py)] <sup>2+</sup>	1	-0.04	0.01	-0.01	0.01
	2		0.18	0.20	0.17
[Fe(O)(Bn-TPEN)] <sup>2+</sup>	1	0.01	0.04	0.02	0.04
	2		0.18	0.20	0.17
[Fe(O)(TAML)] <sup>-</sup>	1/2	-0.42	-0.49	-0.47	-0.43
	3/2		-0.19	-0.19	-0.16
[Fe(O)(bTAML)] <sup>-</sup>	1/2	-0.44	-0.50	-0.48	-0.44
	3/2		-0.41	-0.22	-0.36
MAE			0.034	0.031	0.018
MSE			0.02	0.07	0.004

<sup>a</sup>Linear equation used:  $\delta[\text{mm s}^{-1}] = -0.3594 \cdot (\rho(\text{DFT}) - 11800) + 10.521$  <sup>b</sup>Linear equation used:  $\delta[\text{mm s}^{-1}] = -0.3767 \cdot (\rho(\text{DFT}) - 11800) + 11.033$  <sup>c</sup>The linear equation was fitted to the isomer-shift test of Neese's test set [79]. <sup>d</sup>Linear equation used:  $\delta[\text{mm s}^{-1}] = -0.3182 \cdot (\rho(\text{DFT}) - 11800) + 9.3185$  <sup>e</sup>The linear equation was fitted to the experimental isomer shifts of the iron-oxo complexes from this Table (without [Fe(O)(H<sub>2</sub>O)<sub>5</sub>]<sup>2+</sup>).

Table S6: Calculated quadrupole splittings for a selected group of ten iron-oxo compounds by different optimization protocols. Uncontracted def2-QZVPP basis set used for iron in all single-point calculations (not specified in Table).

			B3LYP-D3/ def2-TZVP //B3LYP-D3/ def2-TZVP	B3LYP-D3BJ/ def2-TZVPP //RIBP86-D3BJ/ def2-TZVPP
	S	$\Delta\text{EQ}$ expt. [mm s <sup>-1</sup> ]	$\Delta\text{EQ}$ [mm s <sup>-1</sup> ]	$\Delta\text{EQ}$ [mm s <sup>-1</sup> ]
[Fe(O)(tpa <sup>P</sup> h)] <sup>-</sup>	1		1.42	-2.32
	2	0.51	-0.30	0.20
[Fe(O)(TMG <sub>3</sub> tren)] <sup>2+</sup>	1		-1.50	-1.52
	2	-0.29	-0.35	-0.17
[Fe(O)(H <sub>3</sub> buea)] <sup>-</sup>	1		2.00	2.04
	2	0.43	0.82	1.08
[Fe(O)(H <sub>2</sub> O) <sub>5</sub> ] <sup>2+</sup>	1		0.23	-0.22
	2	-0.33	-0.96	-0.93
[Fe(O)(TMC)(NCCH <sub>3</sub> )] <sup>2+</sup>	1	1.23	1.17	0.98
	2		-0.56	-0.77
[Fe(O)(TMCS)] <sup>+</sup>	1	-0.22	0.66	0.57
	2		-2.31	-2.25
[Fe(O)(N4Py)] <sup>2+</sup>	1	0.93	0.83	1.05
	2		-0.51	-0.43
[Fe(O)(Bn-TPEN)] <sup>2+</sup>	1	0.87	0.80	1.05
	2		-0.67	-0.62
[Fe(O)(TAML)] <sup>-</sup>	1/2	4.25	4.30	4.34
	3/2		3.27	3.19
[Fe(O)(bTAML)] <sup>-</sup>	1/2	4.27	4.24	4.28
	3/2		-0.56	3.07
MAE			0.304	0.312
MSE			-0.044	0.080

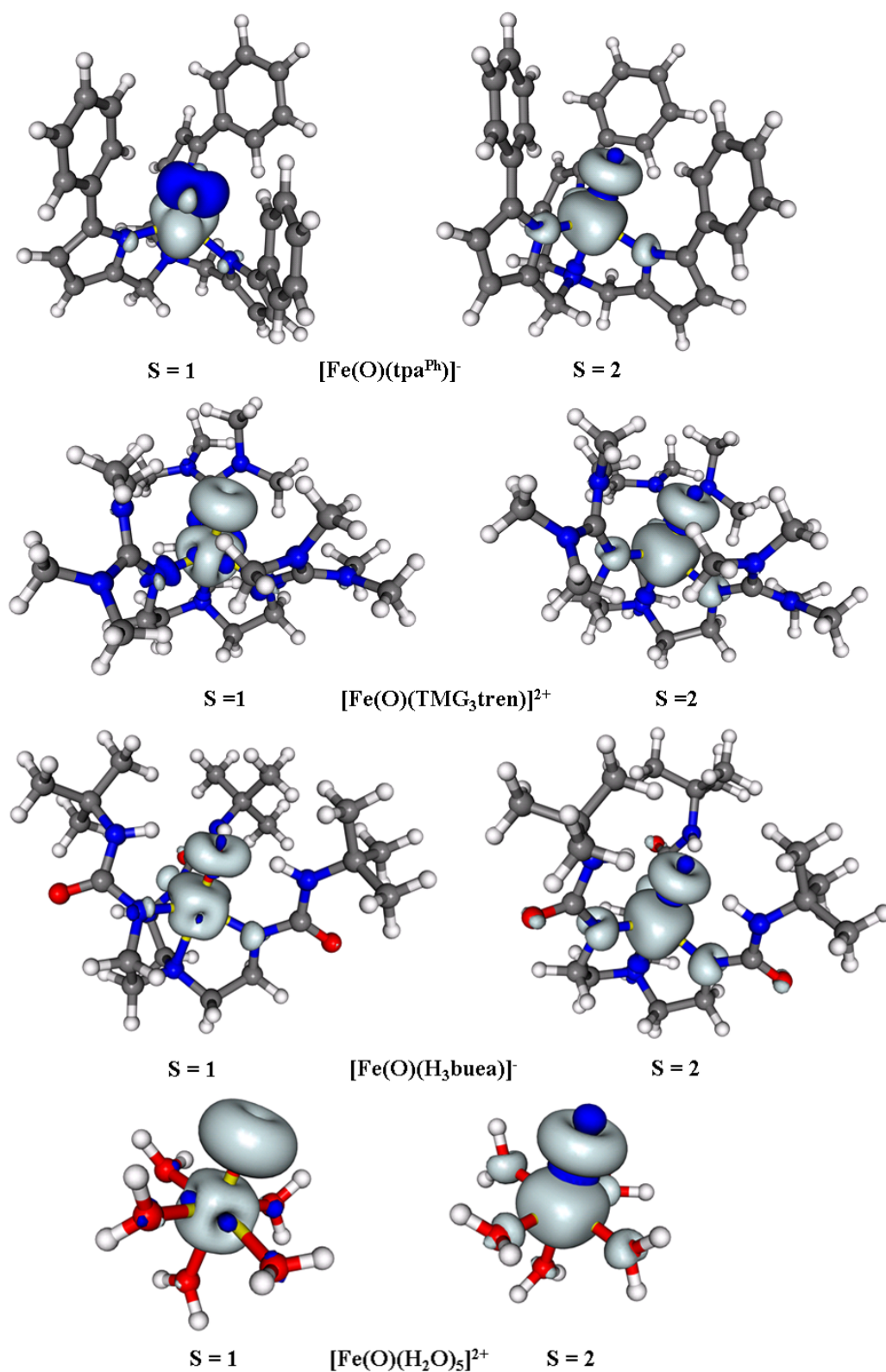


Figure S2: Isosurface plots of the spin density ( $\pm 0.005$  a.u.) of four selected  $S = 2$  iron(IV)-oxo complexes in their triplet and quintet states. B3LYP-D3/def2-TZVP optimized structures.

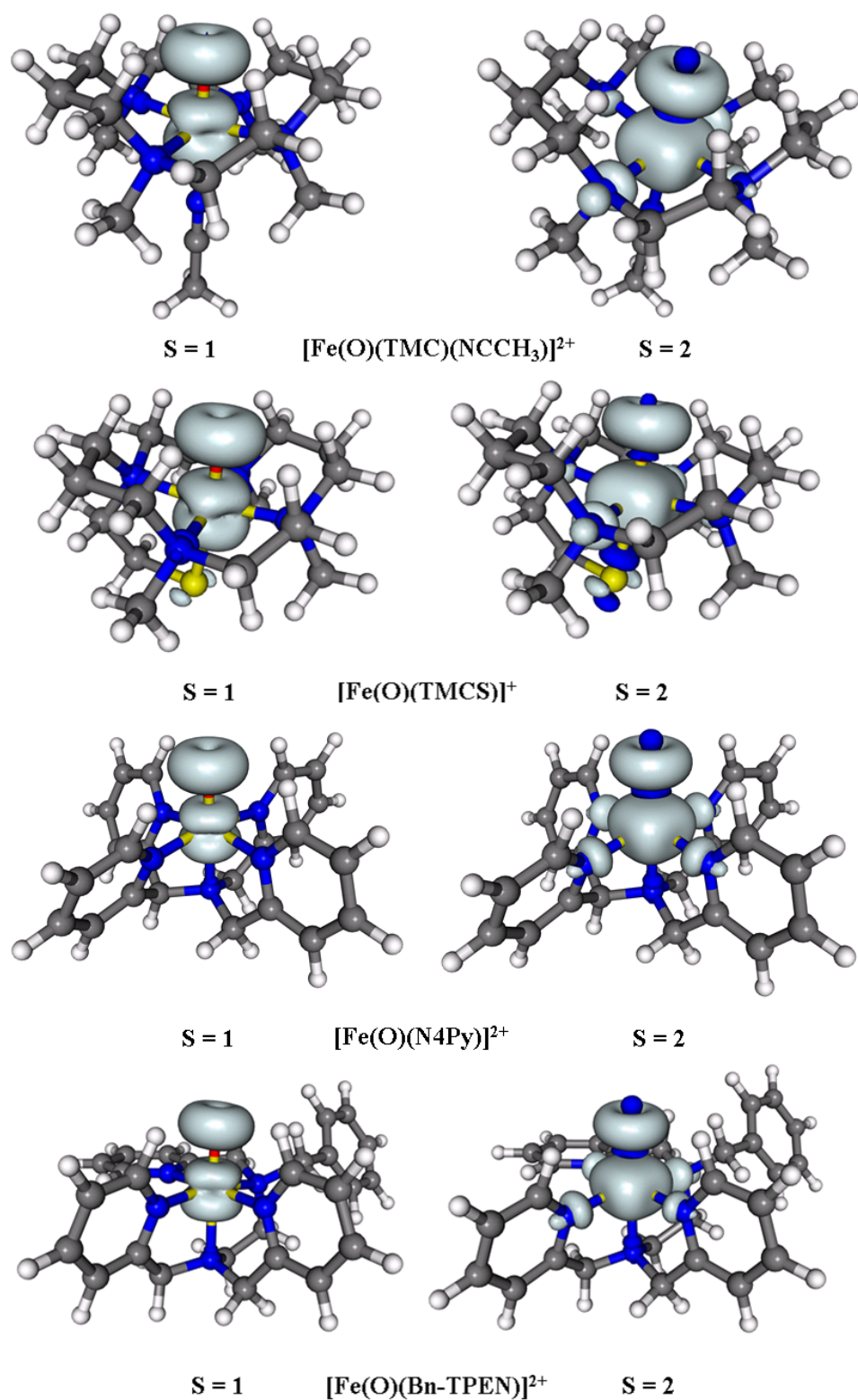


Figure S3: Isosurface plots of the spin density ( $\pm 0.005$  a.u.) of four selected  $S = 1$  iron(IV)-oxo complexes in their triplet and quintet states. B3LYP-D3/def2-TZVP optimized structures.

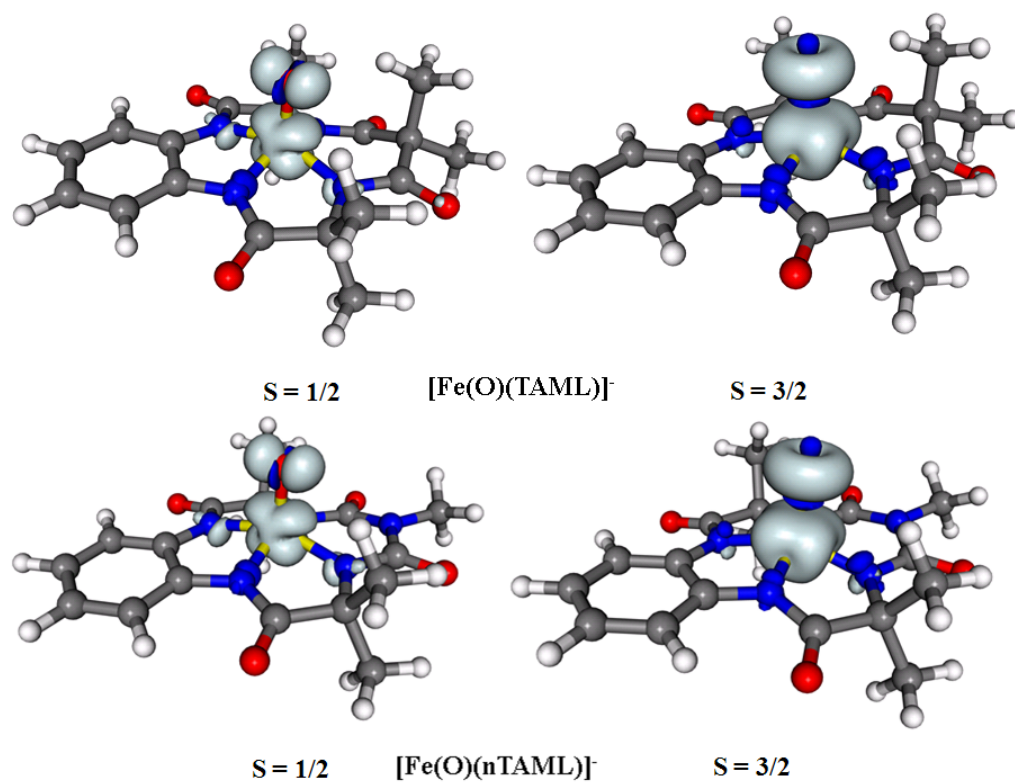


Figure S4: Isosurface plots of the spin density ( $\pm 0.005$  a.u.) of two selected  $S = 1/2$  iron(V)-oxo complexes in their doublet and quartet states. B3LYP-D3/def2-TZVP optimized structures.

Table S7: Comparison of calculated and experimental g values of the g-tensor of  $[\text{Fe}(\text{O})(\text{TAML})]^-$  (see Computational Details in Chapter 3.2 for the exact level of theory). BP86/def2-TZVP and B3LYP/def2-TZVP optimized structures were used for both spin states ( $S = 1/2$  ground state). BHLYP calculations are single-points on top of B3LYP/def2-TZVP optimized structures.

	S	g <sub>11</sub>	g <sub>22</sub>	g <sub>33</sub>
Experiment	1/2	1.74	1.97	1.99
B3LYP	1/2	1.87	2.01	2.02
BP86	1/2	1.85	2.00	2.02
BHLYP	1/2	1.96	2.02	2.05
BP86	3/2	2.02	2.03	2.04
B3LYP	3/2	2.03	2.05	2.06
BHLYP	3/2	2.01	2.04	2.04

Table S8: Spin-state energy differences in  $\text{kJ mol}^{-1}$  for three iron(III)-hydroxo complexes. def2-TZVP basis used for all atoms.

	spin state	$\Delta E$	
		BP86	B3LYP
$[\text{Fe}(\text{O})(\text{tpa}^{\text{P}^{\text{H}}})]^-$	S = 1/2	36.6	89.8
	S = 3/2	0	33.5
	S = 5/2	3.1	0
$[\text{Fe}(\text{O})(\text{TMG}_3\text{tren})]^{2+}$	S = 1/2		86.0
	S = 3/2	0	25.9
	S = 5/2	12.0	0
$[\text{Fe}(\text{O})(\text{H}_3\text{buea})]^-$	S = 1/2		74.9
	S = 3/2	3.4	43.5
	S = 5/2	0	0

Table S9: Important bond lengths and energy differences between isomers of the iron-oxo complex  $[\mathbf{1}(\mathbf{O})]^{2+}$  for different functionals, as well as NPA and Mulliken (in brackets) spin populations. def2-TZVP basis for all atoms. Values in parentheses are for D3 corrected calculations.

functional		bond lengths in Å		spin population		$\Delta E$ in $\text{kJ mol}^{-1}$
		Fe-O	Fe-N <sup>a</sup>	NPA [Mulliken] Fe	O	
BP86	<i>mer</i> - $[\mathbf{1}(\mathbf{O})]^{2+}$ (S = 1)	1.650	2.150	1.29 [1.27]	0.74 [0.83]	0
		(1.651)	(2.142)	(1.29 [1.27])	(0.74 [0.83])	(0)
	<i>mer</i> - $[\mathbf{1}(\mathbf{O})]^{2+}$ (S = 2)	1.642	2.172	2.99 [2.99]	0.64 [0.71]	+45.2
		(1.641)	(2.153)	(2.98 [2.99])	(0.64 [0.71])	(+46.3)
	<i>fac</i> - $[\mathbf{1}(\mathbf{O})]^{2+}$ (S = 1)	1.656	2.127	1.29 [1.26]	0.74 [0.84]	+10.5
		(1.658)	(2.106)	(1.28 [1.26])	(0.74 [0.84])	(+15.7)
	<i>fac</i> - $[\mathbf{1}(\mathbf{O})]^{2+}$ (S = 2)	1.649	2.080	2.94 [2.96]	0.66 [0.73]	+38.5
		(1.649)	(2.066)	(2.93 [2.95])	(0.66 [0.73])	(+37.0)
B3LYP	<i>mer</i> - $[\mathbf{1}(\mathbf{O})]^{2+}$ (S = 1)	1.629	2.163	1.29 [1.21]	0.75 [0.86]	0
		(1.629)	(2.157)	(1.29 [1.22])	(0.74 [0.86])	(0)
	<i>mer</i> - $[\mathbf{1}(\mathbf{O})]^{2+}$ (S = 2)	1.621	2.184	3.15 [3.10]	0.57 [0.65]	+3.5
		(1.620)	(2.174)	(3.14 [3.10])	(0.57 [0.65])	(+3.1)
	<i>fac</i> - $[\mathbf{1}(\mathbf{O})]^{2+}$ (S = 1)	1.629	2.173	1.30 [1.22]	0.76 [0.87]	+4.6
		(1.631)	(2.156)	(1.29 [1.22])	(0.75 [0.87])	(+10.0)
	<i>fac</i> - $[\mathbf{1}(\mathbf{O})]^{2+}$ (S = 2)	1.625	2.104	3.11 [3.06]	0.60 [0.69]	+1.8
		(1.626)	(2.091)	(3.10 [3.05])	(0.61 [0.69])	(+0.2)
B15LYP <sup>b</sup>	<i>mer</i> - $[\mathbf{1}(\mathbf{O})]^{2+}$ (S = 1)			1.23	0.85	0
	<i>mer</i> - $[\mathbf{1}(\mathbf{O})]^{2+}$ (S = 2)			3.06	0.67	+10.0
	<i>fac</i> - $[\mathbf{1}(\mathbf{O})]^{2+}$ (S = 1)			1.23	0.86	+4.1
	<i>fac</i> - $[\mathbf{1}(\mathbf{O})]^{2+}$ (S = 2)			3.02	0.70	+7.6
B35LYP <sup>b</sup>	<i>mer</i> - $[\mathbf{1}(\mathbf{O})]^{2+}$ (S = 1)			1.03	1.00	+20.7
	<i>mer</i> - $[\mathbf{1}(\mathbf{O})]^{2+}$ (S = 2)			3.34	0.44	0
	<i>fac</i> - $[\mathbf{1}(\mathbf{O})]^{2+}$ (S = 1)			1.10	0.96	+29.4
	<i>fac</i> - $[\mathbf{1}(\mathbf{O})]^{2+}$ (S = 2)			3.25	0.54	+2.9
PBE0	<i>mer</i> - $[\mathbf{1}(\mathbf{O})]^{2+}$ (S = 1)	1.614	2.133	1.31 [1.23]	0.73 [0.86]	+3.9
		(1.614)	(2.129)	(1.31 [1.23])	(0.73 [0.85])	(+2.4)
	<i>mer</i> - $[\mathbf{1}(\mathbf{O})]^{2+}$ (S = 2)	1.606	2.161	3.24 [3.21]	0.51 [0.59]	+0.5
		(1.604)	(2.177)	(3.25 [3.21])	(0.50 [0.58])	(0)
	<i>fac</i> - $[\mathbf{1}(\mathbf{O})]^{2+}$ (S = 1)	1.616	2.127	1.32 [1.24]	0.74 [0.86]	+13.2
		(1.617)	(2.115)	(1.32 [1.24])	(0.74 [0.86])	(+14.7)
	<i>fac</i> - $[\mathbf{1}(\mathbf{O})]^{2+}$ (S = 2)	1.611	2.082	3.19 [3.15]	0.55 [0.64]	0
		(1.612)	(2.072)	(3.18 [3.14])	(0.56 [0.64])	(+4.5)

<sup>a</sup>Trans to the oxo ligand.

<sup>b</sup>B15LYP and B35LYP results are from single-point calculations at the B3LYP structure.

Table S10: Important bond lengths and energy differences between isomers of the iron-oxo complex  $[2(\text{O})]^{2+}$  for different functionals, as well as NPA and Mulliken (in brackets) spin populations. def2-TZVP basis for all atoms. Values in parentheses are for D3 corrected calculations.

functional		bond lengths in Å		spin population NPA [Mulliken]		$\Delta E$ in kJ mol <sup>-1</sup>
		Fe-O	Fe-N <sup>a</sup>	Fe	O	
BP86	<i>mer</i> - $[2(\text{O})]^{2+}$ (S = 1)	1.645	2.208	1.30 [1.29]	0.74 [0.84]	0
		(1.646)	(2.190)	(1.29 [1.28])	(0.74 [0.84])	(0)
	<i>mer</i> - $[2(\text{O})]^{2+}$ (S = 2)	1.640	2.176	3.01 [3.02]	0.64 [0.71]	+66.4
		(1.639)	(2.170)	(3.00 [3.02])	(0.64 [0.71])	(+63.4)
	<i>fac</i> - $[2(\text{O})]^{2+}$ (S = 1)	1.648	2.093	1.30 [1.29]	0.73 [0.82]	+76.7
		(1.650)	(2.061)	(1.29 [1.28])	(0.73 [0.83])	(+80.2)
	<i>fac</i> - $[2(\text{O})]^{2+}$ (S = 2)	1.643	2.071	3.01 [3.05]	0.66 [0.73]	+125.5
		(1.643)	(2.043)	(3.00 [3.04])	(0.66 [0.73])	(+124.7)
B3LYP	<i>mer</i> - $[2(\text{O})]^{2+}$ (S = 1)	1.622	2.227	1.30 [1.25]	0.75 [0.85]	0
		(1.623)	(2.210)	(1.29 [1.24])	(0.75 [0.85])	(0)
	<i>mer</i> - $[2(\text{O})]^{2+}$ (S = 2)	1.617	2.196	3.17 [3.12]	0.56 [0.64]	+22.1
		(1.617)	(2.188)	(3.17 [3.12])	(0.56 [0.64])	(+19.1)
	<i>fac</i> - $[2(\text{O})]^{2+}$ (S = 1)	1.626	2.120	1.30 [1.25]	0.76 [0.85]	+82.5
		(1.628)	(2.092)	(1.29 [1.24])	(0.76 [0.86])	(+86.4)
	<i>fac</i> - $[2(\text{O})]^{2+}$ (S = 2)	1.620	2.096	3.17 [3.12]	0.59 [0.67]	+89.7
		(1.621)	(2.071)	(3.16 [3.11])	(0.59 [0.68])	(+89.2)
B15LYP <sup>b</sup>	<i>mer</i> - $[2(\text{O})]^{2+}$ (S = 1)			1.30 [1.25]	0.75 [0.85]	0
	<i>mer</i> - $[2(\text{O})]^{2+}$ (S = 2)			3.12 [3.08]	0.59 [0.67]	+29.1
	<i>fac</i> - $[2(\text{O})]^{2+}$ (S = 1)			1.31 [1.26]	0.75 [0.84]	+81.6
	<i>fac</i> - $[2(\text{O})]^{2+}$ (S = 2)			3.12 [3.08]	0.62 [0.69]	+95.6
B35LYP <sup>b</sup>	<i>mer</i> - $[2(\text{O})]^{2+}$ (S = 1)			1.25 [1.16]	0.80 [0.92]	+7.7
	<i>mer</i> - $[2(\text{O})]^{2+}$ (S = 2)			3.46 [3.40]	0.31 [0.39]	0
	<i>fac</i> - $[2(\text{O})]^{2+}$ (S = 1)			1.16 [1.09]	0.88 [0.98]	+90.0
	<i>fac</i> - $[2(\text{O})]^{2+}$ (S = 2)			3.42 [3.35]	0.39 [0.47]	+72.4
PBE0	<i>mer</i> - $[2(\text{O})]^{2+}$ (S = 1)	1.607	2.190	1.32 [1.27]	0.74 [0.84]	0
		(1.607)	(2.181)	(1.32 [1.26])	(0.74 [0.85])	(0)
	<i>mer</i> - $[2(\text{O})]^{2+}$ (S = 2)	1.603	2.169	3.26 [3.22]	0.50 [0.59]	+14.4
		(1.603)	(2.162)	(3.25 [3.21])	(0.50 [0.59])	(+20.1)
	<i>fac</i> - $[2(\text{O})]^{2+}$ (S = 1)	1.612	2.087	1.31 [1.27]	0.74 [0.85]	+79.9
		(1.613)	(2.071)	(1.31 [1.26])	(0.74 [0.85])	(+82.2)
	<i>fac</i> - $[2(\text{O})]^{2+}$ (S = 2)	1.606	2.071	3.25 [3.22]	0.53 [0.62]	+78.9
		(1.605)	(2.067)	(3.25 [3.22])	(0.53 [0.62])	(+79.5)

<sup>a</sup>Trans to the oxo ligand.

<sup>b</sup>B15LYP and B35LYP results are from single-point calculations at the B3LYP structure.

Table S11: Isodesmic reactions of the iron-oxo complexes to form their corresponding Fe(II) intermediates of type IV and their relative energies (kJ mol<sup>-1</sup>; B3LYP-D3/def2-TZVP/COSMO(MeCN)).

Isodesmic reaction	$\Delta E$ (products - educts)
$mer-[1(O)]^{2+}$ (S = 1) + $^-OTf \rightarrow mer-IV$ (S = 2) + HOTf	-19.7
$mer-[1(O)]^{2+}$ (S = 2) + $^-OTf \rightarrow mer-IV$ (S = 2) + HOTf	-29.6
$fac-[1(O)]^{2+}$ (S = 1) + $^-OTf \rightarrow fac-IV$ (S = 2) + HOTf	-4.9
$fac-[1(O)]^{2+}$ (S = 2) + $^-OTf \rightarrow fac-IV$ (S = 2) + HOTf	-5.4

Table S12: Relative energies (kJ mol<sup>-1</sup>) for the spin states of different Fe(II) intermediates from proposed decomposition reactions of the iron-oxo complexes (def2-TZVP basis for all atoms). B15LYP and B35LYP results are from single-point calculations at the B3LYP structure.

functional	derived from isomer	$\Delta E$ (triplet - quintet)		
		<b>II</b>	<b>IV</b>	<b>V</b>
BP86	<i>mer-</i>	-16.4	-22.7	+1.6
	<i>fac-</i>	-17.0	+7.7	+9.0
B3LYP-D3	<i>mer-</i>	+32.4	+39.5	+49.2
	<i>fac-</i>	+32.2	+66.1	+55.7
B15LYP	<i>mer-</i>	+30.1	+36.5	+49.8
	<i>fac-</i>	+28.6	+55.1	+55.4
B35LYP	<i>mer-</i>	+73.8	+84.0	+92.8
	<i>fac-</i>	+72.8	+98.9	+96.5

Table S13: Calculated Mössbauer parameters (see Computational Details in Chapter 3.4 for the exact level) and spin-state energy differences (B3LYP-D3/def2-TZVP) for other possible products of  $[2(OH)]^{2+}$ . In case of two-core iron complexes, values for both iron centers are given.

	S	$\delta$ [mm s <sup>-1</sup> ]	$\Delta EQ$ [mm s <sup>-1</sup> ]	$\Delta E$ [kJ mol <sup>-1</sup> ]
$[2(O)-(O)2]^{4+}$	0	0.44	1.85	12.6
		0.46	2.53	
	1	0.44	1.90	16.3
		0.46	2.55	
	2	0.62	0.48	0
		0.47	2.50	
$[2-O-2]^{4+}$	0	0.46	1.99	22.2
		0.47	2.06	
	1	0.47	1.92	18.8
		0.47	2.12	
	2	0.44	2.11	0
		0.49	-1.10	
$mer-[2(OH)]^{2+}$	5/2	0.54	0.92	

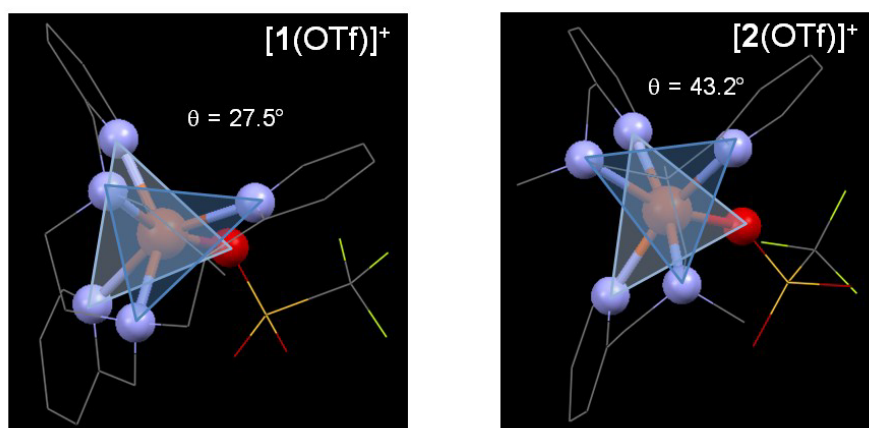


Figure S5: Optimized structures (B3LYP-D3/def2-TZVP/COSMO(MeCN)) of the complex ions  $[1(\text{OTf})]^+$  and  $[2(\text{OTf})]^+$ ; view along a pseudo-threefold axes. Average trigonal-distortion angles  $\theta$  are shown.

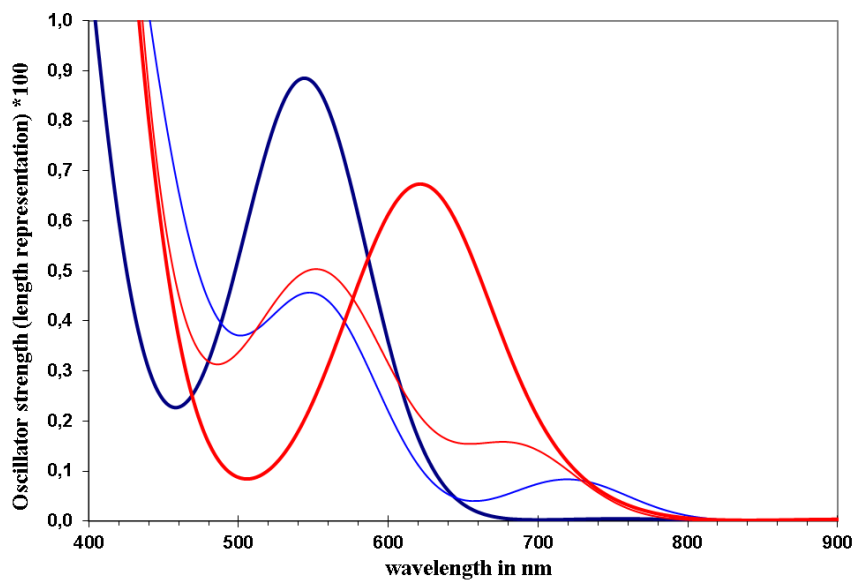


Figure S6: Calculated (B3LYP-D3/def2-TZVP/COSMO(MeCN)) UV/VIS spectra of the two conformers  $mer\text{-}[2(\text{O})]^{2+}$  (blue) and  $fac\text{-}[2(\text{O})]^{2+}$  (red) in the triplet (bold lines) and the quintet state (thin lines).

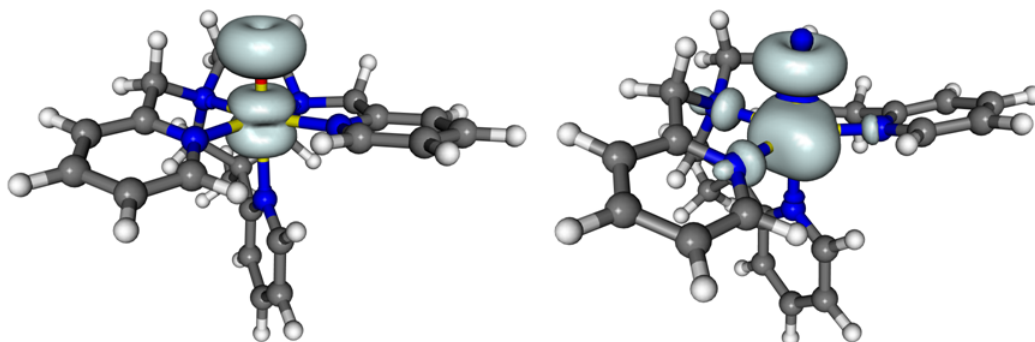


Figure S7: Isosurface plots of the spin density ( $\pm 0.005$  a.u.) of  $fac-[1(O)]^{2+}$  with  $S = 1$  (left) and  $S = 2$  (right).

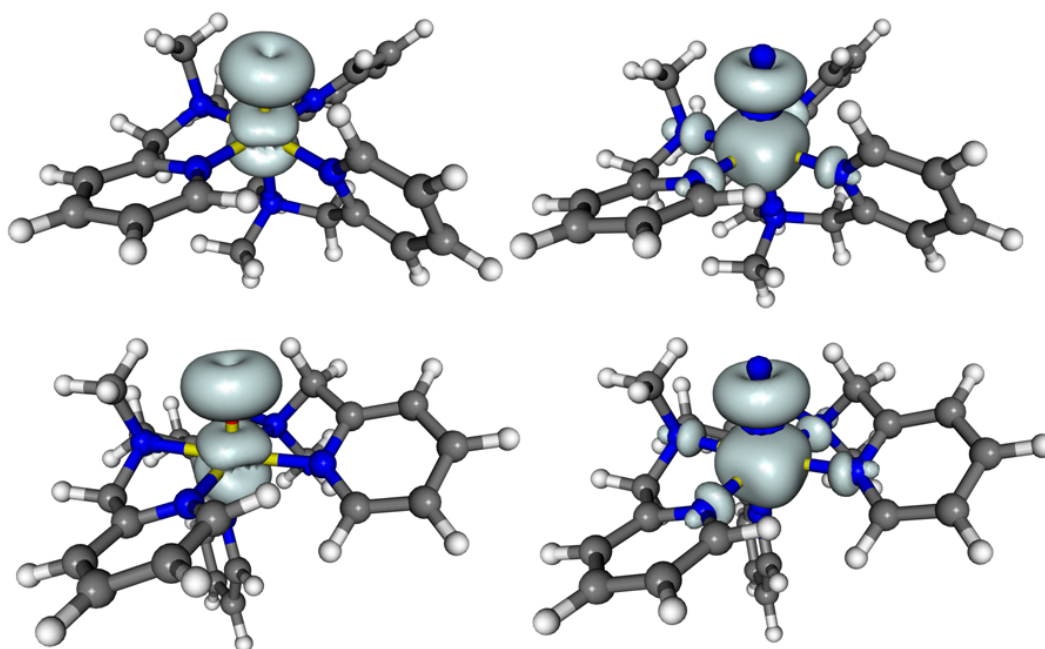
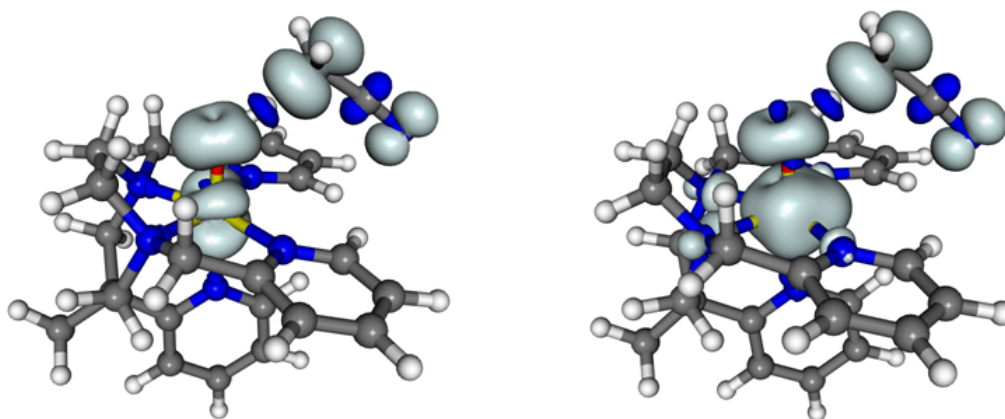


Figure S8: Isosurface plots of the spin density ( $\pm 0.005$  a.u.) of  $mer-[2(O)]^{2+}$  with  $S = 1$  (top left) and  $S = 2$  (top right) and  $fac-[2(O)]^{2+}$  with  $S = 1$  (bottom left) and  $S = 2$  (bottom right).

Table S14: Spin-state energy differences in  $\text{kJ mol}^{-1}$  for  $[\mathbf{1}(\text{OH})]^{2+}$  and  $\bullet\text{CH}_2\text{CN}$  (def2-TZVP basis used for all atoms).

	spin state	$\Delta E$	
		B3LYP	B3LYP-D3
<i>mer</i> - $[\mathbf{1}(\text{OH})]^{2+}$	S = 1/2	19.8	18.3
	S = 3/2	38.0	35.8
	S = 5/2	0	0
<i>fac</i> - $[\mathbf{1}(\text{OH})]^{2+}$	S = 1/2	12.0	13.4
	S = 3/2	14.0	9.7
	S = 5/2	0	0
$\bullet\text{CH}_2\text{CN}$	S = 1/2	0	0
	S = 3/2	409.7	409.6
	S = 5/2	828.0	827.5

Figure S9: Isosurface plots of the spin density ( $\pm 0.005$  a.u.) of the transition state *fac*- $[\mathbf{1}(\text{O})]^{2+} + \text{MeCN}$  with S = 1 (left) and S = 2 (right) from B3LYP/def2-TZVP optimized structures.

# Appendix II

Table S1: Comparison of wave-function results for gas-phase activation barriers,  $\Delta E^\ddagger$ , and reaction energies,  $\Delta E$ , in  $\text{kJ mol}^{-1}$  for Diels-Alder reactions with cyclopentadiene<sup>a,b</sup>

Method and basis set	MVK+CP		NQ+CP	
	$\Delta E^\ddagger$	$\Delta E$	$\Delta E^\ddagger$	$\Delta E$
HF/aug-cc-pVDZ	148.9	-71.8	149.1	-54.2
HF/aug-cc-pVTZ	159.9	-54.6	163.5	-34.2
HF/aug-cc-pVQZ	161.6	-53.4	166.0	-32.6
HF/aug-cc-pV5Z	162.0	-53.0	166.5	-32.0
HF/CBS	162.4	-52.5	167.1	-31.5
MP2/aug-cc-pVDZ	-28.3	-171.4	-65.0	-170.3
MP2/aug-cc-pVTZ	-24.9	-172.8	-57.2	-166.5
MP2/aug-cc-pVQZ	-7.9	-151.9	-33.9	-141.4
MP2/aug-cc-pV5Z	-7.1	-155.9	-33.5	-145.6
MP2/CBS	-6.3	-160.2	-33.2	-150.0
SCS-MP2/aug-cc-pVDZ	10.9	-151.3	-18.0	-147.2
SCS-MP2/aug-cc-pVTZ	13.1	-154.2	-12.2	-145.6
SCS-MP2/aug-cc-pVQZ	32.2	-130.8	13.7	-117.8
SCS-MP2/aug-cc-pV5Z	32.8	-135.9	13.7	-123.2
SCS-MP2/CBS	33.5	-141.2	13.7	-128.8
CCSD/aug-cc-pVDZ	41.9	-146.8		
CCSD/aug-cc-pVTZ	46.6	-149.1		
CCSD(T)/aug-cc-pVDZ	14.7	-150.9		
CCSD(T)/aug-cc-pVTZ	19.5	-152.3		

<sup>a</sup>PBE0-D3/def2-TZVP gas-phase structures were used for the single-point wave-function calculations.

<sup>b</sup>Complete basis-set estimates for HF, MP2, and SCS-MP2 from two-point extrapolations of aug-cc-pVQZ and aug-cc-pV5Z data.

Table S2: Comparison of PBE0 results with different basis sets for gas-phase activation barriers,  $\Delta E^\ddagger$ , and reaction energies,  $\Delta E$ , in kJ mol<sup>-1</sup>, for Diels-Alder reactions with cyclopentadiene<sup>a</sup>

Basis set	MVK+CP		NQ+CP	
	$\Delta E^\ddagger$	$\Delta E$	$\Delta E^\ddagger$	$\Delta E$
def2-SVP	37.3	-139.1	34.8	-118.8
def2-TZVP	46.9	-115.9	46.7	-92.7
def2-QZVP	48.4	-113.9	48.2	-90.4
6-31G*	33.2	-143.7	30.6	-120.6
6-311G**	40.2	-126.7	37.7	-106.1

<sup>a</sup>Single-point calculation at the PBE0/def2-TZVP gas-phase structure.

Table S3: Calculated activation barriers,  $\Delta E^\ddagger$ , and reaction energies,  $\Delta E$ , in kJ mol<sup>-1</sup>, for the MVK+CP reaction in the gas phase and with COSMO or D-COSMO-RS solvent models, using three different density functionals and def2-TZVP basis sets

	RIBP86		B3LYP		PBE0	
	$\Delta E^\ddagger$	$\Delta E$	$\Delta E^\ddagger$	$\Delta E$	$\Delta E^\ddagger$	$\Delta E$
gas phase	45.6	-71.1	78.1	-49.5	46.9	-115.9
gas phase+D3	10.6	-101.5	48.4	-75.6	27.4	-132.6
gas phase+2H <sub>2</sub> O	26.1	-72.0	57.8	-49.2	27.0	-116.1
gas phase+2H <sub>2</sub> O+D3	-21.1	-108.1	18.0	-79.6	0.4	-136.1
COSMO-water	45.9	-62.2	77.1	-40.6	44.3	-109.9
D-COSMO-RS-water	30.3	-69.2	59.9	-47.4	29.4	-115.4
D-COSMO-RS-water+D3	-4.1	-99.2	31.1	-73.0	15.4	-128.7
COSMO-water+2H <sub>2</sub> O <sup>a</sup>	39.3	-62.6	70.3	-40.6	40.5	-106.1
D-COSMO-RS-water+2H <sub>2</sub> O <sup>a</sup>	32.6	-70.6	63.1	-48.5	34.1	-114.7
COSMO-hexane	46.4	-68.0	78.6	-46.3	48.0	-112.4
D-COSMO-RS-hexane	53.5	-59.1	85.8	-37.3	55.5	-103.2
COSMO-methanol	46.0	-62.4	77.3	-40.9	44.4	-110.2
D-COSMO-RS-methanol	41.7	-62.0	71.0	-40.5	39.9	-109.4
COSMO-acetonitrile	46.0	-62.4	77.3	-40.9	44.4	-110.1
D-COSMO-RS-acetonitrile	51.1	-58.6	82.9	-37.2	49.5	-106.5

<sup>a</sup>Single-point calculation at the gas-phase+2H<sub>2</sub>O structure.

Table S4: Calculated activation barriers,  $\Delta E^\ddagger$ , and reaction energies,  $\Delta E$ , in  $\text{kJ mol}^{-1}$ , for the NQ+CP reaction in the gas phase and with COSMO or D-COSMO-RS solvent models, using three different density functionals and def2-TZVP basis sets

	RIBP86		B3LYP		PBE0	
	$\Delta E^\ddagger$	$\Delta E$	$\Delta E^\ddagger$	$\Delta E$	$\Delta E^\ddagger$	$\Delta E$
gas phase	52.3	-44.7	85.8	-24.5	46.7	-92.7
gas phase+D3	5.8	-83.9	46.5	-57.8	20.1	-114.5
gas phase+4H <sub>2</sub> O	26.5	-51.7	59.9	-30.4	17.8	-100.2
gas phase+4H <sub>2</sub> O+D3	-30.8	-100.5	11.5	-71.9	-15.7	-128.1
COSMO-water	47.6	-39.0	81.3	-18.3	42.2	-86.1
D-COSMO-RS-water	30.5	-48.8	64.4	-28.0	25.4	-95.5
D-COSMO-RS-water+D3	-16.2	-89.0	24.5	-62.3	-1.9	-118.1
COSMO-water+4H <sub>2</sub> O <sup>a</sup>	37.5	-42.4	71.2	-22.1	30.4	-90.5
D-COSMO-RS-water+4H <sub>2</sub> O <sup>a</sup>	31.7	-48.8	68.5	-26.2	26.2	-95.8
COSMO-hexane	51.3	-42.6	84.9	-22.2	45.8	-90.3
D-COSMO-RS-hexane	59.4	-33.5	93.0	-13.1	54.0	-81.0
COSMO-methanol	47.8	-39.2	81.6	-18.4	42.5	-86.3
D-COSMO-RS-methanol	48.9	-36.5	82.1	-16.3	43.1	-83.7
COSMO-acetonitrile	47.8	-39.1	81.5	-18.4	42.4	-86.3
D-COSMO-RS-acetonitrile	54.5	-33.1	88.5	-12.5	49.2	-80.2

<sup>a</sup>Single-point calculation at the gas-phase+4H<sub>2</sub>O structure.

Table S5: Effect of structure on wave-function results for gas-phase activation barriers,  $\Delta E^\ddagger$ , and reaction energies,  $\Delta E$ , in  $\text{kJ mol}^{-1}$ , for the MVK+CP reaction<sup>a</sup>

Structures: Method and basis set	PBE0-D3		B3LYP	
	$\Delta E^\ddagger$	$\Delta E$	$\Delta E^\ddagger$	$\Delta E$
HF/aug-cc-pVDZ	148.9	-71.8	153.6	-72.2
HF/aug-cc-pVTZ	159.9	-54.6	165.2	-54.9
HF/aug-cc-pVQZ	161.6	-53.4	166.9	-53.7
HF/aug-cc-pV5Z	162.0	-53.0	167.3	-53.3
HF/CBS	162.4	-52.5	167.8	-52.8
MP2/aug-cc-pVDZ	-28.3	-171.4	-25.3	-170.0
MP2/aug-cc-pVTZ	-24.9	-172.8	-21.2	-169.5
MP2/aug-cc-pVQZ	-7.9	-151.9	-4.5	-149.0
MP2/aug-cc-pV5Z	-7.1	-155.9	-3.8	-152.9
MP2/CBS	-6.3	-160.2	-3.0	-156.9
SCS-MP2/aug-cc-pVDZ	10.9	-151.3	14.6	-150.6
SCS-MP2/aug-cc-pVTZ	13.1	-154.2	17.5	-151.7
SCS-MP2/aug-cc-pVQZ	32.2	-130.8	36.3	-128.9
SCS-MP2/aug-cc-pV5Z	32.8	-135.9	36.8	-133.7
SCS-MP2/CBS	33.5	-141.2	37.4	-138.8
CCSD/aug-cc-pVDZ	41.9	-146.8	46.9	-146.2
CCSD/aug-cc-pVTZ	46.6	-149.1	52.5	-146.5
CCSD(T)/aug-cc-pVDZ	14.7	-150.9	17.8	-150.5
CCSD(T)/aug-cc-pVTZ	19.5	-152.3	23.2	-149.9

<sup>a</sup>Complete basis-set extrapolations for HF, MP2, and SCS-MP2 from two-point extrapolations with aug-cc-pVQZ and aug-cc-pV5Z results.

Table S6: Important distances (in Å) in the transition state and natural charges on the ketone oxygen atom for the NQ+CP Diels-Alder reaction in different environments<sup>a</sup>

	$d_1$	$d_2$	$q_{educt}$	$q_{trans}$	$q_{product}$
gas phase	2.212	2.212	-0.49	-0.54	-0.53
gas phase+D3	2.202	2.202	-0.49	-0.54	-0.53
gas phase+4H <sub>2</sub>	2.210	2.210	-0.57	-0.63	-0.61
gas phase+4H <sub>2</sub> +D3	2.195	2.195	-0.57	-0.63	-0.61
COSMO-water	2.214	2.214	-0.54	-0.61	-0.58
COSMO-water+D3	2.204	2.204	-0.54	-0.61	-0.58
D-COSMO-RS-water	2.220	2.216	-0.59	-0.68	-0.64
D-COSMO-RS-water+D3	2.220	2.212	-0.59	-0.68	-0.64
COSMO-water+4H <sub>2</sub>	2.219	2.216	-0.58	-0.65	-0.62
COSMO-water+4H <sub>2</sub> +D3	2.215	2.205	-0.58	-0.65	-0.62
D-COSMO-RS-water+4H <sub>2</sub>	2.238	2.252	-0.58	-0.66	-0.63
D-COSMO-RS-water+4H <sub>2</sub> +D3	2.269	2.264	-0.58	-0.66	-0.63
COSMO-methanol	2.214	2.214	-0.54	-0.60	-0.58
COSMO-methanol+D3	2.204	2.203	-0.54	-0.60	-0.58
D-COSMO-RS-methanol	2.210	2.213	-0.54	-0.62	-0.58
D-COSMO-RS-methanol+D3	2.194	2.204	-0.54	-0.63	-0.58
COSMO-acetonitrile	2.214	2.214	-0.54	-0.60	-0.58
COSMO-acetonitrile+D3	2.205	2.205	-0.54	-0.61	-0.58
D-COSMO-RS-acetonitrile	2.212	2.211	-0.53	-0.59	-0.57
D-COSMO-RS-acetonitrile+D3	2.201	2.202	-0.53	-0.59	-0.57
COSMO-hexane	2.212	2.212	-0.51	-0.56	-0.54
COSMO-hexane+D3	2.202	2.202	-0.51	-0.56	-0.54
D-COSMO-RS-hexane	2.212	2.212	-0.51	-0.57	-0.55
D-COSMO-RS-hexane+D3	2.202	2.202	-0.51	-0.57	-0.55

<sup>a</sup>PBE0/def2-TZVP results with and without D3 dispersion corrections. See Figure 4.2 for definition of the distances.

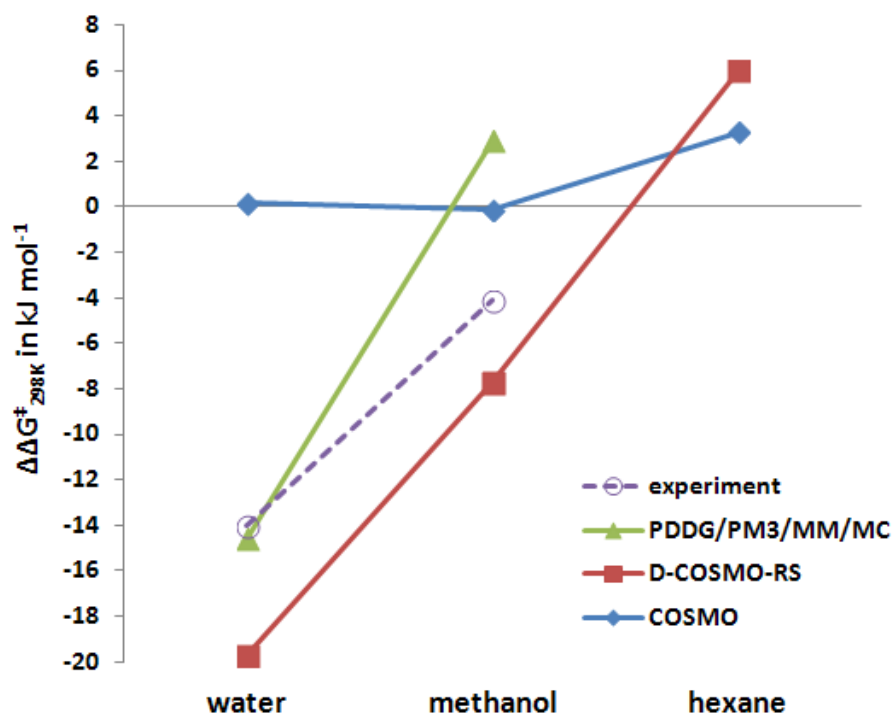


Figure S1: Solvent contributions to the Gibbs free activation energy of the MVK+CP reaction relative to acetonitrile using different methods. The semi-empirical PDDG/PM3/MM/MC calculations are from ref. [244]. The present calculations are provided at PBE0/def2-TZVP level without dispersion corrections. Experimental data from ref. [240].

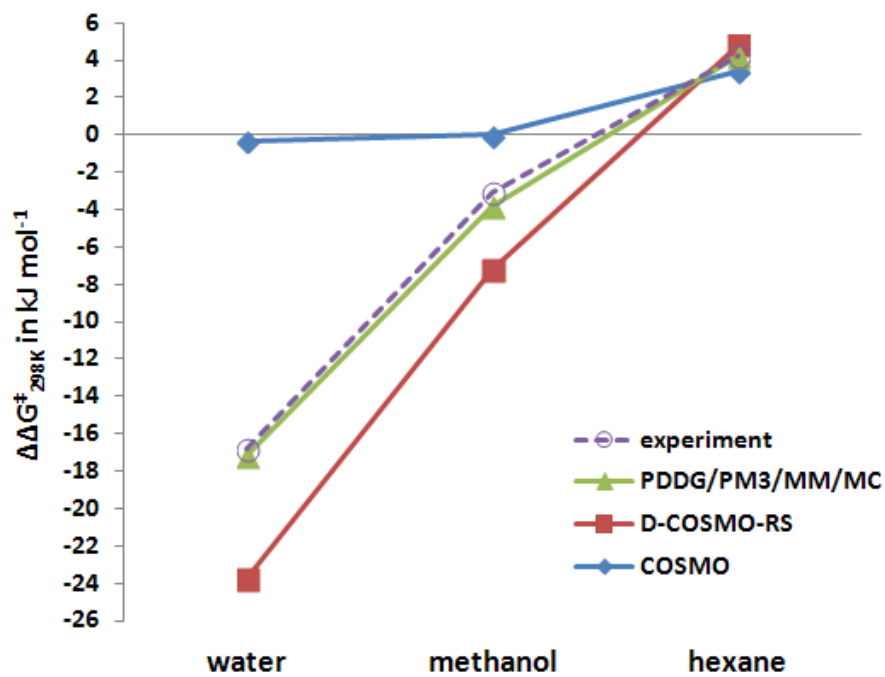


Figure S2: Solvent contributions to the Gibbs free activation energy of the NQ+CP reaction relative to acetonitrile using different methods. The semi-empirical PDDG/PM3/MM/MC calculations are from ref. [244]. The present calculations are provided at PBE0/def2-TZVP level without dispersion corrections. Experimental data from ref. [240].

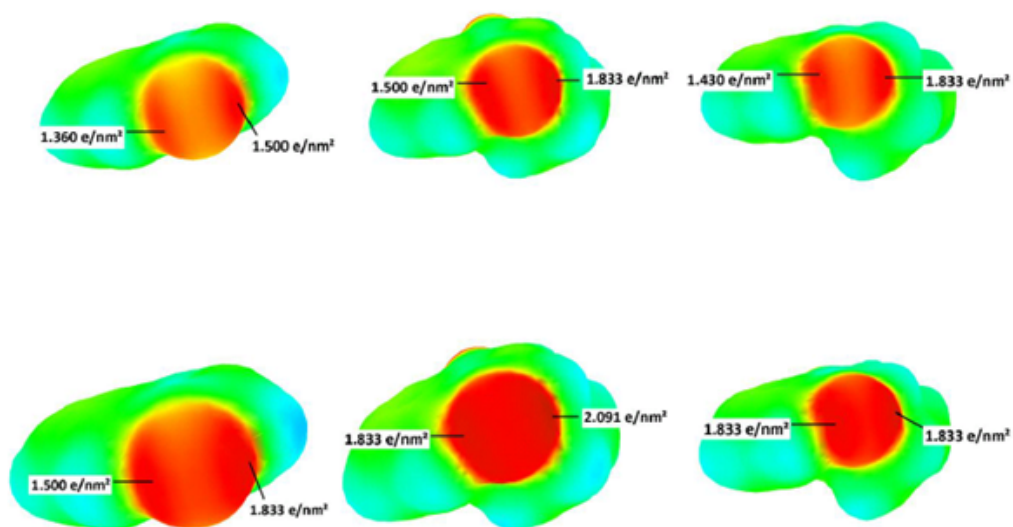


Figure S3: Mapping of surface charges for NQ+CP system. Upper row from left to right: educt, transition state and product with COSMO-water. Lower row from left to right: educt, transition state and product with D-COSMO-RS-water. PBE0/def2-TZVP+D3 results.

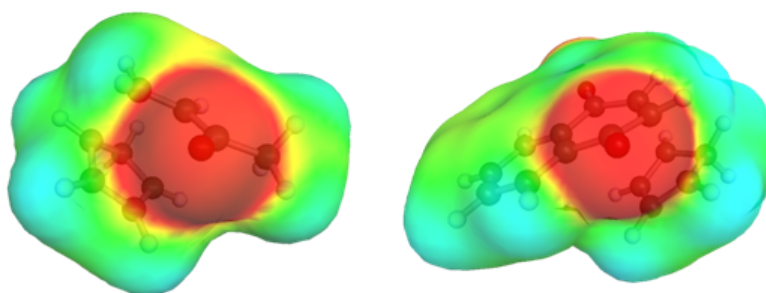


Figure S4: Mapping of surface charges for the MVK+CP and the NQ+CP transition states in D-COSMO-RS-water with atoms shown. PBE0/def2-TZVP+D3 results.

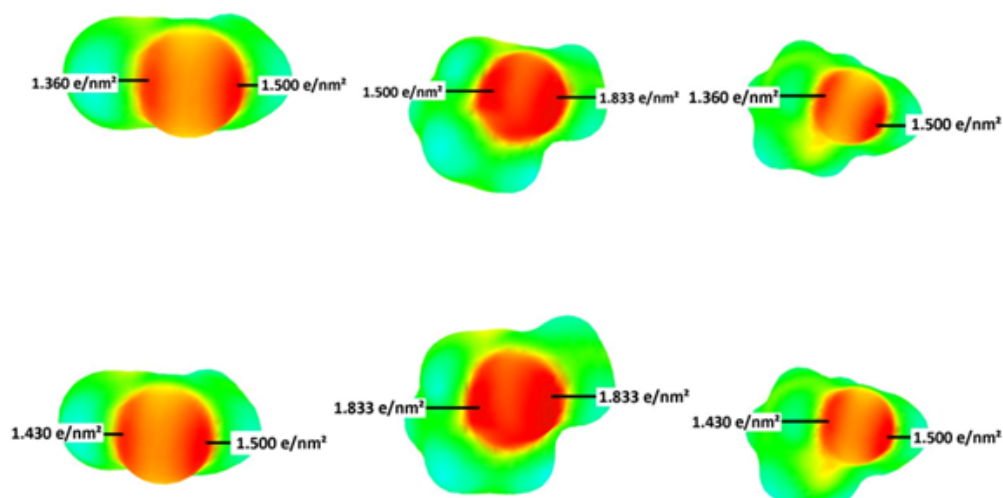


Figure S5: Mapping of surface charges for the MVK+CP system in hexane. Upper row from left to right: educt, transition state and product with COSMO-hexane. Lower row from left to right: educt, transition state and product with D-COSMO-RS-hexane. PBE0/def2-TZVP+D3 results.

Table S7: MP2-optimized valence basis sets for non- and scalar-relativistic small-core Stuttgart-type gold ECPs in GAUSSIAN format.

Au basis NR-ECP (10s/11p/6d/3f)		Au basis SR-ECP (11s/11p/6d/3f)	
Au 0		Au 0	
S 1 1.00	P 1 1.00	S 1 1.00	P 1 1.00
13.548766 1.0	0.654920 1.0	19.44656 1.0	1.308277 1.0
S 1 1.00	P 1 1.00	S 1 1.00	P 1 1.00
11.015011 1.0	0.306968 1.0	12.21650 1.0	0.648004 1.0
S 1 1.00	P 1 1.00	S 1 1.00	P 1 1.00
5.936089 1.0	0.124711 1.0	6.683783 1.0	0.304676 1.0
S 1 1.00	P 1 1.00	S 1 1.00	P 1 1.00
2.501871 1.0	0.065057 1.0	2.704808 1.0	0.164092 1.0
S 1 1.00	P 1 1.00	S 1 1.00	P 1 1.00
1.891346 1.0	0.023 1.0	1.794396 1.0	0.091945 1.0
S 1 1.00	D 1 1.00	S 1 1.00	P 1 1.00
0.831034 1.0	4.239889 1.0	1.144536 1.0	0.042428 1.0
S 1 1.00	D 1 1.00	S 1 1.00	D 1 1.00
0.370618 1.0	3.289635 1.0	0.662835 1.0	4.234847 1.0
S 1 1.00	D 1 1.00	S 1 1.00	D 1 1.00
0.173459 1.0	1.354964 1.0	0.267503 1.0	3.390436 1.0
S 1 1.00	D 1 1.00	S 1 1.00	D 1 1.00
0.049479 1.0	0.630038 1.0	0.079484 1.0	1.359430 1.0
S 1 1.00	D 1 1.00	S 1 1.00	D 1 1.00
0.0158 1.0	0.270917 1.0	0.033387 1.0	0.634206 1.0
P 1 1.00	D 1 1.00	S 1 1.00	D 1 1.00
18.515736 1.0	0.105538 1.0	0.0158 1.0	0.274309 1.0
P 1 1.00	F 1 1.00	P 1 1.00	D 1 1.00
8.515736 1.0	2.3161 1.0	18.515736 1.0	0.107320 1.0
P 1 1.00	F 1 1.00	P 1 1.00	F 1 1.00
6.928483 1.0	1.2353 1.0	8.656024 1.0	2.3161 1.0
P 1 1.00	F 1 1.00	P 1 1.00	F 1 1.00
3.570905 1.0	0.4878 1.0	7.469250 1.0	1.2353 1.0
P 1 1.00		P 1 1.00	F 1 1.00
2.212222 1.0		3.113937 1.0	0.4878 1.0
P 1 1.00		P 1 1.00	
1.285103 1.0		2.190455 1.0	

Table S8: Spin-Orbit contributions at two component B3LYP/dhf-QZVP-2c level with two-component ECPs. All energies are in  $\text{kJ mol}^{-1}$ . Values in parentheses are spin-orbit energies without two-component ECPs for bromine or iodine. Two-component reaction energies are for the  $\text{AuX}_4^- \rightleftharpoons \text{AuX}_2^- + \text{X}_2$  ( $\text{X}=\text{Br}, \text{I}$ ) reaction. The scalar-relativistic one-component reaction energies were calculated at the same level.

spin-orbit energy			reaction energy	reaction energy
			(two-component)	(sc.-relativistic)
$\text{AuBr}_4^-$	$\text{AuBr}_2^-$	$\text{Br}_2$		
-1170.6 (-902.4)	-1022.1 (-886.9)	-137.6 (0)	88.66 (91.21)	83.12
$\text{AuI}_4^-$	$\text{AuI}_2^-$	$\text{I}_2$		
-1778.5 (-898.9)	-1322.5 (-886.0)	-445.7 (0)	38.30 (39.62)	32.94

# Appendix III

Table S1: List of LMFs covered in this work and their semi-empirical parameters, D3 dispersion correction parameters and weighted total mean absolute errors (WTMAE) for the GMTKN30 test set database. All errors are in kcal/mol. Data for four global hybrids are given for comparison.

Name	semi-empirical parameters	D3 dispersion parameters			
		$s_{r,6}$	$s_8$	WTMAE	WTMAE+D3
B3LYP		1.261	1.703	5.72	3.70
PBE0		1.287	0.928	4.34	3.64
TPSSh		1.223	1.219	5.32	3.96
B35LYP		1.122	0.925	6.18	4.62
<i>t</i> -LMF	$b=0.48$	0.959	1.021	5.48	2.80
<i>s</i> -LMF	$b=0.22$	0.863	1.597	6.47	2.89
common	$b=0.534$	1.450	3.025	6.27	3.25
$\zeta$ - <i>t</i> -LMF	$b=0.446, c=0.0531$	1.011	0.972	4.94	2.66
$\zeta$ - <i>s</i> -LMF	$b=0.197, c=0.0423$	0.912	1.452	5.95	2.84
comb. opt. $\zeta$ - <i>t</i> -LMF	$b=0.455, c=0.0531$	1.070	1.055	5.06	2.88
<i>Lh</i> -LSDA-SIF-SRc	$b=0.709, \mu=0.8, \lambda=1.0$ ; erfgau	0.770	1.429	6.42	2.96
<i>Lh</i> -LSDA-SIR-SRc	$b=0.646, \mu=0.8, \lambda=0.646$ ; erfgau	0.765	1.714	6.26	2.72
<i>Lh</i> -LSDA-SIR-SRc	$b=0.622, \mu=0.5, \lambda=0.622$ ; erf	0.766	1.304	6.43	2.62
<i>Lh</i> -BLYP-CG	$b=0.488, \eta=0.5, c=-0.000894,$ $nlx=0.206, nlc=0.497$	1.060	0.975	4.47	2.63
<i>Lh</i> -PBE-CG	$b=0.5, \eta=0.12, c=-0.00238,$ $nlx=0.507, nlc=0.451$	1.204	0.792	3.71	2.60

Table S2: Mean absolute errors (MAE) and mean signed errors (MSE) for the subsets of the GMTKN30 test set database for different global hybrid functionals with and without D3 dispersion correction. All errors are in kcal/mol. The weighted total mean absolute error (WTMAE) for the whole database is given at the bottom

test set	B3LYP	+D3	PBE0	+D3	TPSSH	+D3
	MAE (MSE)	MAE (MSE)	MAE (MSE)	MAE (MSE)	MAE (MSE)	MAE (MSE)
MB08-165	8.14 (-6.79)	6.38 (-3.97)	8.65 (-0.42)	8.66 (1.30)	8.65 (-5.13)	8.05 (-2.87)
W4-08	3.94 (-2.35)	3.86 (-2.14)	3.70 (-1.88)	3.67 (-1.76)	4.54 (-1.18)	4.55 (-1.02)
G21IP	3.55 (-0.09)	3.55 (-0.10)	3.68 (0.03)	3.69 (0.02)	3.94 (-0.70)	3.94 (-0.71)
G21EA	1.92 (0.48)	1.93 (0.48)	2.61 (-0.46)	2.61 (-0.46)	2.70 (-0.66)	2.71 (-0.66)
PA	2.23 (1.90)	2.38 (2.06)	2.66 (2.66)	2.76 (2.76)	4.60 (4.60)	4.72 (4.72)
SIE11	7.63 (6.17)	8.70 (7.32)	7.13 (6.38)	7.79 (7.06)	8.63 (7.75)	9.50 (8.65)
BHPERI	5.80 (5.36)	2.78 (2.18)	2.37 (1.07)	2.58 (-2.12)	2.43 (0.90)	1.85 (-1.69)
BH76	4.67 (-4.57)	5.21 (-5.14)	4.11 (-3.86)	4.43 (-4.20)	6.62 (-6.59)	7.07 (-7.05)
BH76RC	2.32 (-0.24)	2.25 (-0.28)	2.52 (-0.01)	2.55 (-0.03)	3.44 (0.15)	3.48 (0.12)
RSE43	2.37 (-2.37)	1.97 (-1.97)	2.00 (-2.00)	1.76 (-1.76)	2.10 (-2.10)	1.78 (-1.78)
O3ADD6	1.99 (-0.88)	2.75 (-2.75)	4.81 (-4.59)	5.71 (-5.71)	3.24 (-2.83)	4.34 (-4.34)
G2RC	2.64 (0.46)	2.76 (0.21)	6.47 (-3.52)	6.77 (-3.67)	5.65 (1.22)	6.01 (1.02)
AL2X	8.46 (-8.46)	4.28 (-4.28)	2.68 (-1.80)	1.89 (0.75)	3.38 (-2.50)	2.20 (0.88)
NBPRC	4.78 (3.99)	3.02 (1.67)	2.61 (0.19)	3.27 (-1.21)	2.37 (0.89)	1.94 (-0.98)
ISO34	2.28 (-0.23)	1.86 (-0.09)	1.81 (-0.22)	1.61 (-0.14)	2.18 (-1.35)	1.87 (-1.22)
ISOL22	9.08 (-5.53)	6.96 (-4.39)	4.15 (-1.87)	2.94 (-1.18)	8.75 (-6.27)	7.21 (-5.52)
DC9	15.10 (6.92)	11.92 (4.68)	10.41 (1.89)	9.36 (0.45)	10.37 (4.88)	7.97 (2.98)
DARC	15.28 (15.28)	10.11 (10.11)	3.52 (0.00)	3.32 (-3.19)	8.06 (8.06)	4.02 (3.80)
ALK6	9.23 (-9.14)	4.82 (-4.63)	2.42 (0.81)	3.50 (3.33)	2.17 (-0.36)	3.38 (2.98)
BSR36	11.32 (-11.32)	6.00 (-6.00)	8.24 (-8.24)	4.73 (-4.73)	10.62 (-10.62)	6.17 (-6.17)
IDISP	17.46 (3.75)	6.62 (3.58)	10.59 (0.78)	3.48 (0.70)	13.32 (2.46)	4.21 (2.40)
WATER27	6.50 (-6.20)	4.26 (4.12)	2.80 (-0.76)	6.46 (6.10)	5.65 (-4.99)	4.27 (3.79)
S22	3.79 (-3.79)	0.36 (0.17)	2.38 (-2.34)	0.57 (0.29)	3.29 (-3.29)	0.38 (0.10)
ADIM6	5.02 (-5.02)	0.43 (0.43)	3.41 (-3.41)	0.36 (0.36)	4.61 (-4.61)	0.22 (0.22)
RG6	0.80 (-0.80)	0.07 (0.01)	0.43 (-0.43)	0.03 (0.03)	0.60 (-0.60)	0.05 (0.02)
HEAVY28	1.37 (-1.37)	0.16 (-0.05)	0.66 (-0.66)	0.17 (0.11)	0.97 (-0.97)	0.17 (0.05)
PCONF	3.98 (-3.98)	0.34 (-0.26)	3.33 (-3.33)	0.89 (-0.89)	4.10 (-4.10)	0.94 (-0.94)
ACONF	0.96 (0.96)	0.14 (0.14)	0.64 (0.64)	0.10 (0.10)	0.72 (0.72)	0.03 0.03
SCONF	0.98 (-0.70)	0.52 (-0.52)	0.47 (-0.39)	0.32 (-0.30)	0.36 (-0.25)	0.52 (-0.14)
CYCONF	0.46 (-0.38)	0.24 (-0.14)	0.58 (0.36)	0.55 (0.49)	0.71 (0.39)	0.68 (0.59)
WTMAE	5.72	3.70	4.34	3.64	5.32	3.96

Table S3: Mean absolute errors (MAE) and mean signed errors (MSE) for the subsets of the GMTKN30 test set database for different local hybrid functionals with and without D3 dispersion correction. All errors are in kcal/mol. The weighted total mean absolute error (WTMAE) for the whole database is given at the bottom

test set	<i>t</i> -LMF	+D3	<i>s</i> -LMF	+D3	common	+D3
	MAE (MSE)	MAE (MSE)	MAE (MSE)	MAE (MSE)	MAE (MSE)	MAE (MSE)
MB08-165	8.79 (-4.31)	7.31 (-0.68)	9.34 (-7.89)	6.64 (-2.12)	10.77 (-6.32)	8.70 (-1.99)
W4-08	3.46 (-1.50)	3.49 (-1.17)	4.13 (-1.19)	4.29 (-0.48)	2.98 (0.54)	3.12 (0.90)
G21IP	4.57 (3.64)	4.58 (3.63)	4.00 (2.25)	3.99 (2.24)	5.11 (4.76)	5.11 (4.75)
G21EA	4.11 (4.11)	4.12 (4.11)	3.39 (3.38)	3.41 (3.40)	4.89 (4.89)	4.89 (4.89)
PA	1.48 (0.12)	1.55 (0.38)	1.72 (0.90)	1.89 (1.44)	1.59 (0.67)	1.66 (0.92)
SIE11	6.39 (4.75)	7.69 (6.27)	6.75 (4.95)	8.82 (7.30)	5.78 (3.79)	7.72 (5.64)
BHPERI	5.90 (5.48)	1.92 (0.99)	6.20 (5.34)	2.14 (-1.88)	7.48 (7.31)	2.75 (2.50)
BH76	2.55 (-2.00)	3.19 (-2.85)	3.39 (-3.01)	4.76 (-4.51)	1.69 (-0.68)	2.15 (-1.58)
BH76RC	2.96 (-0.93)	2.78 (-0.99)	3.01 (-0.86)	2.84 (-0.93)	2.31 (-0.63)	2.11 (-0.69)
RSE43	1.92 (-1.92)	1.34 (-1.32)	2.22 (-2.22)	1.32 (-1.32)	2.26 (-2.26)	1.65 (-1.62)
O3ADD6	1.64 (0.08)	2.45 (-2.43)	1.82 (1.09)	3.19 (-3.05)	1.49 (1.39)	1.52 (-1.43)
G2RC	2.60 (0.42)	2.79 (0.00)	2.81 (-0.09)	3.64 (-0.91)	3.07 (1.23)	2.84 (0.84)
AL2X	8.13 (-8.13)	3.14 (-3.14)	9.89 (-9.89)	2.97 (-2.97)	9.72 (-9.72)	3.40 (-3.40)
NBPRC	5.56 (4.54)	2.28 (1.40)	5.35 (4.91)	0.98 (0.01)	7.23 (5.79)	3.53 (2.21)
ISO34	1.73 (-0.60)	1.33 (-0.40)	1.92 (-0.56)	1.40 (-0.32)	1.85 (-0.67)	1.41 (-0.48)
ISOL22	6.97 (-4.51)	4.27 (-2.87)	6.78 (-4.52)	2.91 (-1.56)	7.50 (-5.11)	4.56 (-3.34)
DC9	8.68 (6.48)	5.20 (3.59)	9.32 (7.09)	5.59 (2.44)	9.19 (7.23)	4.52 (4.08)
DARC	11.18 (11.18)	4.14 (4.14)	10.09 (10.09)	1.79 (-0.92)	13.65 (13.65)	6.04 (6.04)
ALK6	7.43 (-7.43)	3.42 (-3.16)	9.14 (-9.14)	3.71 (-1.64)	8.98 (-8.98)	4.64 (-1.28)
BSR36	6.41 (-6.38)	0.48 (-0.15)	10.33 (-10.33)	2.06 (-2.06)	7.05 (-7.01)	0.99 (0.50)
IDISP	15.92 (2.35)	2.93 (2.22)	19.74 (2.17)	1.48 (1.42)	17.81 (2.68)	3.47 (2.35)
WATER27	17.00 (-16.98)	3.86 (-3.68)	22.79 (-22.76)	3.48 (-3.00)	22.92 (-22.92)	8.89 (-8.88)
S22	4.92 (-4.92)	0.33 (-0.06)	6.27 (-6.27)	0.31 (0.01)	5.69 (-5.69)	0.54 (-0.31)
ADIM6	6.64 (-6.64)	0.17 (0.01)	8.76 (-8.76)	0.64 (-0.64)	7.44 (-7.44)	0.46 (-0.46)
RG6	1.10 (-1.10)	0.25 (-0.25)	1.30 (-1.30)	0.24 (-0.14)	1.24 (-1.24)	0.42 (0.12)
HEAVY28	1.88 (-1.88)	0.44 (-0.44)	2.24 (-2.24)	0.28 (-0.13)	2.19 (-2.19)	0.38 (-0.05)
PCONF	4.57 (-4.57)	0.34 (-0.10)	6.31 (-6.31)	0.82 (-0.80)	4.83 (-4.83)	0.43 (0.28)
ACONF	1.27 (1.27)	0.19 (0.19)	1.61 (1.61)	0.04 (-0.03)	1.44 (1.44)	0.29 (0.29)
SCONF	1.02 (-0.54)	0.32 (-0.22)	1.34 (-0.71)	0.82 (0.13)	1.44 (-0.75)	0.36 (-0.35)
CYCONF	0.52 (-0.14)	0.31 (0.20)	0.70 (-0.06)	0.55 (0.53)	0.56 (-0.40)	0.31 (-0.06)
WTMAE	5.48	2.80	6.47	2.89	6.27	3.25

Table S4: Mean absolute errors (MAE) and mean signed errors (MSE) for the subsets of the GMTKN30 test set database for different local hybrid functionals with and without D3 dispersion correction. All errors are in kcal/mol. The weighted total mean absolute error (WTMAE) for the whole database is given at the bottom

test set	$\zeta$ - <i>t</i> -LMF	+D3	$\zeta$ - <i>s</i> -LMF	+D3	comb. opt. $\zeta$ - <i>t</i> -LMF	+D3
	MAE (MSE)	MAE (MSE)	MAE (MSE)	MAE (MSE)	MAE (MSE)	MAE (MSE)
MB08-165	7.68 (-2.95)	6.74 (0.08)	8.43 (-6.30)	6.61 (-1.48)	7.96 (-3.34)	6.95 (-0.63)
W4-08	2.74 (-1.03)	2.73 (-0.78)	3.18 (-0.51)	3.36 (-0.01)	2.91 (-1.94)	2.83 (-1.74)
G21IP	4.47 (3.49)	4.47 (3.48)	3.94 (2.09)	3.94 (2.08)	4.47 (3.50)	4.47 (3.50)
G21EA	4.14 (4.14)	4.14 (4.14)	3.47 (3.41)	3.48 (3.42)	4.08 (4.08)	4.08 (4.08)
PA	1.53 (-0.24)	1.51 (-0.04)	1.62 (0.51)	1.69 (0.90)	1.51 (-0.14)	1.50 (0.02)
SIE11	6.94 (5.45)	8.02 (6.70)	7.35 (5.62)	9.10 (7.63)	6.77 (5.22)	7.70 (6.30)
BHPERI	4.98 (4.33)	1.84 (0.64)	5.27 (4.12)	2.08 (-1.88)	5.21 (4.64)	2.36 (1.42)
BH76	2.95 (-2.62)	3.53 (-3.28)	3.85 (-3.63)	4.92 (-4.81)	2.75 (-2.39)	3.22 (-2.95)
BH76RC	2.39 (-0.62)	2.25 (-0.67)	2.35 (-0.45)	2.27 (-0.51)	2.40 (-0.62)	2.29 (-0.67)
RSE43	2.08 (-2.08)	1.58 (-1.58)	2.46 (-2.46)	1.68 (-1.68)	2.02 (-2.02)	1.59 (-1.59)
O3ADD6	1.96 (-0.75)	2.83 (-2.83)	2.18 (0.29)	3.19 (-3.07)	1.88 (-0.53)	2.41 (-2.37)
G2RC	2.74 (-0.09)	3.07 (-0.41)	3.37 (-0.51)	4.05 (-1.10)	2.69 (0.04)	2.91 (-0.22)
AL2X	7.14 (-7.14)	2.72 (-2.72)	8.81 (-8.81)	2.56 (-2.56)	7.40 (-7.40)	3.34 (-3.34)
NBPRC	4.51 (3.75)	2.04 (1.15)	4.48 (4.09)	0.98 (-0.06)	4.79 (3.96)	2.49 (1.67)
ISO34	1.67 (-0.56)	1.31 (-0.38)	1.92 (-0.53)	1.42 (-0.30)	1.69 (-0.57)	1.33 (-0.40)
ISOL22	6.66 (-4.14)	4.30 (-2.81)	6.50 (-3.87)	3.14 (-1.66)	6.74 (-4.24)	4.57 (-3.10)
DC9	8.17 (5.82)	5.83 (3.29)	9.20 (6.46)	6.44 (2.69)	8.36 (6.05)	5.96 (3.71)
DARC	9.62 (9.62)	3.64 (3.64)	8.77 (8.61)	1.82 (-0.55)	10.03 (10.03)	4.70 (4.70)
ALK6	6.45 (-6.45)	2.91 (-2.88)	8.14 (-8.14)	3.53 (-2.05)	6.71 (-6.71)	3.34 (-3.34)
BSR36	6.00 (-5.98)	0.68 (-0.52)	9.56 (-9.56)	1.85 (-1.85)	6.11 (-6.09)	1.17 (-1.03)
IDISP	14.73 (2.14)	3.19 (2.18)	18.30 (1.96)	1.86 (1.54)	15.04 (2.20)	4.17 (2.30)
WATER27	13.31 (-13.24)	2.25 (-1.77)	19.35 (-19.26)	3.08 (-2.38)	14.28 (-14.23)	4.09 (-3.82)
S22	4.44 (-4.44)	0.27 (0.00)	5.83 (-5.83)	0.29 (-0.01)	4.56 (-4.56)	0.47 (-0.42)
ADIM6	6.13 (-6.13)	0.17 (0.08)	8.37 (-8.37)	0.67 (-0.67)	6.27 (-6.27)	0.37 (-0.37)
RG6	1.00 (-1.00)	0.24 (-0.24)	1.26 (-1.26)	0.24 (-0.20)	1.03 (-1.03)	0.31 (-0.31)
HEAVY28	1.68 (-1.68)	0.43 (0.43)	2.10 (-2.10)	0.31 (-0.22)	1.73 (-1.73)	0.58 (-0.58)
PCONF	4.42 (-4.42)	0.41 (-0.29)	6.12 (-6.12)	0.86 (-0.83)	4.46 (-4.46)	0.59 (-0.59)
ACONF	1.16 (1.16)	0.25 (0.25)	1.48 (1.48)	0.08 (0.08)	1.19 (1.19)	0.36 (0.36)
SCONF	0.75 (-0.40)	0.35 (-0.22)	0.98 (-0.52)	0.70 (0.03)	0.82 (-0.44)	0.38 (-0.34)
CYCONF	0.51 (0.02)	0.46 (0.33)	0.75 (0.14)	0.64 (0.59)	0.51 (-0.02)	0.46 (0.27)
WTMAE	4.94	2.66	5.95	2.84	5.06	2.88

Table S5: Mean absolute errors (MAE) and mean signed errors (MSE) for the subsets of the GMTKN30 test set database for different local hybrid functionals with and without D3 dispersion correction. All errors are in kcal/mol. The weighted total mean absolute error (WTMAE) for the whole database is given at the bottom

test set	<i>Lh</i> -LSDA-SIF-SRc		<i>Lh</i> -LSDA-SIR-SRc		<i>Lh</i> -LSDA-SIR-SRc	
	erfgau MAE (MSE)	+D3 MAE (MSE)	erfgau MAE (MSE)	+D3 MAE (MSE)	erf MAE (MSE)	+D3 MAE (MSE)
MB08-165	9.48 (-5.85)	6.63 (1.30)	9.73 (-5.91)	6.53 (0.82)	10.40 (-6.51)	6.65 (0.07)
W4-08	3.69 (-1.51)	4.04 (-0.13)	3.13 (-0.65)	3.68 (0.65)	2.86 (-0.72)	3.42 (0.60)
G21IP	3.41 (1.65)	3.37 (1.67)	3.81 (2.74)	3.79 (2.75)	4.29 (2.71)	4.30 (2.73)
G21EA	2.56 (2.39)	2.60 (2.45)	3.40 (3.39)	3.45 (3.44)	3.78 (3.78)	3.84 (3.84)
PA	1.71 (-0.90)	1.69 (0.17)	1.59 (-0.36)	1.67 (0.65)	1.65 (-0.38)	1.72 (0.65)
SIE11	4.58 (1.66)	6.90 (4.73)	4.98 (2.42)	7.30 (5.28)	5.10 (2.51)	7.41 (5.34)
BHPERI	7.53 (7.25)	2.77 (-2.07)	6.92 (6.69)	2.59 (-2.11)	8.56 (8.33)	1.53 (-0.35)
BH76	1.79 (1.43)	1.98 (-0.84)	1.55 (0.67)	2.25 (-1.47)	1.53 (0.42)	2.35 (-1.72)
BH76RC	2.21 (-1.03)	1.82 (-1.16)	2.23 (-0.88)	1.81 (-1.00)	2.24 (-0.78)	1.76 (-0.90)
RSE43	2.28 (-2.28)	1.38 (-1.28)	2.29 (-2.29)	1.40 (-1.33)	2.31 (-2.31)	1.45 (-1.39)
O3ADD6	2.94 (2.58)	4.07 (-3.46)	2.42 (2.16)	3.97 (-3.51)	2.35 (2.30)	3.80 (-3.34)
G2RC	2.85 (-0.68)	3.83 (-2.31)	2.54 (0.00)	3.09 (-1.54)	2.56 (0.45)	2.77 (-1.12)
AL2X	11.13 (-11.13)	3.47 (-2.96)	10.61 (-10.61)	3.38 (-3.09)	10.87 (-10.87)	3.59 (-3.53)
NBPRC	8.23 (7.01)	2.27 (0.81)	7.85 (6.56)	1.97 (0.74)	8.05 (6.66)	1.97 (0.93)
ISO34	2.28 (-0.33)	1.88 (0.15)	2.01 (-0.44)	1.58 (-0.01)	1.98 (-0.51)	1.47 (-0.06)
ISOL22	6.31 (-4.09)	2.39 (-0.28)	6.70 (-4.45)	2.39 (-0.86)	6.99 (-4.71)	2.69 (-1.14)
DC9	8.80 (8.61)	7.35 (1.02)	7.89 (7.29)	6.82 (1.28)	8.27 (7.73)	5.69 (1.80)
DARC	11.42 (11.42)	4.11 (-4.11)	12.22 (12.22)	2.39 (-2.39)	13.01 (13.01)	1.50 (-1.50)
ALK6	10.45 (-10.45)	4.02 (0.10)	9.91 (-9.91)	3.58 (-0.23)	10.35 (-10.35)	3.25 (-0.87)
BSR36	5.81 (-5.63)	3.14 (3.14)	6.23 (-6.10)	1.95 (1.95)	6.36 (-6.26)	1.60 (1.60)
IDISP	19.39 (1.38)	3.20 (-0.13)	19.50 (1.91)	2.41 (1.76)	19.00 (2.08)	1.75 (0.64)
WATER27	32.11 (-32.11)	5.75 (-5.53)	28.85 (-28.85)	4.08 (-3.84)	28.21 (-28.21)	3.64 (-3.39)
S22	7.00 (-7.00)	0.47 (-0.09)	6.54 (-6.54)	0.44 (-0.11)	6.47 (-6.47)	0.42 (-0.21)
ADIM6	9.23 (-9.23)	0.76 (-0.76)	8.59 (-8.59)	0.68 (-0.68)	8.48 (-8.48)	0.80 (-0.80)
RG6	1.59 (-1.59)	0.39 (-0.37)	1.46 (-1.46)	0.37 (-0.37)	1.44 (-1.44)	0.40 (-0.40)
HEAVY28	2.89 (-2.89)	0.53 (-0.51)	2.67 (-2.67)	0.50 (-0.49)	2.58 (-2.58)	0.48 (-0.48)
PCONF	5.72 (-5.72)	0.57 (-0.47)	5.41 (-5.41)	0.60 (-0.56)	5.35 (-5.35)	0.74 (-0.73)
ACONF	1.77 (1.77)	0.13 (-0.13)	1.65 (1.65)	0.14 (-0.14)	1.65 (1.65)	0.11 (-0.10)
SCONF	1.85 (-0.72)	1.31 (0.53)	1.73 (-0.84)	1.35 (0.59)	1.72 (-0.83)	1.35 (0.60)
CYCONF	0.61 (-0.42)	0.65 (0.65)	0.59 (-0.41)	0.60 (0.60)	0.60 (-0.43)	0.59 (0.59)
WTMAE	6.42	2.96	6.26	2.72	6.43	2.62

Table S6: Mean absolute errors (MAE) and mean signed errors (MSE) for the subsets of the GMTKN30 test set database for different density functionals with and without D3 dispersion correction. All errors are in kcal/mol. The weighted total mean absolute error (WTMAE) for the whole database is given at the bottom

test set	B35LYP	+D3	<i>Lh</i> -BLYP-CG	+D3	<i>Lh</i> -PBE-CG	+D3
	MAE (MSE)	MAE (MSE)	MAE (MSE)	MAE (MSE)	MAE (MSE)	MAE (MSE)
MB08-165	9.71 (-8.28)	8.55 (-6.43)	6.89 (-2.49)	6.17 (0.18)	5.98 (-0.50)	5.83 (1.23)
W4-08	12.23 (-12.15)	12.10 (-12.02)	2.69 (-1.98)	2.60 (-1.78)	3.42 (-2.85)	3.35 (-2.73)
G21IP	4.15 (-1.60)	4.15 (-1.60)	3.35 (-0.26)	3.36 (-0.26)	4.46 (3.46)	4.47 (3.46)
G21EA	3.76 (-2.78)	3.76 (-2.78)	1.95 (1.00)	1.96 (1.00)	3.84 (3.75)	3.84 (3.75)
PA	2.68 (2.40)	2.78 (2.50)	2.02 (-1.16)	2.01 (-0.99)	1.40 (0.71)	1.44 (0.80)
SIE11	5.99 (3.95)	6.26 (4.67)	6.87 (5.39)	7.80 (6.45)	6.98 (5.98)	7.60 (6.65)
BHPERI	6.04 (6.01)	3.92 (3.89)	3.03 (2.33)	1.15 (-0.85)	1.33 (0.44)	1.60 (-1.57)
BH76	2.43 (-1.73)	2.61 (-2.10)	3.22 (-2.94)	3.72 (-3.49)	3.16 (-2.83)	3.46 (-3.17)
BH76RC	2.84 (-0.59)	2.81 (-0.62)	2.30 (-0.61)	2.19 (-0.66)	2.10 (-0.45)	2.08 (-0.48)
RSE43	1.52 (-1.52)	1.26 (-1.25)	1.91 (-1.91)	1.49 (-1.48)	1.48 (-1.46)	1.24 (-1.21)
O3ADD6	3.20 (-2.55)	3.79 (-3.79)	2.86 (-1.91)	3.72 (-3.72)	4.08 (-3.71)	4.88 (-4.88)
G2RC	2.95 (-1.33)	3.03 (-1.49)	2.52 (-0.25)	2.73 (-0.51)	3.34 (-0.83)	3.58 (-0.97)
AL2X	7.61 (-7.61)	4.81 (-4.81)	6.79 (-6.79)	2.80 (-2.80)	4.10 (-4.07)	1.66 (-1.44)
NBPRC	4.75 (3.81)	3.61 (2.28)	4.11 (3.43)	1.95 (1.17)	2.46 (1.99)	1.57 (0.55)
ISO34	1.99 (0.02)	1.71 (0.13)	1.58 (-0.50)	1.21 (-0.33)	1.44 (-0.60)	1.22 (-0.49)
ISOL22	7.66 (-4.55)	6.24 (-3.80)	6.67 (-3.98)	5.27 (-1.89)	5.43 (-3.31)	4.03 (-2.61)
DC9	12.99 (6.36)	10.96 (4.75)	7.91 (5.37)	4.94 (3.07)	6.54 (3.19)	5.86 (1.64)
DARC	12.42 (12.42)	8.87 (8.87)	9.57 (9.57)	4.30 (4.30)	5.55 (5.52)	2.60 (2.14)
ALK6	10.05 (-9.61)	7.53 (-7.02)	7.43 (-7.43)	4.21 (-4.21)	2.81 (-2.81)	1.24 (-0.52)
BSR36	11.32 (-11.32)	7.52 (-7.52)	5.81 (-5.80)	0.92 (-0.84)	5.94 (-5.94)	2.33 (-2.33)
IDISP	16.72 (2.87)	8.95 (2.85)	13.76 (2.09)	8.54 (8.26)	10.36 (1.79)	2.93 (1.81)
WATER27	5.95 (-5.72)	1.84 (1.84)	9.49 (-9.32)	1.62 (0.97)	5.07 (-4.69)	2.79 (2.58)
S22	3.45 (-3.45)	0.71 (-0.53)	3.99 (-3.99)	0.28 (0.10)	2.71 (-2.71)	0.25 (0.12)
ADIM6	4.64 (-4.64)	0.39 (-0.39)	5.70 (-5.70)	0.20 (0.13)	3.81 (-3.81)	0.36 (0.36)
RG6	0.75 (-0.75)	0.27 (-0.26)	0.95 (-0.95)	0.25 (-0.25)	0.56 (-0.56)	0.12 (-0.11)
HEAVY28	1.34 (-1.34)	0.53 (-0.53)	1.61 (-1.61)	0.49 (-0.49)	0.87 (-0.87)	0.22 (-0.12)
PCONF	3.42 (-3.42)	0.72 (-0.72)	4.15 (-4.15)	0.43 (-0.34)	3.17 (-3.17)	0.56 (-0.56)
ACONF	0.95 (0.95)	0.36 (0.36)	1.04 (1.04)	0.22 (0.22)	0.71 (0.71)	0.16 (0.16)
SCONF	1.23 (-0.83)	0.76 (-0.76)	0.50 (-0.27)	0.37 (-0.17)	0.40 (-0.31)	0.31 (-0.27)
CYCONF	0.57 (-0.57)	0.41 (-0.41)	0.47 (0.03)	0.45 (0.32)	0.39 (0.10)	0.38 0.26
WTMAE	6.18	4.62	4.47	2.63	3.71	2.60

Table S7: Deviations from S22 reference values (in kcal/mol) for two uncalibrated local hybrids, with and without D3 corrections.

	ref. values <sup>a</sup>	<i>Lh</i> -LSDA-SIF-SRc	<i>Lh</i> -LSDA-SIR-SRc deviations		
			+D3	+D3	+D3
<b>H-bonded complexes</b>					
(NH <sub>3</sub> ) <sub>2</sub>	-3.17	3.29	1.00	2.99	0.83
(H <sub>2</sub> O) <sub>2</sub>	-5.02	2.79	0.58	2.48	0.40
formic acid dimer	-18.80	5.33	-0.77	4.82	-0.87
formamide dimer	-16.12	6.30	-0.16	5.79	-0.25
uracil dimer	-20.69	7.22	-0.05	6.72	-0.07
2-pyridoxine-2-aminopyridine	-17.00	7.78	-0.11	7.24	-0.13
adenine*thymine WC	-16.74	8.99	0.72	8.39	0.67
<b>dispersion-dominated complexes</b>					
(CH <sub>4</sub> ) <sub>2</sub>	-0.53	2.12	0.82	1.94	0.73
(C <sub>2</sub> H <sub>4</sub> ) <sub>2</sub>	-1.50	4.38	0.47	4.05	0.42
benzene*CH <sub>4</sub>	-1.45	4.14	0.60	3.86	0.57
PD benzene dimer	-2.62	9.46	0.47	8.90	0.55
pyrazine dimer	-4.20	10.08	0.21	9.48	0.33
stacked uracil dimer	-9.74	13.51	-0.76	12.72	-0.52
stacked indole*benzene	-4.59	13.34	0.25	12.61	0.45
stacked adenine*thymine	-11.66	19.00	-0.88	17.95	-0.50
<b>mixed complexes</b>					
ethene*ethine	-1.51	2.28	0.51	2.10	0.45
benzene*H <sub>2</sub> O	-3.29	3.65	-0.35	3.37	-0.36
benzene*NH <sub>3</sub>	-2.32	3.87	0.08	3.60	0.07
benzene*HCN	-4.55	4.77	-0.58	4.47	-0.51
T-shaped benzene dimer	-2.71	6.05	0.16	5.69	0.20
T-shaped indole benzene	-5.62	7.86	-0.54	7.43	-0.44
phenol dimer	-7.09	7.85	0.31	7.33	0.29

<sup>a</sup>Relative energies were calculated as  $E(\text{dimer}) - \sum E(\text{monomers})$ .

Table S8: Deviations from S22 reference values (in kcal/mol) for two calibrated local hybrids, with and without D3 corrections.

	ref. values <sup>a</sup>	<i>Lh</i> -BLYP-CG <i>Lh</i> -PBE-CG deviations			
		+D3		+D3	
<b>H-bonded complexes</b>					
(NH <sub>3</sub> ) <sub>2</sub>	-3.17	1.43	0.52	0.80	0.19
(H <sub>2</sub> O) <sub>2</sub>	-5.02	0.72	-0.01	0.27	-0.20
formic acid dimer	-18.80	1.05	-1.35	0.14	-1.37
formamide dimer	-16.12	2.32	-0.31	1.24	-0.46
uracil dimer	-20.69	3.04	-0.29	2.02	-0.30
2-pyridoxine-2-aminopyridine	-17.00	3.55	-0.40	2.35	-0.43
adenine*thymine WC	-16.74	4.45	0.12	3.07	0.03
<b>dispersion-dominated complexes</b>					
(CH <sub>4</sub> ) <sub>2</sub>	-0.53	1.26	-0.26	0.79	0.03
(C <sub>2</sub> H <sub>4</sub> ) <sub>2</sub>	-1.50	2.53	-0.11	1.56	0.12
benzene*CH <sub>4</sub>	-1.45	2.53	-0.18	1.65	0.03
PD benzene dimer	-2.62	6.30	-0.06	4.43	-0.05
pyrazine dimer	-4.20	6.60	-0.02	4.70	0.17
stacked uracil dimer	-9.74	8.73	0.76	6.37	-0.25
stacked indole*benzene	-4.59	9.02	-0.16	6.57	0.34
stacked adenine*thymine	-11.66	12.49	0.49	9.28	0.36
<b>mixed complexes</b>					
ethene*ethine	-1.51	1.22	-0.12	0.67	-0.09
benzene*H <sub>2</sub> O	-3.29	1.96	0.42	1.12	-0.55
benzene*NH <sub>3</sub>	-2.32	2.29	0.13	1.43	-0.27
benzene*HCN	-4.55	2.79	-0.04	1.73	-0.04
T-shaped benzene dimer	-2.71	3.91	-0.21	2.73	0.07
T-shaped indole benzene	-5.62	5.13	-0.18	3.62	0.03
phenol dimer	-7.09	4.44	-0.03	3.16	0.11

<sup>a</sup>Relative energies were calculated as E(dimer) -  $\sum$ E(monomers).

Table S9: Deviations from S22 reference values (in kcal/mol) for the B35LYP global hybrid, with and without D3 corrections.

	ref. values <sup>a</sup>	B35LYP deviations	
<b>H-bonded complexes</b>		+D3	
(NH <sub>3</sub> ) <sub>2</sub>	-3.17	0.78	0.13
(H <sub>2</sub> O) <sub>2</sub>	-5.02	0.20	-0.30
formic acid dimer	-18.80	0.72	-0.86
formamide dimer	-16.12	1.48	-0.30
uracil dimer	-20.69	2.06	-0.36
2-pyridoxine-2-aminopyridine	-17.00	2.91	0.03
adenine*thymine WC	-16.74	3.47	0.33
<b>dispersion-dominated complexes</b>			
(CH <sub>4</sub> ) <sub>2</sub>	-0.53	0.84	0.09
(C <sub>2</sub> H <sub>4</sub> ) <sub>2</sub>	-1.50	1.77	0.29
benzene*CH <sub>4</sub>	-1.45	2.04	0.37
PD benzene dimer	-2.62	6.14	1.54
pyrazine dimer	-4.20	6.32	1.67
stacked uracil dimer	-9.74	7.99	1.17
stacked indole*benzene	-4.59	9.01	2.59
stacked adenine*thymine	-11.66	12.00	2.80
<b>mixed complexes</b>			
ethene*ethine	-1.51	0.70	-0.09
benzene*H <sub>2</sub> O	-3.29	1.66	-0.06
benzene*NH <sub>3</sub>	-2.32	1.92	0.16
benzene*HCN	-4.55	2.19	0.31
T-shaped benzene dimer	-2.71	3.37	0.61
T-shaped indole benzene	-5.62	4.70	0.99
phenol dimer	-7.09	3.65	0.50

<sup>a</sup>Relative energies were calculated as  $E(\text{dimer}) - \sum E(\text{monomers})$ .

# List of Publications

- I. M. Renz, K. Theilacker, C. Lambert, M. Kaupp "A reliable quantum-chemical protocol for the characterization of organic mixed-valence compounds" *J. Am. Chem. Soc.* **2009**, *131*, 16292.
- II. K. Theilacker, A. V. Arbuznikov, H. Bahmann, M. Kaupp "Evaluation of a combination of local hybrid functionals with DFT-D3 corrections for the calculation of thermochemical and kinetic data" *J. Phys. Chem. A* **2011**, *115*, 8990.
- III. K. Theilacker, D. Buhrke, M. Kaupp "Validation of the Direct-COSMO-RS Solvent Model for Diels-Alder Reactions in Aqueous Solution" *J. Chem. Theor. Comput.* **2015**, *11*, 111.
- IV. K. Theilacker, H. B. Schlegel, M. Kaupp, P. Schwerdtfeger "Relativistic and Solvation Effects on the Stability of Gold(III) Halides in Aqueous Solution" *Inorg. Chem.* **2015**, *54*, 9869.
- V. N. Kroll, K. Theilacker, M. Schoknecht, D. Baabe, D. Wiedemann, M. Kaupp, A. Grohmann, G. Hörner "Controlled ligand distortion and its consequences for structure, symmetry, conformation and spin-state preferences of iron(II) complexes" *Dalton Trans.* **2015**, *44*, 19232.
- VI. M. Kaupp, S. Gückel, M. Renz, S. Klawohn, K. Theilacker, M. Parthey, C. Lambert "Electron Transfer Pathways in mixed-valence paracyclophane-bridged bis-triarylamine radical cations" *J. Comput. Chem.* **2016**, *37*, 93.
- VII. K. Theilacker, A. V. Arbuznikov, M. Kaupp "Gauge effects in local hybrid functionals evaluated for weak interactions and the GMTKN30 test set" *Mol. Phys.* **2016**, *114*, 1118.

# Copyright

Chapter 3.3 is reproduced in part/adapted with permission from N. Kroll, K. Theilacker, M. Schoknecht, D. Baabe, D. Wiedemann, M. Kaupp, A. Grohmann, G. Hörner "Controlled ligand distortion and its consequences for structure, symmetry, conformation and spin-state preferences of iron(II) complexes" *Dalton Trans.* **2015**, 44, 19232, doi:10.1039/C5DT02502H. Copyright 2015 The Royal Society of Chemistry.

Chapter 4.1 is reproduced in part/adapted with permission from K. Theilacker, D. Buhrke, M. Kaupp "Validation of the Direct-COSMO-RS Solvent Model for Diels-Alder Reactions in Aqueous Solution" *J. Chem. Theor. Comput.* **2015**, 11, 111, doi:10.1021/ct5008857. Copyright 2014 American Chemical Society.

Chapter 4.2 is reproduced in part/adapted with permission from K. Theilacker, H. B. Schlegel, M. Kaupp, P. Schwerdtfeger "Relativistic and Solvation Effects on the Stability of Gold(III) Halides in Aqueous Solution" *Inorg. Chem.* **2015**, 54, 9869, doi:10.1021/acs.inorgchem.5b01632. Copyright 2015 American Chemical Society.

Chapter 5 is reproduced in part/adapted with permission from K. Theilacker, A. V. Arbuznikov, M. Kaupp "Gauge effects in local hybrid functionals evaluated for weak interactions and the GMTKN30 test set" *Mol. Phys.* **2016**, 114, 1118, doi:10.1080/00268976.2016.1139209. Copyright 2016 Taylor&Francis.

# Acknowledgements

*"Good friends, good books, and a sleepy conscience: this is the ideal life."*

- Mark Twain

First of all, I would like to thank my supervisor *Prof. Dr. Martin Kaupp* for his continuing support and for the interesting and diverse projects during my PhD work. Working with you always meant new and interesting routes to take, often with the danger of learning something new. I am especially thankful for the opportunity to attend the Sostrup Summer School and for the different conferences and workshops we went together. The decision to stay with the group after my diploma thesis and follow you to Berlin was certainly not a hard choice for me to make.

Speaking of Berlin, I want to mention all the non-chemists in the TU Berlin, who provided much needed help and were often essential for the success of my work. My thanks go to *Heidi Grauel* for her help with all workstation related problems and to *Nadine Rechenberg* for her help with all kinds of administrative issues that came up during my stay at the TU. I also want to thank *Sven Grottke* and *Norbert Paschedag* for taking good care of the numerik cluster (my 'laboratory' and all important workhorse so to speak). Thanks also for all the quick and uncomplicated answers to my questions, and for your help with computer problems of all sorts.

At this point I want to thank all my cooperation partners I had the pleasure to work with. From the TU Berlin: *Marc Schoknecht*, *Nicole Kroll*, *Gerald Hörner*, and, of course, *Prof. Dr. Andreas Grohmann*. Thank you for the interesting discussions we had and for the fruitful joint experimental and theoretical work in our collaboration. My best wishes go to my former Bachelor student *David Buhrke* who did not stay in the Kaupp group, but was always pleasant to work with. Sometimes good ideas come from far away places and so my thanks also go to *Prof. Dr. Peter Schwerdtfeger* from the other side of the planet and to *Prof. Dr. Bernhard Schlegel*. Out of the blue I found myself involved in an interesting new project with them and discovered that

cold winters in Berlin, combined with hot summers on the southern hemisphere, seem to provide perfect conditions for good scientific results, as our collaboration clearly showed.

Since the beginning of my diploma thesis in Würzburg, *Dr. Alexey Arbuznikov* has always been my reliable expert on local hybrids. Of course he was also in charge of the best team of quantum chemistry teaching assistants ever assembled, so it is no wonder the QC courses with him were like a breeze (not so much for some of the students though). My thanks go to all the members of the Kaupp group and especially to *Robert Müller*, who shared an office with me since we moved to Berlin, and to *Martin Enke*, whom we inherited from *Hilke Bahmann* and *Johannes Schraut*. *Toni Maier*, *Sascha Klawohn*, *Caspar Schattenberg*, *Matthias Haasler*, *Simon Gückel*, *Sebastian Gohr*, and all occasional visitors to our regular gaming group, will also be thoroughly missed by me, as will our many work and non-work related discussions.

Finally, I want to thank my parents *Kilian* and *Marina* and my brother *Karsten* and his wife *Vanessa* for all their love and support during my work on this thesis. Thanks to my happy little sunshine *Lena* and to *Eva*, *Robert*, *Emma*, *Marianne*, and *Klaus*. This thesis is dedicated to my grandmother *Marlies Theilacker*, who always believed in me.

*"There is nothing in the world so irresistibly contagious as laughter and good humor."*

- Charles Dickens, A Christmas Carol